SOLUTION FABRICATION FOR MULTIFILAMENTARY TAPES OF THE SECOND-GENERATION HIGH-TEMPERATURE SUPERCONDUCTOR

A Dissertation

Presented to

the Faculty of the Department of Mechanical Engineering

University of Houston

In Partial Fulfillment

of the Requirements for the Degree

Doctor of Philosophy

in Materials Engineering

by

Xinwei Cai

August 2016

SOLUTION FABRICATION FOR MULTIFILAMENTARY TAPES

OF THE SECOND-GENERATION HIGH-TEMPERATURE SUPERCONDUCTOR

Xinwei Cai

Approved:

Chair of the Committee
Venkat Selvamanickam, Professor,
Mechanical Engineering

Co-chair of the Committee
Anima Bose, Associate Professor,
College of Technology

Committee Members:

Haleh Ardebili, Assistant Professor,
Mechanical Engineering

Jae-Hyun Ryou, Assistant Professor,
Mechanical Engineering

James K. Meen, Assistant Professor,
Department of Chemistry

Suresh K. Khator, Associate Dean,
Cullen College of Engineering

Dmitri Litvinov, Professor and
Director, Interdisciplinary Program
in Materials Engineering

Acknowledgments

I would like to express my sincere gratitude to my advisor, Prof. Venkat Selvamanickam, for the opportunity to finish this degree and for his support for the past six years. His patience, motivation, and enthusiasm have inspired me countless times on my way to finishing this dissertation. I cannot imagine a better mentor than he is.

I would like to thank Dr. Yunfei Qiao and Dr. Anima Bose for their excellent guidance and insightful suggestions over the past few years. I would also like to show my thanks to my committee members, Dr. Haleh Ardebili, Dr. Jae-Hyun Ryou, and Dr. James K. Meen for their evaluations and comments.

I would like to express my gratitude to all other researchers and students in our group, including Dr. Goran Majkic, Dr. Eduard Galstyan, Dr. Yimin Chen, Dr. Xuming Xiong, Dr. Xiaofen Li, Dr. Aixia Xu, Dr. Senthil Sambandam, Dr. Yong Suk Cho, Dr. Wei Li, Yue Zhang, Ibrahim Kesgin, Yuhao Liu, Rehan Mallick, Yao Yao, Meysam Heydari Gharahcheshmeh, Anis Ben Yahia, Narayan Das Khatri, Tuo Shi, Albert P. Guevara, Ying Gao, Yongkuan Li, Haichao Guo, Yuan Zhang, Wenbo Luo, Jian Cao, Yangxing Zhang, Aarthi Sundaram, Xin Tao, Yuanfei Bi, Louis Delgado, and Jeong Kim. I do appreciate their help and support while I worked on my PhD. I would also like to thank the staff at TcSUH: Bernadette Williams and Helen Espinoza, and graduate advisors Trina Johnson and Monica A. Sanchez.

In addition, I appreciate the funding for this research provided by Superpower Inc., the U.S. Department of Energy, and the National Science Foundation.

Finally, I want to dedicate this work to my mother and father, Huan Huang and Yixiang Cai. Thank you very much for all the support. I hope this work makes you proud.

SOLUTION FABRICATION FOR MULTIFILAMENTARY TAPES OF THE SECOND GENERATION HIGH-TEMPERATURE SUPERCONDUCTOR

An Abstract

Of a

Dissertation

Presented to

the Faculty of the Department of Mechanical Engineering

University of Houston

In Partial Fulfillment

of the Requirements for the Degree

Doctor of Philosophy

in Materials Engineering

by

Xinwei Cai

August 2016

Abstract

Energy loss is generated in 2G-HTS in AC applications. Multifilamentization is proved effective for AC loss reduction. In this dissertation, attempts on developing an etch-free, lower cost and scalable solution fabrication of multifilament of 2G-HTS have been made. Three different approaches are developed with inkjet printing insulator lines, MOD YBCO superconductor filaments, and selective electrodepositing Ag overlayer and Cu stabilizer.

Inkjet printing insulator lines of the multifilament tape are studied as the replacement of the more common laser-striation technique of multifilamentizing 2G-HTS. The insulator materials selection, ink preparation, inkjet-printing drop stream and printed line formation control are studied. Buffer tape is divided into 12 filaments by 11 0.17 mm-wide inkjet-printed BTO insulator lines. Selective epitaxial growth of REBCO is achieved on the printed buffer. 17.6 times AC loss reduction is achieved with only 25% reduction of I_c. A 1 m long tape is printed and filamentized successfully.

TFA-MOD is used as a substitution of MOCVD, for a bottom-up low-cost YBCO deposition process that utilize the benefit of the printed buffer. Studies on MOD buffer selection, precursor preparation, coating technique, heat treatment condition and their impact on superconducting performance has been done. TFA-MOD YBCO thin film has shown J_c of 0.67 MA/cm^2 and T_c of 89.9 K. MOD has been adapted to the inkjet-printed buffer and selective deposition is achieved due to the hydrophobic nature of BTO lines.

Selective deposition of Ag overlayer has been achieve on inkjet-printed multifilamentary samples, selective electroplating of Cu stabilizer has been achieved on both inkjet-printed and laser-striated multifilamentary samples. Electroplating condition optimization, electrolyte potential and ion flux distribution simulation, interfacial bonding and superconductivities

evaluation have been studied. Electrodeposited Ag and Cu has smooth and dense surfaces, good thickness uniformity and strong interfacial bonding, and has minimal coupling between the superconducting filaments. 3.44 times less AC loss is achieved on a fully-stabilized 12-filament 2G-HTS with the cost of 10% I_c reduction. The electrodeposition process has been scaled up to reel-to-reel fabrication, a 100 m-long bare REBCO tape is electrodeposited with Ag overlayer and a 30 m-long 12-filmant laser-striated 2G-HTS has been electroplated with Cu stabilizer.

Table of Contents

List of Figures

List of Tables

Chapter 1. Introduction

1.1 Second-generation high-temperature superconductor

$YBa_2Cu_3O_{7-\delta}$ (YBCO) is the first material discovered to show superconductivity above 77 K (boiling point of liquid nitrogen). It has an orthorhombic three-layered perovskite structure (Fig. 1.1). Because of its anisotropic crystallography, YBCO also shows anisotropy in superconductivity, with better superconducting performance is shown along the a-b plane. The Cu-O planes between the Ba-centered and Y-centered sub-cells are responsible for the transport of superconducting current.

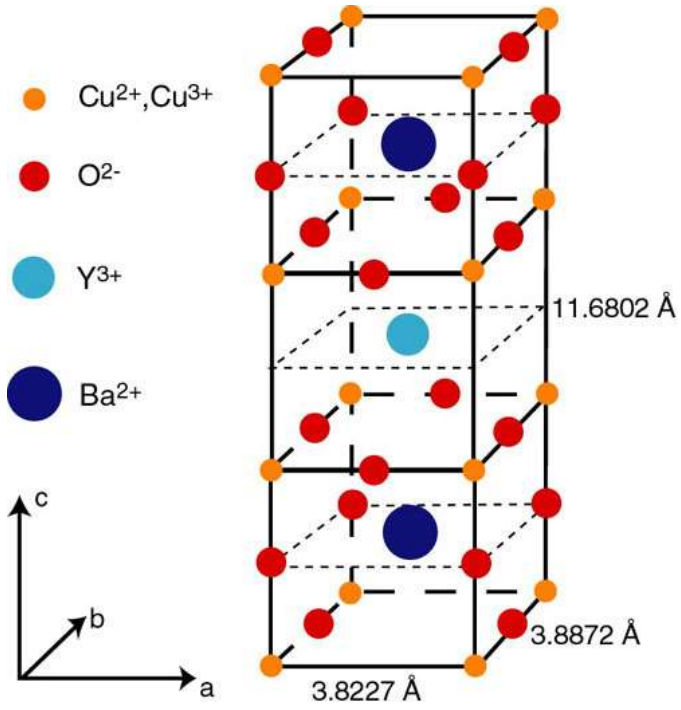

Fig. 1.1. Schematic of a YBCO unit cell.

Second-generation high-temperature superconductor (2G-HTS) tapes were developed to achieve superior performance by alignment of grains along the a-b planes. Fig. 1.2 shows a typical configuration of 2G-HTS tape from Superpower Inc. [1]. In this case, the

superconducting (RE)$Ba_2Cu_3O_{7-\delta}$ (REBCO; RE=rare earth, e.g. Y, Gd etc.) is fabricated with metal-organic chemical vapor deposition (MOCVD). REBCO thin film is deposited on Hastelloy C-276 substrate with complex buffer-layers that exhibits biaxial texture wherein the grains are aligned in the plane (a-b plane) as well as out the plane (c-axis). The Hastelloy substrate serves as the mechanical backbone of the conductor and as the foundation for growing the subsequent layers [2]. The buffer protects the superconducting film from chemical contamination from the substrate, and its biaxial texture structure serves as the template for the epitaxial growth of the REBCO layer [3]. After MOCVD, REBCO is covered by sputtered Ag overlayer and the tape is then encapsulated by electroplated Cu stabilizer on all sides.

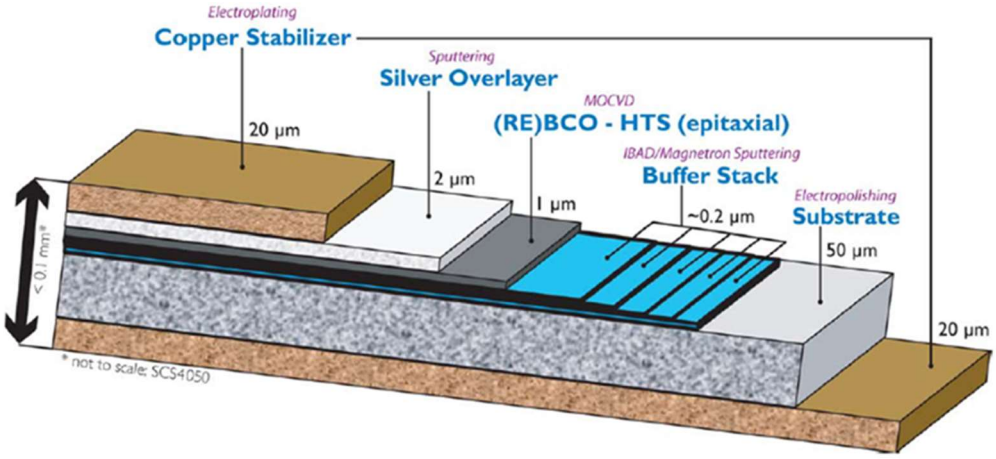

Fig. 1.2. Schematic of Superpower Inc. 2G-HTS tape.

1.2 AC loss in superconductors

In direct current (DC) applications, the energy loss of a superconductor is negligible due to its zero resistance. However, the situation is different when the superconductor is operating under an alternating current (AC) environment with alternating transport current and transverse magnetic field. Based on the source, AC loss that occurs in 2G-HTS can be categorized as transport loss and magnetization loss.

Transport loss, also known as self-field loss, is caused by its own transverse field induced by transport AC current [4]. Transport loss is generally a few magnitudes smaller than magnetization loss. Magnetization loss can be categorized into three groups: Hysteresis loss, eddy current loss and coupling loss.

Hysteresis loss is generated by the magnetic hysteresis inside the superconductor [5-7]. Fig. 1.3 shows the cross section of a superconductor in a time-varying magnetic field [8]. The magnetic field penetrates the material in the form of flux lines. If the magnetic field is changed, the flux-line pattern and internal magnetic field change as well. The magnetic-field variation inside the material induces an electric field E according to Faraday's law: $\nabla \times E = -dB/dt$. The electric field drives screening currents in the material. The middle of the superconductor, shown in grey in Fig. 1.3 is screened from the magnetic field. The screening currents determine the magnetic-field distribution in the superconductor according to Ampere's law: $\nabla \times B = \mu_0 J$. As the result, the screening currents dissipate energy at a local power density given by $E \cdot J$. The energy is spent on depinning and moving the flux lines, and is dissipated as heat. Hysteresis loss the major component of AC loss.

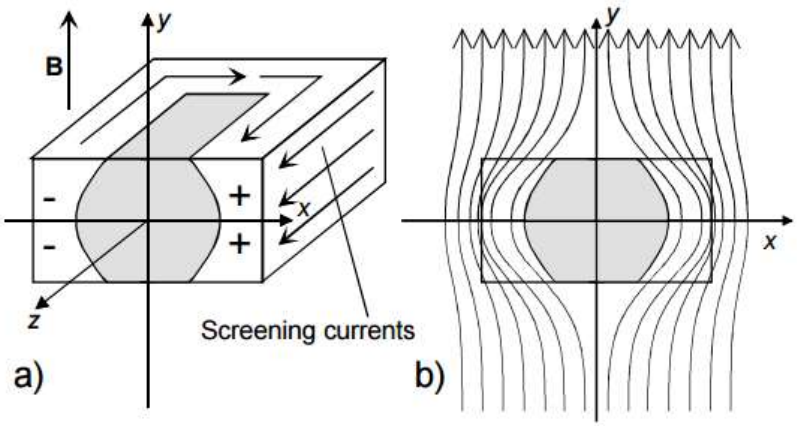

Fig. 1.3. Cross-section of a superconductor in a changing external magnetic field.

Eddy current loss, is generated by the conductive metal component of 2G-HTS inside the alternating magnetic field [9, 10]. Eddy current is induced by the time-varying field inside the metal substrate and stabilizer, and generates the resistive losses. The energy loss is also dissipated as heat and carried away by the liquid nitrogen. Eddy current loss is relatively small compared with the other components.

Coupling loss typically take place in a multifilament sample. Filamentization of 2G-HTS is an effective approach to reduce the AC loss where the flat 2G-HTS tape is filamentized into narrow stripes. The inductive screening current is limited inside each filament. Both the screening current and its loop size reduces with filamentization and results in a reduction in the magnetic hysteresis of the tape and thus lower loss. Theoretically, a *n*-filament 2G-HTS can result in *n*-times reduction of AC loss [7]. Fig. 1.4 shows the schematic of the screening current induced in multifilamentary 2G-HTS by transverse magnetic field [11]. When the superconducting filaments are electrically coupled, the induced screening current loop will exceed a single filament through the non-superconducting coupling junctions where resistive loss is generated. The undesirable coupling loss in multifilament samples can completely cancel out the benefit from filamentization [12-14].

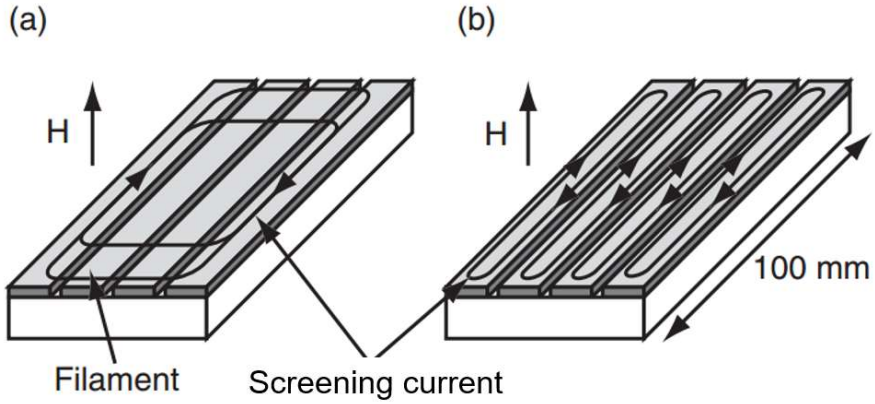

Fig. 1.4. Schematic of the screening current induced in multifilamentary 2G-HTS by transverse magnetic field.

1.3 Stabilizer layer in 2G-HTS

Quench is an abnormal termination of operation in the superconducting device. At the moment of quench, part of the superconducting coil enters the normal state. That particular part of the coil will suffer from a large amount of Joule heating generated by the high current in the superconducting coil, which might result in irreversible damage to the superconductor.

The stabilizer, which is made of a thermally and electrically conductive metal, would help to temporarily bypass the current and dissipate the heat, protecting the superconducting device from damage by the quench. The stabilizer plays a crucial role by enabling bypass of over-current and transferring the heat generated at the moment of fault current passing through the superconductor [15].

The concept of stabilizer layer has been used broadly in first-generation (1G) HTS material and low-temperature superconductors (LTS). 1G-HTS wires are made using a powder-in-tube thermal mechanical process [16]. Ag is widely chosen as a sheath material for 1G-HTS wires and tapes and has high thermal and electrical conductivity to serve as stabilizer [17, 18].

In the case of 2G-HTS, the Hastelloy substrate does not have the conductivity to stabilize the superconductor [19] and so a thick layer of Cu is laminated or electrodeposited on both sides of the 2G-HTS. The thickness of the Cu stabilizer depends on the application and the critical current (I_c) of the specific tape [20].

In an AC environment, heat generated from AC loss can potentially leads to quench of the superconducting devices. Therefore, stabilization on the multifilamentary tapes is essential. The Cu stabilizer layer also needs to be filamentized along with the superconductor below to minimize the coupling loss. Otherwise, the multifilamentary 2G-HTS may have even higher AC loss compared to non-striated tape [12].

1.4 Research procedure and objectives, outline of the dissertation

1.4.1 Research procedure

Two different approaches are employed to achieve the fully stabilized multifilamentary 2G-HTS: the more common approach of utilizing laser striation to filamentize the Ag coated 2G-HTS tapes and electroplating to selectively deposit the Cu stabilizer, and a novel etch-free bottom-up solution deposition process to build up the multifilamentary 2G-HTS tapes from the buffer layer.

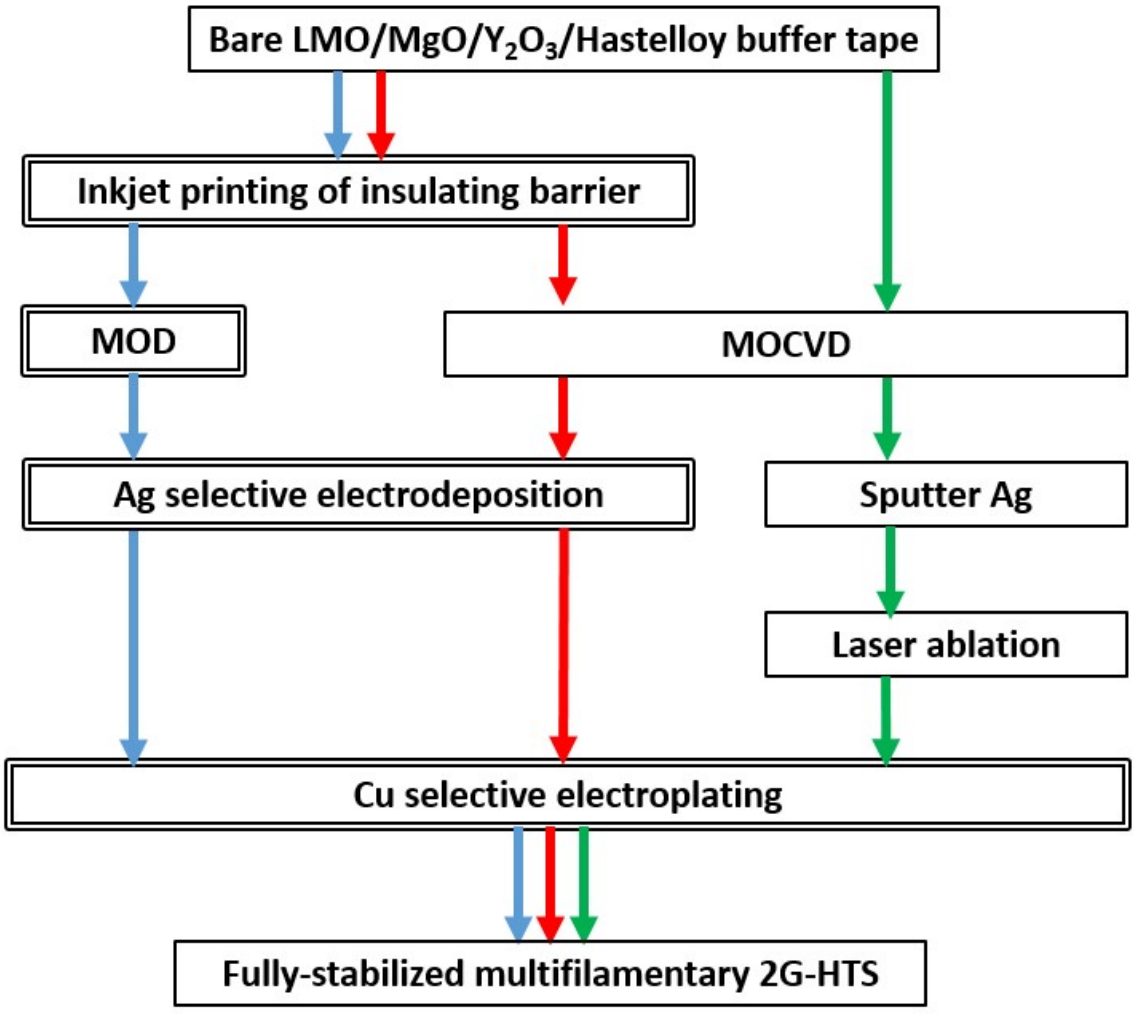

Fig. 1.5. A schematic of the procedures used in this work. The main tasks of this dissertation are emphasized.

In this dissertation, three different solution methods are implemented: inkjet-printing, metal organic deposition (MOD) and reel-to-reel selective electroplating Ag and Cu to fabricate fully stabilized multifilamentary 2G-HTS (Fig. 1.5).

First is the inkjet printing of insulating barriers. Instead of filamentizing the superconductor after REBCO deposition, inkjet printing is employed to build insulating barriers on the buffered Hastelloy tape before the deposition of the superconducting layer. Insulating lines are printed along the length of the buffer tape to divide the tape into multiple filaments. Filamentization is achieved by selective deposition. The following MOD/MOCVD of superconducting layer, electrodeposition of Ag overlayer and electroplating of Cu stabilizer are selectively done on the bare buffer surface between inkjet-printed lines. Thus, this method is an etch-free deposition process for multifilamentary REBCO tapes.

MOD is employed to this work as a replacement of our state-of-art MOCVD process. MOD is a low-cost solution fabrication process that is capable of making high quality YBCO. With MOD introduced to this work, an all-solution fabrication procedure of fabricating the multifilamentary tapes is achieved. The cost of the all-solution process can be significantly lower than the more conventional MOCVD/sputtered Ag/laser-ablation approaches. Additionally, MOD is a bottom-up deposition process, which can benefit more from the inkjet-printed buffer and selective deposition of MOD is easier to achieve.

Finally, a reel-to-reel selective electroplating process is used to build the stabilizer layer for the multifilamentary tapes. This can be applied to both inkjet-printed and laser-striated samples. For inkjet printing tapes, due to the resistivity difference between the Ag-coated superconducting filament and the highly-resistive inkjet-printed lines, selective deposition could be directly achieved. Laser-striated samples are annealed in oxygen is to oxide the expose

Hastelloy before electroplating. The resistive oxide layer formed on the laser ablation groove surface blocks the deposition current and makes the subsequent selective plating possible.

1.4.2 Objectives

The objective of this work is to develop an etch-free, lower cost and scalable fabrication of multifilament of 2G-HTS. In this dissertation, three different solution processing methods are developed to fabricate multifilamentary tapes as follows.

- A novel multifilamentary technique is developed as a replacement of the more common laser-striation technique of 2G-HTS. Insulating lines are inkjet-printed on the buffer tape surface. Combining with selective epitaxial growth of MOCVD YBCO and selective electrodeposition of Ag overlayer and Cu stabilizer, an etch-free and fully-stabilized procedure for multifilamentary 2G-HTS is accomplished. The insulator selection, ink preparation, inkjet-printing drop stream and printed line formation control on different buffer tapes is studied. The superconductive performance of the multifilamentary 2G-HTS is evaluated.
- Metal Organic Deposition (MOD) is introduced as a bottom-up low-cost process for fabricating YBCO on inkjet-printed buffers. MOD conditions, including buffer selection, precursor preparation, coating techniques and heat treatment conditions are studied and their impact on morphology and performances of deposited YBCO is evaluated. MOD YBCO is demonstrated on the inkjet-printed buffer tape and selective Ag electrodeposition is conducted, showing the possibility of a lower cost and all-solution fabrication.
- Selective deposition of Ag overlayer and selective electroplating of Cu stabilizer have been evaluated on both inkjet-printed and laser-striated multifilamentary samples. The deposition conditions, plating cell configuration and post-deposition heat treatment for

both selective electrodeposition processes are studied, and both deposition processes are scaled up reel-to-reel fabrication practice. The superconducting performance of the fully-stabilized 2G-HTS is measured.

1.4.3 Dissertation outline

The outline of the dissertation is as follows:

- Chapter 1 provides a background about superconductivity, 2G-HTS construction, AC loss, stabilization and describes the overall procedure and objective of this work.
- Chapter 2 introduces the background and current status of multifilamentary 2G-HTS and three major technologies in this work: inkjet printing, MOD, and electrodeposition, and discusses their current developments.
- Chapter 3 introduces the experiments used in this work, including the work process of inkjet printing, MOD, and electroplating. The characterization and testing equipment in this work are also introduced.
- Chapter 4 shows the results of inkjet printing deposition of the insulation barriers, including ink material selection, drop stream and line formation optimization, and superconducting property measurement.
- Chapter 5 provides the results of TFA-MOD YBCO for the work. Buffer selection, precursor preparation, coating technique and heat treatment conditions are studied. Selective TFA-MOD on an inkjet-printed buffer is also demonstrated.
- Chapter 6 demonstrates the reel-to-reel selective electrodeposition for Ag overlayer and Cu stabilizer in this work. Surface morphology, interfacial binding of the deposition layer and its impact on superconducting performance are studied.
- Chapter 7 summarizes the results for the entire solution fabrication approach.

Chapter 2. Technology Status

2G-HTS tapes exhibit many advantages compared with 1G-HTS and low temperature superconductors (LTS), but their applications are limited by their fabrication cost[21]. Conventional fabrication process of the multilayer 2G-HTS tape consists of multiple high cost vacuum processes, including the ion beam assist deposition (IBAD) and magnetron sputtering (MS) of the buffer stacks, the MOCVD or pulsed laser deposition (PLD) of the superconducting YBCO and the sputtering of the Ag over layer.

Solution fabrication process, including chemical solution deposition and electrodeposition have a good potential of replacing the expensive vacuum deposition processes. In this work, we focused on solution fabrication technologies for the fabrication of multifilamentary 2G-HTS, including inkjet printing of the insulating lines, MOD of YBCO superconducting layer and electrodeposition of Ag overlayer and Cu stabilizer.

2.1 Multifilamentary 2G-HTS.

2.1.1 Type-II superconductors

According to London theory by F & H London in 1935 [22], penetration depth(λ_L) is a phenomenological parameter that characterizes a distance which magnetic field penetrates into superconductor. Pippard studied the non-local electrodynamic of superconductors and introduced a characteristic parameter called coherence length(ζ). This parameter describes the superconducting electron distribution inside the superconductor. V. L. Ginzburg and L. Landau established the Ginzburg-Landau theory to describe the superconductivity process mathematically The penetration depth and coherence length can be used together to distinguish type-I or type-II superconductors. The Ginzburg-Landau parameter κ is introduced:

$$\kappa = \lambda_L / \xi \qquad 2\text{-}1$$

for type-I superconductors,

$$0 < \kappa < 1/\sqrt{2}, \tag{2-2}$$

and for type-II superconductors,

$$\kappa > 1/\sqrt{2}. \tag{2-3}$$

For a given temperature, the highest magnetic field under which a material remains superconducting is known as the critical field (H_c). Type-I superconductors lose superconductivity when the external magnetic field is higher than H_c. On the other hand, a type-II superconductor has two critical fields, denoted by H_{c1} and H_{c2}. When the applied magnetic field is higher than H_{c1} but lower than H_{c2}, a negative surface energy is present, and formation of a mixed state called vortex state is preferable. Abrikosov vortices are formed and the magnetic flux can penetrate the through the normal state cores of the vortices [23], while the matrix of the superconductor remains superconducting. As a result, a type-II superconductor is capable of maintaining superconductivity in magnetic fields that are far greater than the critical fields of the type-I superconductor.

In YBCO, the penetration depth is ~150 nm in the ab-plane and ~800 nm along the c-axis, while the coherence length is only ~2 nm and ~0.4 nm respectively, and so YBCO is a type-II superconductor.

2.1.2 Magnetic hysteresis in 2G-HTS

Magnetic hysteresis happens when the type-II superconductor is in the vortex state in time-varying magnetic fields. As the field penetrates the type-II superconductor, a screening current is induced as the field varies. Magnetic moments are generated by the screening current. When

the external field varies, the flux-line pattern and internal magnetic field change as well. Energy is spent on moving the flux lines against the pinning force and is dissipated as heat [24].

C. P. Bean [25] introduced the Critical State model, which is also called Bean's model, that explains the magnetic hysteresis of type-II superconductors. In Bean's model, the current density in certain parts of the superconductor is either zero or at the critical current density (J_c) level. A 1D slab of Bean's model is shown in Fig. 2.1, assuming that the superconductor is cooled down to the superconducting state in zero external magnetic field. As the applied magnetic field increases, the field penetrates into the superconductors from both sides, and screening current is induced to circulate around the sample, and the magnetic field is screened way from the middle part of the superconductor, as shown by the blue line in Fig. 2.1a. However, when the external field starts diminishing, the screening current reverses in direction from the edge of the slab, and the field inside the superconductor changes, following the red dotted lines in Fig. 2.1a. The magnetic field is trapped by the superconductor, even when the external field reaches zero. A full hysteresis loop of the model is shown in Fig. 2.1b, from which the AC loss per cycle can be obtained by calculating the area of the hysteresis loop $W = \oint HdB$ [26].

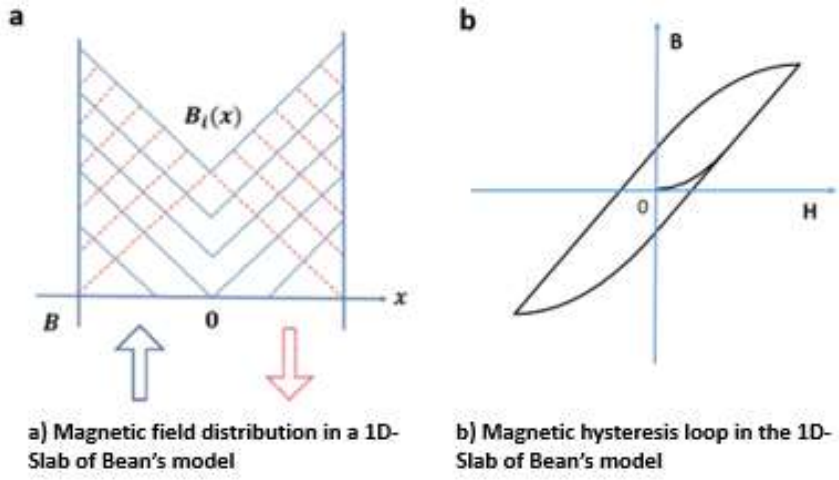

Fig. 2.1. Schematic of a 1D-slab in Bean's model and its hysteresis loop.

2.1.3 Brandt-Indenbom model

Brandt and Indenbom [7] established the Brandt-Indenbom model to describe AC losses. The hysteresis loss, according to the model, is

$$P = 4J_c f \mu_0 H_0 a^2 g\left(\frac{H_0}{H_c}\right), \quad 2\text{-}4$$

where

$$g(x) = \frac{2}{x}\ln(coshx) - \tanh(x), \quad 2\text{-}5$$

and P is the AC loss, J_c is the critical current density, f is the frequency, μ_0 is the permeability of free space, H_c is the critical field, H_0 is the applied field, and a is the width of the 2G-HTS.

From the model, it is noticed that the AC loss value is proportional to the filament width (a), and so, reducing the individual width of the tape is effective in reducing the AC loss. For example, assuming with the same amount of superconductor, 12 independent 1 mm-wide superconducting filaments can potentially reach 12-fold reduction in AC losses comparing with the 12 mm-wide tape.

2.1.4 Multifilamentary process.

The idea of filamentization for low AC loss, came from LTS [27] and 1G-HTS [28, 29]. Attempts to filamentize the 2G-HTS tape have been made to reduce the AC loss. Laser micro-machining is the most commonly used technique for filamentizing the 2G-HTS [5, 30, 31]. Cobb et al. [5] demonstrated the laser micromachining of the YBCO deposition on $LaAlO_3$ wafer to reduce its hysteresis loss, YBCO films were cut into thin strips and the linear relationship between the hysteresis loss and the strip width is revealed and the J_c of the film was unaffected. Sumption et al. [32] carried out the similar laser ablation technique to filamentize the stabilizer-free 2G-HTS tapes. Various machining parameter are studied and the component

of AC loss is investigated. Amemiya et al. [11, 30, 33] studied the coupling loss of laser striated 2G-HTS. The coupling loss is caused by the redeposition of materials on the side of the grooves connecting the superconducting filaments to the Hastelloy substrate.

Other similar filamentization procedures have been used to remove the superconductor like wet chemical etching [34], photolithography [35, 36], and mechanical scribing [12]. The multifilamentary process by materials removal can leave the fragile YBCO exposed to the environment. Kopera et al. [37] reported a prefabricated patterned buffer with ion-implantation, which can result in selective epitaxial growth of YBCO. Glowacki et al. [38, 39] demonstrated a bottom-up process by inkjet printing YBCO on CeO_2 buffer with concave strips. Our group has also reported a mechanical scribing method for multifilamentization [40], and an etch-free inkjet printing method that will be discussed in the dissertation [41].

2.1.5 Stabilizer for multifilamentary 2G-HTS

As superconductor tapes will be used in an AC environment, heat generated from AC loss can potentially leads to quench of the superconducting devices. Stabilization of the multifilamentary tapes is essential. However, stabilizing the multifilamentary tapes is difficult. The stabilizer layer should be able to cover every superconducting filament to provide proper stabilization for the multifilamentary 2G-HTS. Meanwhile, the filaments should stay insulated from each other, or the coupling loss generated by induced current loops between the different superconducting filaments and the Cu stabilizers can cancel out the benefit of filamentization [12].

But laser cutting through the over 20 μm thick Cu by laser has proved to be difficult [42, 43]. Laser striating the sample with thick Cu stabilizer will result in intensive heating on the REBCO nearby. The heating can damage the YBCO and degrade the superconductor's

performance [44]. I_c reduction of the whole tape will overshadow the benefit from AC Loss reduction [42].

2.2 Inkjet printing

Inkjet printing is a dropwise additive printing technology that requires no patterning. With a controlled dispenser, different types of liquids, including melted metal [45, 46], colloidal suspensions [47], and sol-gels [48] can be dispensed in droplets of small volume and high frequency. Actuators move the substrate (or dispensers) as drops are jetted onto demanded locations.

Compared with the traditional microfabrication technologies, inkjet print has the potential to lower the manufacturing cost by a great margin. First, inkjet printing requires no patterning in the process; 2D-pattern printing is capable of replacing the entire lithography process with one step [49]. Moreover, inkjet printing is compatible with flexible low-cost substrate materials such as polymers and metal foils, and it is scalable with reel-to-reel large-scale fabrication. Finally, as a drop-on-demand process, inkjet printing can minimize the waste of materials by printing only the necessary active parts.

Because of its low cost and high flexibility, inkjet printing is widely used for the fabrication of different coatings and patterns with various materials on a variety of surfaces [50-52]. Inkjet printing is widely used in microelectronic research and fabrication, printing solder joints [45], transistors [53], solar cells [54, 55], sensors, and detectors [56, 57]. Large industrial arrays composed of thousands of nozzles have been reported [58].

2.2.1 Inkjet printing dispensers

Inkjet printing dispensers come in three types, which vary based on the energy sources used for droplet creation. They are thermal-bubble [59, 60], piezoelectric [61, 62], and electrohydrodynamic [63, 64] (Fig. 2.2.1[65]).

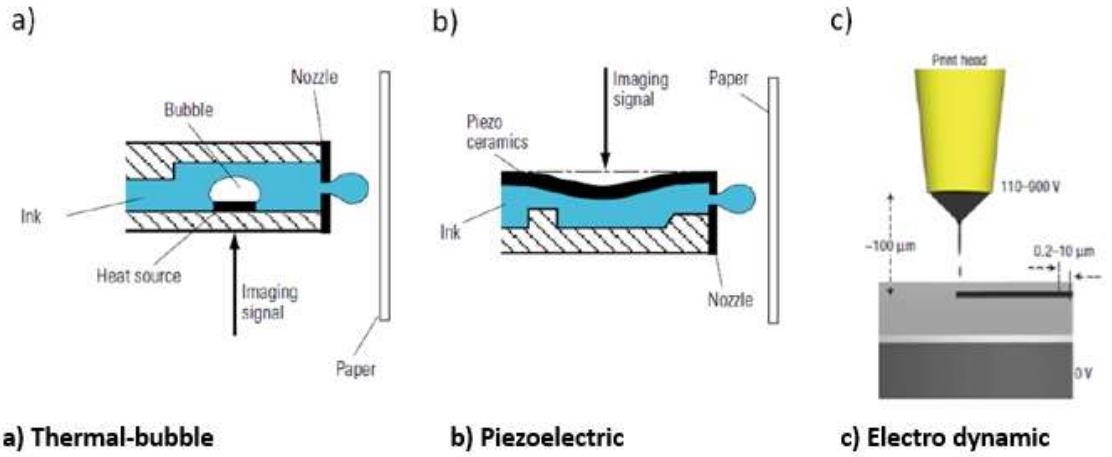

Fig. 2.2. A Schematic of inkjet printing dispenser based on energy sources for droplets creation.

In thermal-bubble inkjet printing (Fig. 2.2a), a heat element is rapidly heated and vaporizes the ink nearby, creating a pressure wave that pushes a droplet from the nozzle. A disadvantage to this jetting mechanism is that the inks used must be compatible with the vaporized pulses.

Piezoelectric inkjet printing (Fig. 2.2b) does not thermally stress the ink. A piezoelectric element is bonded to a glass tube with an integrated nozzle. When a voltage differential is applied, the piezoelectric element squeezes the glass tube, creating an acoustic wave within the ink and forcing out a droplet. This jetting mechanism works with a broad range of inks of intermediate viscosity and surface tension, and it scales for mass production [58].

Electrohydrodynamic printing (Fig. 2.2c) is notable for its ability to create small jetting drops, which are useful for printing high-resolution patterns. Printing is achieved by applying an

electric field between a pendant drop of ink at the jetting nozzle and the substrate to deform the solution on the tip of the nozzle, forming a very small drop [66].

2.2.2 Inkjet printing line formation

Inkjet printing is capable of fabricating dots [67], lines [68], 2D patterns [69], thin film [70], and even some 3D structures [71]. In this section, we focus on the inkjet-printed lines. This section base on the work of P. C. Duineveld [72] and D. Soltman et al. [65].

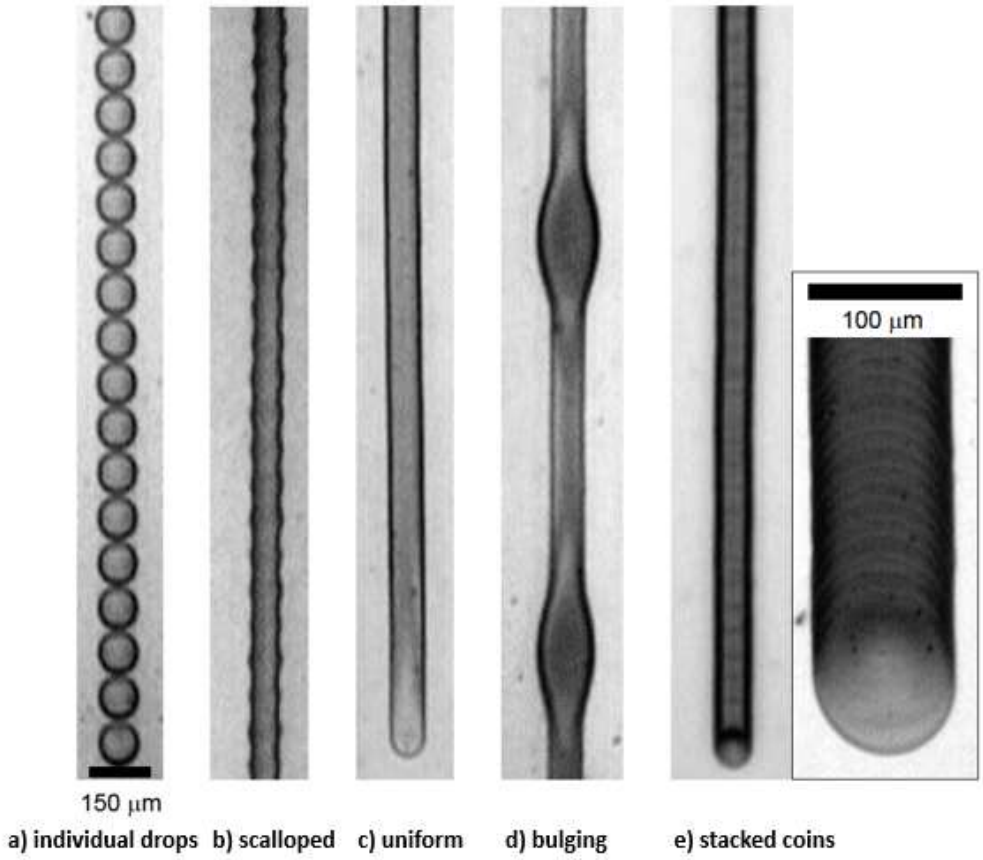

Fig. 2.3. Examples of principal printed-line behaviors. Drop spacing decreases from left to right.

Depending on the differences in the drop spacing, delay periods, and substrate temperature, D. Soltman et al. [65] have labeled the five different inkjet-printed patterns as individual drops, scalloped line, uniform line, bulging line, and stacked coins (Fig. 2.3). Drop spacing is the

distance between the landing point of the two neighboring drops, and delay period is the delay between the landing times of the two neighboring drops.

Among the five patterns, individual drops pattern (Fig. 2.3a) is the result of large drop spacing that prevents droplets from merging. As the drop spacing decreases, the edges of the drop beads start to merge, forming the scalloped lines (Fig. 2.3b). When the droplet spacing is right, a uniform straight-line pattern (Fig. 2.3c) is formed. The straight line pattern has a smaller diameter than the individual drops, which is because the droplet expansion on the tape surface is partially arrested along the line. When the droplet spacing is too small and the excess liquid starts to accumulate, the balance of the drop beads will be broken periodically, forming the bulging pattern (Fig. 2.3d). The stacked coin pattern (Fig. 2.3e) is the result of a large delay period between the drops that first drop dry before the second one lands. The typical printed line behavior at an intermediate temperature is shown in Fig. 2.4. Careful optimization of the drop frequency, temperature, and tape speed is needed to print a smooth, narrow line with even edges.

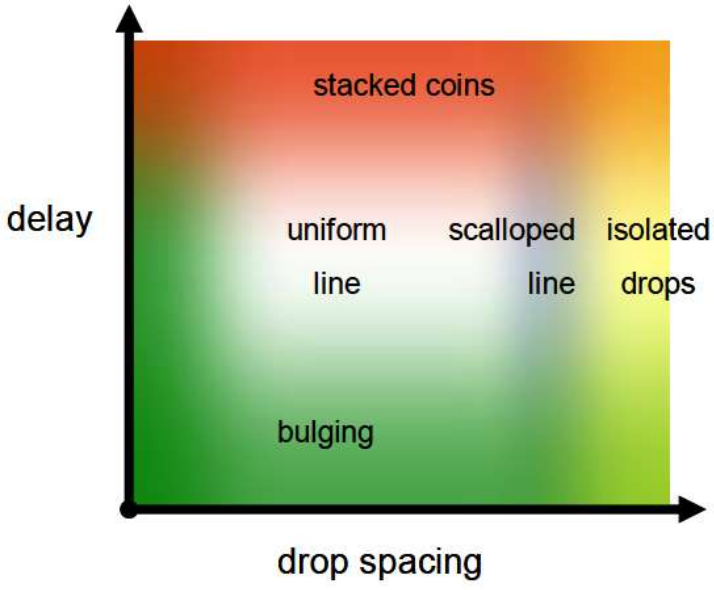

Fig. 2.4. Typical printed line behavior at an intermediate temperature.

2.2.3 Inkjet printing applications in 2G-HTS

Inkjet printing is also used in 2G-HTS research. It has been used in the thin-film fabrication method for the epitaxial buffer layer and even for YBCO deposition.

Inkjet printing has been employed to build the textured buffer layer for YBCO deposition. Chen et al. [73, 74] reported inkjet printing deposition of lanthanum zirconium oxide films with texture on Ni-5%W metal tape in 2007. Later, in 2010, Mosiadz et al. [75] reported the printing of biaxial textured $Ce_{0.8}Gd_{0.2}O_2$ buffer film on Ni-5%W metal tape, which could be used as potential substrate for YBCO epitaxial growth.

Meanwhile, attempts on combining inkjet printing and MOD for YBCO have been reported in recent years. Mosiadz et al. [76] announced a fully chemical solution deposition of 2G-HTS by inkjet printing. Vandaele et al. [77] studied the heat treatment parameter for inkjet-MOD YBCO. Bartolome et al. [78] reported an inkjet-printed 2G-HTS tape with current density of J_c=1.3 MA/cm^2 in 77 K 0 T.

Glowacki et al. [38] reported the idea of building multifilamentary 2G-HTS tapes by inkjet printing in 2009. He demonstrated two possible ways of fabricating the multifilamentary 2G-HTS with inkjet printing (Fig. 2.5): a direct printing process using inkjet printing to directly print YBCO lines, and an inverse printing with prefabricated inkjet-printed buffer tracks for YBCO deposition. In 2012, Van Driessche [79] demonstrated the direct inkjet printing of the YBCO lines. And at the same year, we demonstrated a completely etch-free process of multifilamentary superconductor, using inkjet printing to make the prefabricated insulating barriers inside MOCVD REBCO [41]. More recently, Hopkins et al. [39] reported a complete inkjet printing fabrication process for multifilamentary superconductor using the two inkjet printing methods.

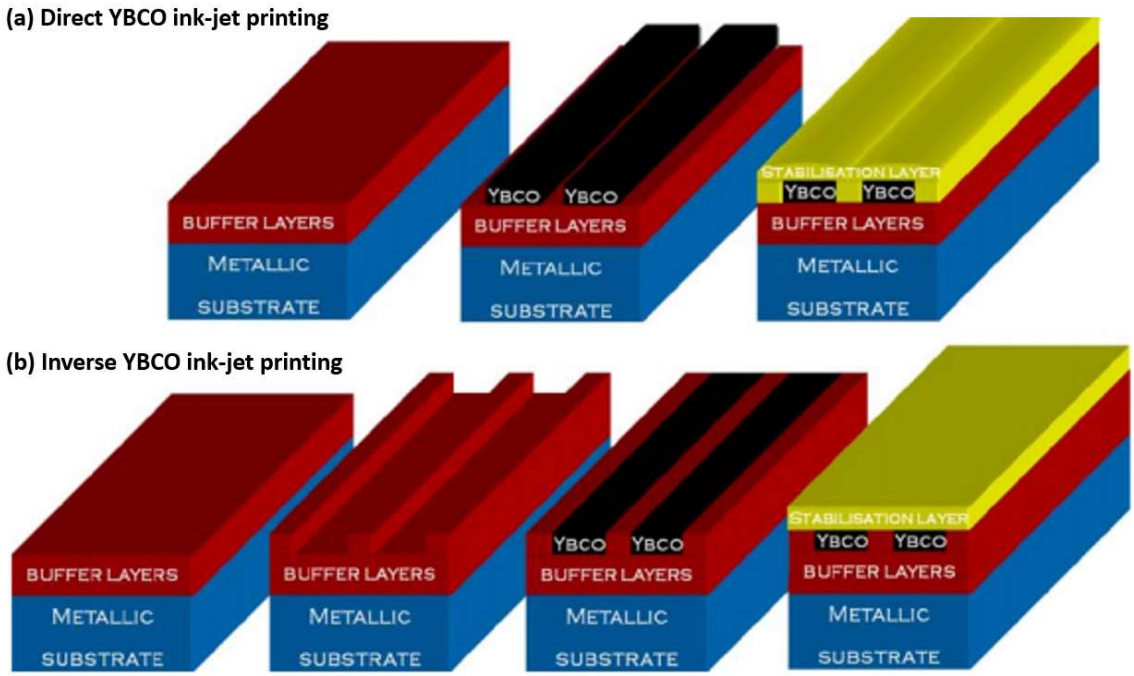

Fig. 2.5. Schematic representation of two possible parallel printing sequences by Glowacki et al.

2.3 Metal-organic deposition of YBCO

Several methods can be used to make YBCO superconductor film. These include PLD [80-82], thermal evaporation [83], MOCVD [84, 85], liquid phase epitaxy [86, 87], and MOD [88, 89].

MOD YBCO has been featured in multiple studies as a non-vacuum alternative process for the expensive PLD and MOCVD methods. Trifluoroacetate-based MOD (TFA-MOD) [90, 91] is one of the most commonly-used processes for YBCO fabrication. Because of its capability to make large-area uniform YBCO with high performance, TFA-MOD is regarded as one of the most suitable candidates for YBCO tape fabrication.

The TFA-MOD process typically starts with the metal (Y, Ba, and Cu) acetate. Metal acetates are mixed with trifluoroacetic acid (TFA) to form a fluorinated precursor. The

precursor is spin coated or dip coated on the target substrate and heat treated. YBCO crystal is formed during the heat treatment.

The following section is primarily based on the work of T. Araki [88, 91-96]. It covers the mechanism study of the MOD process and explains the reactions and mechanisms behind the process.

2.3.1 Precursor preparation

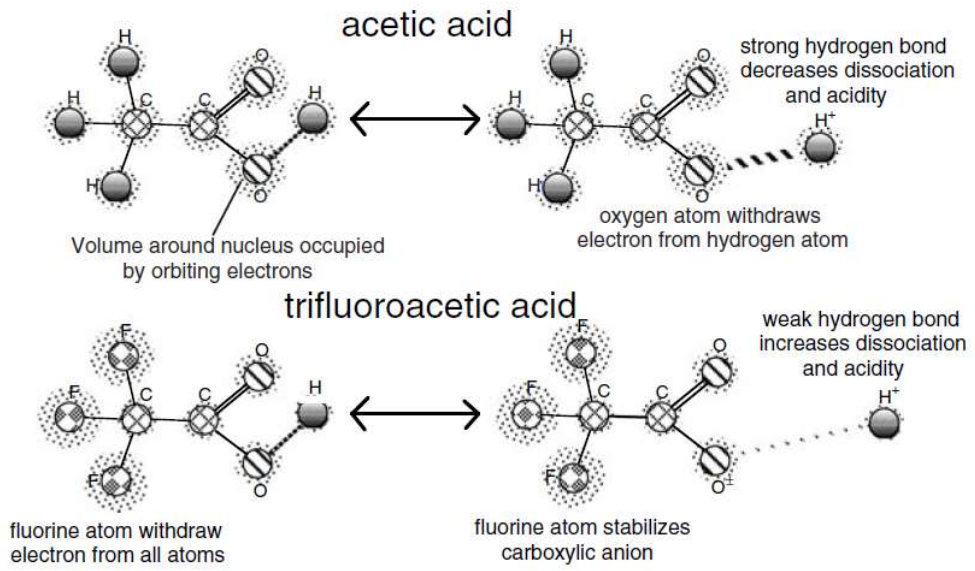

Fig. 2.6. Structures of acetic and trifluoroacetic acids.

TFA has a similar structure to acetate acid, but its chemical nature is quite different. The molecular structures of these two carboxylic acids are illustrated in Fig. 2.6 [88]. Due to the significant difference in electron negativity between fluorine and hydrogen, the oxygen atoms in acetic acid withdraw electrons from the other atoms because they have the strongest electronegativity in this acid. The carboxylic anion from acetic acid is unstable because the hydrogen bond between oxygen and hydrogen atoms decreases the dissociation constant. However, the oxygen atom in trifluoroacetic acid cannot withdraw electrons because fluorine atoms strongly withdraw them. As a result, TFA has a stronger acidity than acetic acid, and its

three fluorine atoms make TFA acid 10,000 times stronger than acetic acid. In fact, TFA is one of the strongest organic acids. Because of this, TFA can replace acetate after the refluxing and refining of the precursor, as

$$(CH_3COO)_nM + CF_3COOH \rightarrow (CF_3COO)_nM + CH_3COOH. \quad 2\text{-}6$$

2.3.2 Heat treatment

The precursor solution is coated on the substrate to form a solution film, which is typically done by spin coating or dip coating. The coated solution films go through a calcination process, where the sample is slowly calcined from 200 to 400 ˚C to remove the moisture and organic component from the solution film. The reactions occur in the thin film during the calcination process is given as

$$(CF_3COO)_3Y \rightarrow Y - O - F(amorphous) + C - O - F(residue), \quad 2\text{-}7$$

$$(CF_3COO)_2Ba \rightarrow Ba - O - F(amorphous) + C - O - F(residue), \text{ and} \quad 2\text{-}8$$

$$(CF_3COO)_2Cu \rightarrow CuO(nanocrystalline) + C - O - F(residue). \quad 2\text{-}9$$

During the calcination, the solution film is dried and decomposed, and precursor films with amorphous Y-Ba-O-F matrix and CuO nanocrystals is formed.

During the crystallization process, the diameter of the CuO nanocrystals decreases, forming a Cu-rich amorphous matrix. A quasi-liquid phase is formed in the CuO/amorphous interface, which supports the transport of both HF and H_2O. The diameter of the CuO nanocrystals is decreased by the formation of the quasi-liquid, which slowly releases YBCO grains and HF gas on the YBCO growth front for reasons of thermodynamic stability. So this results in epitaxial YBCO growth (Fig. 2.7 [92]), in the reaction of

$$Y - Ba - O - F\ (amorphous\ matrix) + CuO + H_2O \rightarrow YBa_2Cu_3O_{7-\delta} + HF\uparrow. \qquad 2\text{-}10$$

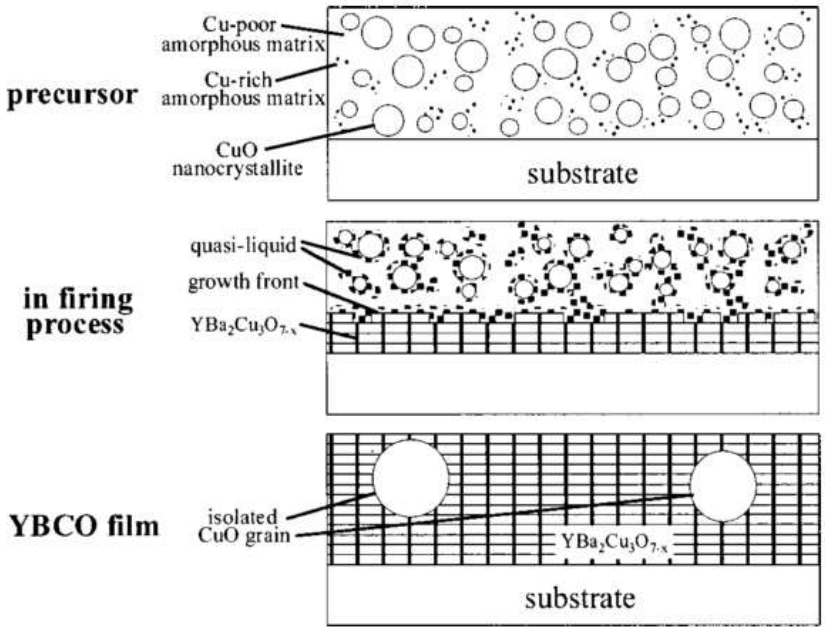

Fig. 2.7. Schematic of the growth mechanism of YBCO grains prepared by TFA-MOD in the crystallization process.

2.3.3 Development on MOD 2G-HTS

Great improvements have been made in the past decades on MOD of YBCO. MOD of YBCO has been vastly studied as a low-cost approach to high performance 2G-HTS. In recent years, the research on MOD 2G-HTS has been focused on high J_c, thick tape, fluorine free precursors, and all-solution fabrication.

The highly-textured YBCO layer obtained from TFA-MOD leads to high J_c. Araki et al. have dedicated their work on enhancing the J_c of MOD YBCO film through optimization on the precursor purity [94] and the heat treatment condition [92, 96]. A very high J_c of >11 MA/cm^2 was obtained in 77 K 0 T on single crystalline wafers with good reproducibility[88], and TFA-MOD YBCO films on flexible metal substrate with 2.9 MA/cm^2 of J_c has also been reported [97]. A lot of research also focused on improving the in-field J_c;

different dopants have been added to the YBCO films as artificial pinning center to improve performance of the MOD derived 2G-HTS in high magnetic fields [98-101].

Very high J_c can be obtained by the TFA-MOD process, but the performance of the MOD derived 2G-HTS tape is limited by the thickness of the YBCO. The stress generated by the volume shrinkage during the heat treatment can destroy the film integrity and also result in voids, cracks and wavy surfaces. As a result, most MOD YBCO films are very thin and few can exceed the thickness of 1 μm by single layer coating. The conventional approach towards thicker film is achieved by multi-coating method, in which additional layer(s) of gel-film is directly coated on the calcined film. MOD-derived 2G-HTS with thick YBCO film up to 2 μm and maintaining the high J_c of 2.0 MA/cm^2 has been demonstrated [102]. American Superconductor (AMSC) is now capable of manufacturing 2G-HTS tapes with 1.2 μm with multi-coating MOD [103]. Because the epitaxial growth of YBCO will inevitably deteriorate in thicker films, crack-preventing chemicals have been added to the precursor [95].

All-solution processes have been studied to replace the expensive vacuum-based processes to reduce the production cost. Ion-beam assisted deposition (IBAD) of a poly crystalline surface on top or rolling assisted biaxial textured substrate (RaBITS) metal tape are used as the template for 2G HTS tapes. Epitaxial solution coating of the buffer stacks consist of yttria-stabilized zirconia (YSZ), perovskites ($SrTiO_3$, $BaZrO_3$, $LaAlO_3$ etc.) or CeO_2 is conducted on the templates. Obradors et al. [104] demonstrated an all-solution fabricated buffer stack with YSZ/$SrTiO_3$ on a single crystal $LaAlO_3$ which yield YBCO with a high J_c of 3 MA/cm^2. Zhao [105] has conducted MOD of YBCO on RaBITS Ni-W substrate with solution-fabricated $Ce_{0.9}La_{0.1}O_2/Gd_2Zr_2O_7$ buffers and achieved a J_c of 2 MA/cm^2. Mosiadz et al. [76] reported a full chemical solution deposition of 2G-HTS by inkjet printing.

2.4 Electrodeposition

2.4.1 Electrodeposition of Ag overlayer on 2G-HTS

Electrodeposition is referred to as either 'potentiostatic,' which is studied under constant potential [106] or 'galvanostatic,' which is studied under constant current density [107], depending on whether the external power supply is used to fix the potential applied to the substrate or the current passing through it respectively.

A simple galvanostatic cell is used in this work. The 2G-HTS tape is connected to the negative pole of the DC power source and served as the cathode, and a piece of platinum is used as the anode. The Ag source for deposition is supplied by the Ag^+ ions in the electrolyte. During the deposition process, Ag^+ ions are attracted by the negative potential and migrates towards cathode surface, where the ions are reduced and metal deposition occurs. The reaction on the cathode can be shown as

$$Ag^+(aq) + e^- \rightarrow Ag(s), \qquad 2\text{-}11$$

and the corresponding Nernst equation is

$$E = E_0(Ag/Ag^+) - \frac{RT}{F \ln[Ag^+]}, \qquad 2\text{-}12$$

where R and F are the universal gas constant and Faraday constant, respectively; T is the temperature; $E_0(Ag/Ag^+)$=0.7994 V, is the standard potential for the reduction reaction of Ag.

Water reacts with YBCO in room temperature and results in degradation of the superconducting performance [108, 109], the reaction can be shown as

$$2YBa_2Cu_3O_{7-x} + 3H_2O \rightarrow Y_2BaCuO_5 + 3Ba(OH)_2 + 5CuO + (0.5 - x)O_2. \qquad 2\text{-}13$$

As the result, a non-aqueous electrodeposition process is required for depositing the Ag overlayer on YBCO.

Different approaches of non-aqueous electrodeposition process have been reported. Angurel et al. [110] has reported a DC Ag deposition process for 1G-HTS superconducting material $Bi_2Sr_2CaCu_2O_8$. A dimethylsolfoxide (DMSO)-based electrolyte with 2.0 M $AgNO_3$ and 50 mM thiourea was used at a deposition current density between 2-30 mA/cm^2. Dense Ag deposition with a very low contact resistance of $<10^{-9}$ $\Omega \cdot cm^2$ was achieved by post-deposition 2-step heat treatment at 870 ˚C for 36.5 h and 801 ˚C for 34.8 h.

For 2G-HTS, we have developed methanol-based non-aqueous Ag electrodeposition process [111, 112]. Methanol-based $AgNO_3$ solution with ammonium hydroxide is used as the electrolyte. A dense Ag coating was achieved at a deposition current density of 15 mA/cm^2 and post-deposition annealing at 450 ˚C for 30 min in oxygen. The electrodeposited Ag has exhibited good density and contact resistance that is comparable to magnetron sputtered Ag overlayer is conventional applications.

In this dissertation, we adopted the Ag electrodeposition process to the inkjet-printed multifilamentary tape. Utilizing the resistivity difference between the highly insulating inkjet-printed ceramic lines and the relatively low resistive REBCO, selective deposition is achieved. Superconducting REBCO filaments are covered with dense Ag overlayer, while the printed lines remain Ag free, so the coupling loss can be minimized.

2.4.2 Electroplating of Cu stabilizers for 2G-HTS

Electroplated Cu has been widely used in different fields, including anti-corrosive metals [113-115], printed circuit boards [116], and metallic powder preparation [117, 118]. In this work, we are using a simple DC electroplating method.

A simple DC galvanic cell electrodeposition process is used for this work. Cu is used as the anode and the sample to deposit on is the cathode. As the current passes through the plating cell, the oxidation reaction occurring on the Cu anode is

$$Cu(s) \rightarrow Cu^{2+}(aq) + 2e^{-}. \quad 2\text{-}14$$

Due to the electric field generated between the two electrodes, Cu^{2+} ions move through the electrolyte and to reach the surface of the cathode, where the deposition reaction happens as

$$Cu^{2+}(aq) + 2e^{-} \rightarrow Cu(s). \quad 2\text{-}15$$

The plating parameters are governed by the Nernst equation, as

$$E = E_0(Cu/Cu^{2+}) - \frac{RT}{2F} ln \frac{C_{cat}}{C_{an}}, \quad 2\text{-}16$$

where R and F are the universal gas constant and Faraday constant, respectively; T is the temperature; $E_0(Cu/Cu^{2+})$ is the standard potential for the reduction reaction of Cu, which is 0.337 V; and C_{cat} and C_{an} ($C_{cat} > C_{an}$) are the electrolytic concentrations around the two electrodes.

A simple Cu sulfate electrolyte is used in this work. The equilibrium diagram of the interface electrolyte potential versus the pH level ($E_{cu/cu2+}$-pH diagram) can be constructed by calculating the Gibbs free energy (Fig. 2.8a) [119]. The Cu ion stable area is confined into the region between pH 0 and 4.2 and solution potential over -20 mV. The solubility is also an important parameter. Because the solubility of Cu rapidly dropped in two orders of magnitude within only one unit of pH range (Fig. 2.8b) [119], the electrodeposition process could only be conducted when both conditions were satisfied.

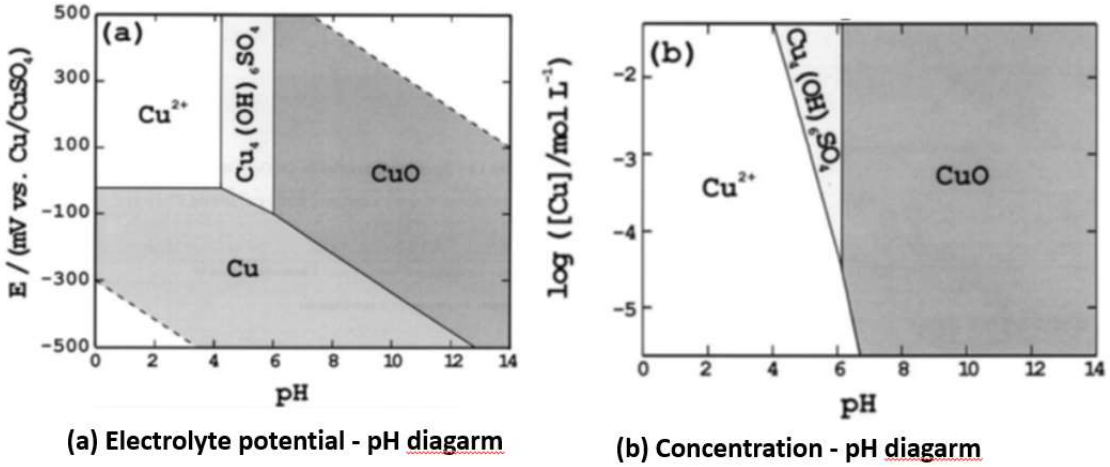

Fig. 2.8. Equilibrium diagrams for $CuSO_4$-H_2O system.

Numerical analysis of the electroplating in this work is done with the electrodeposition module from COMSOL Multiphysics 5.0. The models are built base on Nernst-Planck equation and the kinetic study on Cu/$CuSO_4$ system by Mattson et al. [120].

According to the Nernst-Planck equation, the flux for each of the ions in the electrolyte is given as

$$\boldsymbol{N}_i = -D_i \nabla c_i - z_i u_i F c_i \nabla \varphi_l, \qquad 2\text{-}17$$

where N_i denotes the transport vector, D_i is the diffusivity of the ions, c_i is the concentration of the ion in the electrolyte, z_i is the charge for the ionic species, u_i is the mobility of the charged species, F is Faraday's constant, and φ_l is the potential in the electrolyte. The material balances in the deposition process are expressed as

$$\frac{\partial c_i}{\partial t} + \nabla \cdot \boldsymbol{N}_i = 0. \qquad 2\text{-}18$$

There are only two type of ions in this system, Cu^{2+} and SO_4^{2-}, so i=1, 2. For electroneutrality, it is given by

$$\sum_i z_i c_i = 0. \qquad 2\text{-}19$$

According to the Butler-Volmer equation, the local current density at the anode and cathode can be expressed as a function of potential and Cu concentration, as

$$j_s = j_0 \left(e^{\frac{\alpha_a F \eta}{RT}} - \frac{c_{Cu^{2+}}}{c_{Cu^{2+},ref}} e^{-\frac{\alpha_c F \eta}{RT}} \right), \quad 2\text{-}20$$

where j_s is the local current density at the electrode, j_0 is the exchange current density. The anodic and cathodic charge transfer coefficient, α_a and α_c, equals to 1.5 and 0.5 [120]. η is the overpotential, which can be defined as

$$\eta = \varphi_s - \varphi_l - \Delta\varphi_{eq}, \quad 2\text{-}21$$

where φ_s is the electronic potential of the respective electrode. Define $\boldsymbol{n}$ as normal vector to the boundary, the boundary condition for the cathode and anode is

$$\boldsymbol{N}_{Cu^{2+}} \cdot \boldsymbol{n} = -\frac{j_0}{2F} \left(e^{\frac{1.5F(\varphi_{s,cat} - \varphi_l - \Delta\varphi_{eq})}{RT}} - \frac{c_{Cu^{2+}}}{c_{Cu^{2+},ref}} e^{-\frac{\alpha_c F(\varphi_{s,cat} - \varphi_l - \Delta\varphi_{eq})}{RT}} \right), \text{ and} \quad 2\text{-}22$$

$$\boldsymbol{N}_{Cu^{2+}} \cdot \boldsymbol{n} = -\frac{j_0}{2F} \left(e^{\frac{1.5F(\varphi_{s,an} - \varphi_l - \Delta\varphi_{eq})}{RT}} - \frac{c_{Cu^{2+}}}{c_{Cu^{2+},ref}} e^{-\frac{\alpha_c F(\varphi_{s,an} - \varphi_l - \Delta\varphi_{eq})}{RT}} \right). \quad 2\text{-}23$$

The other boundaries are insulating or symmetric, as

$$\boldsymbol{N}_i \cdot \boldsymbol{n} = 0. \quad 2\text{-}24$$

With 1:1 stoichiometric between Cu^{2+} and $SO4^{2-}$, the initial condition of the composition of electrolyte is set $c_i = c_0$. The electrolyte potential, ion concentration, ion flux and deform geometry interface are studied in the numerical analysis.

Electroplating Cu over HTS was demonstrated soon after its discovery [121, 122]. Cu stabilizer can been obtained by acidic or alkaline, aqueous [123] or non-aqueous [124] electrochemical processes. Conventional solutions for electroplating Cu layers use a cyanide-

based solution to prevent the uncontrolled hydrogen evolution from the aqueous-based solution, which is very reactive with the superconductor layer and destroys its superconducting capability.

U. Floegel-Delor et al. [124-126] reported a reel-to-reel deposition process that is capable of 2 km-long tape deposition. The researchers also studied different Cu stabilizer designs for various applications.

Stabilizing the multifilamentary 2G-HTS tapes has proved to be difficult, but some research has been done in this area. Attempts like directly laser cutting through the Cu stabilized 2G-HTS has been done[42, 43], but without much success. We have innovated the selective electrodeposition process for both Ag overlayer [41] and Cu stabilizers [12, 13], and the Cu selective deposition process has scaled up to a reel-to-reel continuous process in this work [127].

Chapter 3. Experiments

3.1 Fabrication procedure

Two different approaches are employed to achieve the fully stabilized multifilament 2G-HTS tape. The first is an etch-free solution fabrication process to fabricate multifilament tapes of 2G-HTS from the buffer with inkjet printing, MOD/MOCVD and selective electrodeposition. The second is a laser-striation of 2G-HTS tapes coated with Ag followed by selectively-electroplated Cu stabilizer.

3.1.1 Etch-free solution fabrication approaches

A bottom-up process involving no material removal has been developed for multifilament 2G-HTS tapes [128]. A bare buffer tape is used as the substrate consisting of Hastelloy base tape and the textured buffer stacks (Fig. 3.1a).

11 insulator lines are inkjet-printed along the length of tape with inks dividing the buffer tape into 12-filament grooves. The insulator lines are heat-treated in moist oxygen at 400 ˚C for 30 min to remove organic component. The insulating barriers are thus formed (Fig. 3.1b).

A REBCO superconductor layer can be deposited by MOCVD and MOD process followed by oxygenation at 500 °C (Fig. 3.1c).

Ag electrodeposition is conducted on the oxygenated surface of REBCO. A simple two-electrode direct current (DC) deposition method was used with methanol and ammonia-based Ag nitrate solution as the electrolyte (Fig. 3.1d). The tape with deposited Ag is oxygenated at 450 °C to improve the interfacial bonding and lower the contact resistance between the Ag overlayer and the superconductor layer. A thick Cu stabilizer is then electroplated on the Ag overlayer by a similar DC deposition (Fig. 3.1e).

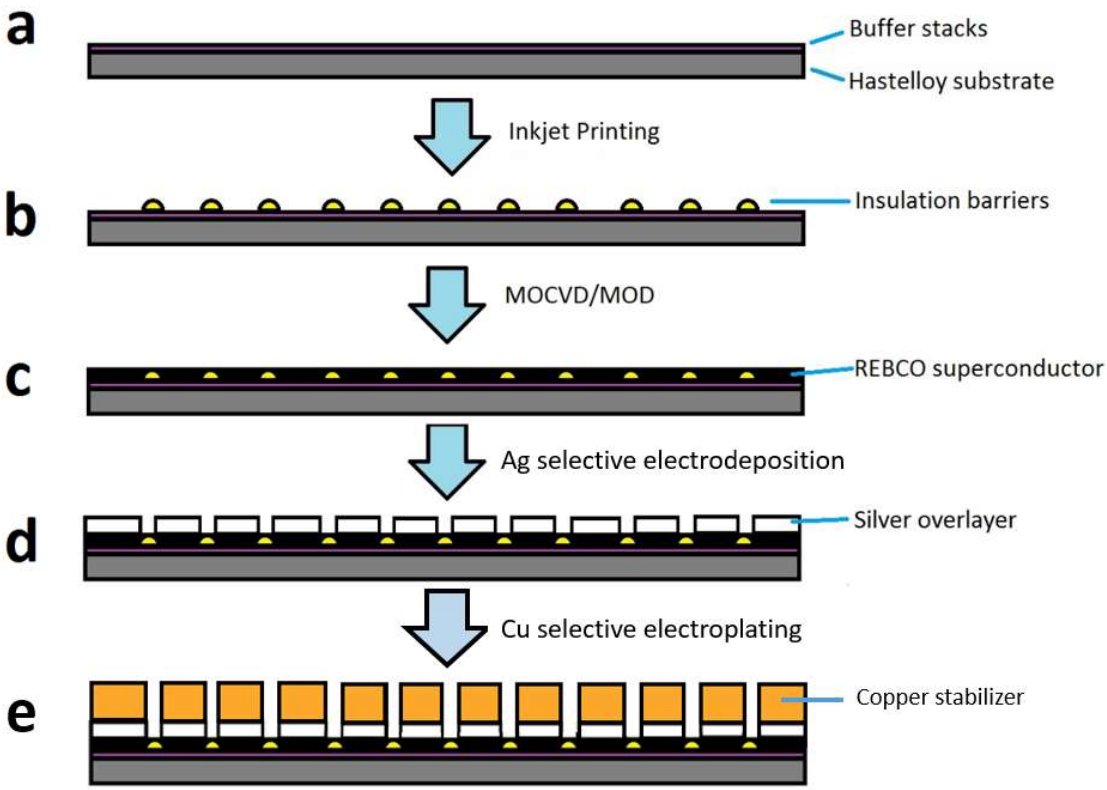

Fig. 3.1. Schematic of the etch-free solution fabrication of fully-stabilized multifilament 2G-HTS tape.

There are several advantages of the approaches used in this work. The first, it is an etch-free process which involves no materials removal during the procedure. The REBCO deposition is left as-is, without concerns such as remnant deleterious etchant, which might destroy superconductivity in the lithography process, or exposed REBCO surface which could result in delamination. The second advantage is that inkjet printing is less expensive than high-energy laser ablation or lithography; replacement of MOCVD with MOD, an all-solution process without expensive vacuum deposition is possible which might further reduce manufacture cost. The third advantage is that most processes in this work including MOCVD, inkjet printing, and electroplating have been done with reel-to-reel systems, which are scalable to production.

3.1.2 Laser striation and selective electroplating approaches

Laser striation is used in research for filamentization of 2G-HTS, but it is limited to tapes without Cu stabilization layers. 2G-HTS tapes with a thick Cu stabilizer striated directly using high-power laser ablation have been report [42] but the large amount of heat generated by the laser-striating might cause I_c reduction, which overshadows the benefit of AC losses reduction. Utilizing a selective electroplating process, a Cu stabilization layer on the superconductor filaments is deposited resulting in fully-filamentized 2G-HTS tapes.

Stabilizer-free 2G-HTS tapes with 12 mm width from Superpower Inc. are used for this work (Fig. 3.2a). The tape has identical multiple layer structure, only without the Cu stabilizer.

Filamentization is achieved by laser ablation. A Yb:KYW (ytterbium-doped potassium yttrium tungstate) diode-pumped femtosecond laser (Jenoptik JenLas *D2.fs*) is employed to striate the 2G-HTS tapes into 12 uniform filaments. All the grooves are cut through Ag, REBCO, and buffer stacks, leaving a shallow slot on Hastelloy substrate tape exposed for a subsequent oxidation process (Fig. 3.2b).

After striation, the samples are annealed at 550 ºC for 2 h in oxygen when the exposed Hastelloy is oxidized. A dense and high resistive oxide layer is formed on the groove, which can make the subsequent selective electroplating possible (Fig. 3.2c).

Due to the resistivity difference between the filaments with Ag overlayer and the grooves covered oxide films, Cu stabilizer is selectively electroplated only on the filaments and so a fully stabilized multifilament 2G-HTS tape is obtained (Fig. 3.2d).

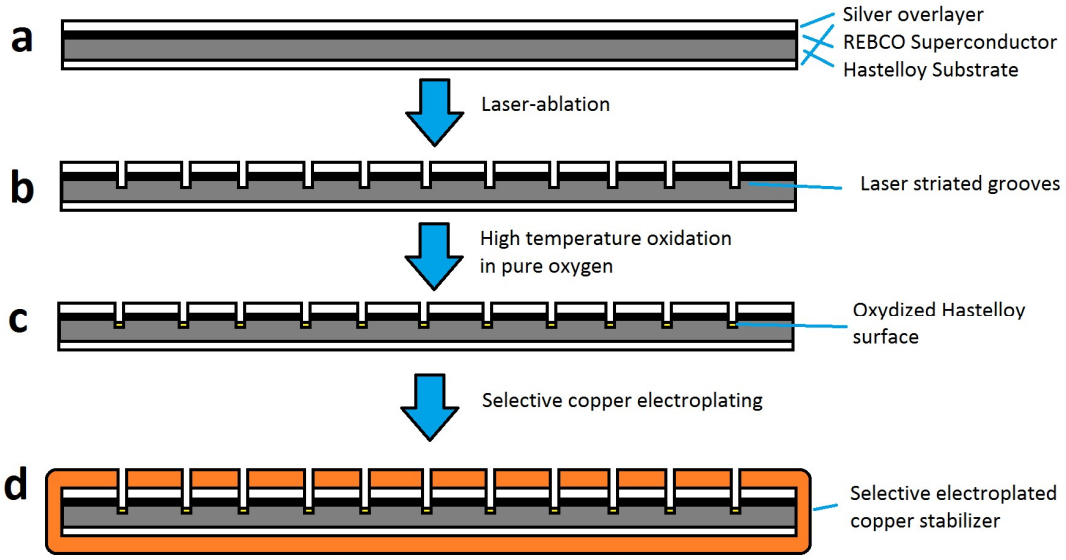

Fig. 3.2. Schematic of laser-striation and selective electroplating Cu for a fully-stabilized multifilament 2G-HTS tape.

3.2 Inkjet printing insulator lines for multifilamentization

In this work, a ceramic sol-gel is prepared as an ink for printing insulating barriers. Different sol-gels are prepared and diluted to proper viscosity for inkjet operation. Due to the difference of ink and buffer in each run, inkjet printing parameters need to be optimized before printing. After printing, the lines are heat-treated in an inline furnace to become solid lines. A schematic of the procedure is shown in Fig. 3.3.

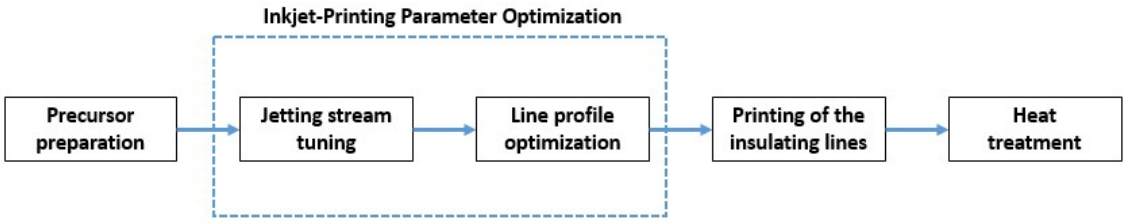

Fig. 3.3. A schematic of the inkjet printing procedure for filamentization.

3.2.1 Reel-to-reel inkjet printing system

A custom-built inkjet printing system is employed in this work to accomplish the continuous reel-to-reel filamentization process (Fig. 3.4). The system consists of four different components (Fig. 3.5): reel-to-reel tape motion, jetting stage and platform, inkjet microdispenser with ink and signal supply and inline heat-treatment furnace.

Fig. 3.4. A photo of the reel-to-reel inkjet printing system.

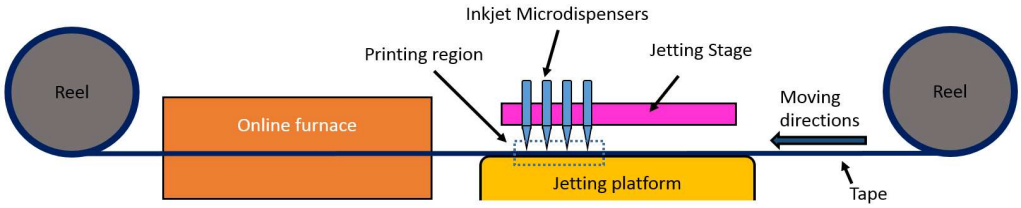

Fig. 3.5. A schematic of the reel-to-reel inkjet printing system.

3.2.1.1 Reel-to-reel tape motion

To obtain continuous and stable ink emission from the dispensing nozzle, the inkjet microdispensers remain static during the printing process. The tape moves below the jetting nozzle, which enables drawing of a continuous line along the tape length. Precise control of the tape movement is required, because even small speed changes in the tape can result in non-uniformity or breaking of the drawn lines.

A controllable and stable tape speed and the tension on tape are very crucial. To obtain precision control of the tape speed, both spools are loaded on a clutch connected to a torque motor, providing a constant tension of 2 kg along the tape. Tape speed is controlled by a stepper motor and a pair of pinch rollers. The two pinch rollers are pressed against each other while the tape is delivered through them. The step motor controls the main roller which drives the tape movement precisely from 0.03 to 10 m/min, in both directions. The control error is within 2 cm for the 10 m back-and-forth movement.

3.2.1.2 Jetting stage and platform

Temperature is a critical factor in this process. The morphology of lines is governed by drop spacing and evaporation rate on the tape surface. A susceptor is installed in the jetting platform to heat the tape to proper temperature.

A three-axis actuator is employed to carry the microdispensers and align them with the tape. The microdispensers are sensitive to the changes of feeding pressure and so, ink bottles are also loaded upon the jetting stage. 12 different nozzles with their inkbottles can be loaded and dispensed simultaneously on the stage.

The stage has two different working positions. One is the dispensing position where the inkjet printing operation occurs. Dispensers are moved to 1.5 mm above the jetting platform,

through where the tape is sliding. The jetting nozzles are aligned with the location where the inkjet lines are supposed to be printed. The other working position is the view position where the jetting streams are adjusted to stabilize before they are moved toward the dispensing position. The inkjet printing nozzles are moved in front of a camera, a light-emitting diode (LED) is synchronized with a pulse that generates a drop. By adjusting the delay between the actuation pulse and the pulse applied to the LED, the drops can be captured at different spots along flight path.

3.2.1.3 Inline heat-treated furnace

Before the tape is rolled into the take-up spool, the gel-like printed line must be calcined to solid state, or else the roller and the taps stack will destroy the printed lines. An inline furnace is installed in the downstream location of the reel-to-reel process, in which the tape can be heated to 500 ˚C for drying the ink and calcining the gel-like line into solid. For some of the ink, long term heat treatment is required, so the lines are baked dry with the inline furnace, and the printed sample are send to a furnace for further heat treatment.

3.2.1.4 Inkjet dispenser with ink and signal supply

MicroFab piezoelectric inkjet microdispensers are used in this work. An annular radially-poled piezoelectric element is bonded to a glass tube that contains an integrated nozzle. The glass tube is mounted in a protective housing and bonded to a fitting that connects it to the ink supply (Fig. 3.6). The nozzle orifice sizes are 30 μm and 60 μm in this work.

When a voltage is applied between the inner and outer electrodes, the piezoelectric actuator expands or shrinks radially which depends on the voltage polarity. The action occurs only in the portion where both electrodes are present. A trapezoidal waveform signal is applied to the

nozzle whenever a drop is needed; the signal can be sent to the dispenser at the frequency of 400-2000 Hz in this system.

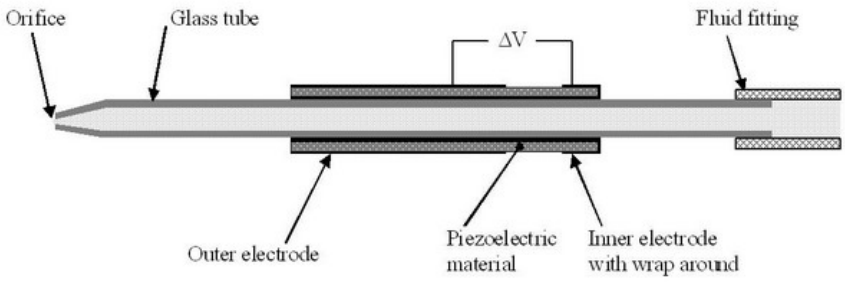

Fig. 3.6. A schematic of the MicroFab piezoelectric inkjet microdispenser.

A pneumatic controller is employed to feed the precursor ink into the dispenser continuously. By applying pressure to air inside the ink bottle, the precursor ink is pushed through the capillary and fed into the nozzle. A high pressure can be used for cleaning purposes, purging air bubbles and small impurities inside the glass tube.

3.2.2 Sol-gel ink preparation

Sol-gel inks for six ceramic materials are studied in this dissertation: MgO, Fe_2O_3, SnO_2, $BaZrO_3$ (BZO), $BaTiO_3$ (BTO) and Cu doped BTO (BCTO).

3.2.2.1 Sol-gel preparation

a. Tin oxide

A methanol-based sol-gel was employed in this work [129, 130]. Table 3.3 provides the recipe for the SnO_2 sol-gel. Tin(II) chloride is dissolved into methanol, and the sol is stirred continuously and aged for 24 h. DEA is added into the sol as binding agent and surfactant before it is used. During inkjet printing process, the printed lines are baked in online furnace at 200 ˚C. Then the tape is heat treated in an offline furnace at 500 ˚C for 3 h to finish the synthesis reaction. Synthesis reaction of SnO_2 is shown as

$$SnCl_2 \cdot 2H_2O + ROH \rightarrow Sn(OH)_2 + RCl, \text{ and} \quad 3\text{-}1$$

$$Sn(OH)_2 + O_2 \xrightarrow{500^{\circ}C} SnO_2 + H_2O. \quad 3\text{-}2$$

Table 3.1. Recipe of SnO_2 sol-gel for inkjet printing.

Methyl alcohol	50 ml
Tin(II) chloride ($SnCl_2 \cdot 2H_2O$)	2.3 g
Diethanolamine	2 ml
Viscosity	4.3 cSt

b. Iron oxide

Ammonia-acetate-based sol-gel of Fe_2O_3 synthesis method [131, 132] is adapted in this work. Table 3.2 shows the recipe for the Fe_2O_3 sol-gel. The precursor is obtained by dissolving 2 g of $FeCl_3 \cdot 6H_2O$ into 15 ml of deionized (DI) water and 15 ml of methanol. 3 ml of ammonium hydroxide ($NH_3 \cdot H_2O$) is slowly added to the solution. Dark red precipitates are found after the addition of ammonium hydroxide. The precipitates are filtered and then dissolved by addition of 10 ml acetic acid. Then, 35 ml of methanol and 2 ml of DEA are added to control the solution viscosity and surface tension. The sol is stirred continuously and aged for 12 h before use. The finished product has a viscosity of 10.5 cSt. The inkjet-printed lines are heat treated in the inline furnace at 380 ˚C.

Table 3.2. Recipe of the Fe_2O_3 sol-gel for inkjet printing.

Methyl alcohol	15+35 ml
Iron(III) chloride ($FeCl_3 \cdot 6H_2O$)	2.00 g
D. I. water	15 ml
Acetic acid	10 ml
Diethanolamine	1 ml
Viscosity	10.5 cSt

c. Magnesium oxide

Organic sol-gel synthesis of MgO thin film has been reported [133-135]. The acetate-based sol-gel precursor is successfully adapted with the inkjet printing system in this work. Magnesium acetate is dissolved with methanol. Diethanolamine (DEA) is added into the solution as surfactant to adjust the surface tension of the ink. The precursor recipe is given in Table 3.3. The inkjet-printed lines are heat treated at 350 ˚C in the inline furnace.

Table 3.3. Recipe of the MgO sol-gel for inkjet printing.

Methyl alcohol	50 ml
Magnesium acetates ($Mg(C_2H_3O_2)_2$)	10.00-20.00 g
Diethanolamine	1-5 ml
Viscosity	2.8-8.7 cSt

d. Barium zirconate

BZO ink is prepared by a methanol-acetate sol-gel process [136]. Table 3.4 provides a recipe for $BaZrO_3$ sol-gel. Zirconium butoxide is dissolved in methanol and the stoichiometric amount of barium acetate is dissolved in acetic acid at 40 ˚C. The two solutions are mixed together with DEA, and ultrasonicated for 20 minutes before the ink is used. During the inkjet printing process, the printed lines are baked at 200 ˚C in the inline furnace and then heat treated in an offline furnace at 400 ˚C for 3 h.

Table 3.4. Recipe of $BaZrO_3$ sol-gel for inkjet printing.

Methyl alcohol	30 ml
Acetic acid	20 ml
Barium acetate ($Ba_2(C_2H_3O_2)$)	2.55 g
Zirconium(IV) butoxide ($Zr(OC_4H_9)_4$)	4.79 g
Diethanolamine	5 ml
Viscosity	6.3 cSt

e. Barium titanate

BTO sol-gel precursor is prepared in a similar process to the BZO precursor[48]. Table 3.5 shows the recipe for $BaTiO_3$ sol-gel. Barium acetate is dissolved warm acetic acid at 40 ˚C and titanium butoxide is mixed in methanol. Two solutions are mixed together with DEA and ultrasonicated for 20 min before use. The finished sol-gel has a viscosity of 7.3 cSt. The inkjet-printed lines are baked at 200 ˚C in the inline furnace, and then heat treated at 400 ˚C for 3 h in offline furnace.

Table 3.5. Recipe of the $BaTiO_3$ sol-gel for inkjet printing.

Methyl Alcohol	30 ml
Acetic acid	20 ml
Barium acetate ($Ba(C_2H_3O_2)_2$)	2.55 g
Titanium(IV) butoxide ($Ti(OC_4H_9)_4$)	3.50 g
Diethanolamine	5 ml
Viscosity	7.3 cSt

f. Cu-doped barium titanate

To further increase the resistivity of the printed lines, doping of BTO is taken into considerations. Multiple reports have stated that Cu-doped BTO ($Ba(Cu_xTi_{1-x})O_3$, $0.02<x<0.05$, BCTO) has larger dielectric constant than BTO [137-139]. Cu doping is achieved by adding Cu acetate into the Ba acetate-acetic acid solution, and the amount of Ti butoxide is decreased stoichiometrically. The ink becomes light blue due to the addition of Cu ions, but the viscosity of the ink remains the same. The printed line is heat treated the same way as BTO lines.

Table 3.6. Recipe of the $Ba(Cu_xTi_{1-x})O_3$ sol-gel for inkjet printing.

Methyl Alcohol	30 ml
Acetic acid	20 ml
Barium acetate ($Ba(C_2H_3O_2)_2$)	2.5 g
Copper acetate monohydrate ($Cu(C_2H_3O_2)_2 \cdot 6H_2O$)	0.04-0.1g
Titanium(IV) butoxide ($Ti(OC_4H_9)_4$)	3.43-3.32 g
Diethanolamine	5 ml
Viscosity	7.3 cSt

3.2.2.2 Ink preparation

According to the manufacturer, the microdispensers have a wide window for sol-gels and fluids with viscosity less than 20 cPs can be dispensed. However, it is noticed that the operational window of jetting parameter is limited when the solution viscosity is too high (>10 cSt) or too low (<2 cSt). The viscosity of the sol-gel can be controlled by solution concentration; diluting the prepared sol-gel with methanol can effectively lower its viscosity. In some of the sol-gel recipes for Fe_2O_3, BZO and BTO, the concentration is limited by their solubility. Aging the sol-gel is another factor that affects viscosity. Most sol-gels will increase viscosity through an aging process [140-142]. So, in order to obtain good consistency of the ink viscosity, the precursor ink is specifically prepared before each inkjet printing run.

The surface tension of ink is another factor that affected the jetting behavior and line formation. DEA is added to precursor as a surfactant to modify the ink's surface tension. Meanwhile, DEA also served as complexing agent in the precursor, to decrease the reaction and condensation rate and prevent crack formation during heat treatment.

3.3 Metal organic deposition for YBCO thin film

Metal-organic deposition (MOD) of YBCO has been vastly studied as a low-cost alternative for making 2G-HTS. Among different MOD approaches, trifluoroacetate (TFA) based precursor

has yielded better performances and reproducibility [88, 89]. In this work, the TFA-MOD process is used as a replacement for MOCVD, so that a complete all-solution process can be used for the multifilament tapes of 2G-HTS.

Fig. 3.7 shows the procedure for TFA-MOD YBCO film. The process starts with precursor preparation. The metal acetates are reacted with TFA to form the crude precursor with metal TFAs and impurities like acetic acid, water and excess TFA. The crude precursor is then refined many times to form the higher purity coating solution. Coating of the precursor can be done in two ways, spin coating for short tapes and dip coating for long and multifilament tapes. The tape coated with solution film is quickly moved into the furnace for calcination and crystallization heat treatment.

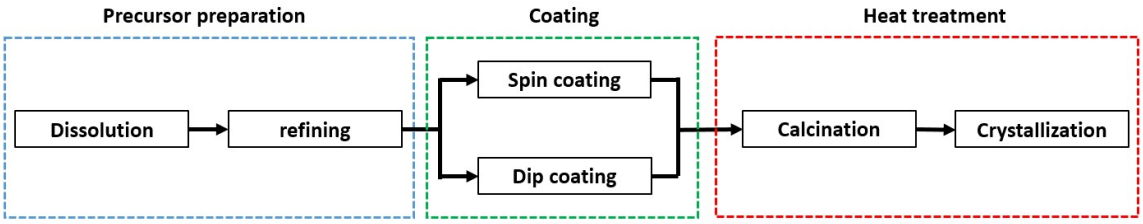

Fig. 3.7. A schematic of the procedure of TFA-MOD YBCO.

3.3.1 Precursor preparation

In the TFA-MOD process for YBCO films, the coating solution is synthesized from an aqueous solution of metal (Y, Ba, and Cu) acetates and TFA. The synthesis process is the starting point of a series of reactions in the production of TFA-MOD, and a highly purified coating solution is required to obtain high performance YBCO superconductors.

An IKA RV8V rotary evaporator is employed for the precursor preparation. The procedure to synthesize the precursor is summarized in Fig. 3.8.

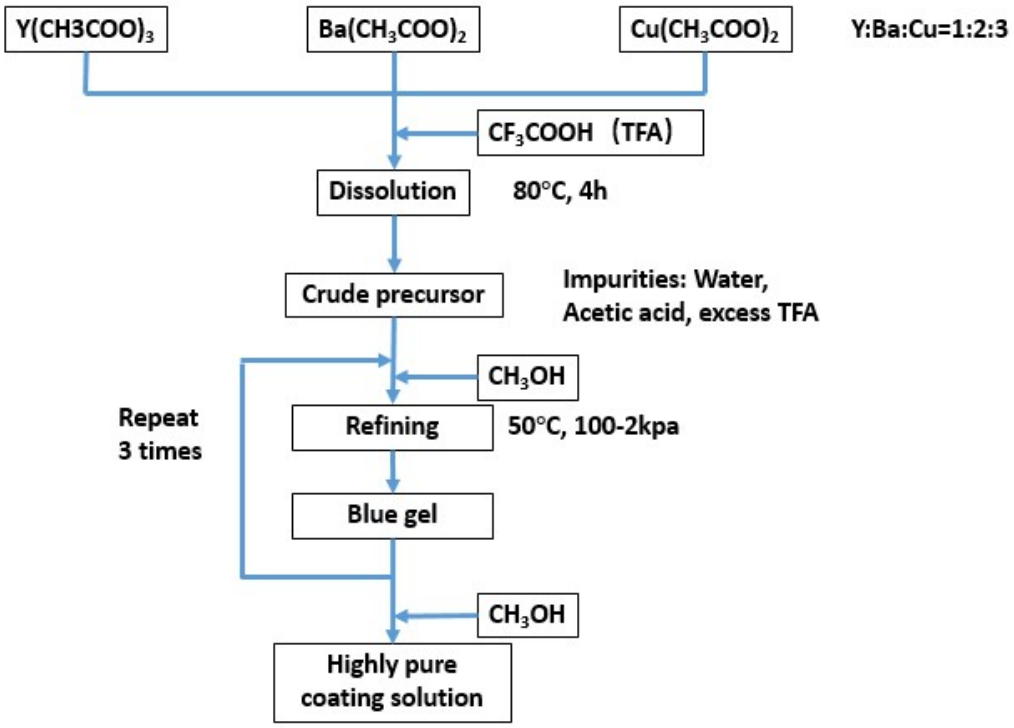

Fig. 3.8. The precursor preparation procedure of TFA-MOD.

3.3.1.1 Dissolution and reaction

Metal (Y, Ba, and Cu) acetates are mixed with a molar ratio of 1:2:3 and dissolved in a stoichiometric amount of TFA inside evaporating flask. The solution inside evaporating flask is rotated at 80 ˚C for 4 h while the replacement reaction of TFA takes place.

3.3.1.2 Refining

To remove the impurities (water and acetate) from precursor, the solution is refined three times under decompression. Methanol is added to the solution before decompression. The refining process is conducted at 50 ˚C. The decompression pressure is controlled carefully from 100-2 kpa to prevent boiling. The pressure slowly reduces as refining continues and the precursor is condensed into a viscous blue gel. After the solution is refined into a dark blue gel, methanol is added into the evaporating flask to dissolve the gel before the next decompression run. The refining process is repeated three times to obtain the higher purity coating precursor.

Then the finished gel is dissolved in methanol into various concentrations for the spin coating or dip coating.

3.3.2 Coating

The finished sol-gel is coated on the bare buffer tapes. The coating process can be accomplished by both dip coating and spin coating. Before coating, the buffer tapes are cleaned and wiped with methanol and blow dried with compressed air to ensure there is no contamination on the tape surface.

Spin coating is a technique used for most of MOD samples in this work. In spin coating, the sol-gel has a metallic ion concentration of 1.5 M. The sample is loaded horizontally on the spinning platform, and the precursor coating solution is dropped on the tape surface to cover the entire sample. A uniform and thin gel film is coated on the sample after a spin at 4000 rpm for 120 s. The acceleration time is 5 s.

Spin-coating is a quick and simple technique for uniform solution coating, but the sample size is limited to the spinning platform. Moreover, the inkjet-printed buffer where its upper surface is uneven, cannot be spin coated uniformly and so, dip coating is employed. In dip coating, a uniform solution film is obtained in the reel-to-reel dip coating system shown in Fig. 3.9. The tape is slowly pulled through the dipping bath with a metallic ion concentration of 1 M at 30 cm/min of tape speed. Gel films are uniformly coated on both sides of the tape. The samples are baked dry at 150 ˚C in the inline furnace. The deposited gel film is cut and further calcined.

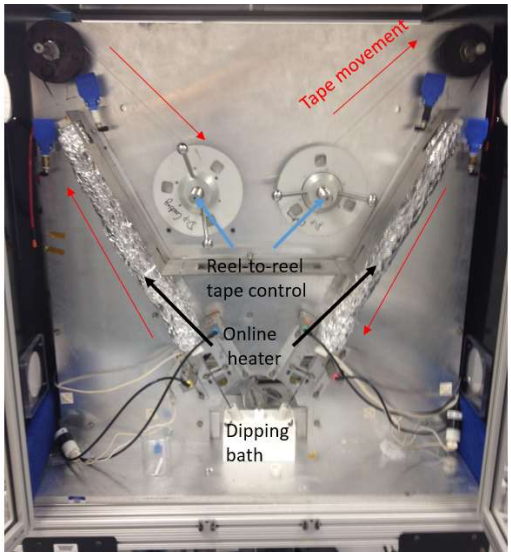

Fig. 3.9. A photo of the reel-to-reel dip coating system.

3.3.3 Heat treatment

The heat treatment for TFA-MOD consists of two steps: the calcination process in which the spin/dip coated solution film is heat-treated into a solid precursor film, and the crystallization process in which the amorphous precursor film is crystallized into the superconducting YBCO.

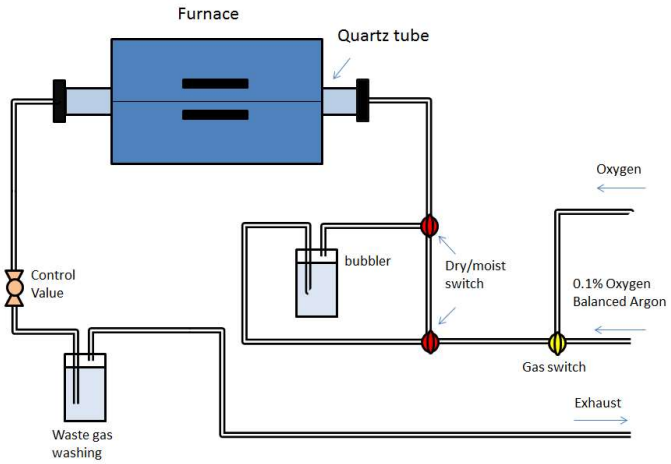

Fig. 3.10. A schematic of the heat treatment system.

The entire heat treatment process is performed inside a Lindberg 1-inch diameter tube furnace. Multiple switches used to control gas supply enable changing the atmosphere in the

furnace during heat treatment (Fig. 3.10). Two kinds of gases are used in this work: ultra-high pure oxygen (≥99.98%) and argon with 0.1% oxygen. Another set of switches is used to create a detour for the gas through a bubbler with DI water and so the gas humidity is adjusted from dry to moist. The level of humidity can be controlled by water temperature inside bubbler. In this work, the bubbler is heated to 30 ˚C to provide about 4.2% humidity during calcination and crystallization processes.

3.3.3.1 Calcination

Calcination of the gel film removes the organic component from the precursor. Samples are heat treated in humidified oxygen. The typical calcination profile is shown in Fig. 3.11. Dry gas is flowed below 100 ˚C to avoid absorption of water vapor into gel film. The oxygen is humidified above 100 ˚C to partially hydrolyze $Cu(TFA)_2$ to avoid sublimation [143, 144]. All metal TFAs are decomposed at 200-250 ˚C to become CuO nanocrystals and Y-Ba-O-F amorphous matrix.

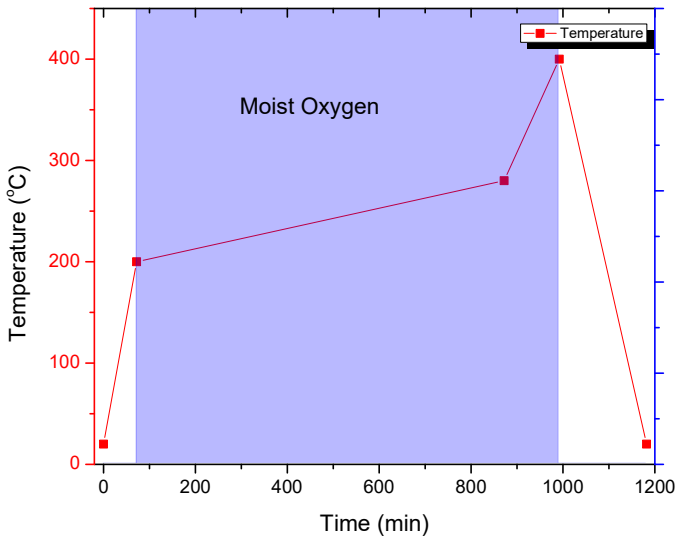

Fig. 3.11. Calcination process for TFA-MOD YBCO.

Because the volume of the gel film decreases over 10 times during this process, a very slow ramp up (0.1 ˚C/min) in temperature is required to prevent the gel film from cracking. The harmful C-O-F residues are decomposed and expelled above 250 ˚C. The details of the heat treatment process are shown in Fig. 3.11. Oxygen with 4.2% humidity is introduced after the furnace temperature is exceeds 100 ˚C to avoid condensation.

3.3.3.2 Crystallization process

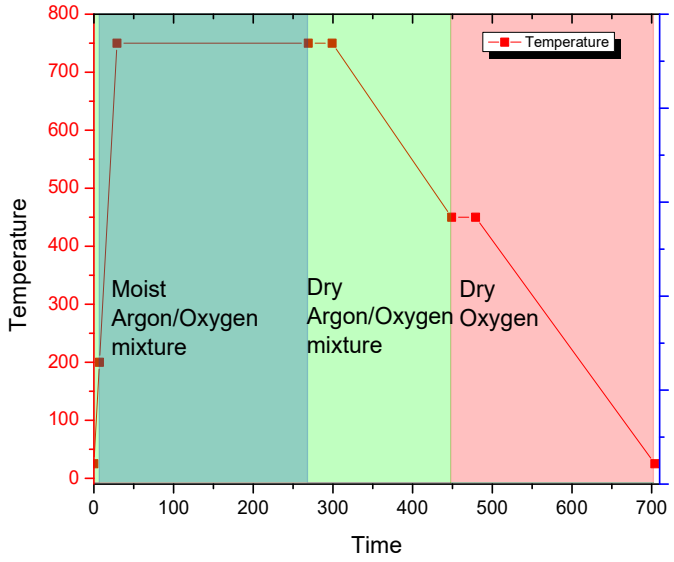

Fig. 3.12. Crystallization process for TFA-MOD YBCO.

The amorphous precursor film must be crystallized into YBCO crystal. The crystallization heat treatment is shown in Fig. 3.12. Fluorides can react with water vapor and HF is generated above 650 ˚C, but YBCO structure formation starts above 725 ˚C [77, 92, 145]. The temperature in furnace is raised sharply up to 750 ˚C as fast as possible. Humidified 0.1% O_2/Ar mixed gas is used in this work. Because it is a solid-gas reaction, the flowrate of the supply gas is crucial [146, 147]; the humidified 0.1% O_2/Ar mixture flows through the 1-inch tube of the system at 120 sccm. of flow rate. The crystallization process takes 2-4 h. By the end of the

crystallization process, YBCO films are oxygenated at 450 ˚C for 1 h to become a complete superconductor.

3.4 Electrodeposition

3.4.1 Electrodeposition of Ag overlayer

Ag electrodeposition is based on the work of the former graduate from our team, Y. Zhang [111, 112]. A non-aqueous Ag electrodeposition process for bare YBCO tapes has been developed.

For the inkjet-printed samples, Ag deposition is required only to cover the superconducting filaments with the selective process, while the insulating inkjet-printed line remains uncoated. Fortunately, due to the large resistivity difference between the insulating printed lines and the less resistive superconductor filaments, selective deposition is obtained by electrodeposition.

3.4.1.1 Beaker size Ag electrodeposition cell

Fig. 3.13 shows the experimental setup of the Ag electrodeposition cell. In this cell, a piece of platinum electrode is used as the anode and bare YBCO tape is used as the cathode. Silver nitrate is dissolved in methanol as Ag source and the electrolyte. The Ag solution is stirred continuously for 20 h before electrodeposition. Ammonium hydroxide is added to the electrolyte for 30 min before deposition. The recipe of the electrolyte is given in Table 3.7.

Table 3.7. Recipe for electrolyte of Ag electrodeposition.

Silver nitrate ($AgNO_3$)	3 g
Methyl Alcohol	135 ml
Ammonium hydroxide	15 ml

A simple DC electrodeposition process is employed for the Ag deposition setup. A Fisher Scientific (FB300) external power supply is used to electrodeposit Ag films. To improve the

deposition uniformity, the superconductor tape is mounted in a polytetrafluoroethylene (Teflon) sample holder, shown in Fig. 3.14, which is designed to cover two edges where the Ag electrolyte ion concentration is higher than other areas of the tape.

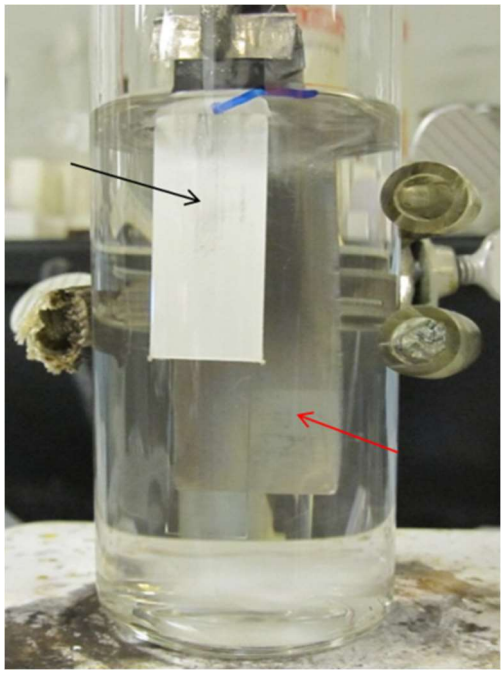

Fig. 3.13. A photo of the Ag electrodeposition cell.

Fig. 3.14. A Teflon shield for better deposition uniformity across the tape width.

For the case of multifilament tapes, as YBCO has low resistivity at room temperature[148, 149], the resistivity of the printed ceramic lines like MgO or BTO is over 10 orders magnitude higher than that of YBCO. As the result, the deposition current is not able to flow in the inkjet-printed lines, as a result of which selective deposition occurs only on the superconducting filament surface.

3.4.1.2 Reel-to-reel Ag electrodeposition

A reel-to-reel electrodeposition system is built for Ag electrodeposition (Fig. 3.15). Because the $AgNO_3$ electrolyte contains methanol and ammonium hydroxide, the system is built inside a screened hood with venting system.

The reel-to-reel tape movement is controlled by a step motor and a torque motor, with the torque motor provide the tension and step motor control the speed. The system can provide accurate back and forth tape movement control for the tape. The speed of the tape can be controlled within the range of 3-11 cm/min.

The 2G-HTS tape is conductive enough to serve as the cathode by itself. The cathodic contact is achieved by passing the tape through a pair silver coated contact roller. And a piece of platinum located 5 cm above the tape and served as the anode. DC power source is supplied by a Pro-Craft electroplater.

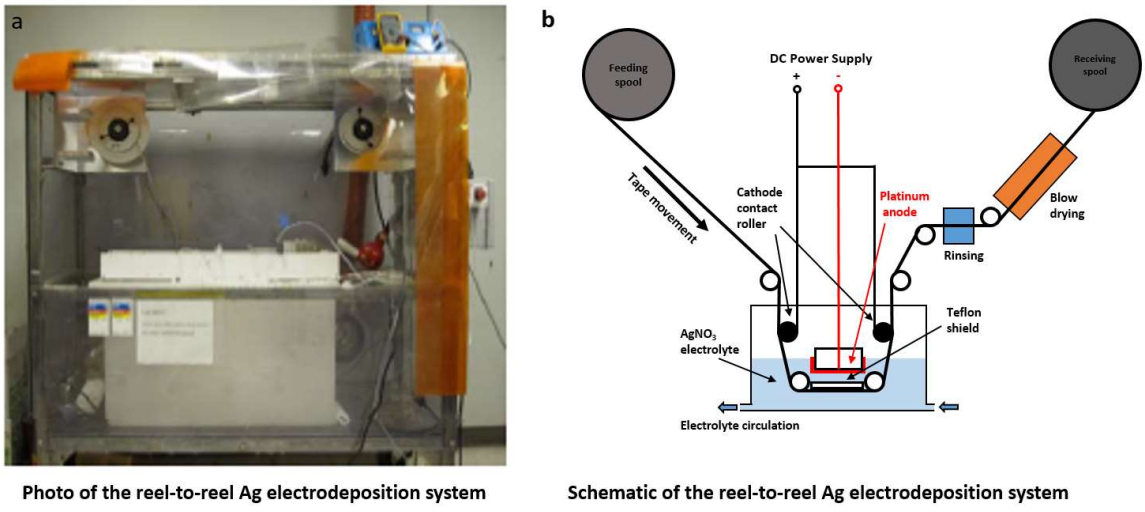

Fig. 3.15. Experiment setup of reel-to-reel Ag electrodeposition system.

A Masterflex I/P peristaltic pump is employed to provide the circulation and agitation for the electrolyte. The electrolyte is pumped in the opposite direction of the tape movement and

provide the agitation of the electrolyte. A filter is installed along to pumping line to remove the impurities and precipitations from the electrolyte. In the long term operation. The consumed electrolyte is replenished manually.

Methanol rinsing and blow drying of the tape is installed in the downstream of the plating process to remove the remnant electrolyte from the sample surface.

3.4.2 Reel-to-reel electroplating of Cu stabilizer

A simple DC electroplating process is employed with $CuSO_4$ aqueous solution as the electrolyte. The process was initially developed and optimized in the same beaker mode shown in the previous section before it is transferred into a large-scale, reel-to-reel continuous plating system. Table 3.8 shows the basic parameters of the Cu electroplating process.

For multifilament samples, Cu deposition needs to be done selectively, with Cu only covering the superconducting filaments. Laser-striated tapes are used for the work. High temperature oxidation is needed to oxidize the exposed Hastelloy surface before Cu electroplating. The higher resistive Ni and Cr oxides formed on the groove surface inhibits the deposition current on the laser-scribed groove surface and thus enabling the selective plating.

Table 3.8. Cu electroplating parameters.

$CuSO_4 \cdot 5H_2O$	1 M
H_2SO_4	$0\text{-}5\times10^{-4}$ M
pH	3.8-2.5
Current density	60-600 mA
Temperature	20-60 ˚C

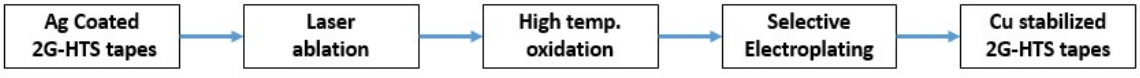

Fig. 3.16. A schematic of multifilament procedure of laser ablation/selective electroplating.

Fig. 3.17. A photo of METFAB reel-to-reel electroplating system.

For fast and continuous plating of long tape, a METFAB Technologies Inc. designed reel-to-reel electroplating system (Fig. 3.17) is employed in this work. The entire system consists of four different components: reel-to-reel tape movement control, electroplating cell and power supply, electrolyte heating and circulation, and tape rinsing and cleaning.

3.4.2.1 Reel-to-reel tape movement control

A simple reel-to-reel tape movement control unit is fitted into the system. The take-up spool is installed on a torque motor, which draws the tape through the system from the pay-off spool that is loaded over a break disc to provide the tension to the tape. An encoder monitors the tape speed and feedback control output of the torque motor. Thus the tapes can move from the pay-off spool to the take-up spool at 4-80 cm/min.

3.4.2.2 Electroplating cell and power supply

A simple DC electroplating set up is used for this work. The conductivity of 2G-HTS in the normal state is primarily determined by the metal substrate and so, the tape itself is used as a cathode. As shown in the schematic of the electroplating system in Fig. 3.18, electrical contact is achieved by Cu brushes sweeping the tape surface. The tape is drawn through the center of the plating cell. Titanium baskets filled with Cu pellets are loaded on both sides of the cell and connected to the positive terminal of the power supply. In this way, both sides of the tape can be plated in one run and the consumed Cu on the anode can be easily replenished by adding Cu pellets into the baskets in a long plating process. The DC power is supplied by a Plating Electronic Power Station pe 1050 DC rectifier. Even though the rectifier provides DC current up to 50 A, high currents (>18 A) will result in heavy electric spark on the brush contacts and will burn the tape surface.

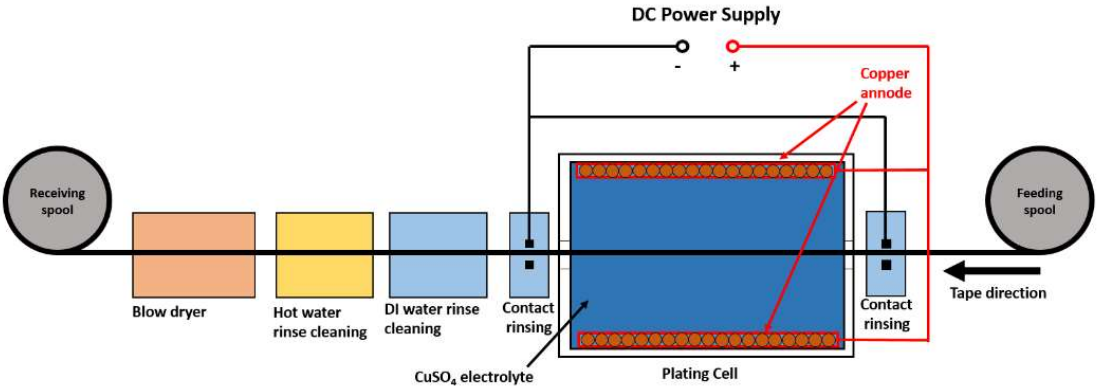

Fig. 3.18. A schematic of the reel-to-reel electroplating system.

3.4.2.3 Electrolyte heating and circulation

Because the reel-to-reel plating system is designed for long-term continuous operation, it is important to keep the electrolyte in a constant condition. A 100 L electrolyte reservoir is built below the plating cell and the electrolyte is pumped and circulated between the reservoir and the plating cell. Filters are installed in the circulation loop to remove the Cu shards and other

impurities generated during the plating process. Meanwhile, the circulation pumping provides the necessary solution agitation. A heater is built inside the solution reservoir to heat up the electrolyte.

3.4.2.4 Tape rinsing and cleaning

The tape surface should be kept as clean as possible because any defect would influence the surface morphology of the electroplated layer, which would result in weak bonding with the silver overlayer or bridging between different filaments. Cleaning of the tape surface is crucial before and after plating and so, multiple rinsing and cleaning units are integrated along the reel-to-reel process for the following purposes (Fig. 3.18):

- Initial DI water rinsing before plating: to clean out possible dust or other defects.
- DI water rinsing over the contact brushes: to dissipate the Joule heat generated by the high current on the brush contact and prevent contact sparks from the brushes burning the tape surface.
- Cold and hot water rinsing after plating and warm air drying: to completely remove remnant electrolyte from the tape surface and inside the grooves. Remnant electrolyte on the tape after plating will result in galvanic interaction, which can damage the plated Cu surface and even destroy superconductor in long term.

3.5 Characterization and performance testing

3.5.1 General characterizations

A KLA Tencor Alpha-Step IQ profilometer is used for surface profile analysis of inkjet printing lines and thickness measurement of the TFA-MOD YBCO layer. Viscosities of the solutions, including inkjet printing sol-gel ink, TFA-MOD precursor and electrolytes are measured by a Cannon-Ubbelohde Semi-Micro Viscometer. An Agilent Inductively coupled

plasma mass spectrometry (ICP-MS) is used for elemental analysis of the MOD YBCO thin film.

The interfacial bonding between the deposited Cu layer (20 μm thick) and the Ag overlayer on a 12-filament sample is examined by peel tests. Peeling tests are conducted at 90° and 180° at 2 mm/s peeling speed as shown in Fig. 3.19.

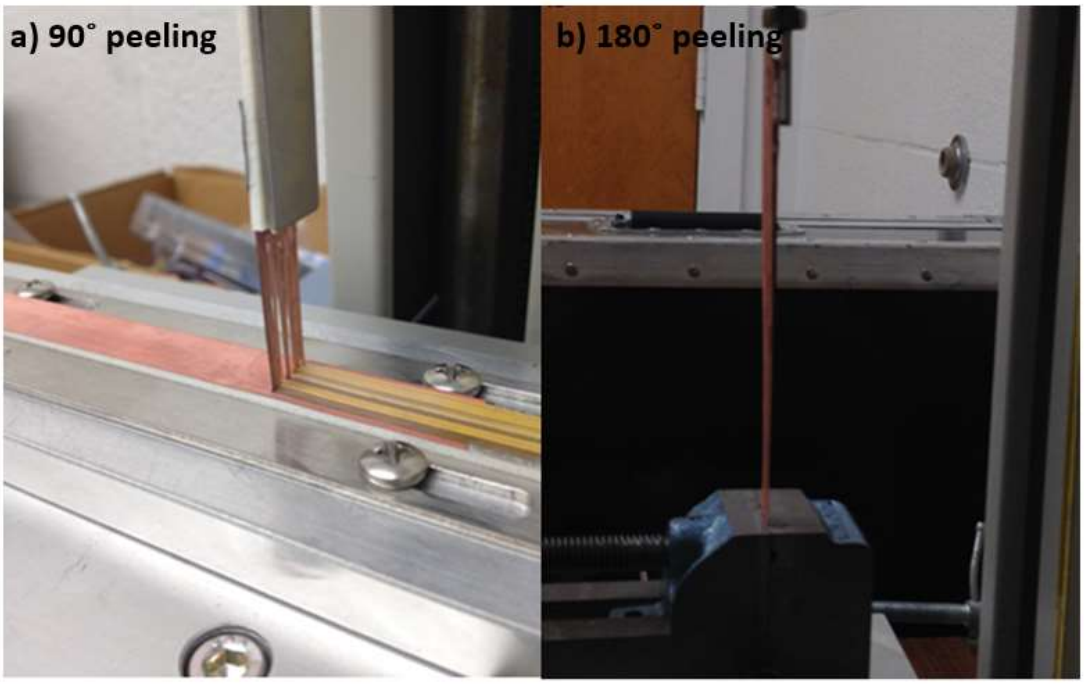

Fig. 3.19. Photos of peel test at 90° and 180° at 2 mm/s peeling speed on a 12-filament Cu-stabilized 2G-HTS.

The resistance across the width of the inkjet-printed insulator lines is measured by four-probe method. An inkjet-printed line is printed in the middle of the sample. Four Ag contacts are made on REBCO surface by sputtering where current taps and voltage taps are both separated by the inkjet-printed line. The sample is submerged in liquid nitrogen during the measurement. The voltage value is recorded when the measurement current slowly ramps up at the speed of 10 mA/s. The slope from the I-V curve shows the resistance across the line.

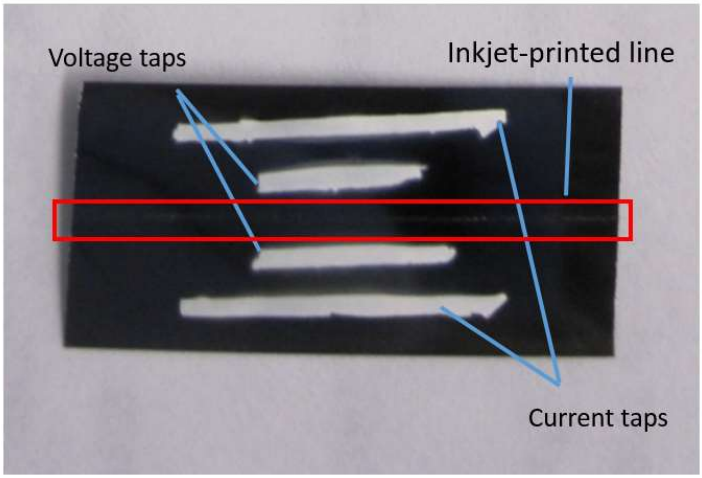

Fig. 3.20. A sample prepared for the resistance measurement.

3.5.2 Microstructural characterizations

X-ray diffraction (XRD) data is obtained using a Bruker General Area Diffraction Detector System (GADDS) with Cu K_α radiation and a 2D detector. GADDS is primarily used to investigate the crystalline characteristics of MOD YBCO. The morphology of the samples is studied with optical microscopy, scanning electron microscopy (SEM) and profilometer. A Keyence optical microscope is employed to investigate the morphology of inkjet printed lines or laser striated grooves and the deposition on them.

Microstructures of the deposited films are studied by a LEO 1525 SEM. The cross-section SEM images were taken with a FEI 235 dual-beam focused ion beam (FIB) SEM. A JEOL JSM 6330F field emission SEM with energy dispersive X-ray spectroscopy (EDX) are employed for chemical characterization of the surface features.

3.5.3 Superconducting performance

3.5.3.1 Critical temperature.

Critical temperature(T_c) of the 2G-HTS is measured using an inductive method (Fig. 3.21) [150]. An alternating magnetic field is generated by an excitation coil. A lock-in amplifier

(Signal Recovery 7265) is employed to analyze the induced signal generated by the pick-up coil. A silicon diode temperature sensor (DT-670, Lake Shore Cryotronics, Inc.) is used to monitor the sample temperature during the measurement.

The sample is placed between the pick-up coil and the excitation coil during the measurement. The sample is cooled in liquid nitrogen and left at the neck of the liquid nitrogen dewar, allowing it to slowly warm up from 77 K. When the sample temperature is below T_c, the induced current inside the superconductor blocks the signal from the pick-up coil. As the temperature reaches T_c, the shielding current generated by the sample can no longer shield the field generated by the excitation coil, and a drastic increase in inductive voltage in the pick-up coil can be observed.

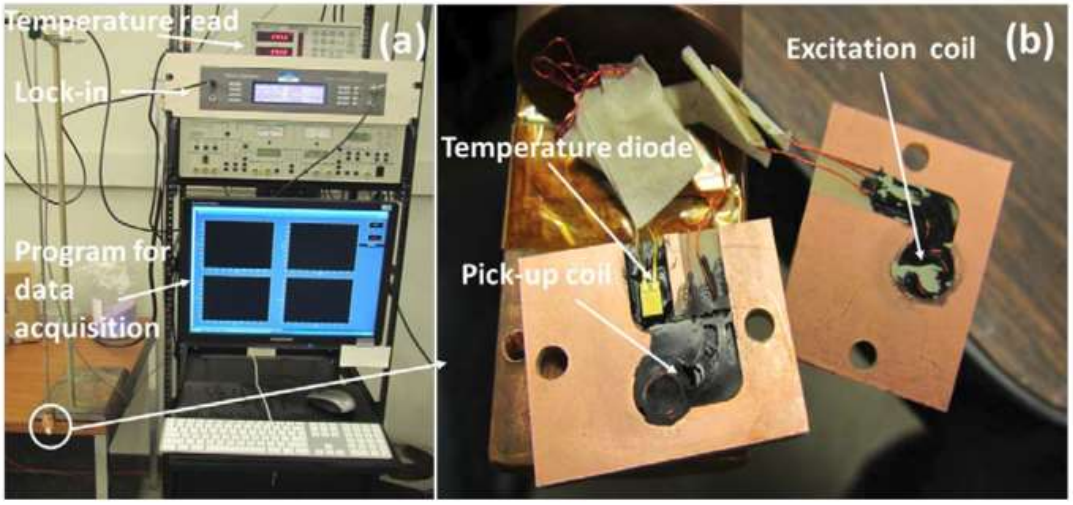

(a) T_c measurement setup (b) Detail of the coils and the diode sensor

Fig. 3.21. A photo of Tc measurement set-up and detail of coils and sensor.

3.5.3.2 Critical current measurement

a. Self-field I_c measurement

The I_c of the Cu electroplated 2G-HTS tape samples is measured by a standard four-probe method at 77 K [13]. Both ends of a sample are soldered to a pair of Ag tapes as the current taps. A DC current provided by a power supply (Lambda, GEN-3300W 600 A) flows through

the entire sample. Two voltage taps are directly soldered on the tape surface (Fig. 3.22a) and connected to a two-channel model nanovoltmeter (Keithley, 2182 A) for voltage measurement.

However, for the multifilamentary samples, because each filament is an independent channel for the measurement current, larger current taps are soldered on the filament for better current sharing, and the voltage taps are connected to a piece of Ag tape soldered across all filaments to measure the maximum critical current for the whole tape (Fig. 3.22b).

The entire sample is dipped in liquid nitrogen during I_c measurements. The measurement current ramps up from 0 V; when the measurement current is lower than I_c, 0 V is measured between the voltage taps due to zero resistance of the 2G-HTS. However, when the measurement current reaches I_c, the tape loses its superconductivity. So, the I_c of a sample can be determined by its sharp take-off in the current-voltage (I-V) curve.

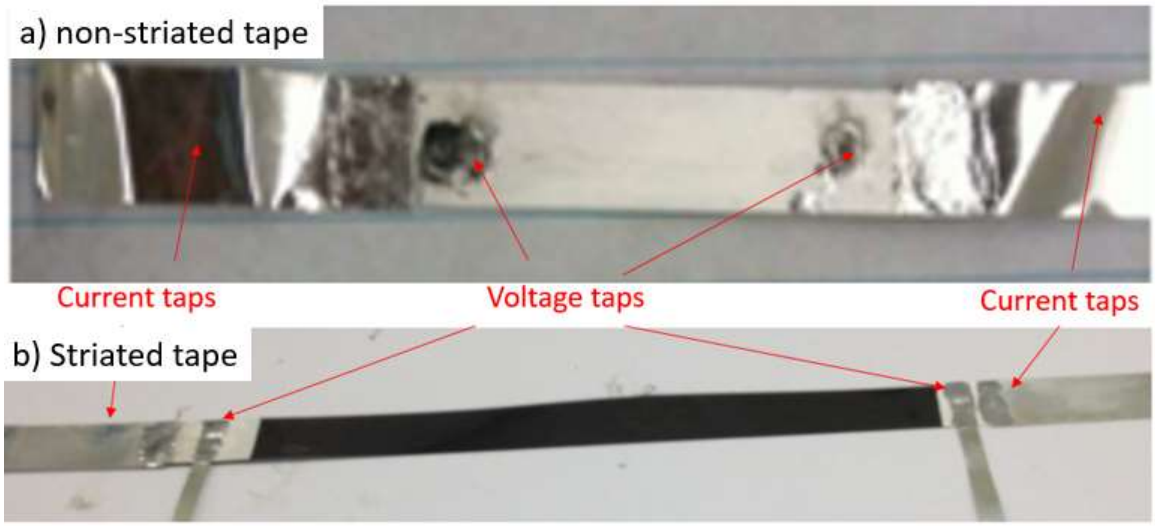

Fig. 3.22. Non-striated and striated samples for four proble transport I_c measurement.

b. Angular-dependence in-field I_c measurement

The angular-dependence of I_c of the tapes is measured in an 1 T magnetic field by a similar four-probe transport measurement (Fig. 3.23). The sample is loaded on a measurement probe and dipped into a liquid nitrogen-filled cryostat and located in the middle of the 1 T magnet.

The measurement probe is rotated 360˚ step-by-step by a motor and the four-probe transport I_c measurement mentioned above is conducted at each step. Thus, the I_c of the tape at 1 T at different angles of the magnetic field are recorded.

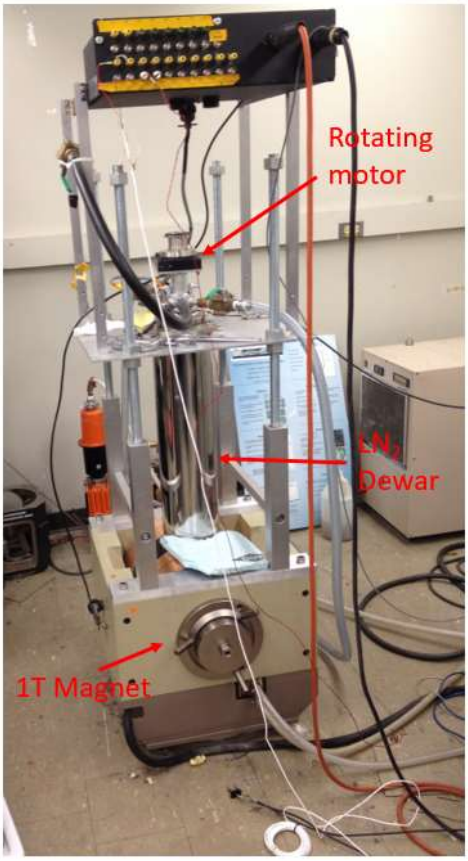

Fig. 3.23. A photo of the 1 T in-field I_c measurement set-up.

c. Inductive I_c measurement by TAPESTAR.

The I_c of the non-striated long tapes can be measured by THEVA TAPESTAR (Fig. 3.24a). TAPESTAR enables rapid, high-resolution inspection of the I_c of the superconducting tape by contactless inductive measurement. During the measurement, the probe head is submerged in liquid nitrogen with the tape moving through. Field coils generate a 60 mT magnetic field that penetrates through the tape (Fig. 3.24c). Seven series-connected Hall probes (Fig. 3.24c), aligned in the transverse direction are buried inside the track above the moving tape. The hall

sensor array picks up the penetration field which is partially shielded by the screening current, and the J_c of the superconducting tape can be calculated through screening current [151, 152]. With the reel-to-reel system continuously moving the superconducting tape through the probe head, TAPESTAR produces continuous scans of the I_c along the tape with millimeter resolution and thus provides detection of local faults and non-uniformities in the superconducting coating.

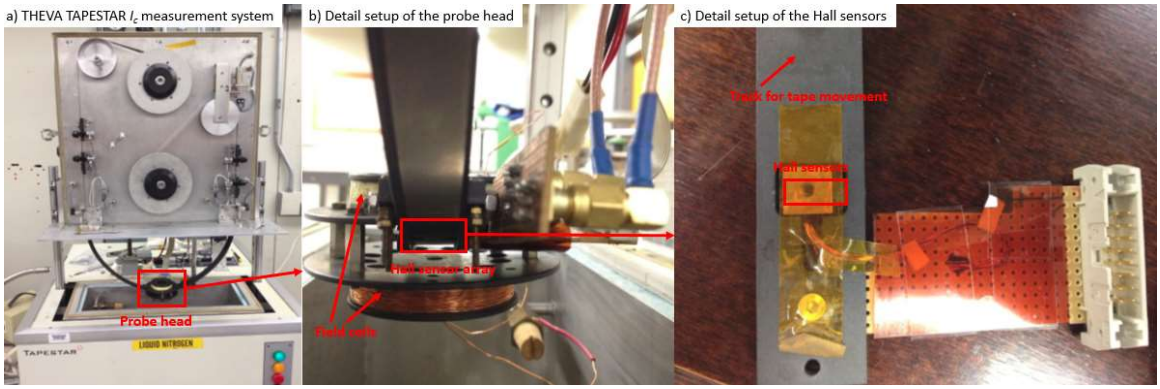

Fig. 3.24. Photos of THEVA TAPESTAR inductive reel-to-reel I_c measurement.

d. Scanning Hall probe microscopy

Scanning Hall probe microscopy is employed to study the J_c distribution in the multifilamentary tape [153]. During the measurement, the sample is glued to an aluminum stage, cooled to 77 K in liquid nitrogen, and then magnetized by a NdFeB permanent magnet. The flux density at the surface of the magnet was above 0.5 T, which is well above twice the penetration field and so, the persistent current inside the tape fully saturated. The saturated persistent current is the critical current.

A Hall probe (Arepoc AXIS-3) scans the sample tape surface and the Hall voltage is picked-up by a Signal Recovery 7280 Lock-in amplifier. The remnant field generated by the persistent current is mapped and defects points with low J_c is shown with low flux density on the field map.

3.5.3.3 AC loss measurement

Magnetization AC losses are measured on samples at 77 K using an inductive technique. Samples are placed in a compensated secondary coil that is axially centered in the middle of the larger solenoid that generates a uniform ac magnetic field perpendicular to the sample surface. The excitation solenoid is powered by an Elgar True Wave AC programmable power source, and the out-of-phase component is extracted using a Signal Recovery 7265 DSP lock-in amplifier. The electrical setup for the system is shown in Fig. 3.25 [154].

The AC power loss is found as [155]

$$P = \beta B_{ac} V'', \tag{3-3}$$

where *V''* is out-of-phase voltage, B_{ac} is the applied field, and β is the calibration coefficient determined using reference samples. In order to distinguish the source of loss, AC loss is measure in different fields and various frequencies.

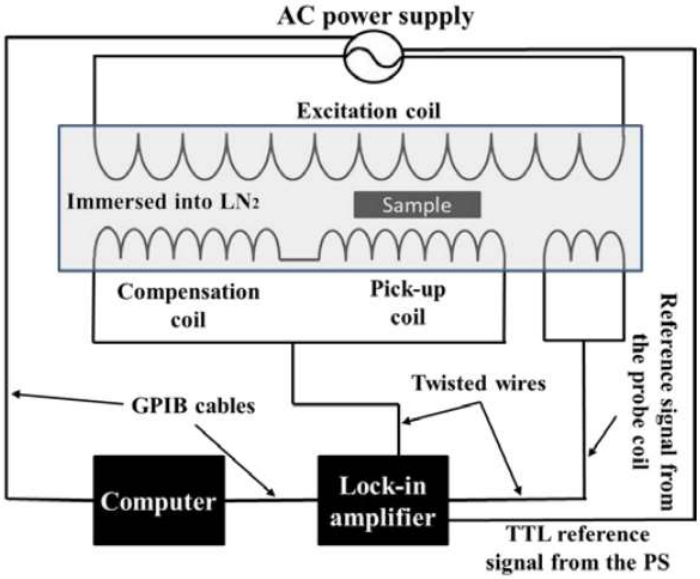

Fig. 3.25. Electrical set-up for the magnetization AC loss measurement system.

Chapter 4. Inkjet Printing for Multifilamentary Tapes

In this chapter, we focus on the inkjet printing of materials mentioned in section 3.1.1, which are used to build a series of parallel insulators along the length of the tape to divide into multiple superconducting filaments in the subsequent MOCVD or MOD process. A superconductor tape with 0.4 μm-thick REBCO film is obtained by MOCVD on the inkjet-printed tape. Ag is selectively electrodeposited on the superconductor filaments with DC electrodeposition in a non-aqueous electrolyte.

4.1 Materials selection and ink preparation

4.1.1 Materials selection criterion

The inkjet-printed lines will serve as insulators along the length of 2G-HTS tape and so, the lines need to be continuous and straight. Any break points in the line or cracks across line width may cause coupling of the filaments and hence higher AC loss. Curvature or wiggling in the line will directly result in reduction of the effective conducting areas of superconductor.

The cross-sectional profile of inkjet-printed lines also needs to be taken into consideration. The I_c is directly affected by the width and the thickness of lines. The wider the lines are, the larger the loss of conducting area. Thicker lines are preferred for the thicker filaments of YBCO.

The resistance between two superconducting filaments is an important parameter for minimization of AC loss in superconductor applications [156]. The high interfilament resistance is achieved by inkjet-printing the insulating ceramic lines on the buffer tape before MOCVD. When REBCO is deposited on the inkjet-printed tape, an epitaxial growth can be achieved on the pristine biaxially-textured buffer. Due to the non-textured and mismatched structure of the insulator lines, epitaxial growth of REBCO may not be possible. Only a thin layer of randomly-

oriented structure which is not capable of carrying superconducting current and a high resistivity about 10^7 Ω·m [37] is preferable on the lines. Selective deposition of HTS film has been studied r superconducting electronic devices fabrication [157-159].

Selective deposition of Ag is achieved by utilizing the resistance difference between the ceramic line and the conductive filament. The tape serves as the electrodeposition cathode. The conductivity of tape is governed by Hastelloy substrate which has the resistivity of 1.3×10^{-8} Ω·m. The buffer consists of a multilayer of insulating ceramic films, but due to low thickness (~0.2 μm) and large area, the resistance across the buffer stack is only the level of 1-1.5 mΩ [160], which is insufficient to stop the electrodeposition current. With the insulating inkjet-printed ceramic lines which has a high resistivity of $>10^{10}$ Ω·m and the textured YBCO filaments which have low resistivity of ~10^{-6} Ω·m. The difference of resistivity results in a biased ion flux near the filaments and selective electrodeposition is achieved on the filaments.

A summary of the ink material selection criteria is as follows:

- Resistance across line high enough to insulate filaments at 77 K & room temperature. The resistance across the lines at 77 K should be comparable with the values (13.3 mΩ and 18 mΩ) obtained from laser-striated samples by Amemiya et al. [30] and Demencik et al. [160].
- Epitaxial growth of REBCO is disrupted on the insulator lines forming random oriented grains of high resistivity.
- Suitable for selective electrodeposition of Ag or Cu. No conducting connection between the filaments on the top of ceramic lines.
- The reduction of I_c should be corresponding with the loss of conducting area. Further degradation should be minimized.

- Stable ink and continually printing uniformity and smooth straight line without breaking points or transverse cracks. The thickness should be higher than YBCO (more than 0.4 μm in this work) and the width should be minimized, no more than 250 μm.

4.1.2 Tin oxide and iron oxide

4.1.2.1 Tin oxide

SnO_2 nanowires were used as artificial pinning centers for REBCO by former graduate student R. Mallick [161]. These nanowires were are grown on the buffer before MOCVD of REBCO and served as pinning centers inside the superconductor film [161]. In this section, SnO_2 is examined whether or not it can serve as an insulating barrier. SnO_2 has certain semiconductor nature, but the mobility of charge carriers is reduced at low temperature and so, it might be a good insulating barrier at superconductor operating temperature.

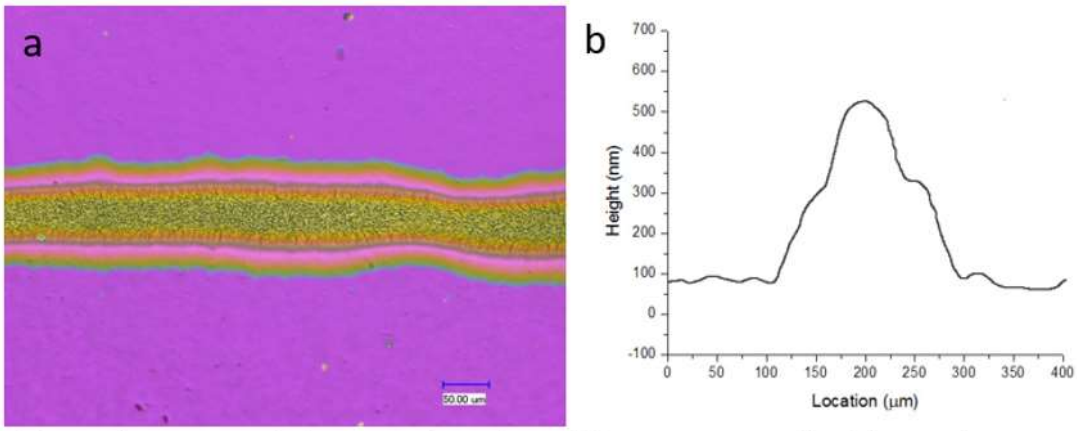

(a) Optical microscopy of inkjet-printed SnO_2 line. (b) Cross-section profile of the SnO_2 line

Fig. 4.1. Optical microscopy and cross-section profile of inkjet-printed SnO_2 line.

Most of gel inks shrink easily in thickness direction or form many pores and cracks during heat treatment. However, it is found SnO_2 line shrinks in the width direction during heat treatment at 500 °C, leaving a wetted track on both sides of the line (Fig. 4.1a). A similar pattern has also been reported by Jang et al. [162] on inkjet-printed ZrO_2 films. Surface tension may be reason for this effect and it can be adjusted by adding a surfactant such as DEA, to the

ink. Surface profilometry shows the printed SnO_2 line has a ridge-shape with two sloped shoulders, with 170 μm width and 450 nm height (Fig. 4.1b).

It is observed from Fig. 4.2 that both MOCVD REBCO and electrodeposited Ag cover the entire surface, including the bare tape surface and the inkjet-printed lines. SnO_2 lines has a resistivity of about 0.1 Ω·m [163] which is only 5 orders of magnitude higher than that of YBCO (~2×10^{-6} Ω·m) . Ag deposition is not affected by the difference of the resistivity between YBCO and SnO_2. The resistivity difference is not large enough to bias the ion flux completely toward the filaments.

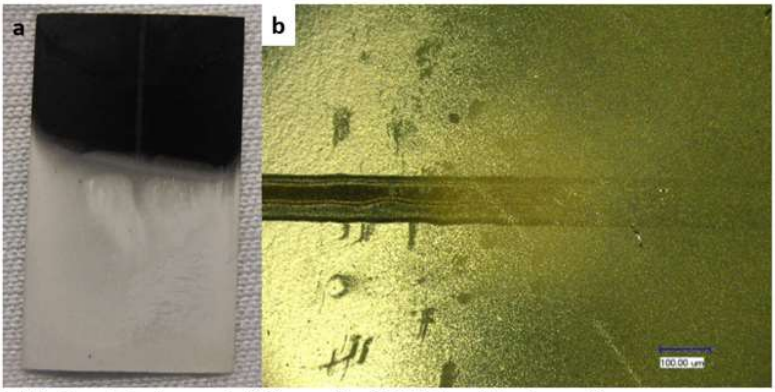

(a) SnO_2 printed sample followed by REBCO and Ag deposition.
(b) Optical microscopy of Ag deposited on SnO_2 printed lines.

Fig. 4.2. SnO_2 printed sample after MOCVD REBCO and Electrodeposited Ag.

4.1.2.2 Iron oxide

To increase the resistivity of printed line, Fe_2O_3, which is chemically reactive with REBCO was considered next. Fe atoms will react with REBCO by replacing Cu site in the lattice, which might form high resistive interfaces and suppress superconductivity of REBCO.

The printed Fe_2O_3 line is about 200 μm wide and shows a craggy surface (Fig. 4.3). Because Fe_2O_3 sol-gel ink used in this work is base-catalyzed, colloids of Fe hydroxide aggregate and crystallize before the ink is dried on the tape. The phenomenon is usually observed in aged sol-gel, which will cause rough surface in thin film synthesis or in liquid-

phase powder synthesis [164, 165]. The craggy surface might provide more surface area in contact with REBCO deposition.

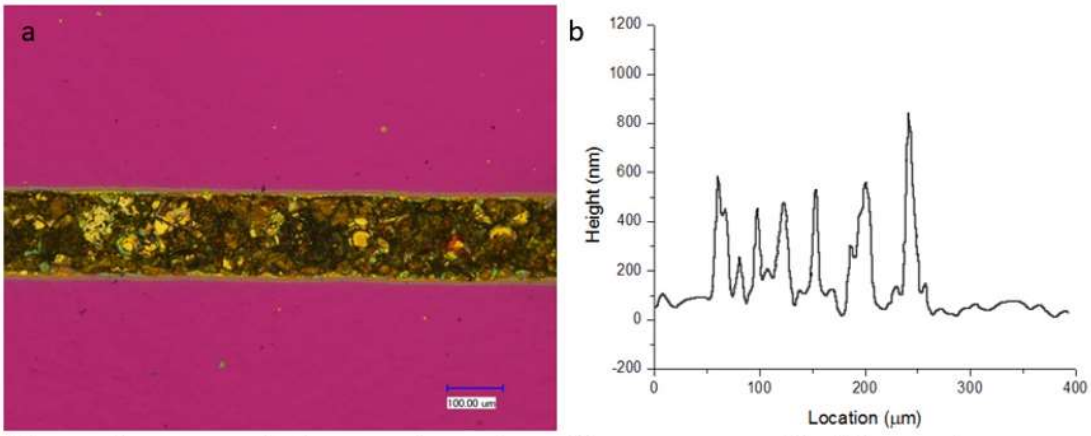

(a) Optical microscopy of inkjet-printed Fe_2O_3 line. (b) Cross-section profile of the Fe_2O_3 line

Fig. 4.3. Optical microscopy and cross-section profile of an inkjet-printed Fe_2O_3 line.

However, Fe_2O_3 line has a huge impact on the REBCO around it. SEM analysis shows that the affected areas on both sides of the line are very large. REBCO at 0.1 mm away from the line is still heavily misoriented (Fig. 4.4b). Large number of a-axis grains and defects can still be found in REBCO deposited 2 mm away for the Fe_2O_3 line(Fig. 4.4a).

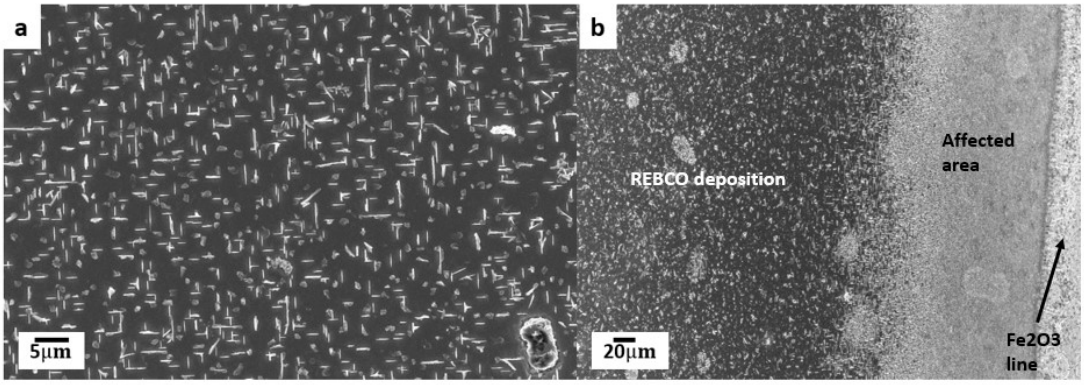

(a) REBCO deposition 2mm away from Fe_2O_3 line (b) Large affected area on the side of Fe_2O_3 line

Fig. 4.4. SEM image of the sample printed Fe_2O_3 line after MOCVD REBCO.

As the microstructure of REBCO is so badly affected, degradation on superconducting performance can be expected. A large degradation of I_c from 100 A to 60 A is observed in the

sample with only one Fe_2O_3 line printed in the middle (Fig. 4.5). With such a large impact on the sample I_c, Fe_2O_3 cannot be used as the insulating material.

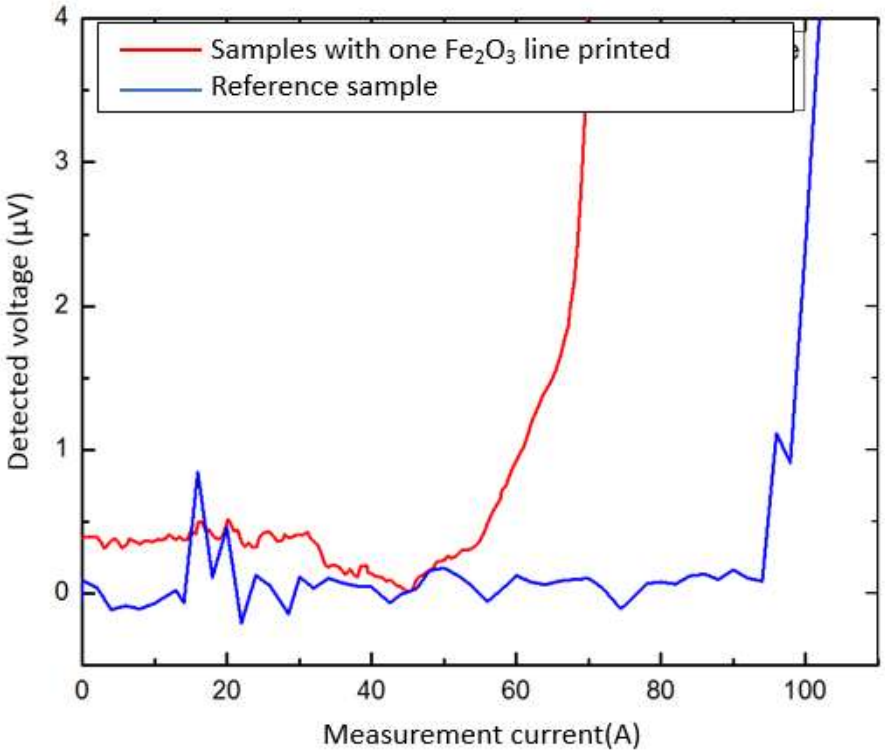

Fig. 4.5. I_c at 77 K in zero field of a YBCO sample with only one Fe_2O_3 printed line compared with a reference YBCO sample, both made by an identical MOCVD process.

4.1.3 Magnesium oxide, Barium Zirconate and Barium Titanate

The inkjet-printed lines should have high resistivity and chemical compatibility with REBCO. MgO, BZO and BTO meet these requirements and are studied next.

Magnesium oxide (MgO) is one of major components in the buffer stack and has good chemical compatibility with REBCO. BZO has a similar perovskite crystal structure as YBCO and is one of the most commonly-used as artificial pinning center doping materials for 2G-HTS [166-168]. BTO, similar to BZO, is also reported as a dopant for 2G-HTS [169]. All these three ceramics have a high resistivity of more than $10^{12}\ \Omega\cdot$m.

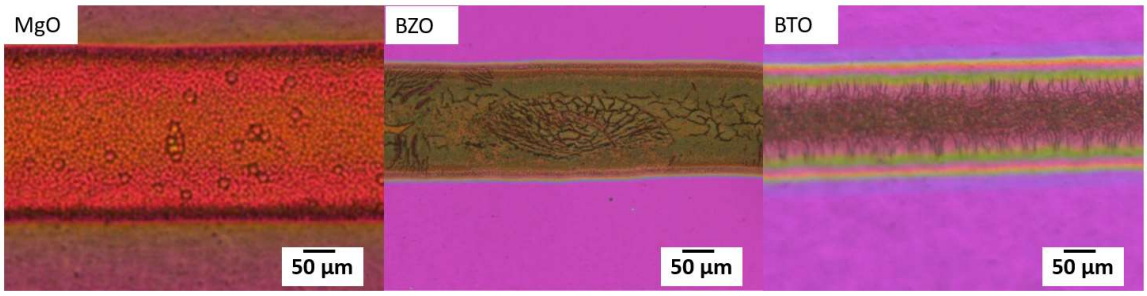

Fig. 4.6. Optical microscopy of inkjet-printed MgO, BZO, and BTO lines.

Fig. 4.6 shows all three inks can be used to print continuous straight lines along the length of tape. No breaking point is found and the lines have straight edges. The average width of the MgO, BZO and BTO lines are 236 µm, 165 µm and 164 µm respectively. The BTO and BZO lines are narrower due to the higher viscosity of those inks which slow down the liquid expansion when drops land on tape. Both MgO and BTO lines show smooth surfaces, but some cracks are found in the thicker part of BZO which are formed by the tension in drying gel. Fig. 4.7 shows the cross-section profile of the lines. All three samples showed a trapezoid shape in the cross section, the average thickness of the lines are respectively 360 nm, 396 nm and 1107 nm. The better BTO printed lines are attributed to subsequent optimization work, which will be discussed in section 4.2.

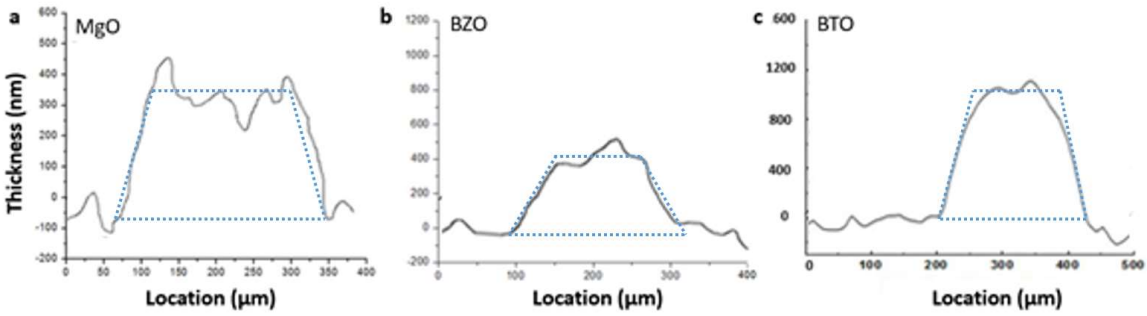

Fig. 4.7. Cross-section profiles of the inkjet-printed MgO, BTO and BZO lines.

All three lines showed good continuity and decent thickness, and the next step is MOCVD REBCO on the samples. 0.4 µm of REBCO is deposited on top of the inkjet-printed buffer tapes

at a heater temperature of 975 ˚C. SEM microscopy images growth features of REBCO on the three kinds of inkjet-printed lines (Fig. 4.8).

Uniform and smooth surfaces of REBCO are observed between the inkjet printed lines which indicates that the epitaxial growth of REBCO on the bare buffer is basically unaffected. Only a small amount of a-axis grains are found in REBCO betweent MgO lines.

The deposition on the printed lines shows porous structures and the randomly-oriented fine-grain structures. The grain size are different from about 400 nm in BTO to about 1 μm in MgO and BZO. The randomly-oriented REBCO has a high reisistivity and is not able to carry any superconducting current. However, REBCO growth on cracks of BZO lines showed smooth plate-shape structures.

On the edge of the inkjet-printed lines, there is a transistion areas between the ‘good’ and ‘bad’ REBCO, different transistion areas in morphology are oberserved in the three samples. In the MgO sample, REBCO showed a transition region about 60 μm width between regular textured and random oriented structure. The density of randomly-oriented grains increases gradually closer to the MgO lines. The superconductivity can be expected be compromised due to the large affected area. In the BZO sample, the transisition region developes towards the middle of the line and textured ‘good’ REBCO is found until the edge of BZO lines. The textured stuctures starts to break into small and randomly-oriented pieces as BZO line thickness increases. In the BTO samples, the transistion is immediate with the transistion area being only 5 μm wide, where some coarse grain misoriented structure is observed between the ‘good’ and ‘bad’ REBCO.

The resistivity across the printed lines are measured by four-probe method at 77 K and the results are listed in Table 4.1. MgO and BTO line show a good resistivity. The BTO line shows

a resistance of 89 mΩ in a 27 mm long sample which is much higher than the reported resistance across laser-striated grooves (13.3 mΩ by Amemiya et al. [30] and 18 mΩ by Demencik et al. [160]). But the resistance measured across the BZO lines are extremely low at only 1.47 μΩ which might be due to growth of plate-shape REBCO on the cracks of BZO lines.

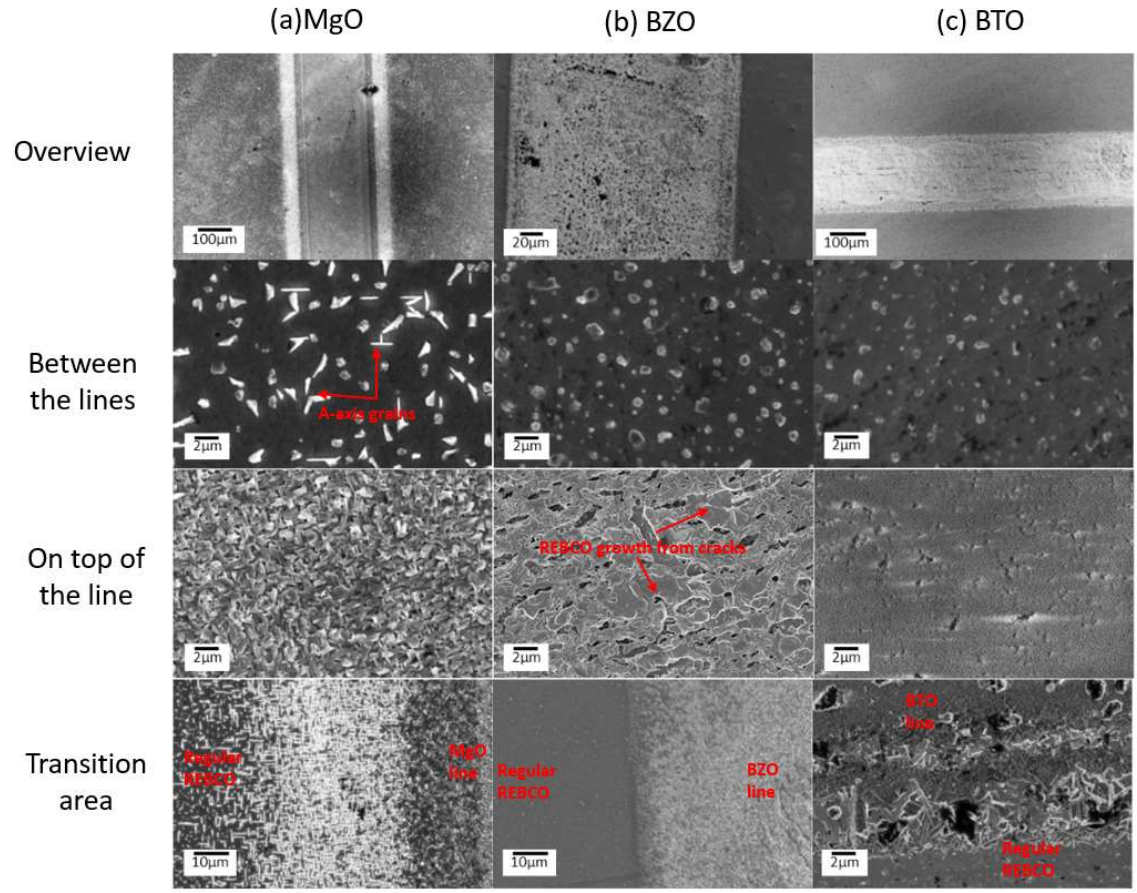

Fig. 4.8. SEM images of the inkjet-printed lines after MOCVD REBCO.

Table 4.1. Resistance measured across the inkjet-printed lines in 77 K.

Line	MgO	BZO	BTO
Resistance (mΩ)	29.1	1.47×10^{-3}	89.2

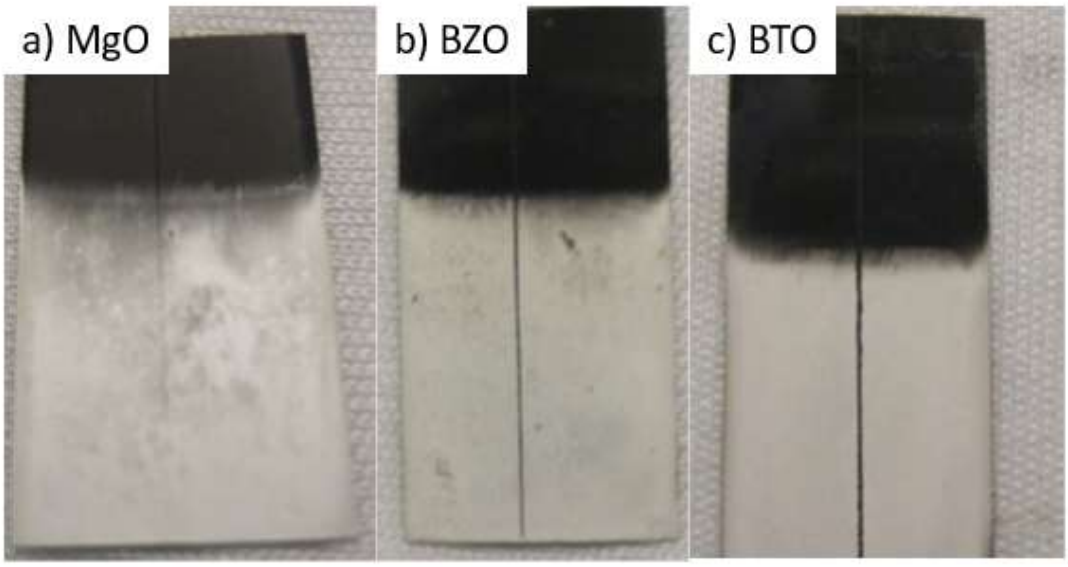

Fig. 4.9. Photos of the samples of MgO, BZO, BTO printed lines after MOCVD REBCO and Ag electrodeposition.

Fig. 4.9 shows the inkjet-printed samples after MOCVD REBCO and Ag electrodeposition. Only one line is inkjet-printed in the middle of each sample. It is found that Ag completely covered the MgO line, but distinguishable selective deposition can be seen on both BZO and BTO samples. It should also be noted that the Ag deposition on MgO sample is stopped before the inkjet-printed line is completely covered by Ag, to reveal more information about the selective deposition process in the following SEM microscopy study.

Fig. 4.10 shows the SEM images of the inkjet-printed line after MOCVD and electrodeposition. On the MgO line printed sample, Ag spherical particles are found all over the sample surface. The Ag deposition is only conducted half way, so neither the line surface nor the filament surface is completely covered by Ag, but Ag particles on the line surface has much lower density. From the SEM image on the edge of the inkjet-printed lines, the Ag density difference between the two regions is clearly distinguishable. This indicates that the resistive MgO line has biased the deposition ions flux, but yet the resistance is not enough to complete the selective electroplating.

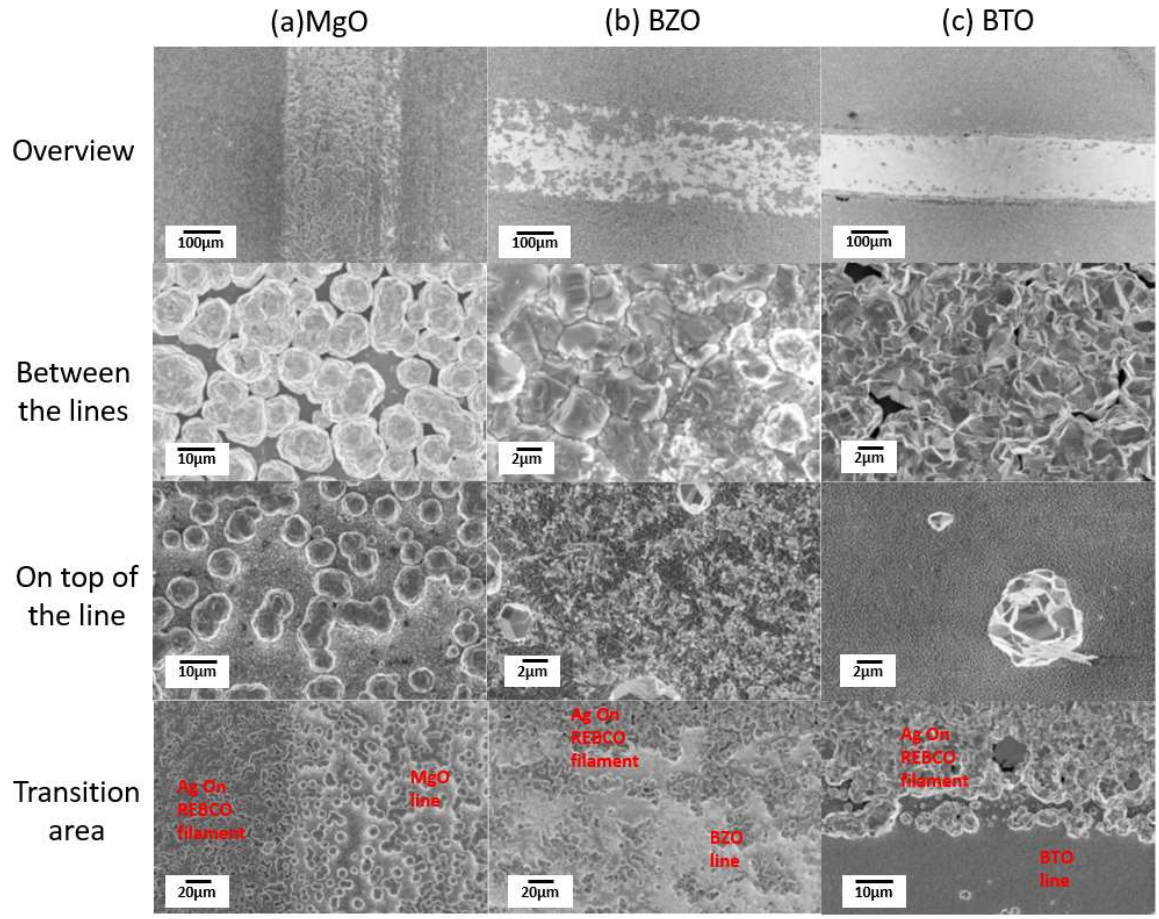

Fig. 4.10. SEM images of the printed lines after MOCVD REBCO and Ag electrodeposition.

On BZO sample, the filaments between lines are completely covered by Ag, and the Ag density gradually reduces on the line surface; this is related to the gradual break down of the textured YBCO shown in Fig. 4.8. In the middle of the inkjet-printed lines, the randomly-oriented fine-grain structure can be seen, which indicates that the surface is almost Ag free, only some small Ag islands are observed. Even though Ag islands are found on the line surface, no Ag connection across the line is observed. Selective deposition of Ag is achieved, but a large amount of Ag particles might create difficulties in the subsequent Cu electrodeposition.

On BTO sample, a dense Ag deposition is found on the filaments. Some Ag deposited on BTO insulator lines as a few isolated Ag islands. Randomly-oriented and fine-grained structure

are still seen after electrodeposition, which indicates absence of Ag coating on BTO lines. The transition region between Ag-covered REBCO filaments and Ag-free BTO lines shows a cliff-shape interface. The highly insulating BTO lines blocked off all deposition currents and result in the complete selective deposition.

4.1.4 Cu doped barium titanate (BCTO)

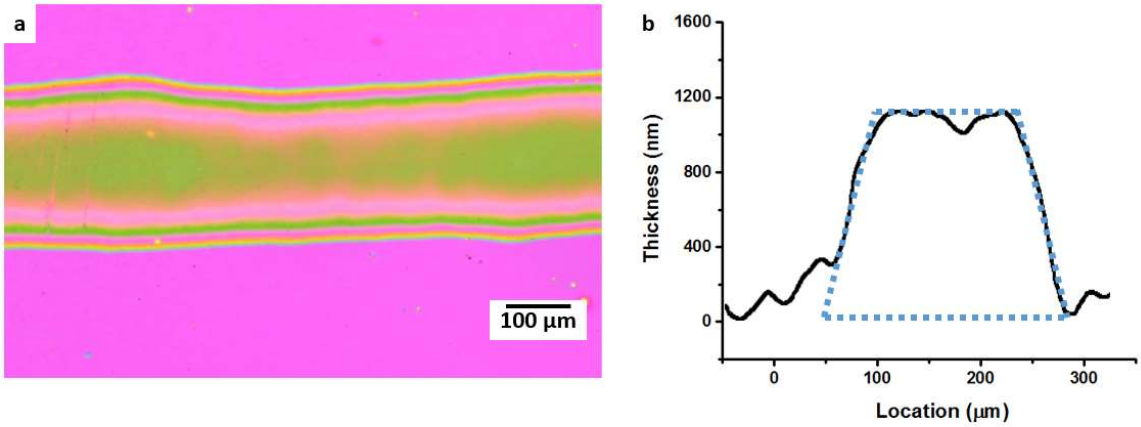

(a) Optical microscopy of inkjet-printed BCTO line. (b) Cross-section profile of a BCTO line

Fig. 4.11. Optical microscopy and cross-section profile of the printed BCTO line.

Cu doping in BTO can raise the dielectric constant at room temperature, which might potentially eliminate the Ag island formation on BTO line. BCTO ink has shown similar viscosity and surface tension as BTO and so the printed lines show a very similar profile. Fig. 4.11 shows the optical microscopy and cross section of BCTO line. The printed BCTO line are 235 µm in width and 1.1 µm in thickness.

Deposition of REBCO can be achieved in the same way as BTO (Fig. 4.12). The MOCVD REBCO on BCTO lines are very similar to that on BTO lines. Smooth deposition is seen on the LMO buffer between two lines and the random-oriented fine-grain structure is observed on the lines. The transition regions showed a similar coarse grain structure. The only noticeable difference between BTO printed sample and BCTO printed samples is that there is some REBCO islands formed on top of BCTO line (Fig. 4.12b).

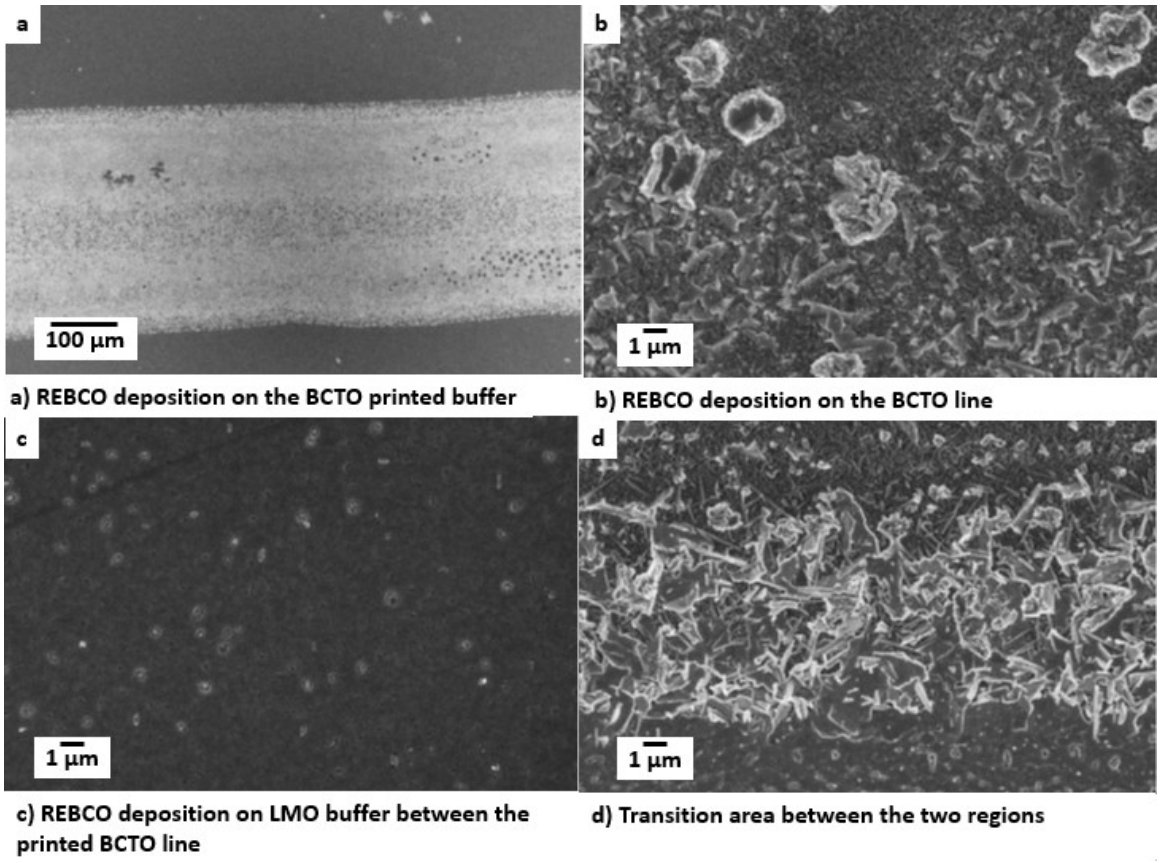

Fig. 4.12. SEM images of an inkjet-printed BCTO line after MOCVD REBCO.

The resistivity across the lines with different amount of Cu doping from 2% to 5% is measured at 77 K (Table 4.2). However, there is no significant increase of resistance across the barriers; the majority of the measurement current passes through the buffer stacks and is conducted through Hastelloy substrate. So the resistance difference among the samples is more likely caused by the different widths of the printed lines and measurement error caused by sputtered Ag contacts on the REBCO surface.

Table 4.2. Resistance measured across the inkjet-printed BCTO lines with different Cu doping in 77 K.

x in $Ba(Cu_xTi_{1-x})O_3$	0.00	0.02	0.03	0.05
Resistance (mΩ)	89	112	72	93

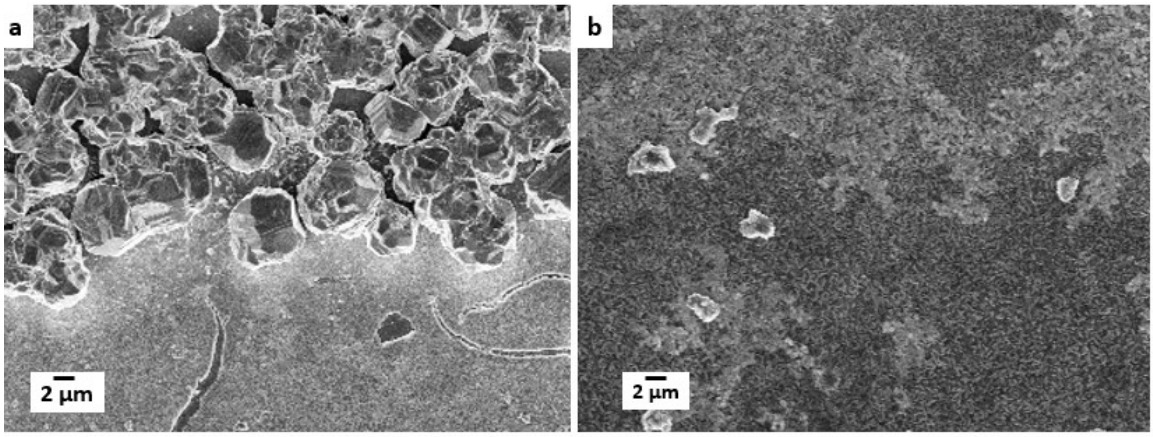

a) Transition area between the Ag coated REBCO filaments and the Ag-free BCTO printed line.

b) Ag deposition on top of the BTO lines after MOCVD

Fig. 4.13. SEM of Ag deposition on the BCTO printed line after MOCVD REBCO.

Selective Ag deposition is achieved just like with BTO line with a cliff-like transition between the Ag coated filaments and the Ag-free BCTO lines (Fig. 4.13a). More Ag islands are observed on the line surface (Fig. 4.13b) and the Ag deposition is mainly found on the REBCO clusters as shown in Fig. 4.12b. The clusters are charged in the electric field and served as seeding centers for Ag deposition. It is found that Cu doping actually increases the Ag island density due to the cluster REBCO formation on the lines. Compared with BTO, BCTO is not suitable for inkjet-printed insulating barrier.

The results are summarized in Table 4.3. Six different ceramics have been evaluated as ink materials for printing insulator lines. The ceramic barriers are formed in longitudinal direction, and has <250 µm width and >400 nm thickness.

The results show BTO is the only one suitable insulator material out of the five. Fe_2O_3 line severely damages REBCO structure and degrades the superconductor performance. The resistivity of SnO_2 is at room temperature is too low to serve as an insulator during the selective electrodeposition. The resistivity of MgO line is not high enough for selective electrodeposition

of Ag without electrical coupling. The resistance of BZO barrier at 77 K is only 1.34 μΩ that cannot meet the decoupling requirement between two filaments.

Table 4.3. Summary of material selection for inkjet printing barriers.

	Uniformity, Dimension (width×thickness)	Selective epitaxial of REBCO	Impact on I_c	Selective Ag electrodeposition	Resistance at 77K (mΩ)
Fe_2O_3	Bad, craggy line 200 μm width	Yes	Large impact on I_c	Partial	38.4
SnO_2	Good, 170×0.45 μm	Yes	Small impact on I_c	No	6.5
MgO	Good, 236×0.36 μm	Yes	Small impact on I_c	Partial	29.1
BZO	Good, 165×0.40 μm	Partially	Very small impact on I_c	Yes	1.47×10^{-3}
BTO	Good, 164×1.10 μm	Yes	Very small impact on I_c	Yes	89.2
BCTO	Good, 235×1.10 μm	Yes	Very small impact on I_c	Yes	112

BTO is found to be the only one suitable insulator material as REBCO grows with an epitaxial orientation on the pristine buffer and as a randomly-oriented structure on the BTO line. The resistivity of the BTO barrier is large enough for selective electrodeposited Ag. Doping BTO with Cu slightly increases the resistance across the line, but the REBCO islands deposited on the BCTO lines benefits Ag deposition. Therefore, BTO is selected for inkjet-printed insulating barrier.

4.1.5 Ink preparation

Inkjet printing is compatible with most of the sol-gel materials, only limited by the viscosity and surface tension of the sol-gel inks. According to the manufacturer, fluids with viscosity less than 20 cPs and surface tension in the range 0.02-0.07 N/m can be dispensed. Viscosity has a large impact on the ink ejection from the orifice and the expansion of the liquid drops as they hit

the tape surface. Inks with viscosity higher than 10 cSt or lower than 3 cSt result in a narrower operation window, which causes difficulties to optimizing jetting parameters. So the kinetic viscosities of the sol-gel inks are preferably controlled within the range of 3-10 cSt.

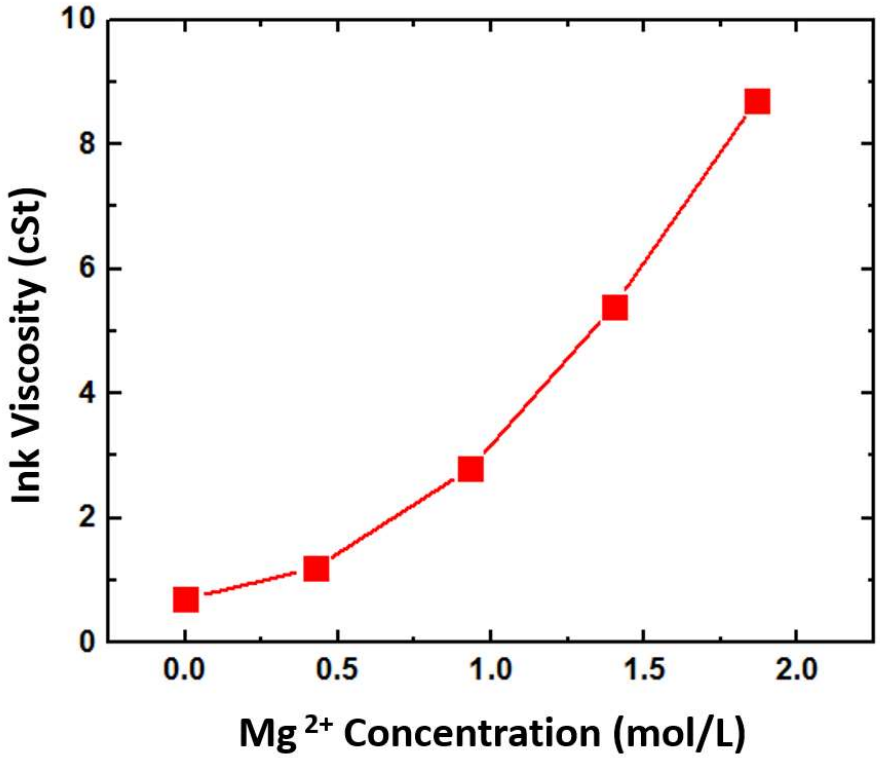

Fig. 4.14. Relationship between the viscosity and Mg^{2+} concentration of MgO precursor ink.

The ink viscosity can be simply adjusted by varying the concentration of sol-gel. Fig. 4.14 shows the relationship between the ink viscosity and the concentration of Mg acetates. It is obvious that the ink viscosity is higher when the solution concentration increase. In this work, the viscous sol-gels are diluted to a workable level with methanol. There are also some special cases like BTO and BZO sol-gels where the solubility of Ba acetate is heavily dependent on the pH level and diluting the sol-gel with only methanol will result in precipitations. So BTO and BZO sol-gels are diluted with methanol/acetate acid (1:1) mixture.

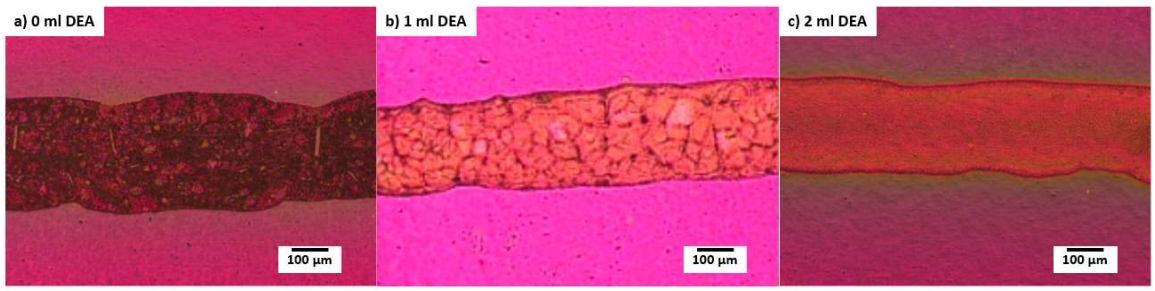

Fig. 4.15. Inkjet-printed MgO lines with different amount of DEA.

DEA is added to most sol gels as a surfactant and complexing agent. Addition of DEA results in a lower surface tension [170] and a higher viscosity. The lowered surface tension results in easier drop formation during jetting, but will also increase chance of satellite droplets. A similar result has been found in study of drop formation during inkjet printing [171]. Simulation of inkjet drops with different surface tension using continuous surface force model has been made to evaluate the drop formation and satellite drops [172]. Fig. 4.15 showed that MgO lines printed by the same MgO sol-gel with adding 0 to 2 ml DEA. It should be noted that the viscosity of the ink was raised from 2.8 to 3.0 cSt with the addition of DEA and the inkjet-printed lines show great improvement in their morphology, with smaller width and smooth surface. Lots of cracks and rough surface are found without DEA (Fig. 4.15a). The line surface is smoothened and less cracks are seen by adding 1ml of DEA to the ink (Fig. 4.15b). Smooth and straight line without any cracks are formed (Fig. 4.15b). DEA serves as a complexing agent in the precursor, which slows down the reaction and solidification of the ink to preventing crack formation during heat treatment. A similar technique is used in sol-gel dip-coating thin film fabrication [173]. However, because DEA fluid is supercooled at room temperature, an ink with too much DEA will solidify after long time (about 24 h) standing. The gel-like solidified ink can be restored by heating in 50 ˚C water bath, but the restored ink clogs the jetting nozzle more frequently. So 2 ml of DEA is used for MgO ink. For BTO or BZO inks, which have very high DEA concentration, the inks must be used right after mixing.

4.2 Drop stream and line formation

This section provides results in the effort to control drop stream and line formation during inkjet printing. It is very important for drop stream and line information to be stable and consistent for printing a straight and smooth long line.

In an ideal inkjet drop stream, only one drop is generated per signal, and the drops have constant size and spacing between each other. The flow velocity of drop stream is matched with the speed of tape movement. For a fine line information, there are many factors involving solution viscosity, orifice size, feeding pressure, jetting frequency, tape speed, treating temperature and delay time etc.

The microdispensers used in this work has two different nozzle orifice size (30 μm and 60 μm). The different nozzle sizes leads to different drop size and so, different the jetting parameters. Fig. 4.16 shows lines with the same MgO sol-gel ink using different dispensers. The drops eject from the 60 μm orifice is larger and the lines drawn by the 60μm nozzle shows a larger width of 210 μm compared to the 170 μm line from the 30 μm nozzle. The thickness of the line from 30 μm nozzle is less than 100 nm which makes it difficult to measure with our profilometer, while the lines from 60 μm nozzle shows a solid thickness of 400 nm. It is concluded that the orifice size has larger impact on the line thickness than the line width.

Nozzles with 30 μm orifice is capable of printing a narrower line, but the line thickness is too low to serve as the insulating barrier. Moreover, the smaller orifice in 30 μm nozzle brings extra difficulties in cleaning and tuning the jetting parameters. So, the 60 μm nozzle is more suitable for this work.

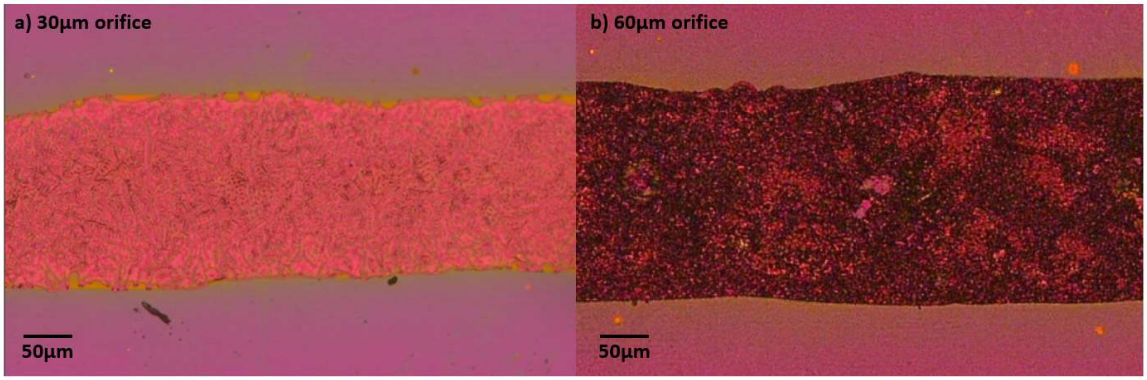

Fig. 4.16. Inkjet-printed MgO lines by different nozzle orifice sizes.

4.2.1 Inkjet drop stream

In an ideal condition, when the electric signal applied to the dispenser, the piezoelectric actuator squeezes the glass tube and a drop is forced out from the nozzle orifice. A liquid thread is stretched out by the main drop from the nadir of the ink at the orifice. The liquid thread breaks from the orifice and contracts as the primary drop during the flight. Fig. 4.32 is a series of photos provide by MicroFab demonstrating the droplet formation [174].

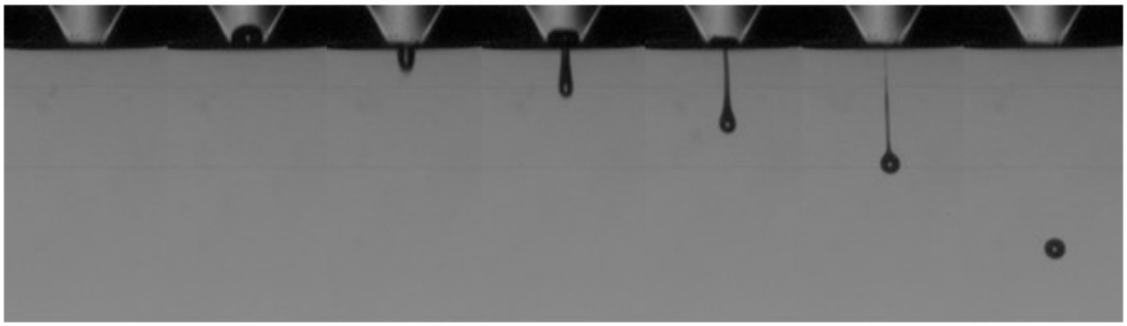

Fig. 4.17. The flight path of the inkjet drops captured by the camera on board.

4.2.1.1 Satellite drops and defects dots

If the condition is not ideal, liquid thread breaks into some small droplets behind primary drop, these droplets are referred as satellite droplets [171]. The satellite droplets are detrimental to the precision of size and location of the landed drop. They might sometimes fall on the buffer between two lines, which might result in defects in the subsequent process. Fig. 4.18a shows a

contaminated buffer surface between two printed lines, which is the result of satellite droplets stream deviating from the main printing course. Larger satellite droplets might crack during subsequent heat-treatment and create secondary defects around it (Fig. 4.18b).

Multifilamentary tapes are more vulnerable to defects compared with the non-striated regular tapes [175]. As we can see in Fig. 4.19 [175], the transport current can bypass most of the defects in a non-striated tape. In filamentized tapes, however, a single defect may completely shut down current flow in one filament. Multiple defects generated by the inkjet printing process might result in a complete shutdown of the superconducting current transmission. As a result, high-quality inkjet printing is required with strict control on the satellite droplets in this process.

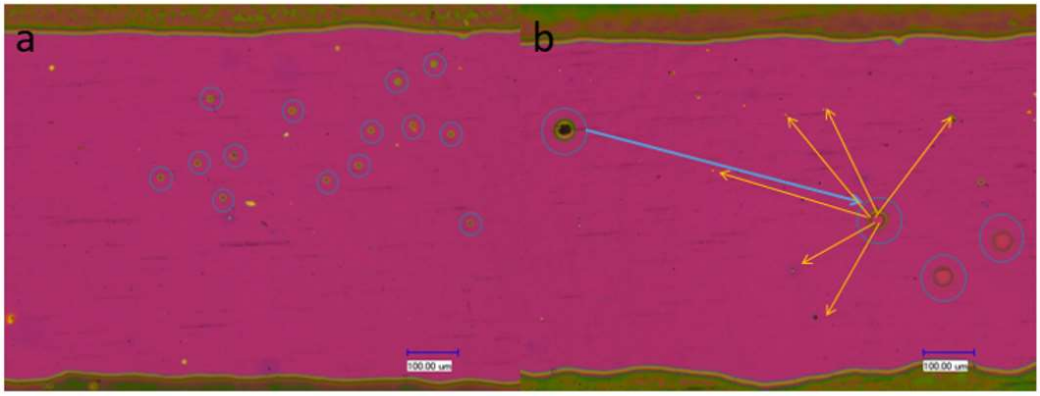

a) Buffer surface contaminated by satellite drop deviated from jetting course

b) Large defect drops crack during heat treatment and result in secondary defects

Fig. 4.18. Optical microscopy of satellite defect deposition.

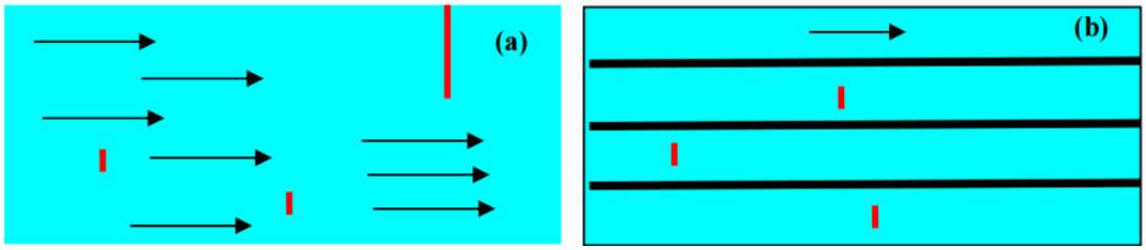

a) Schematic of current flow in a non-striated tape. Current can bypass defects.

b) Schematic of current flow a multifilamentary tape. Defects block the current flow.

Fig. 4.19. Schematic of current flow in non-striated tape and multifilament tape with similar defects.

The main source of satellite droplets formation is the unstable break down of liquid thread behind the primary drop. The liquid thread formation is based on the viscosity and surface tension of the ink [60]. Both viscosity and surface tension of a sol-gel are environmental sensitive and change with the aging of the sol-gel and so, the jetting parameters need to be adjusted for every different ink. The next section will discuss key factors in tuning jetting stream.

4.2.1.2 Feeding pressure and solution viscosity

A pneumatic controller is employed to continuously feed the precursor ink into dispenser. The feeding rate should keep pace with the jetting flow to stabilize the continuous jetting process. The solution feeding rate significantly affects the jetting pattern. Fig. 4.20 shows different jetting drop streams from an MgO ink with various feeding pressures.

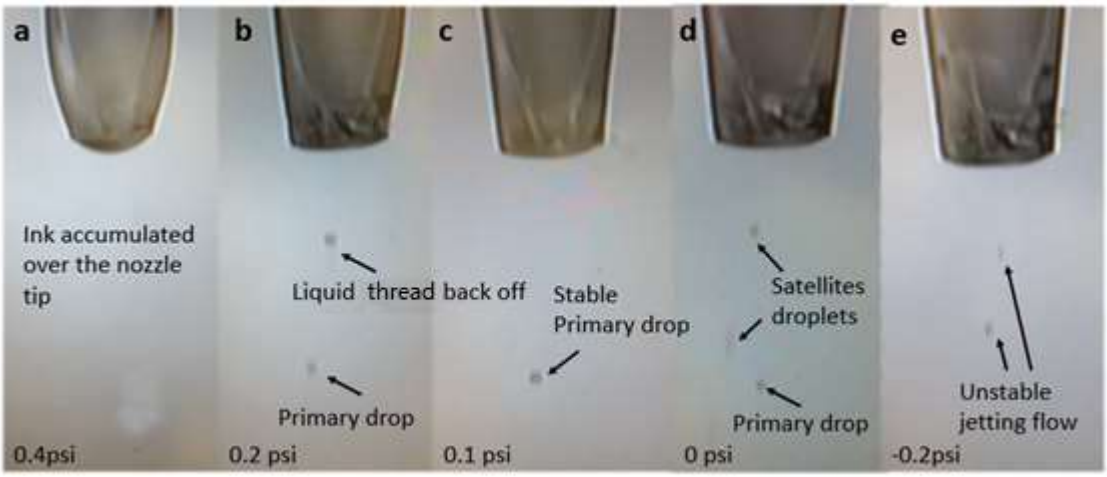

Fig. 4.20. Different jetting pattern of MgO ink under different feeding pressures.

The dispenser starts jetting at a -0.2 psi (-1379 Pa) feeding pressure (Fig. 4.20e). Due to insufficient ink supply, the jetting is not stable, and is stopped easily by disturbance from the environment, such as vibration from stage movement. As the pressure increases to 0 psi (0 Pa), the primary drops start to stabilize, but a large amount of satellite droplets are formed due the

premature breaking of the liquid thread behind (Fig. 4.20d). The satellites droplets start to merge together with the primary drop when the ink feeding becomes sufficient, and finally one single drop is formed and the jetting stream becomes stable at approximately 0.1 psi (689 Pa) (Fig. 4.20c). Small satellite droplets close to the primary drop will be attracted and merge into the primary drops during the flight. There is a window for optimum pressure for stable jetting. As the pressure continues to increase, satellite droplets start to appear again. This time, the long liquid thread is pinched off after the primary drop, and the liquid thread backs off, forming a large satellite behind the primary drop (Fig. 4.20b). Further increase in pressure will result in accumulation of ink over the dispenser head, blocking the droplet ejection (Fig. 4.20a).

Ink feeding into the nozzle orifice is primarily controlled by three factors: jetting frequency, feeding pressure and ink viscosity. Jetting frequency decides the flow rate of the ink, and feeding pressure controls the solution feeding. Inks that are more viscous require a higher feeding pressure for a stable jetting stream. The viscosity of the inks used in this work and their stable feeding pressures are listed in Table 4.4.

Table 4.4. Viscosity and jetting parameters of inkjet printing ceramic sol-gel.

Materials	Kinetic viscosity (cSt)	Fequency (Hz)	Stable feeding pressure (psi)	Optimal jetting signal strength (V)
MgO 0.8M	3.3	600	0.0	20~26
MgO 1.6M	8.7	600	0.1	25~32
SnO_2	4.3	600	0.1	20~26
Fe_2O_3	10.5	400	0.2	30~35
$BaZrO_3$	6.3	400	0.1	25~32
$BaTiO_3$	7.3	600	0.2	25~32

4.2.1.3 Signal waveform and droplet stream pattern.

As mentioned above, droplets are generated by a piezoelectric actuator that squeezes the glass tube, and acoustic wave pushes out a droplet from the nozzle orifice per signal. The shape of signal waveform is determined by the geometry of the glass tube in the dispenser [171]. The typical waveform suggested by the manufacturer is the trapezoid wave with T_{dwell}:T_{echo}=1:2 shown in Fig. 4.21. Signal voltage and wave period are two factors addressed in the following discussion.

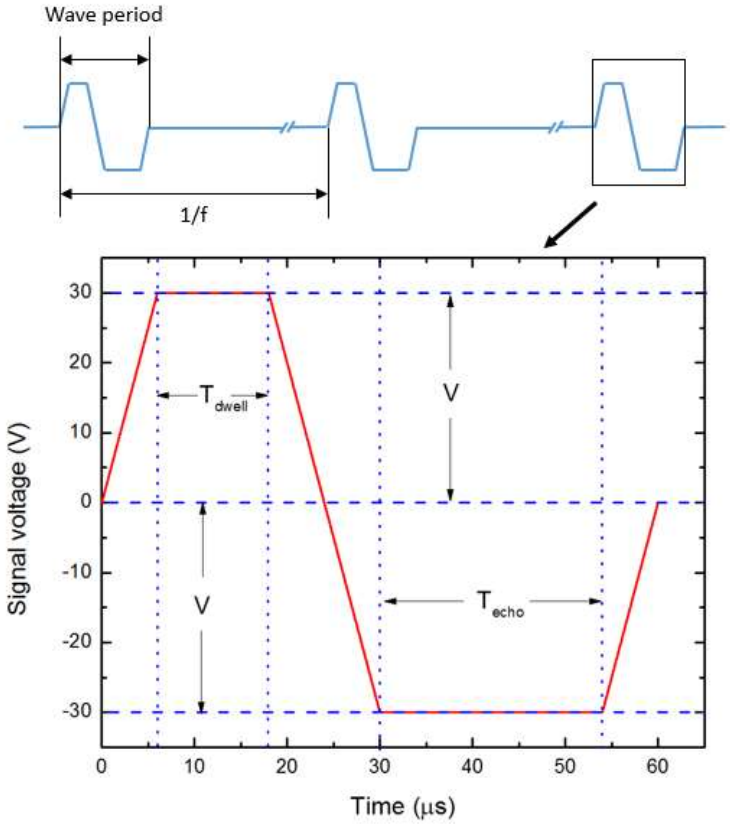

Fig. 4.21. Typical signal waveform for micro-dispenser suggested by MicroFab.

The signal voltage determines the force of the piezoelectric actuator applied to the glass tube, and the acoustic wave generated in the ink. Fig. 4.22 shows MgO sol-gel droplets ejecting from the nozzle under two different signal voltages. It is clear that the drops generated by ±32 V are larger than by ±28 V. Due to the increase of flow rate, stronger signal requires a higher

feeding pressure. In general, ink with higher viscosity requires a stronger signal and a higher feeding pressure to obtain a stable jetting stream.

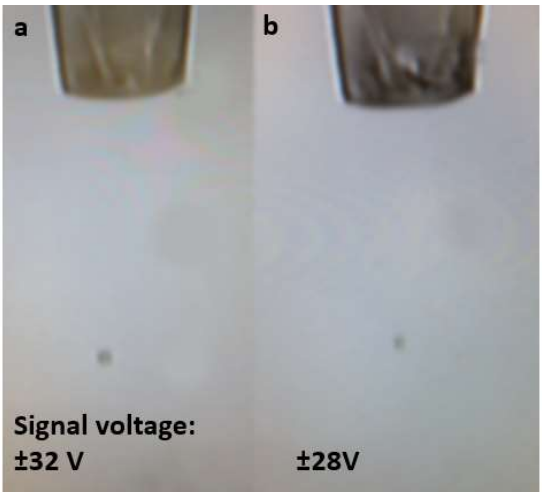

Fig. 4.22. Inkjet drops under different jetting signal voltages ±32 V and ±28 V.

The jetting wave period is dependent on the travel of the acoustic wave inside the glass tube. Inappropriate wave period might result in unfavorable interference inside the nozzle and result in heavy satellites or no jetting at all (Fig. 4.23). Therefore, the wave period is heavily dependent on the ink viscosity and signal strength. Generally, inks with higher viscosity require a higher signal voltage and a longer wave period.

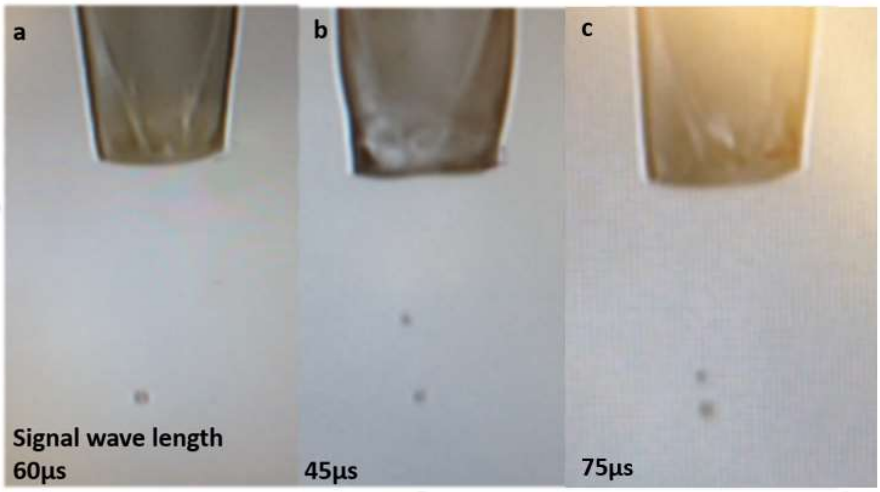

Fig. 4.23. Inkjet droplets under different jetting signal wave periods.

4.2.2 Printed line formation

4.2.2.1 Jetting frequency and drop spacing

In order to print a straight line, ink drops should be able to merge at landing with the liquid on the line that is not yet been dried. This requires two additional factors to investigate: droplet spacing and delay period.

The drop spacing is the distance between two landing points of neighboring drops, which is controlled by the tape speed of the reel-to-reel motion and jetting frequency of the dispenser. Fig. 4.24 shows MgO lines printed with different jetting frequency and tape speed.

If the drop spacing is too large, typically larger than twice a drop's radius, the drops directly land on the substrate and dry in isolation, forming patterns consisting of individual drops. An individual pattern is shown in Fig. 4.24a, where MgO ink printed with 200 Hz and 2 m/min tape speed and the droplets spacing is 167 μm and the droplets failed to merge with each other. As the droplets spacing decreases, the drops merge with each other. The lines start to build up in thickness and the edge of the printed lines is straightened. The line becomes perfectly straight at 600 Hz (Fig. 4.24b). The straight line patterns are narrower than individual drops patterns, which is explained by Soltman et al. [65] as the fluid expansion being partially arrested in the longitudinal direction when the drops merge. Further decrease in the droplets spacing results in irregular over-flooded line (Fig. 4.24c). Too much excess ink accumulates on the line, and the liquid bead's equilibrium is broken by vibrations from reel-to-reel tape movement. The overflow of the excess ink in random direction results in the irregular printed pattern.

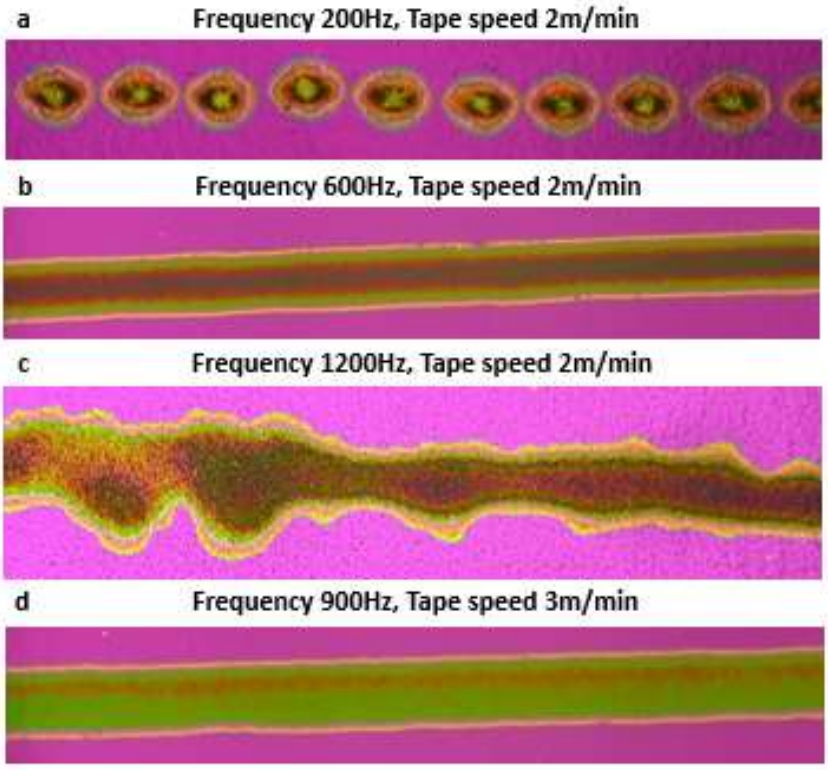

Fig. 4.24. MgO lines printed with different tape speed and jetting frequency.

In our case, the droplet spacing can be adjusted by two different factors, the reel-to-reel tape movement speed and the jetting frequency. To some extent, tape speed and jetting frequency are relative factors. For example, similar straight lines can be printed at 600 Hz with 2 m/min tape speed (Fig. 4.24b) and 900 Hz with 3 m/min tape speed (Fig. 4.24d).

However, in the reel-to-reel inkjet printing system, tape speed is limited by the reel-to-reel inline heat treatment after printing. Passing the sample quickly through the furnace might result in insufficient calcination and cracks in the printed lines. Jetting frequency is limited by the delay period, which will be discussed in next section.

4.2.2.2 Delay period, temperature and drying rate

As the drops land on the tape surface, they merge into a line and are dried by the heated substrate. Properly drying the ink is important to line formation. Two factors control the drying

process: the tape temperature, which control the ink evaporation, and the delay period, which is the time between the landing of the neighboring drops. Tape temperature is primarily controlled by the susceptor below, and the delay period is the reciprocal of the jetting frequency. The drying rate of the ink is controlled by the tape temperature but new drops are added in every delay period. The dry rate needs to match with the delay period for a good straight line.

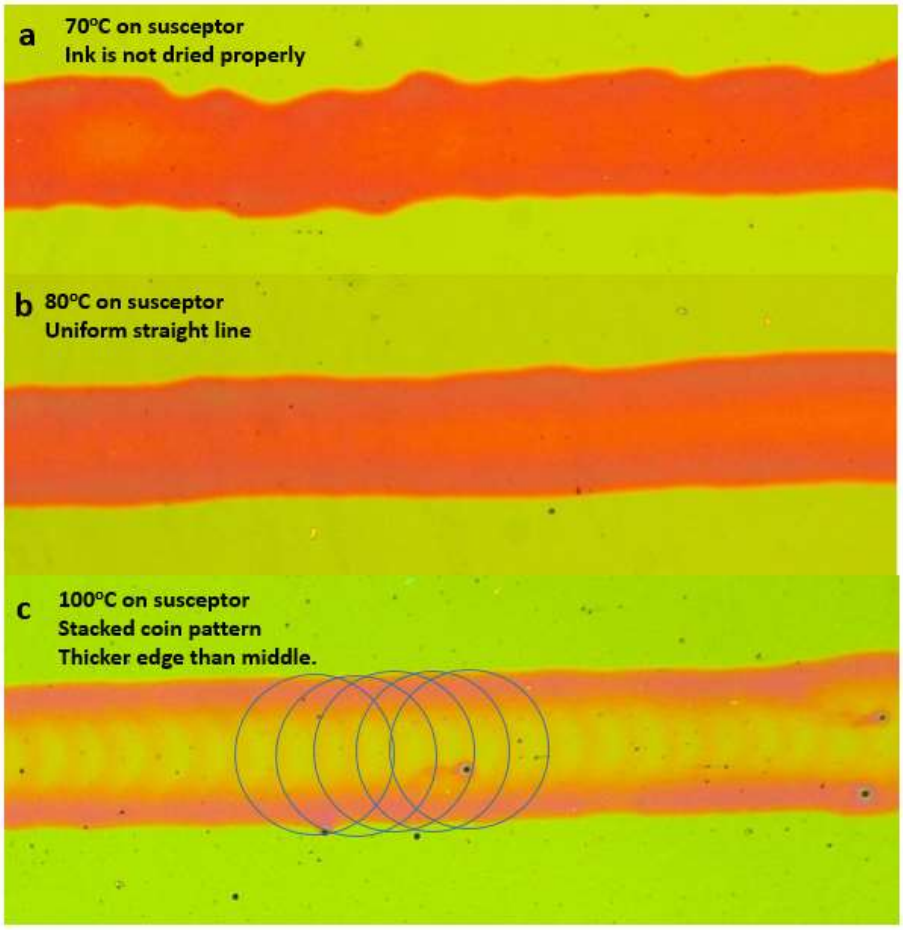

Fig. 4.25. BTO inkjet-printed lines dried with different susceptor temperatures.

Fig. 4.25 show the BTO lines inkjet printed with different temperatures at the same frequency of 400 Hz. As shown in Fig. 4.25b, a uniform straight line is printed at 80 ˚C susceptor temperature. If the temperature is too low, like the line printed at 70 ˚C, the edge of the printed line is not straight, which will result in unnecessary loss in the superconducting area.

The curved edges are formed when the drying rate of the ink is too slow that the ink overflows the adjacent area. If the temperature is too high, when the drying time of a drop is shorter than the delay period, the drops are dried individually regardless of the overlapping, which will result in the stacked coin pattern shown in Fig. 4.25c. In this case, the drop spacing will have no impact on the width of the line. The stacked coin pattern is not preferred because the width of the pattern is much larger than the width of normal lines.

Careful coordination of jetting frequency, tape speed, and susceptor temperature is needed to obtain a smooth, narrow line with a straight edge. From Fig. 4.24b & d, between the two samples printed at 600 Hz and 900 Hz, the difference in average width of the lines is 20 μm. As the result, when coated with REBCO, the 600 Hz sample will have 2% less superconductor area loss and hence 2% less I_c reduction. The reel-to-reel tape speed, susceptor temperature, and jetting frequency used for the five different inks in this work are listed in Table 4.5.

Table 4.5. Tape speed, susceptor temperature and jetting frequency of five different inks.

Ink	Tape speed (m/min)	Susceptor temperature(˚C)	Frequency (Hz)
MgO	1	80	600
Fe_2O_3	1	120	600
SnO_2	0.5	90	400
$BaZrO_3$	0.5	100	400
$BaTiO_3$	0.5	110	600

4.2.3 BTO line optimization

BTO has been chosen as the ink for printing insulating line as discussed in Section 4.1. The width of the inkjet-printed line is directly related to the area loss of the superconductors and hence the I_c reduction and so, it is important to reduce the width of the inkjet printing lines as much as possible. Because the temperature of the inline heating is only 200 °C for BTO heat treatment, slower tape speed is needed for longer baking time to completely dry out the gel

before it is rolled up into the spools. The tape speed is limited to 0.5 m/min and lower. The jetting frequency is limited by the tape speed and so, only 600 Hz is used in most of the work.

BTO precursor contains large amount of acetic acid and DEA and so, the boiling point of the precursor is higher than the methanol-based MgO or SnO_2 ink. Thus, drying BTO lines requires higher temperature; the straight line pattern shown in Fig. 4.25b appears between the susceptor temperature of 90-110 ˚C. Meanwhile, feeding pressure of 0.2 psi (1379 Pa) and jetting signal strength ±28~32 V are chosen based on the viscosity of the ink.

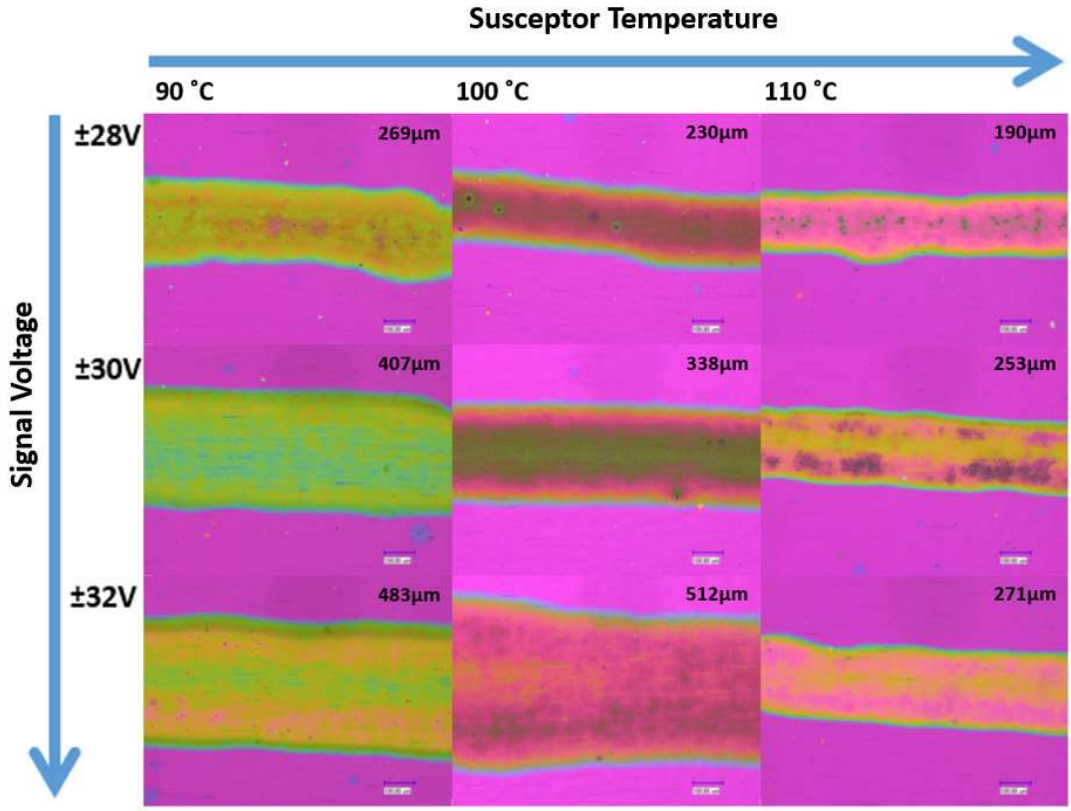

Fig. 4.26. Optical microscopy of inkjet-printed BTO lines with different signal strength and susceptor temperature.

Because the tape speed and jetting frequency are limited by the inline heat treatment, the two factors that have the wider window are focused on: susceptor temperature and signal

voltage. The jetting signal period is carefully tuned with a minor change in supply pressure to find the period length with better jetting stream stability.

Fig. 4.26 shows the BTO inkjet-printed lines with different signal strength and susceptor temperature, and the average width of the printed line is shown on the top-right corner of each image. As mentioned in Section 4.2.1.3, the higher voltage leads to larger droplets. A higher signal voltage results in wider lines as expected at all three temperatures. It is also noticed that the lines printed with 100 ˚C susceptor temperature show the larger width than at 90 ˚C, because the lower viscosity and surface tension from warmer ink make it easier to expand on the tape surface. But when the susceptor temperature increases to 110 ˚C, the ink quickly evaporates from the tape surface, and the liquid expansion is significantly suppressed so the width of the lines are narrowed down. However, when the susceptor temperature further is increased to 120 ˚C, overheating results in vapor bubbles trapped inside the lines (Fig. 4.27a), which results in round shape cracks after the heat treatment (Fig. 4.27b). As a result, ±28 V and 110°C on the susceptor have been chosen as the printing condition for the 12-filament samples.

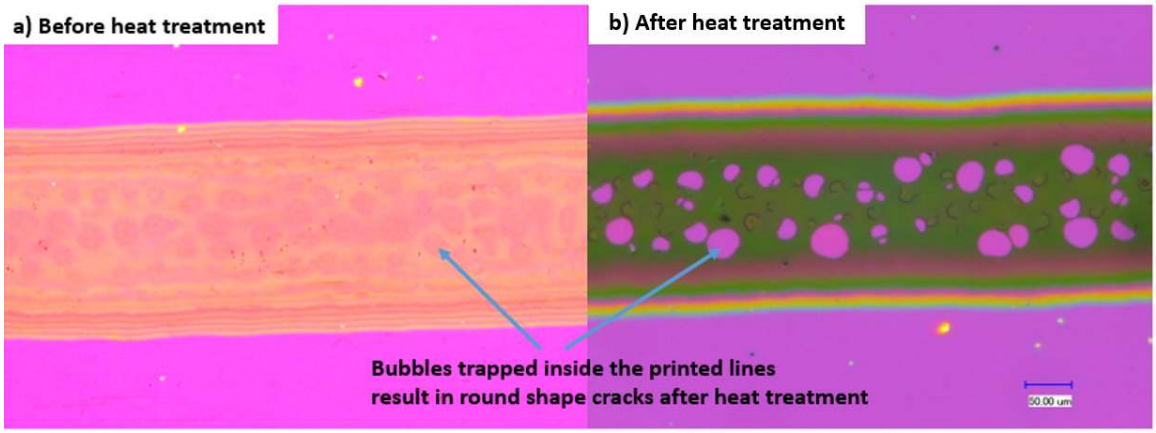

Fig. 4.27. Optical microscopy of printed BTO lines before & after heat treatment at 120 ˚C.

However, it should be noted that a different inkjet nozzle, different substrate tape, different aging of sol-gel ink, and even a difference in room temperature and humidity of the operation

can result in changes on jetting conditions. Therefore, minor adjustment is need before every deposition run.

4.2.4 Substrate buffer tape

Two different kinds of buffer substrate tapes are used for inkjet printing in this work, LMO buffer tape for MOCVD and CeO_2 buffer tape for MOD.

Fig. 4.28a and b show BTO inkjet-printed lines on LMO and CeO_2 buffer tape with identical jetting conditions. It can be noticed that the line printed on CeO_2 buffer tape has larger width (422 μm) comparing with the one on LMO buffer (213 μm). This is because the difference in wettability of the ink on the two buffer surfaces. BTO ink has better wettability on CeO_2 buffer tapes and so, the ink expands and covers larger surface area before it is dried. The expansion of the liquid can be limited by increasing the buffer temperature; quick evaporation of ink limits the ink expansion. As shown in Fig. 4.28c, inkjet-printed line on CeO_2 buffer with 130 ˚C susceptor temperature is only 136 μm wide.

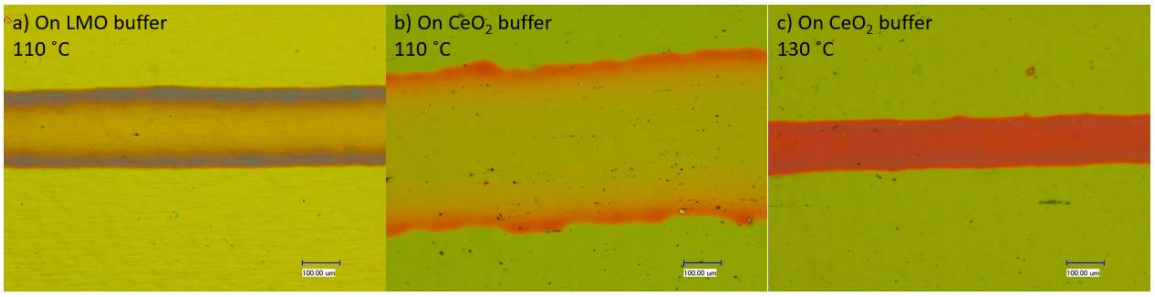

Fig. 4.28. BTO printed lines on LMO and CeO_2 buffer with different susceptor temperatures.

The wettability of the ink on the buffer tape is controlled by the surface tension between the ink, the buffer tape and the air, as shown in Young's equation on contact angle, as

$$\gamma_{SG} - \gamma_{SL} - \gamma_{LG} cos\theta_c = 0, \qquad 4\text{-}1$$

where, γ_{SG}, γ_{SL} and γ_{LG} are the interfacial surface tensions between solid-gas, solid-liquid and liquid-gas, and θ_c is the contact angle of the ink on the buffer surface. In the case of Fig. 4.28a and b, it is obvious that $90^\circ > \theta_c(LMO) > \theta_c(CeO_2) > 0^\circ$. As in the heterogeneous bubble formation inside the liquid lines, the total surface energy difference on a bubble formation ΔG_s is

$$\Delta G_s = 2\pi r^2((1 + cos\ _c)(\gamma_{SG} - \gamma_{SL}) + \gamma_{LG}\sin^2\theta_c), \quad 2$$

combining equations 4-1 and 4-2, we have

$$\Delta G_s = 2\pi r^2 \gamma_{LG}(1 + cos\theta_c). \quad 4\text{-}3$$

From the equation 4-3, it is obvious that the higher the θ_c, the lower the surface energy barrier and so, bubble formation on the CeO_2 buffer surface is more difficult. This also explains why there is no bubble formation like Fig. 4.27 in BTO lines on CeO_2 buffer at higher temperatures.

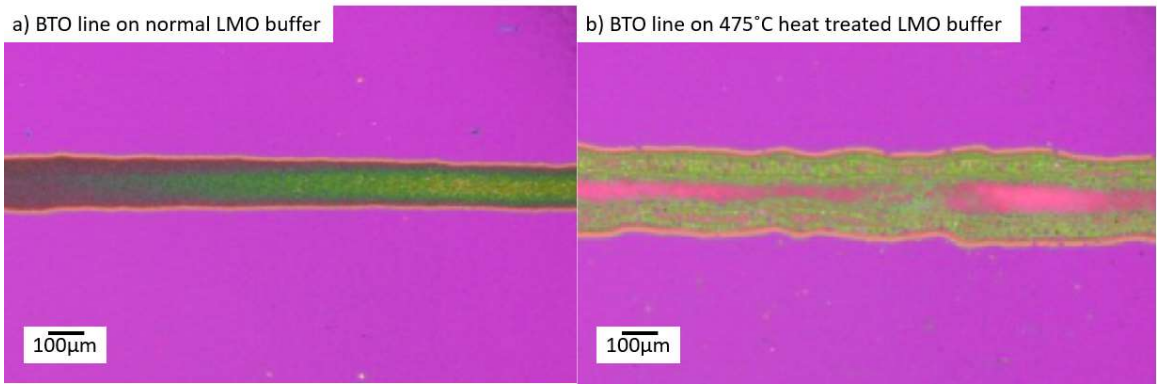

Fig. 4.29. BTO inkjet-printed line on LMO buffers with/without heat treatment.

The wettability on the tape surface can be modified by heat treatment. As shown in Fig. 4.29, BTO lines on LMO buffers heat treated at 475 ˚C in air showed 225 μm width, which is much wider than the line printed without heat treatment. A similar behavior has been found in TiO_2 and ZnO thin films [176, 177]; the heat treatment causes the release of the internal stress

of the sputtered thin film and smoothens the film surface and thus improves the wettability of the film.

4.3 Inkjet printing for multifilament tapes

In order to fabricate a 12-filament 2G-HTS tape, 11 parallel insulator lines with 1 mm equal interval are printed in longitudinal direction on the buffer tape with 12 mm width, each line being about 0.17 mm wide and 1.1 μm thick. The tape now has 12 slots with 0.84 mm width for REBCO to be deposited on (Fig. 4.30).

The 11 insulator lines can be simultaneously printed by 11 active nozzles. However, due to the various and complex parameters to control, it is difficult to keep multiple jetting streams stable at the same time. In order to minimize the risk of satellite droplets formation, only one active nozzle is used to print all 11 lines in this work.

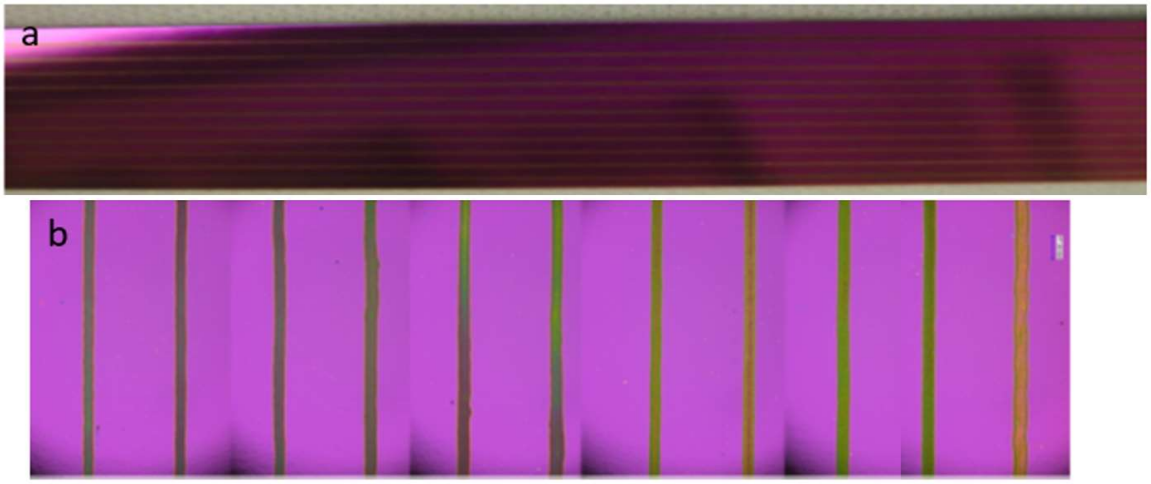

Fig. 4.30. 11 BTO lines printed on the LMO buffer tape.

Fig. 4.30 shows optical microscopic images of the 11 printed BTO lines. It can be noticed that the lines show different color after printing. The difference in color is caused by the thin-film interference of the transparent inkjet-printed lines. The thickness of each printed line is measured by profilometer and showed in Fig. 4.31. The thickness of the BTO lines varies from

980 to 1257 nm. The difference in thickness is caused by uneven heating from the susceptor. When the tape is not perfectly straight, the pressure between the tape and the susceptor is not balanced. One side of the tape is pressed harder against the heated susceptor, which leads to better heating and higher temperature. The buffer tape usually has a small curvature towards the Hastelloy side due to the interfacial stress from the multilayer sputtered buffer and so, the first and the last lines are usually thinner than the middle ones.

From Fig. 4.31, it is also noticed that the MgO lines show larger difference compared with BTO lines; the thickest line (768 nm) is double more than the thinnest one (354 nm). Comparing with BTO, MgO ink has lower viscosity (3.3 cSt) and the lines are printed at a lower susceptor temperature (80 ˚C). So, the better fluidity of the MgO lines before they dried on the tape surface might be the reason for the thickness difference.

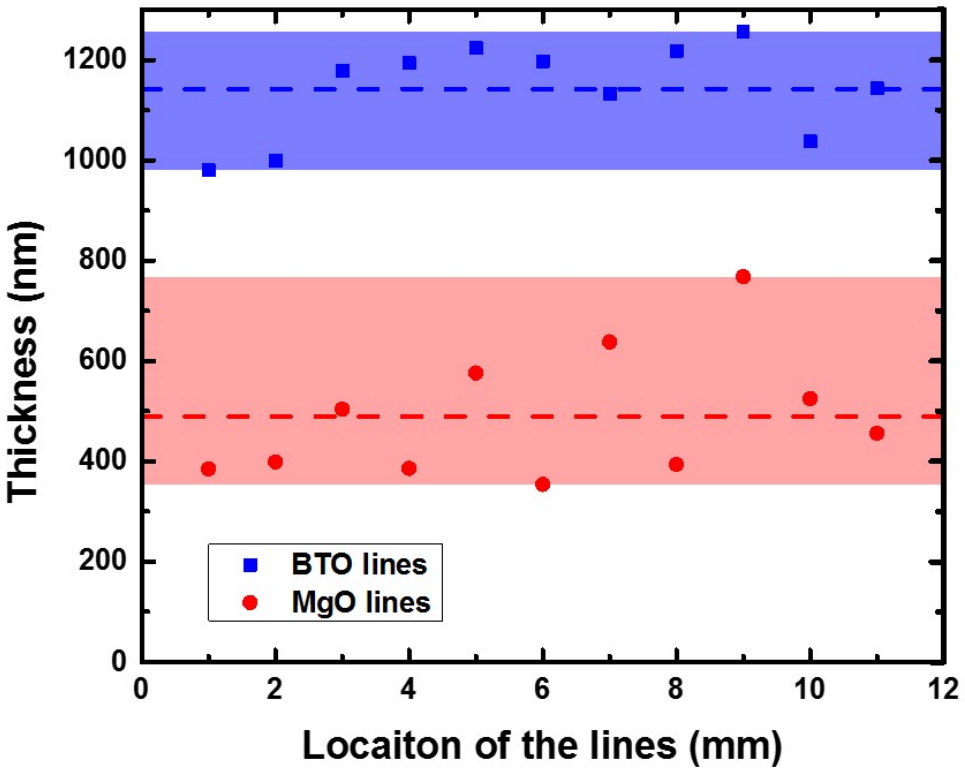

Fig. 4.31. Thickness of the 11 inkjet-printed line on buffer surface.

A 12-filament tape 1 m in length is prepared to demonstrate a feasibility for long tape with the reel-to-reel system. MOCVD REBCO and reel-to-reel Ag selective deposition are also conducted for the 12-filament sample (Fig. 4.32).

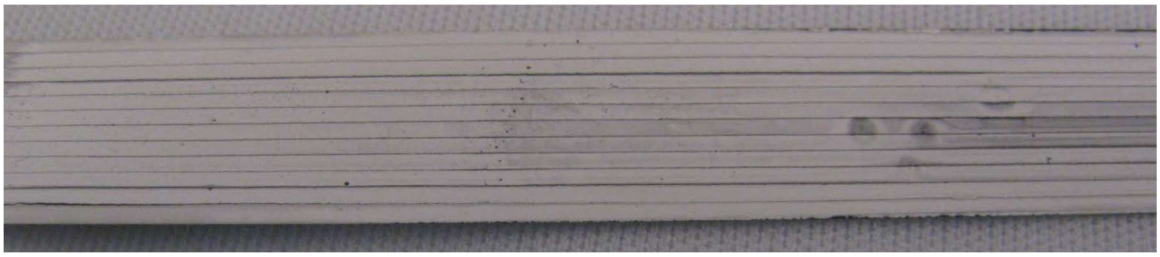

Fig. 4.32. 12-filament 2G-HTS tape with inkjet printing BTO, MOCVD YBCO and selective electrodeposited Ag overlayer.

4.4 Superconductor performance

4.4.1 Critical temperature and critical current

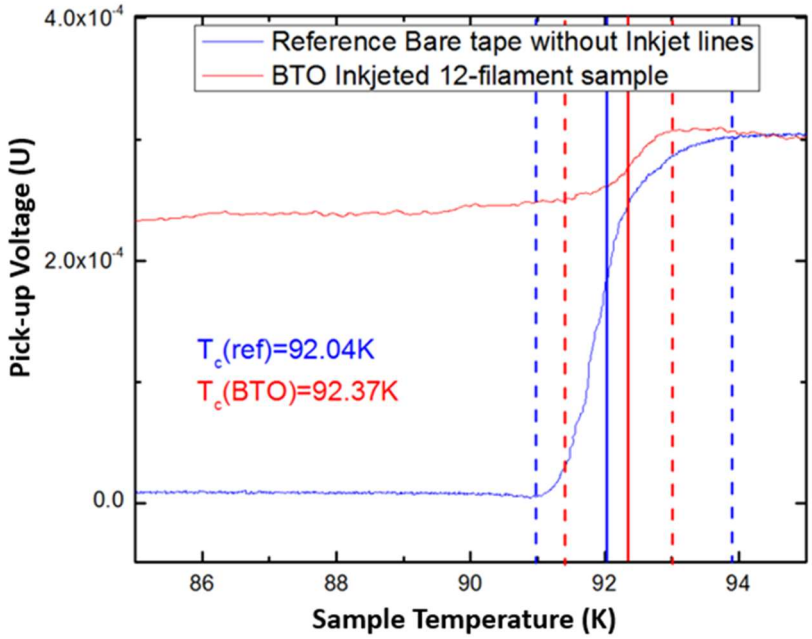

Fig. 4.33. T_c measurements from a 12-filament BTO inkjet-printed sample and a reference non-striated bare tape. The dash lines show the start and finish point of the T_c transition.

Fig. 4.33 shows T_c measurement result for a 12-filament BTO inkjet-printed sample. The measurement signal from the multifilamentary tape is significantly weakened; the induced

voltage from the pick-up coil at 77 K is 2.3×10^{-4} V for the multifilamentary sample compared to the regular 0.1×10^{-4} V in the non-striated regular sample. In normal state, both samples show the same induced voltage of 3×10^{-4} V. The lower induced voltage from the multifilamentary tape in T_c measurement is the result of the smaller shielding current loop inside the sample. The size of the shielding current loop is limited inside each filament. The coils in the measurement system have a diameter of 2.5 mm while the width of the filament in the 12-filament sample is only 0.84 mm. The amount of signal reduction depends on the alignment between the superconducting filaments and the coils. The T_c of the BTO inkjet-printed sample ($T_{c(BTO)}$=92.4 K) is comparable to that of the reference ($T_{c(ref)}$=92.0 K), which indicates no degradation of REBCO quality caused by the prefabricated inkjet-printed lines.

To evaluate the critical current reduction caused by inkjet-printing multifilamentary process, several samples are prepared with different numbers of inkjet-printed BTO lines and followed with MOCVD of REBCO. Critical current measurement results on these samples are shown in Fig. 4.34. The measured current and expected current values based on the reduction in superconducting area due to the presence of insulator lines are shown in Fig. 4.35. The results show that the critical current reduces with the number of printed lines but at a slightly sharper rate than that expected. The expected I_c considers only the superconducting area, calculated as

$$I_{c,theo}(n) = \frac{W-\sum w_n}{W} I_{c0}, \qquad 4\text{-}4$$

where $I_{c,theo}$ is the expected I_c, n is the number of filaments, W is the width of the whole tape which in this case is 12mm, w_n is the average width of each printed line, I_{c0} is the I_c of the reference sample without inkjet-printed lines. The 12-filament sample shows 25% reduction in I_c, and the major source of I_c reduction is the 17.5% area occupied by the inkjet-printed lines.

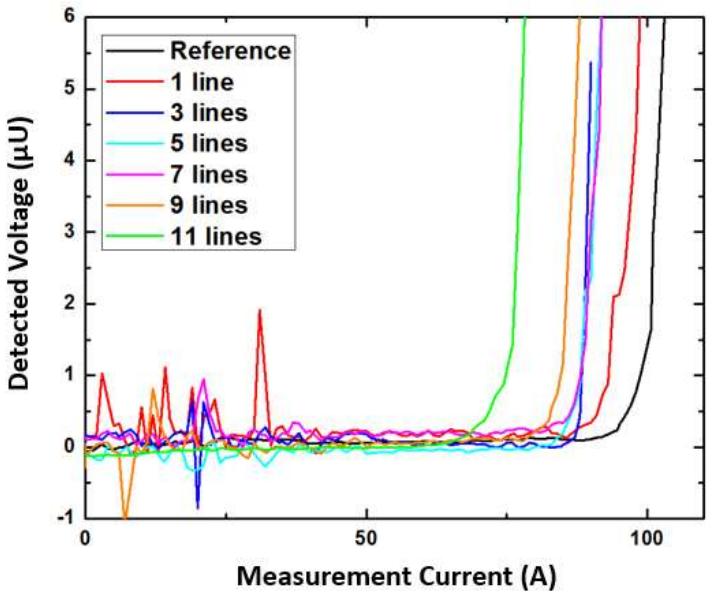

Fig. 4.34. Critical current on non-striated REBCO tape and multifilament tapes with different number of printed BTO lines at 77 K in zero-applied field.

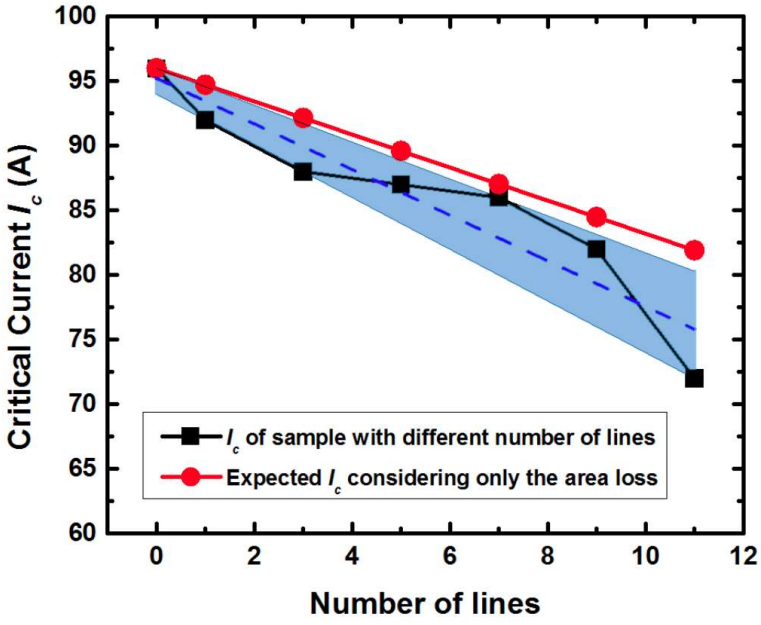

Fig. 4.35. Critical current of samples with different number of inkjet-printed insulator lines. Expected critical current values are also shown.

The extra reduction in critical current might be several reasons, including spray of satellite droplets on adjacent areas. Additionally, the multifilament structure aggravates the impact of

intrinsic non-uniformity in the REBCO layer. Because the area loss is the major reason for I_c reduction, future work should be focused on reducing the width of the printed lines.

4.4.2 Magnetization AC loss

Fig. 4.36 exhibits the results from magnetization AC loss measurement on a multifilament tape. The measured AC loss of the sample increases with the external field. The measured AC loss value in the multifilament tape agrees well with that predicted using the Brandt-Indenbom model[7]. The detail of Brandt-Indenbom model has been discussed in section 2.1.3. According to the model, the 12-filament tape with 0.84 mm-wide filaments will have 17.6 times lower AC loss than the non-striated 12 mm tape with the same J_c.

AC losses per cycle measured at 100 Hz, 200 Hz and 300 Hz showed almost identical value. As coupling loss per cycle is dependent on frequency[4] and so, the coupling loss in this inkjet-printed sample is negligible. The resistive inkjet-printed $BaTiO_3$ lines are effective in blocking electrical coupling current between the superconductor filaments.

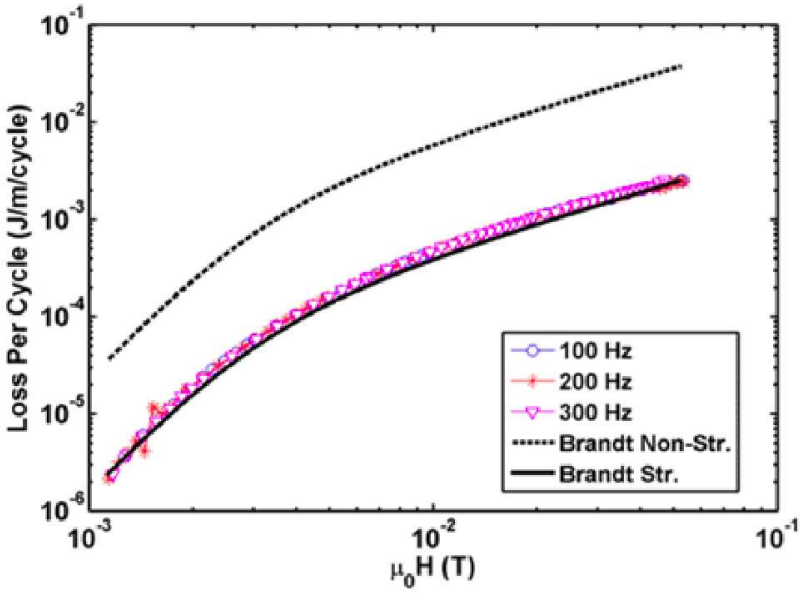

Fig. 4.36. Magnetization AC loss of a multifilament tape at different frequencies, compared with Brandt-Indenbom model for striated and non-striated configurations.

Chapter 5. Metal Organic Deposition of YBCO Superconductor

MOCVD is a top-down deposition process, which may present a challenge with buffers with prefabricated patterns. For example, the top-down deposition vapor will likely cover the entire tape surface with limited selection in our inkjet-printing/MOCVD multifilamentary process. Even though the epitaxial growth of REBCO deposition is interrupted by inkjet-printed lines, any low resistive REBCO deposited on the lines create difficulties for selective Ag electrodeposition

In this chapter, TFA-MOD of YBCO is introduced as the substitute for MOCVD. The liquid-phase bottom-up deposition procedure of TFA-MOD could yield more selectivity from the prefabricated surface feature by inkjet printing. With TFA-MOD process an all-solution fabrication approach of multifilament 2G-HTS tape is demonstrated.

5.1 Precursor preparation

Precursor preparation is crucial to MOD YBCO. In this section, we focus on optimizing the precursor to improve the performances of MOD YBCO.

5.1.1 Elemental stoichiometric

Y, Ba, and Cu acetates are initially mixed in the stoichiometric ratio of 1:2:3 for YBCO. However, not all metallic elements transform to YBCO phase due to second phase formation and materials sublimation. In this section, different elemental compositions and their influence to YBCO deposition is studied. The content of Y in precursor is retained, Ba and Cu content are changed according to different Y: Ba: Cu ratio.

5.1.1.1 Barium concentration

Ba-rich second phase is usually found in XRD $\theta/2\theta$ scan of the sample; the most commonly-found second phase is the Ba-O-F phase at 2θ=28.8˚ [91, 178]. The Y: Ba: Cu ratio

was reduced from 1:2:3 gradually to 1:1.3:3 and the change in YBCO deposition and its superconducting properties was studied.

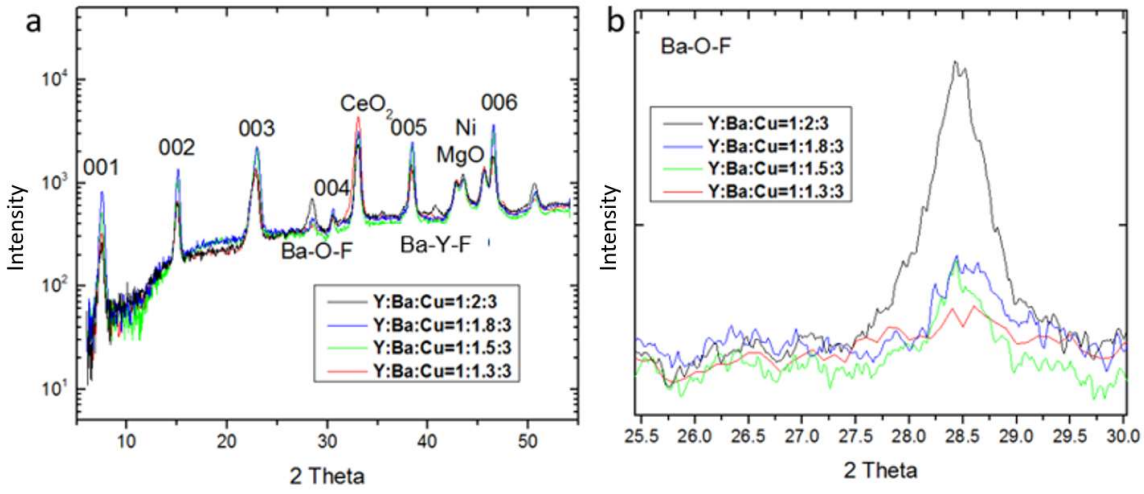

Fig. 5.1. XRD *θ/2θ* scan of TFA-MOD YBCO with different Ba concentration.

The XRD *θ/2θ* scan result is shown in Fig. 5.1. Two different peaks implying excess Ba can be spotted in the 1:2:3 ratio sample: a Ba-O-F peak at 28.8˚ and a Ba-Y-F phase at 41˚ [179]. It is evident that the intensity of both peaks decreases when the Ba ratio is lowered. The Ba-Y-F phase disappears in Y: Ba: Cu =1:1.8:3 and the Ba-O-F peak is significantly reduced. Meanwhile, no other second phases are found with decreasing Ba.

T_c measurement is conducted on the samples with different amounts of barium to study their superconducting properties (Fig. 5.2). All samples showed a relatively broadened T_c transition curve, especially the 1:2:3 sample. The very broad transition over 82-89 K is found, indicating that the J_c of the YBCO film at the specific temperature is too low to shield the applied field. The low J_c is the result of large amount of Ba-rich second phases. With decrease of the Ba content, T_c transition of the YBCO narrowed down to 84-89 K, but the offset of the transition remains unchanged. The sample with the 1:1.8:3 ratio has the best T_c (87.9 K) compared to the other three concentrations.

Further decreasing the Ba content result in lowering the offset of the transition, with the Y:Ba:Cu ratio reduced to 1:1.5:3 and 1:1.3:3, the transition offset has significantly reduced to 87 K and 83 K. The lowered transition offsets indicate that the lack of Ba has affected YBCO formation.

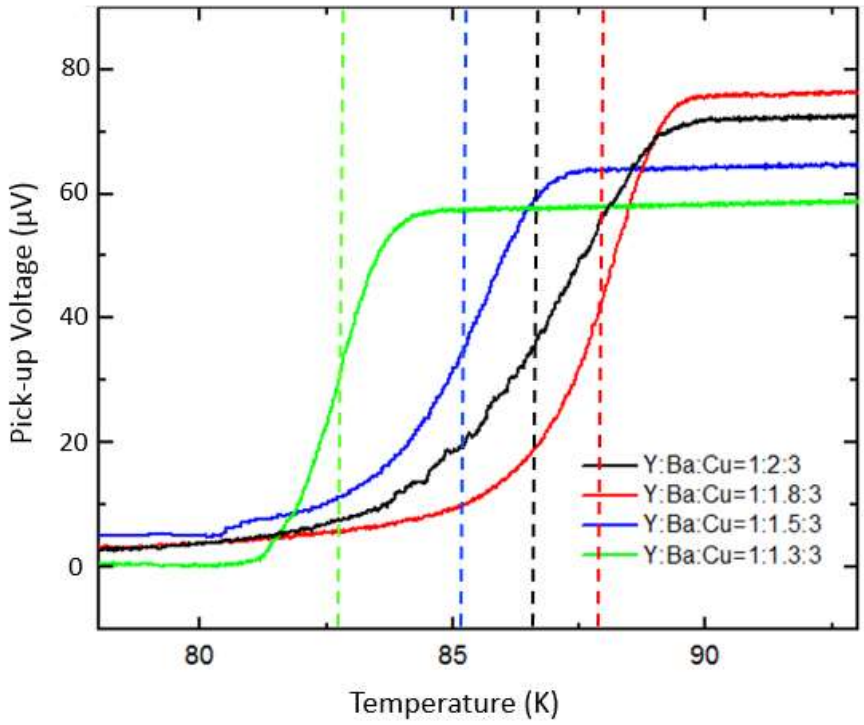

Fig. 5.2. T_c measurement of MOD samples with different Ba concentration.

5.1.1.2 Copper concentration

ICP-MS analysis of the MOD films reveals that Cu concentration is actually 4-9% less than that in the initial precursor (Table 5.1). This is caused by Cu sublimation during the calcination process [91]. The Cu content of the precursor is increased to balance out the sublimation effect and its impact on the performance is studied.

T_c measurements of samples with Y: Ba: Cu ratio of 1:1.8:3 and 1:1.8:3.3 show that with increasing Cu concentration, the T_c increases about 0.7 K (Fig. 5.3). This finding shows that

increasing the amount of Cu in the precursor can counter sublimation during the calcination process.

Table 5.1. Metallic concentration in the precursors and in the deposited films.

Metallic element stoichiometry in the precursor			Metallic element stoichiometry in the deposited film		
Y	Ba	Cu	Y	Ba	Cu
1.00	2.00	3.00	1.00	2.03	2.88
1.00	1.80	3.00	1.00	1.85	2.73
1.00	1.80	3.10	1.00	1.86	2.92
1.00	1.80	3.30	1.00	1.82	3.03

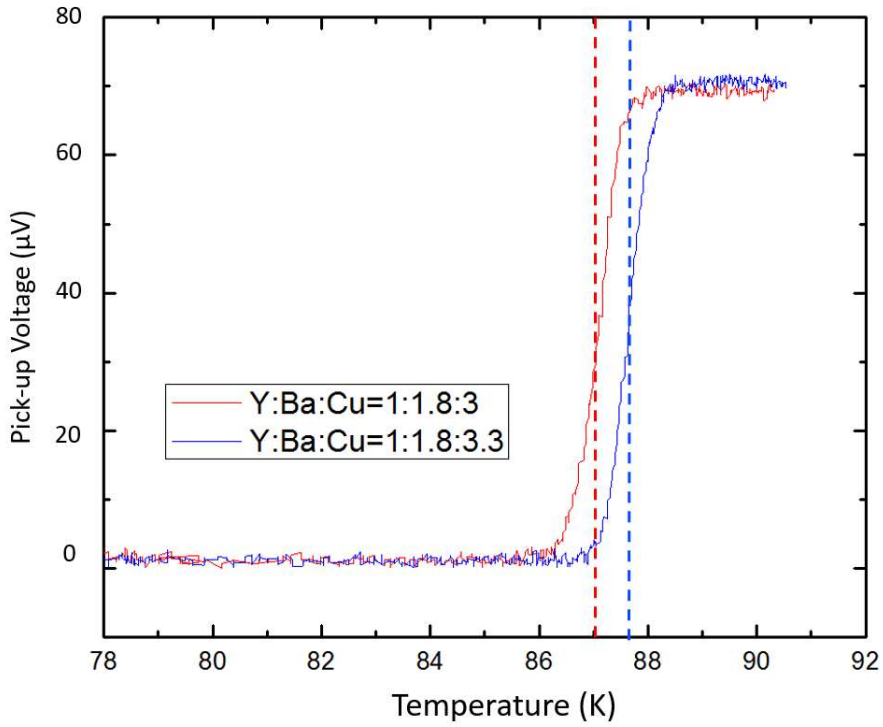

Fig. 5.3. T_c measurement of TFA-MOD YBCO with different Cu concentration.

5.1.2 Precursor concentration

Precursor concentration can be adjusted by dissolution. Diluting the precursor with different amounts of methanol before coating can result in precursors of different concentrations. Precursors prepared with different concentrations are listed in Table 5.2, and photographs of the three samples made with these precursors are shown in Fig. 5.4.

Table 5.2. TFA-MOD Precursor concentration relation to viscosity and thickness.

Total volume (ml)	Metallic ion concentration (M)	Viscosity (cSt)	Spin coating thickness (nm)	Dip coating thickness (nm)
30ml	1.0	1.55	245	278
20ml	1.5	3.89	478	671
10ml	3.0	13.44	1137	N/A

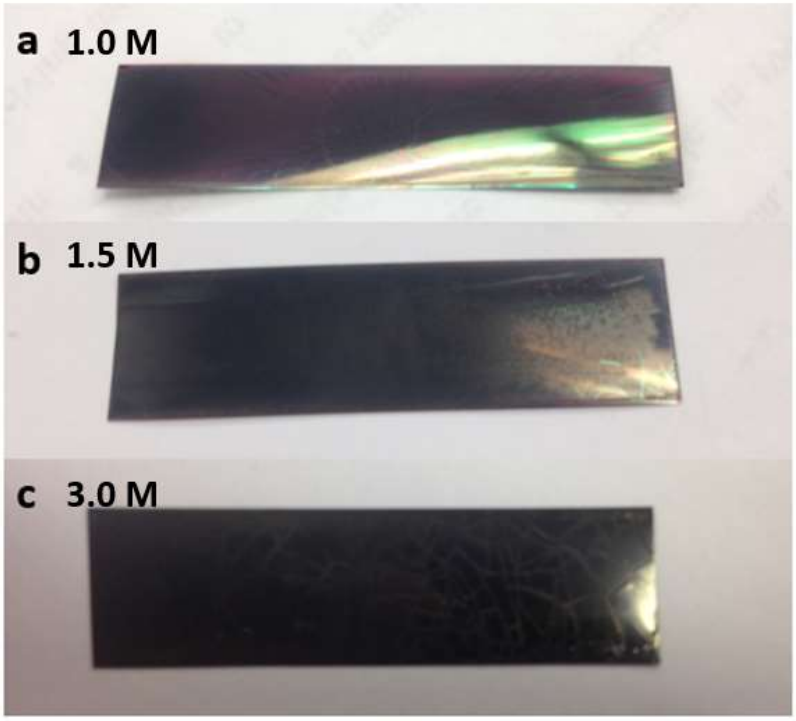

Fig. 5.4. Photos of MOD YBCO samples prepared by spin coating with different precursor concentrations.

Higher concentration results in higher viscosity, and then leads to thicker deposition. The thickness of MOD deposition layer reaches 1.10 μm with precursor metallic concentration of 3.0 M; such thickness is comparable with that of MOCVD samples.

However, the thicker MOD YBCO films crack after heat treatments (Fig. 5.4c). Cracks are found in both 1.5 M and 3.0 M samples. Small cracks are seen on one corner of the 1.5 M sample, which are very likely caused by handling the solution film and might be prevented. Larger cracks are found all over the 3.0 M sample. SEM of the cracks (Fig. 5.5) shows that they

are formed before the film is solidified. The cracks are the result of the intense volume reduction in the calcination process; the total volume of the film decreases drastically as the film loses its organic component during the process and the material flow cannot keep up with shrinking and the film is split into pieces by the internal tension [102].

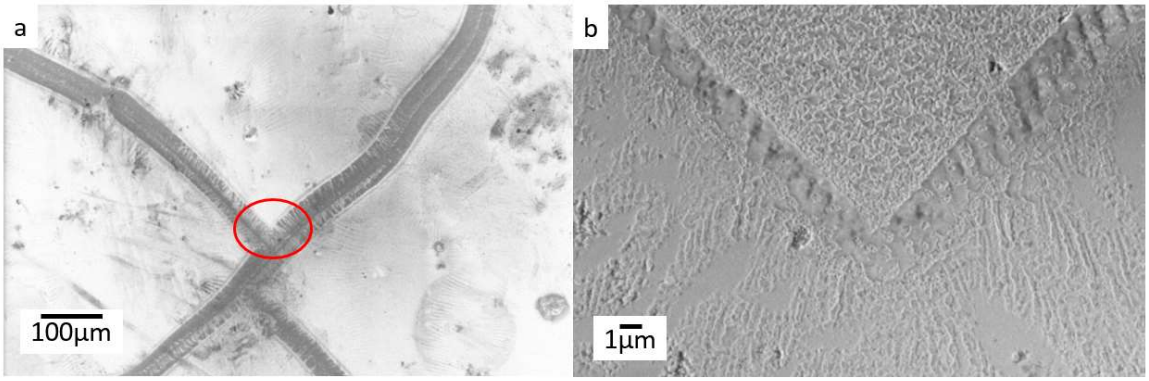

a) SEM microscopy on top of a crack. b) High magnification image of the circled area.

Fig. 5.5. SEM image of cracks on TFA-MOD YBCO with 3M metal-ion concentration.

GADDS 2θ-χ scans of samples with different concentrations are shown in Fig. 5.6. Both 1.0 M and 1.5 M samples show well-textured YBCO structure, but the 3.0 M sample shows no sign of YBCO formation. The 1.1 μm film thickness is too thick to pyrolyze the organic component completely during calcinaition process, so it fails in YBCO crystal formation afterwards.

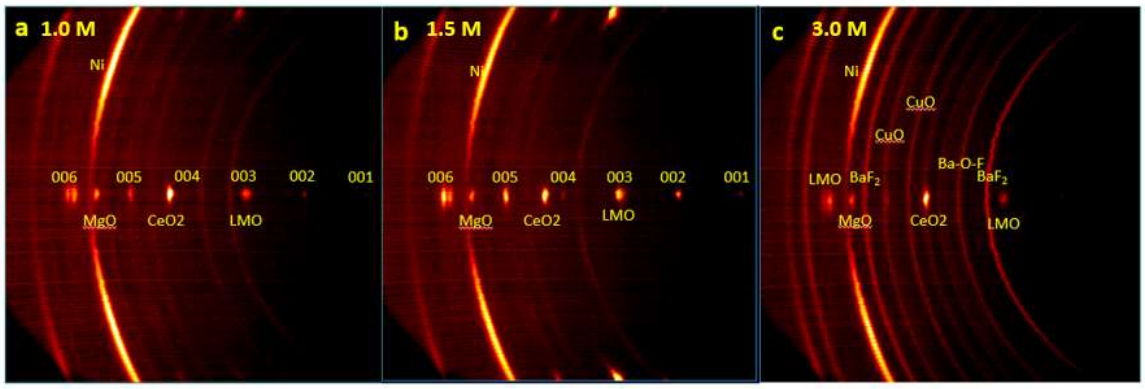

Fig. 5.6. GADDS 2θ-χ of MOD YBCO samples with different metallic ion concentrations.

For dip-coated samples, the viscosity of ink has similar effect on the film thickness (Table 5.2). The higher the viscosity, the higher the thickness. The 1.0 M precursor results in 278 nm thick YBCO films and the 1.5 M precursor results in 671 nm film thickness in the middle of the sample. Fig. 5.7 shows two short CeO_2 buffer tapes dip coated with two different precursor concentrations. In the 1.0 M sample (Fig. 5.7a), a higher thickness is found at the edge of sample, which is caused by the 'edge effect'. The surface tension on the edge of sample holds the fluid from draining and so, more precursor is remained after coating [180, 181]. The middle part of the tape is coated with uniform YBCO, but at the bottom edges of the short sample, a wedge-shape coating with higher thickness is found, which is because of stoppage of the draining of the precursor when the sample is completely withdrawn from the solution. This can be fixed by continuous tape movement in a reel-to-reel process. In the 1.5 M sample (Fig. 5.7b), cracks are found on the tape surface, especially in the higher thickness area in the bottom part. Due to the higher thickness, the brittle YBCO coating at the edges of sample is cracked and falls apart during handling, leaving the edges uncoated. So 1.0 M precursor is chosen for dip coating.

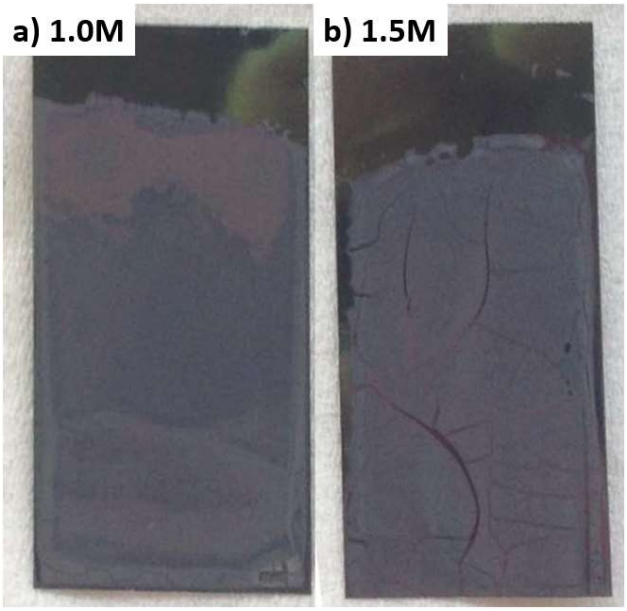

Fig. 5.7. Photos of MOD YBCO samples dip coated with different precursor concentrations.

5.2 Coating techniques

5.2.1 Buffer selection.

High-temperature water vapor and HF gas are involved during calcination and crystallization, which might potentially cause chemical reactions with buffer layers and destroy the YBCO film superconductivity.

Two types of buffer tape are used as the substrate for this work: one is the regular $LaMnO_3$ (LMO) buffer tape with an architecture of LMO/MgO/Y_2O_3/Al_2O_3/Hastelloy C276 that is used in our state-of-art MOCVD process, the other is the CeO_2 buffer tape that used in most TFA-MOD research [88, 89, 96, 182]. Textured CeO_2 tapes in this work are obtained by epitaxial sputter deposition of CeO_2 on textured LMO tapes, with an architecture of CeO_2/LMO/MgO/Y_2O_3 /Al_2O_3/Hastelloy C276.

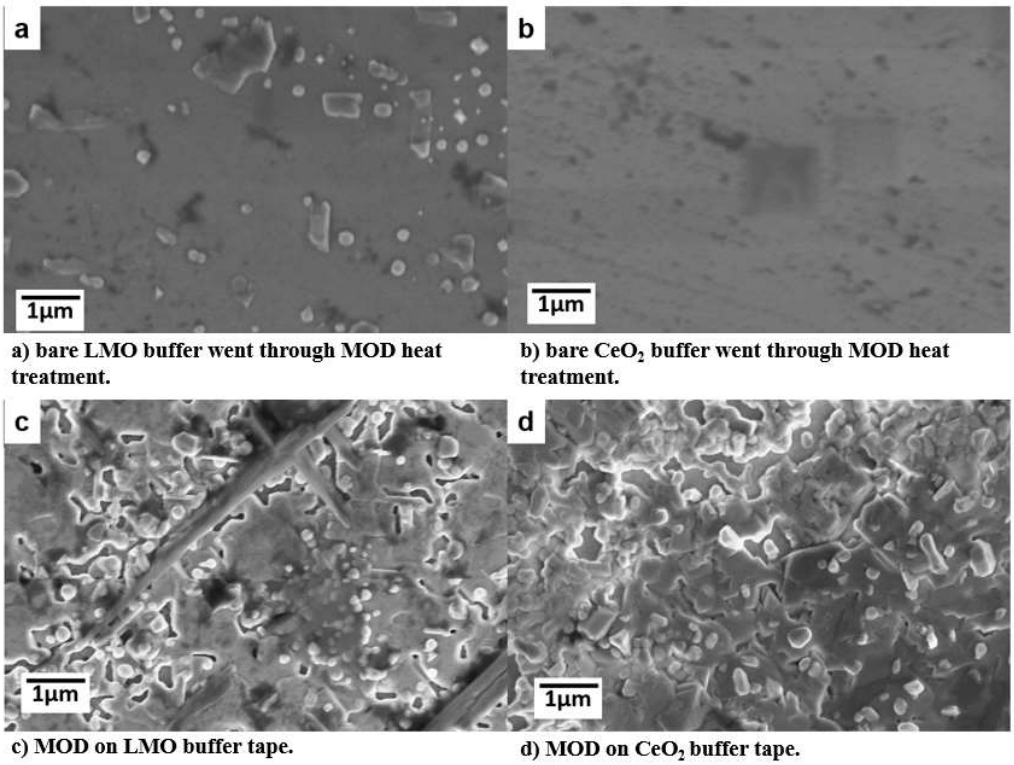

a) bare LMO buffer went through MOD heat treatment.

b) bare CeO_2 buffer went through MOD heat treatment.

c) MOD on LMO buffer tape.

d) MOD on CeO_2 buffer tape.

Fig. 5.8. SEM images of MOD YBCO on LMO and CeO_2 buffers compared with bare buffer subjected the same TFA-MOD heat treatment, without precursor deposition.

TFA-MOD YBCO is conducted upon the two buffer tape surfaces. To inspect the chemical stability of different buffers, both bare LMO and CeO_2 buffer tapes are subjected through the same calcination and crystallization as in a YBCO TFA-MOD process. SEM images show some protrusion on the surface of LMO buffer tape (Fig. 5.8a) but a flat surface on CeO_2 buffer after heat treatment (Fig.5.8b). However, GADDS 2θ-χ scan results show no significant sign of new phase formation for both bare buffers (Fig. 5.9a, b).

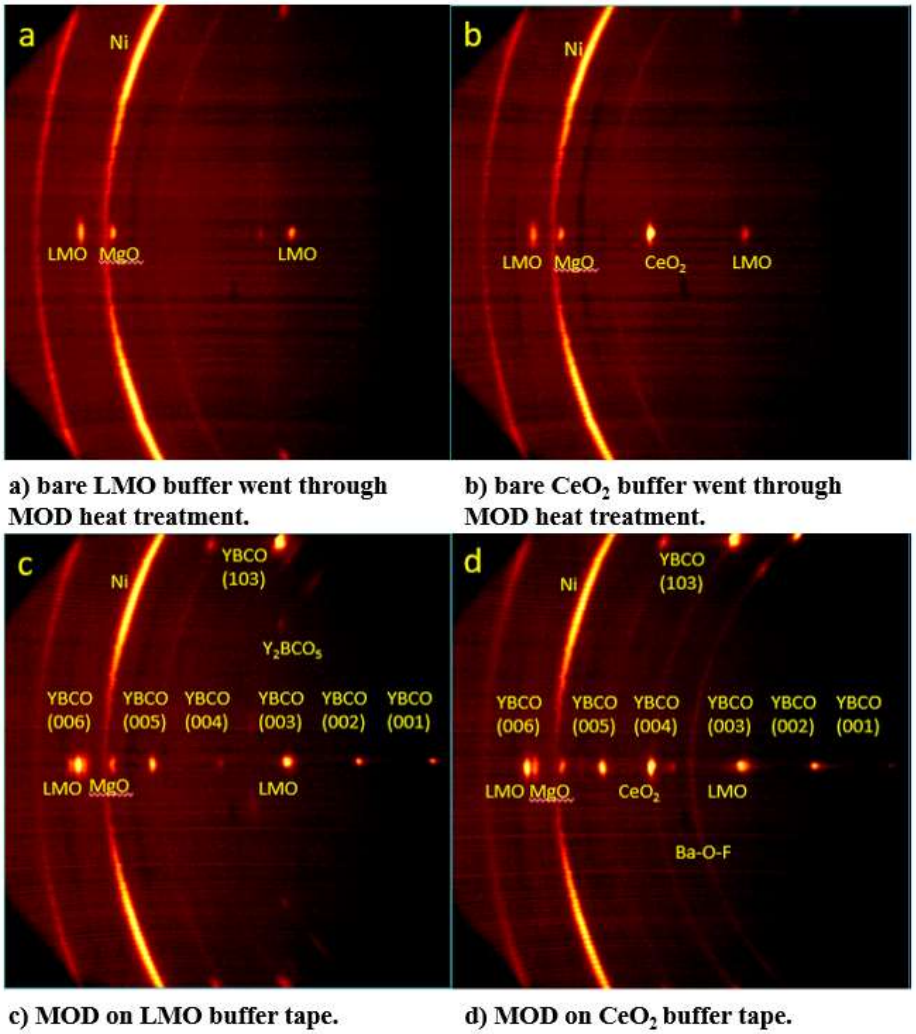

a) bare LMO buffer went through MOD heat treatment.

b) bare CeO_2 buffer went through MOD heat treatment.

c) MOD on LMO buffer tape.

d) MOD on CeO_2 buffer tape.

Fig. 5.9. GADDS 2θ-χ scan of TFA-MOD YBCO on LMO and CeO_2 buffers in comparison with their bare buffers.

SEM analysis shows a well-textured YBCO phase on both buffers (Fig. 5.8c, d), but some long platelet-shaped second phases are found in the film on LMO buffer (Fig. 5.8c). GADDS 2θ-χ scan indicates the existence of Y_2BaCuO_5 (YBCO-211) phase in the film on LMO buffer (Fig. 5.9c), which might be the second phase seen in Fig. 5.8c; a similar result has been found in literature [183, 184]. The formation of YBCO-211 phase might be a byproduct of LMO buffer tape losing its integrity. However, Fig. 5.9d shows a Ba-O-F ring in MOD YBCO on CeO_2 buffer that indicates the crystallization of YBCO is not fully completed.

XRD $\theta/2\theta$ scans are obtained by integrating the intensity of GADDS results along the χ direction (Fig. 5.10). From the XRD $\theta/2\theta$ result, MOD YBCO on LMO buffer tape shows higher intensity than the scan from CeO_2. Considering the higher YBCO diffraction intensity in the LMO buffer sample and the Ba-O-F peak at 2θ =28.5˚ in the CeO_2 buffer sample, it is concluded that the YBCO growth rate on the LMO buffer is faster than on the CeO_2 buffer.

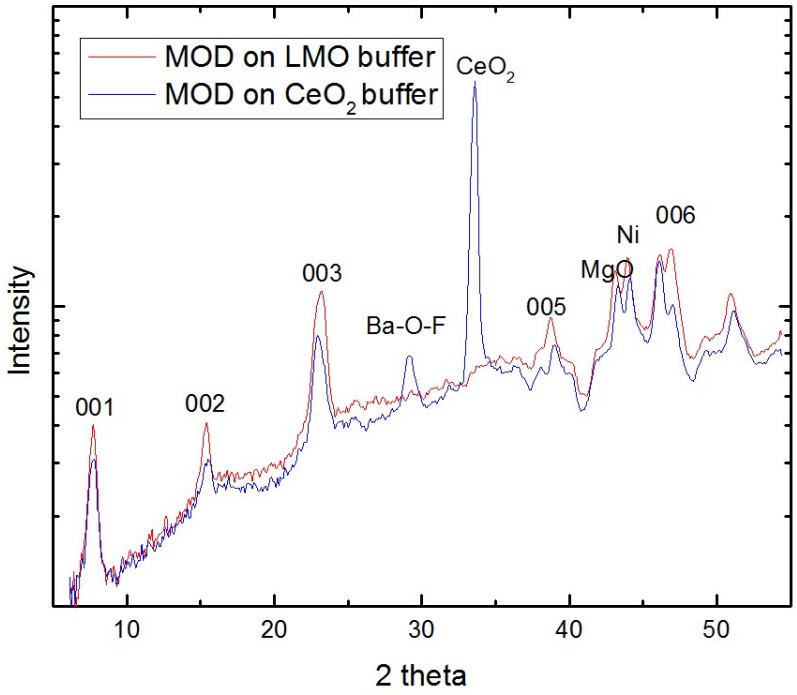

Fig. 5.10. XRD $\theta/2\theta$ scan of TFA-MOD on LMO and CeO_2, obtained by integrating χ angle over GADDS data.

Fig. 5.11 shows the T_c measurement results of YBCO grown on the two different buffers. The YBCO on CeO_2 buffer shows a T_c of 88.5 K, while the YBCO on the LMO buffer shows a lower T_c of 84.7 K with a broadened transition from 78 to 86 K. The T_c measurement result shows that even though YBCO growth rate on LMO buffer is faster than that on CeO_2 buffer, the performance of YBCO deposited on CeO_2 is better. The YBCO-211 second phase observed in SEM might be responsible for the low T_c [185]. The broadened transition in the inductive T_c measurement happens when the superconducting screening current is not large enough to completely shield the applied measurement field in this temperature range [186]. Large YBCO-211 second phase can block the screening current and affect the epitaxial growth of nearby YBCO, which results in low J_c and broadened transition [187].

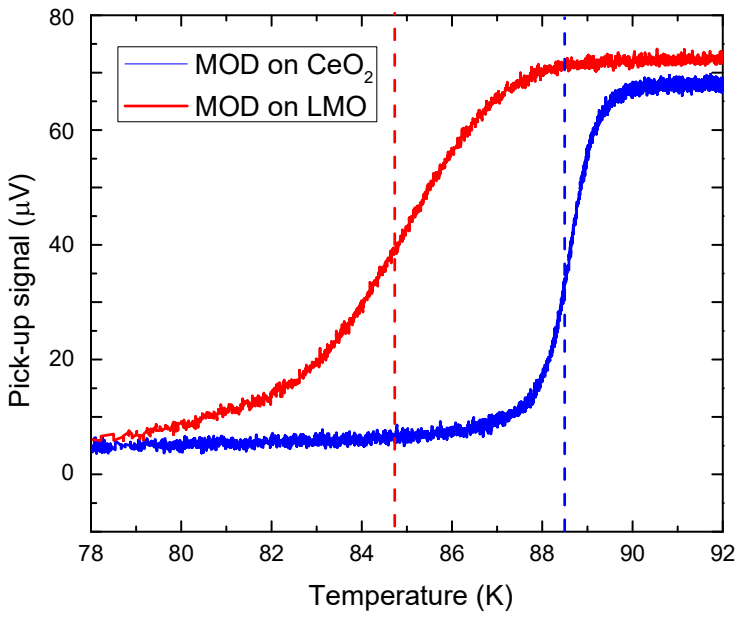

Fig. 5.11. T_c measurement of MOD samples on CeO_2 and LMO buffers

5.2.2 Spin coating

Spin coating is used for most of MOD test samples in this work. A typical program of spin coating shows in Fig. 5.12. After the buffer tape surface is completely covered with precursor,

the spinning rate ramped up to the spinning rate of 4000 rpm in 16 s and the sample kept spinning for 120 s. The spin-coated sample is then directly moved into the heat treatment furnace for calcination.

Two factors addressed in this section, the spinning rate and time. Both impact the coating thickness and film uniformity (Fig. 5.13). As shown in Fig. 5.13a, the YBCO thickness decreases with the spinning rate, and the decrease of thickness slows down as the spinning rate goes up. The thickness of the coated layer is stabilized as the spinning rate increases beyond 4000 rpm. However, striation marks appear when the spinning speed is over 5000 rpm (Fig. 5.14), the striation marks develop in the radial direction from the spinning center. Using optical microscopy, no YBCO is observed on the striated marks. According to the result from Araki et al. [188], the fast spinning results in pores on the substrate which develops into the striated marks. Striated marks can fatally deteriorate the J_c of YBCO film. So a spinning speed of 4000rpm is adopted in this work.

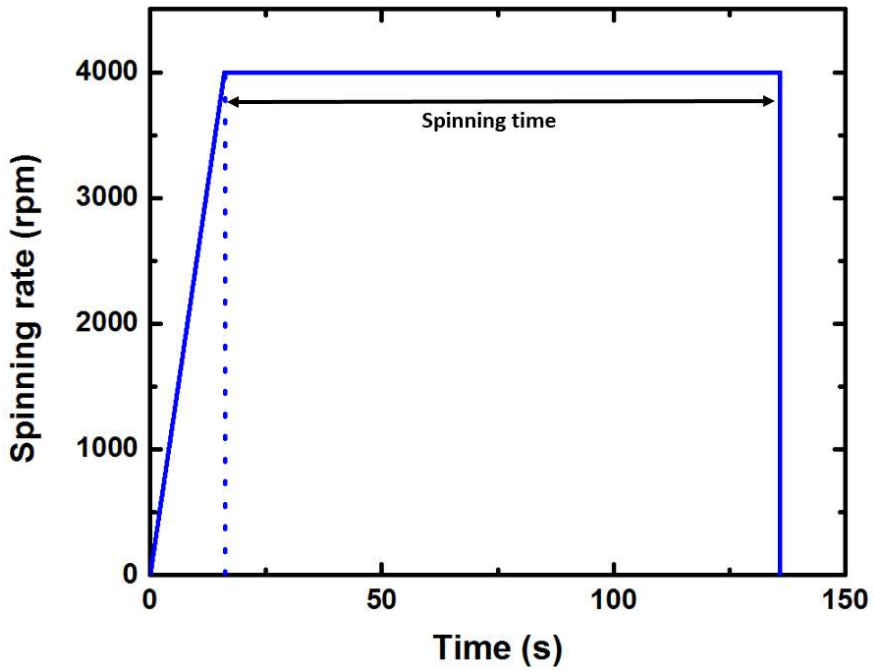

Fig. 5.12. Spin coating program for TFA-MOD.

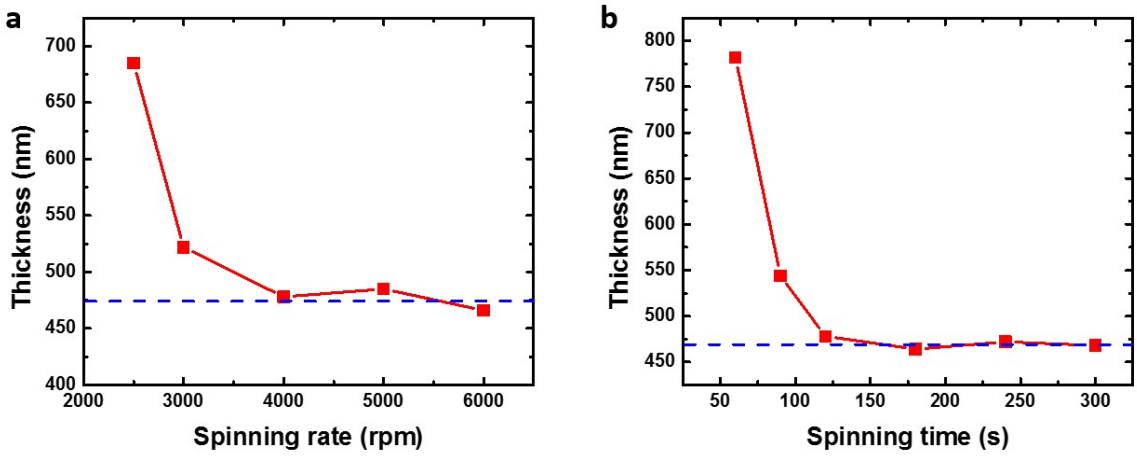

Fig. 5.13. Relationship of YBCO thickness with spinning rate and time.

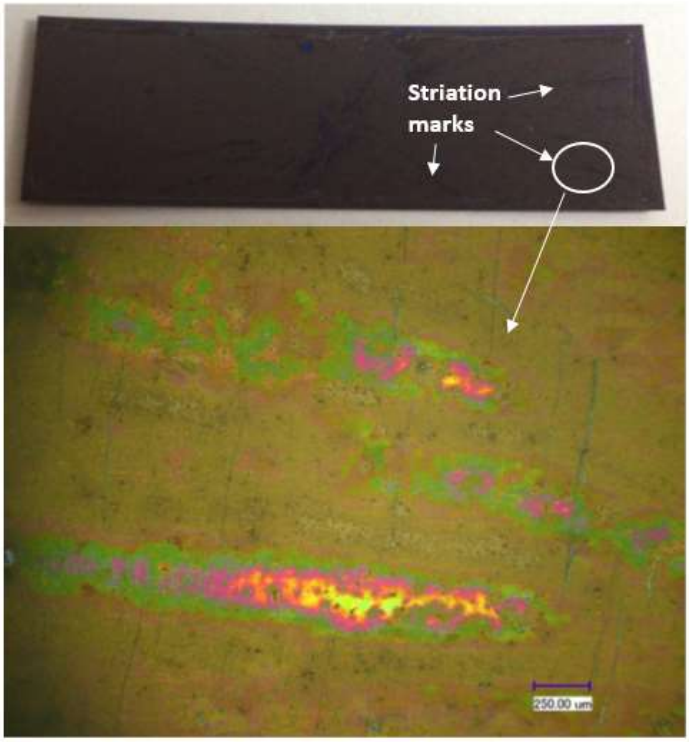

Fig. 5.14. Striation marks on sample of TFA-MOD YBCO with spinning rate of 5000rpm.

The spinning time shows similar relationship with coating thickness (Fig. 5.13b). The thickness of YBCO decreases with longer spinning time in the first 120 s. The thickness of the coated film is stabilized as the spinning time goes beyond 120 s. However, due to the

hygroscopic nature of the precursor [94], the spin-coated precursor film tends to deteriorate if left in atmosphere for a long time. To obtain the better performance for spin-coated YBCO, the spinning time of 120 s is chosen and the coated sample is quickly removed from the spinning platform and sent to the furnace for calcination.

5.2.3 Dip coating

Dip coating has some advantages over spin coating. Dip coating is more compatible with the inkjet-printed samples. Coating can be achieved as the tape is slowly withdrawn from the precursor in longitudinal direction. Also, unlike spinning coating, dip coating can be achieved in a reel-to-reel process.

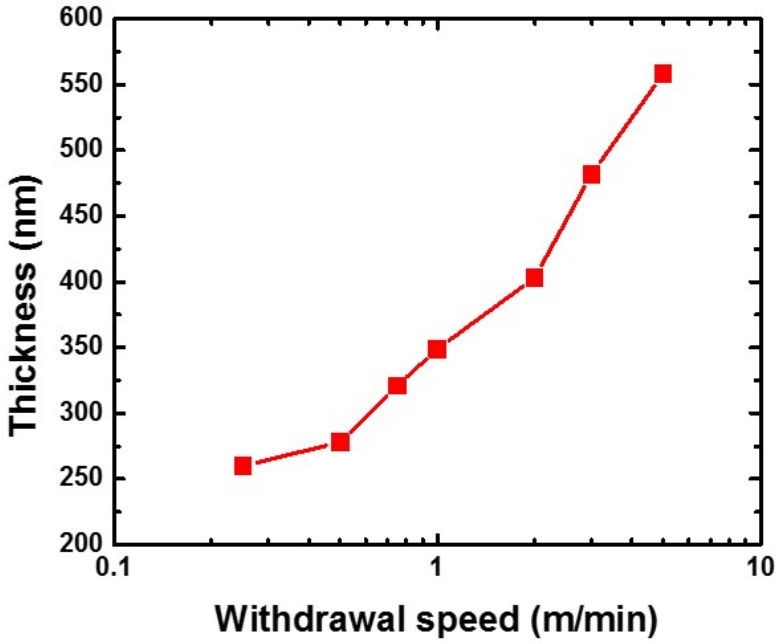

Fig. 5.15 Relationship of the withdrawal speed of dip coating and the thickness of YBCO.

The coating thickness is controlled by the tape withdrawal speed in dip coating (Fig. 5.15). The coating thickness increases with increasing the withdrawal speed. The dip coating thickness is determined by two different factors, the drying and the draining of the precursor. The draining speed is controlled by the precursor viscosity and the drying rate depends on the

temperature. According to the study of Scriven et al. [180], with the faster withdrawal speed, more precursor is carried out by the tape surface, while the draining speed is limited by the viscosity, so more precursor is left on the tape surface after drying. However, in the reel-to-reel process, the high withdrawal speed results in uniformity problems. Sample dip coated at a higher speed (>1 m/min) has shown strong edge effects. The coatings at the edges of tape are too thick that they crack and break during handling, leave the edges uncoated. Hence, a withdrawal speed 0.5 m/min is used in this work.

5.3 Heat treatment

5.3.1 Humidity

Humidity of the gas plays a crucial role in the heat treatment processes [189]. Water vapor is introduced in the calcination process to prevent Cu loss from sublimation, and it is also one of the reactants in YBCO formation reaction in the crystallization process. Samples are heat treated in humidity of 0%, 2.3%, 4.2%, and 12.2%. Humidity of the supply gas is controlled by the temperature inside the bubbler along the gas delivery line (Table 5.3).

Table 5.3. Relationship between temperature in bubbler and humidity of supply gas.

Temperature (˚C)	20	30	40	50	60
Humidity (%)	2.3	4.2	7.3	12.2	15.6

According to GADDS 2θ-χ scan, no YBCO is formed without water vapor during crystallization. A well-textured YBCO is found in the sample heat-treated with 2.3% humidity and above, and YBCO diffraction peak intensity increases with increasing water vapor (Fig. 5.16). However, SEM images (Fig. 5.17) also show that high humidity lead to rough surfaces and large porosity on YBCO layer surface. T_c measurement of the samples shows that samples prepared at 4.2% humidity exhibit the best T_c (89.2 K) (Fig. 5.18).

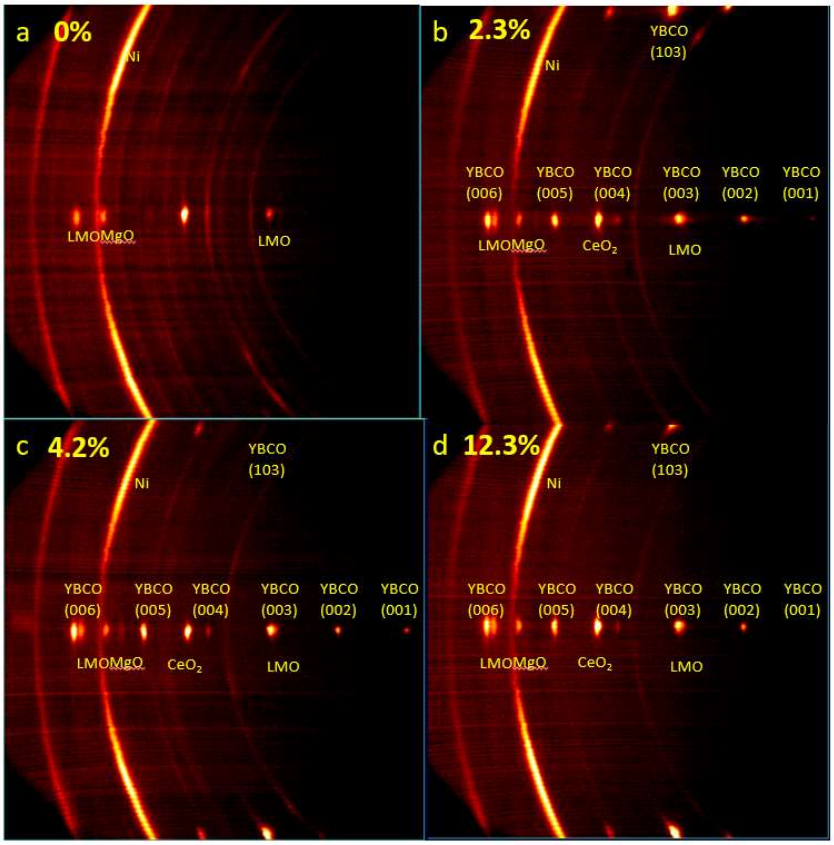

Fig. 5.16. GADDS *2θ-χ* scan of samples made at different humidity levels.

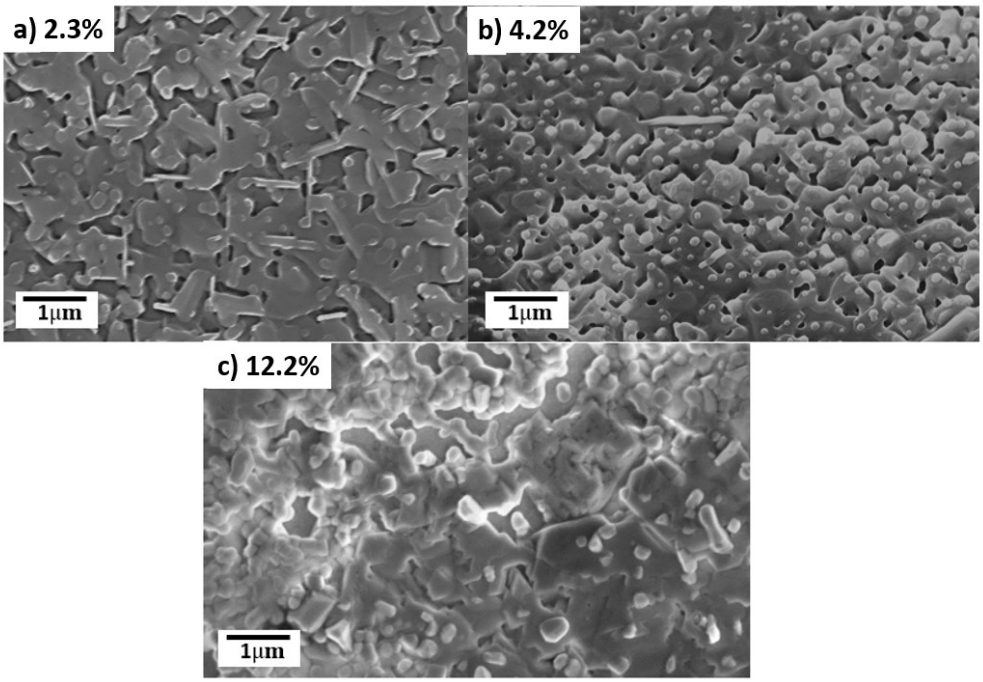

Fig. 5.17. SEM surface microstructures of samples made at different humidity levels.

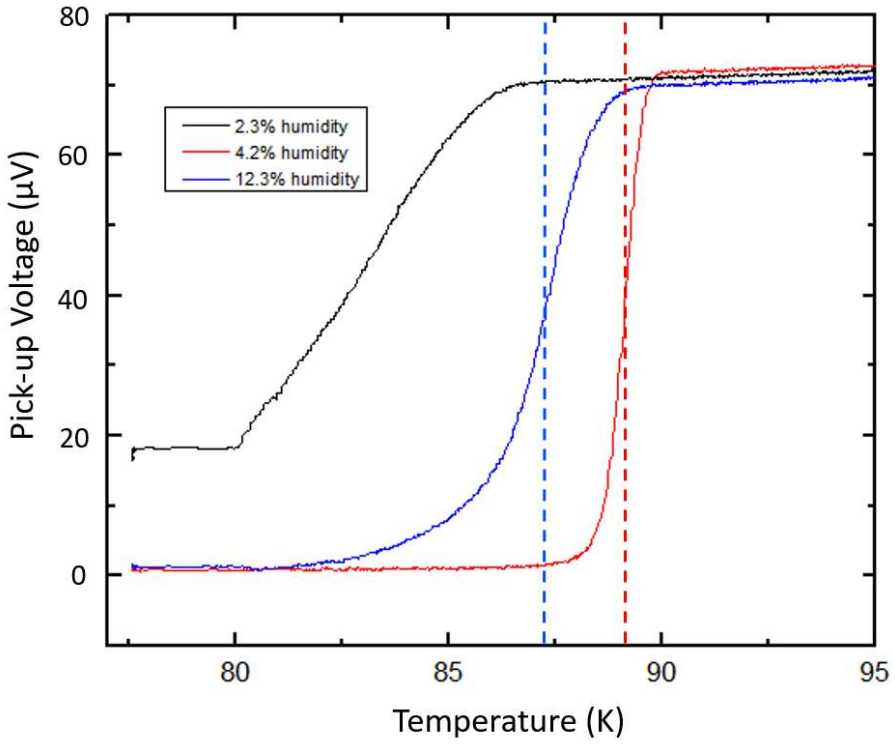

Fig. 5.18. T_c measurement of samples made at different humidity levels.

5.3.2 Calcination

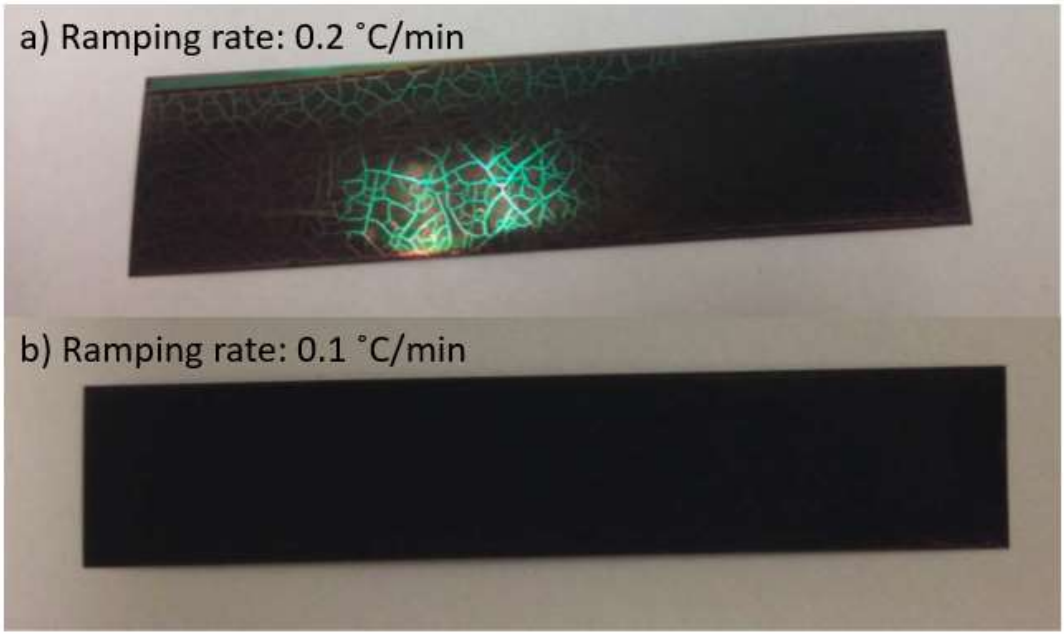

Fig. 5.19. TFA-MOD sample calcined under different ramping rates.

The crucial part of the calcination process is the decomposition of metal TFAs, which happens between 200 to 260 ˚C. During this process, the gel film is dried and Metal TFA is decomposed into nanocrystalline CuO, amorphous Y-Ba-O-F, and some organic residues that contain the excess fluorides. The volume of the film decreases drastically during the decomposition and so, the dried film cracks easily. As the result, calcination procedure is designed for a very slow ramp up in temperature from 200 to 260 ˚C. As shown in Fig. 5.19, the sample calcined at a 0.2 ˚C/min ramping rate between 200 to 260 ˚C shows severe cracking over the entire tape surface, while a smooth coating is obtained in the sample calcined at 0.1 ˚C/min ramping for 10 hours.

5.3.3 Crystallization

5.3.3.1 Crystallization temperature

Fig. 5.20 shows SEM images of samples crystallized at different crystallization temperatures. It is found that the film porosity is progressively reduced when the crystallization temperature is increased. It can also be seen that YBCO tends to form more a-axis grains at lower temperatures. However, it is also found that the microstructure coarsens as the crystallization temperature increases.

XRD θ /2θ scans of samples crystallized at different temperatures are shown in Fig. 5.21. All samples show similar textured YBCO structure. It is evident that the YBCO peak intensity follows the following trend: 760 ˚C>750 ˚C>740 ˚C>770 ˚C. But, from a performance point of view, the sample at 750 ˚C shows the best T_c of 89.8 K followed 89.5 K T_c at 760 ˚C (Fig. 5.22).

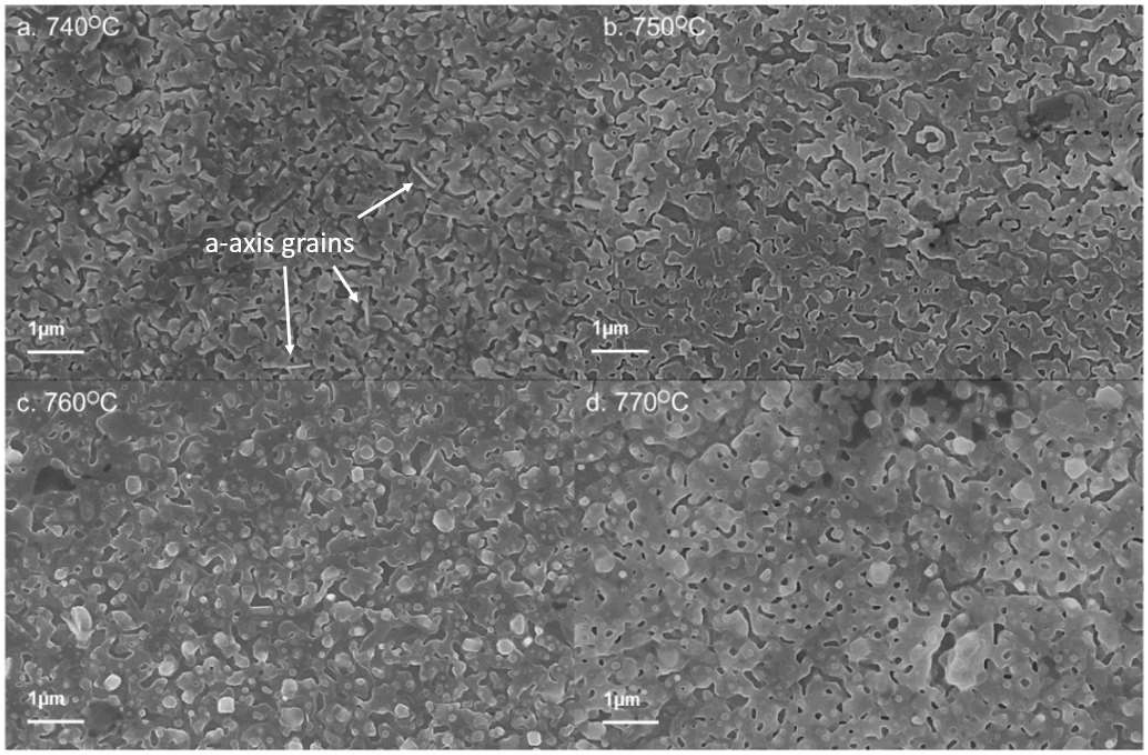

Fig. 5.20. SEM image of samples made at different crystallization temperature.

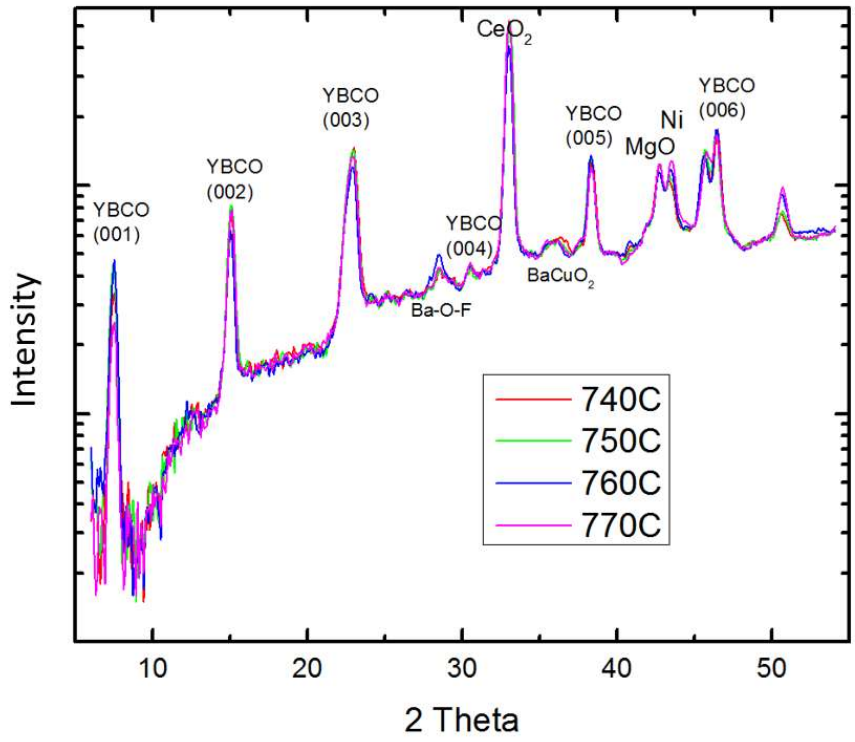

Fig. 5.21. XRD *θ /2θ* scan of samples made at different crystallization temperatures.

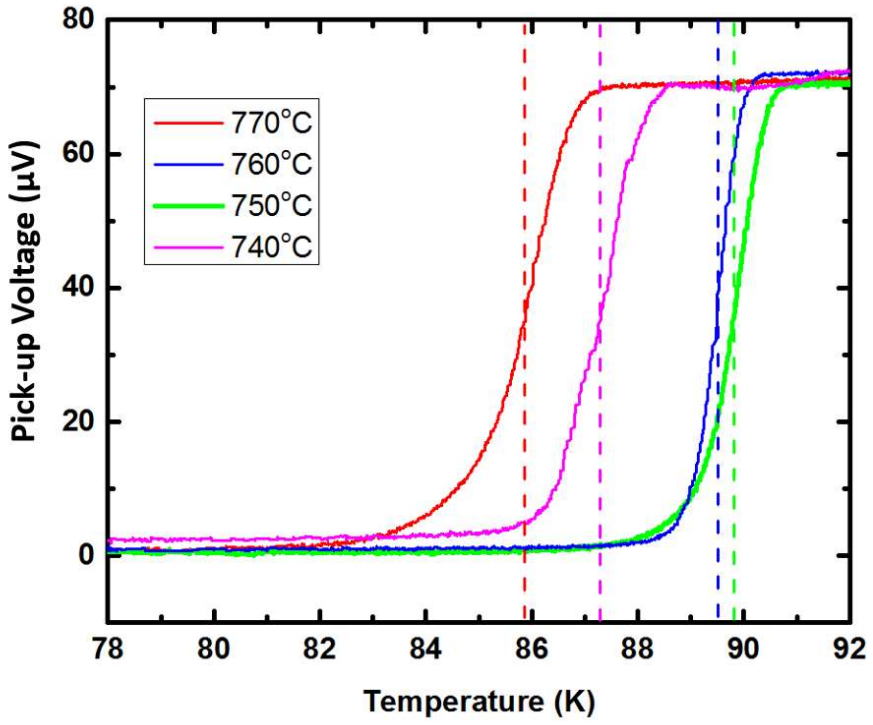

Fig. 5.22. T_c measurement of samples made at different crystallization temperature.

5.3.3.2 Crystallization time

Four samples are prepared at 750 ˚C with different crystallization times: 90 min, 150 min, 270 min, and 520 min. The supply gas is 0.1 % O_2 /Ar mixture with 4.2% humidity. Water is reactive with YBCO at lower temperatures after crystallization, so the gas supply is switched from moist to dry 30min before the temperature starts to ramp down. SEM images of the four sample are shown in Fig. 5.23. As seen in the figure, as the heat treatment time increases, the porosity on YBCO layer decreased. But it is also noticed that the misoriented grains increase as the heat treatment is longer than 150 min. Needle-shaped out-of-plane grains start to appear in the sample crystallized for 270 min, and the sample for 520 min shows a large number of the out-of-plane grains on the sample surface. This might be the result of reaction between the formed YBCO with CeO_2 on the buffer forming $BaCeO_3$, resulting in misoriented grains on the tape surface[96].

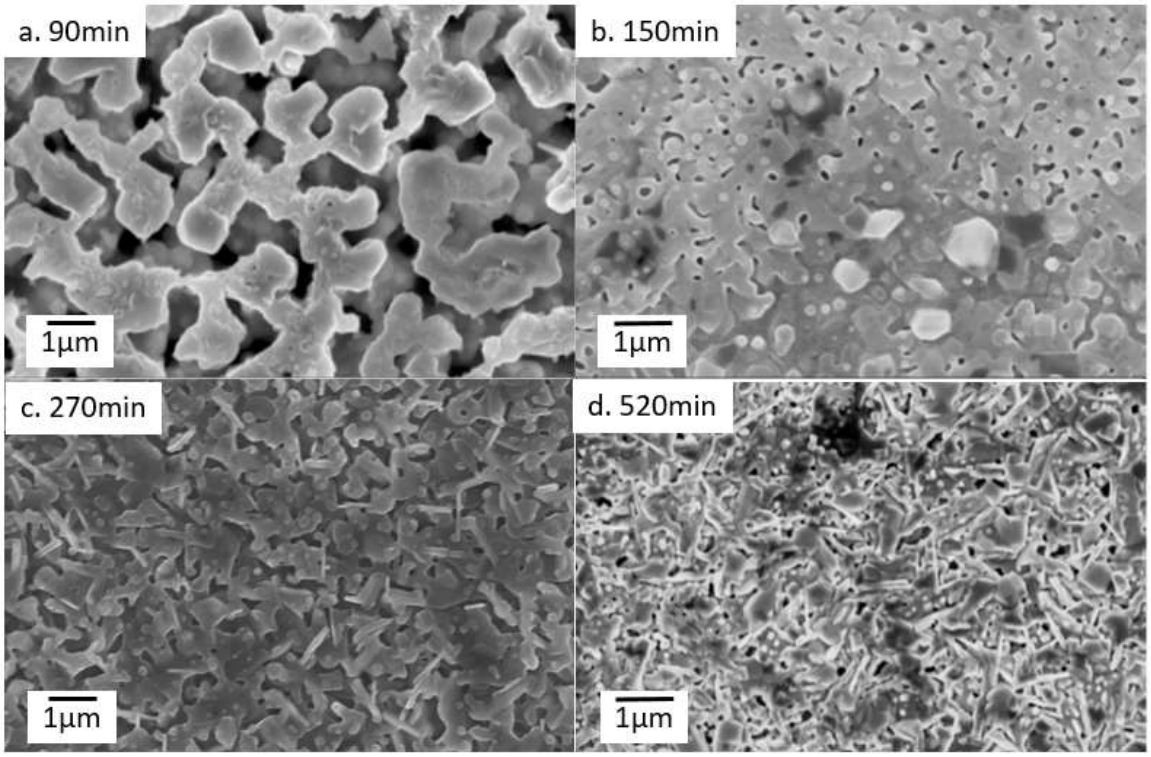

Fig. 5.23. SEM of TFA-MOD YBCO crystallized under 750 ˚C at different times.

GADDS 2θ-χ scans show a clear YBCO phase in all four samples (Fig. 5.24). In the sample crystallized for 90 min (Fig. 5.24a), it is clear that the YBCO formation is not yet finished; YBCO peaks are relatively weaker comparing with those of the other three samples and multiple second phases of CuO and Ba-O-F indicate the unfinished reaction. As the reaction time increases, the CuO and Ba-O-F second phases become weak (Fig. 5.24b, c). But in the sample crystallized for 520 min, the biaxial textured structure of YBCO becomes worse. The [103] peak of YBCO shows a ring pattern in the *2θ-χ* scan instead of singular diffraction point (Fig. 5.24d), indicating a larger amount of misoriented YBCO.

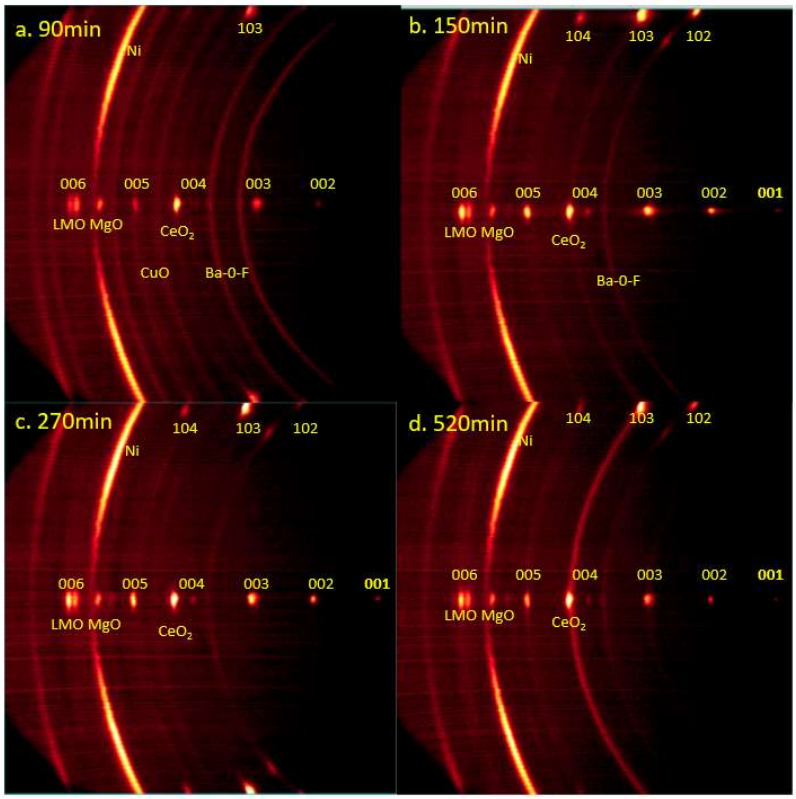

Fig. 5.24. GADDS *2θ-χ* scan of TFA-MOD YBCO crystallized at 750 ˚C for different times.

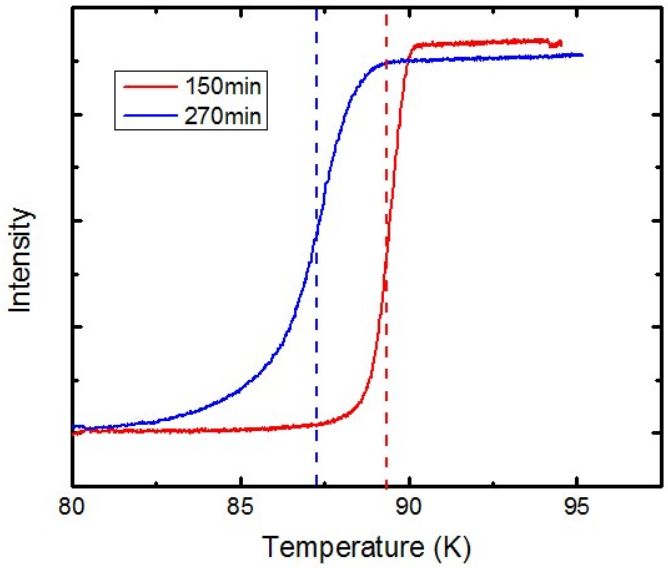

Fig. 5.25. T_c measurement of TFA-MOD YBCO crystallized at 750 ˚C for 150 min and 270 min.

T_c of the four samples crystallized for different times was measured. T_c transition shown by the sample crystallized for 90 min and for 520 min start below 77 K, so the actual T_c of the samples could not be measured by our system. The results of T_c measurement of samples crystallized for 150 min and 270 min are shown in Fig. 5.25. It is seen that the sample crystallized for150min shows the higher T_c of 89.3 K.

5.4 MOD for multifilament tapes of 2G-HTS

5.4.1 Selective deposition

Compared with MOCVD, the bottom-up deposition process of MOD is more suitable for the inkjet-printing multifilamentary process. Even though the inkjet-printed features on the tape surface are not suitable for spin coating, dip coating can be done along the tape length to achieve a good coating on the entire sample surface (Fig. 5.26).

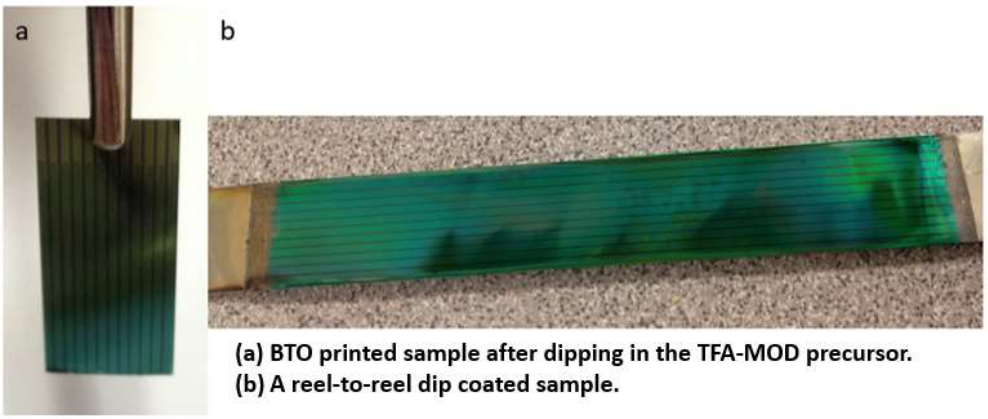

Fig. 5.26. Multifilament samples of TFA-MOD YBCO by dip coating after inkjet printing.

Fig. 5.26a shows a BTO printed sample after dipping in the TFA-MOD precursor. The inkjet-printed lines show hydrophobic behavior and the dip coated precursor is repelled from the BTO line surface, while the buffer surface between the lines is coated by the precursor, which means the superconducting filaments can be selectively deposited automatically. A reel-to-reel dip coated sample is showed in Fig. 5.26b. Unfortunately, the heat treatment furnace for

TFA-MOD is not compatible with reel-to-reel fabrication, and so, the dip coated tape was cut into 2 cm-long small pieces for subsequent processing.

Fig. 5.27 showed a piece from the reel-to-reel dip coating sample after the MOD heat treatment. Uniform YBCO is coated in the middle of the sample, but large defect-rich areas, including non-uniform coating and even uncoated region, are found around the four edges. This is caused by the edge effect of dip coating [190, 191]. Because of the limit of our heat treatment system, the long dip-coated sample is cut into short pieces before heat treatment. Cutting the tape before the dip coated solution film is calcined results in non-uniformity around the cutting edges. The middle part with uniform coating is cut for the performance testing.

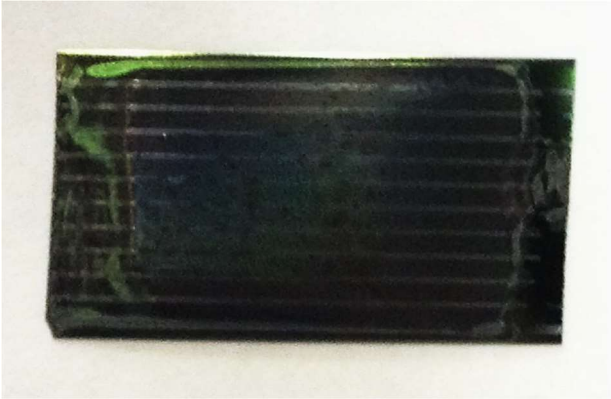

Fig. 5.27. A photo of the BTO inkjet-printed sample after TFA MOD

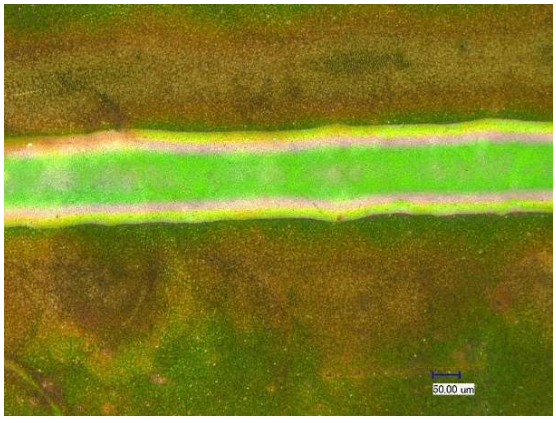

Fig. 5.28. Optical microscopy image of TFA-MOD YBCO filaments separated by BTO line.

Fig. 5.28shows an inkjet-printed BTO line after TFA-MOD YBCO. Judging from a clear definition of color between MOD YBCO and inkjet-printed BTO, it is seen that the deposition of YBCO us completely separated by BTO line. The selective eletrodeposited Ag is easily accomplished with clear definition between TFA-MOD YBCO and inkjet-printed BTO (Fig. 5.29).

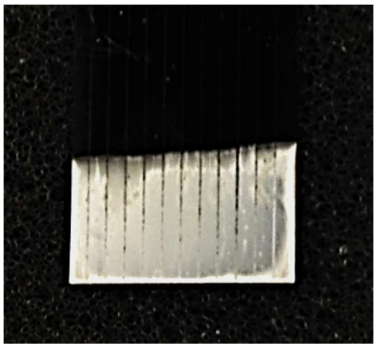

Fig. 5.29. A photo of selective electrodeposited Ag on inkjet-printed/MOD sample.

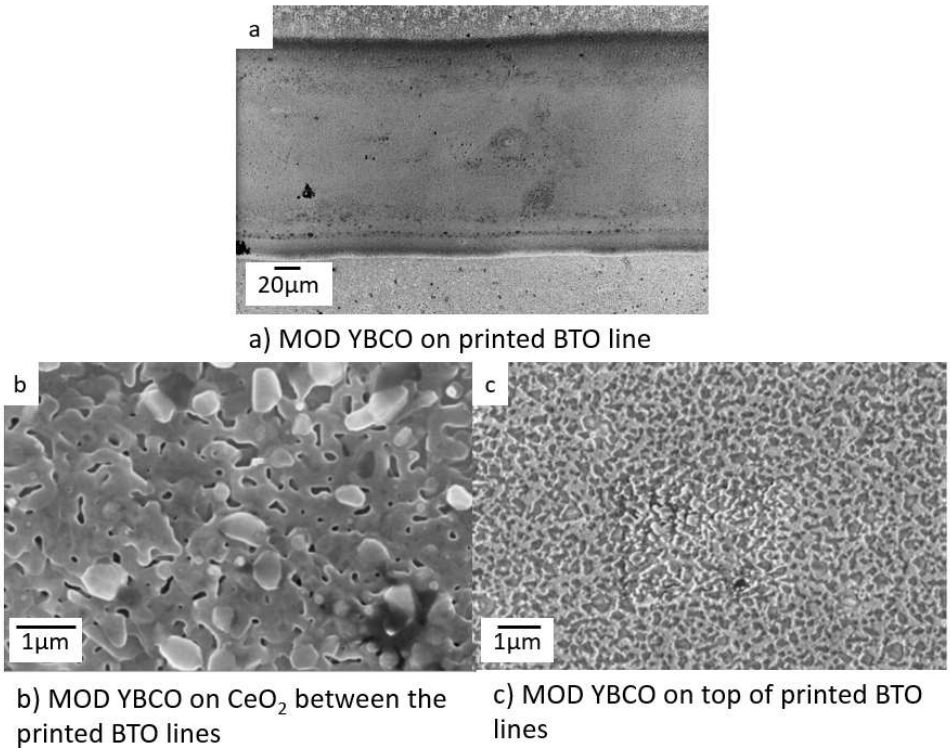

Fig. 5.30. SEM image of inkjet-printed BTO sample after MOD.

SEM images of the printed BTO line after TFA-MOD YBCO are shown is Fig. 5.30. A clear difference is found between the YBCO filaments and BTO line (Fig. 5.30a). On the CeO_2 surface between the lines, a typical MOD YBCO microstructure is observed (Fig. 5.30b). However, on the BTO line surface, no signs of continuous YBCO deposition are observed. Only some small islands of depositon are found on BTO line surface; the islands might be formed from remnant MOD precursor captured by the rough surface of BTO printed line.

5.4.2 Performance

Fig. 5.31 shows the T_c measurement results of the dip coated samples. A bare CeO_2 buffer tape was subjected to the same dip coating process as the reference. The same level of T_c performance was achieved in the inkjet-printed and dip coated sample as with the reference sample indicating that inkjet printing has no impact on the sample T_c. Both the inkjet-printed sample and its reference show the same onset T_c of 89 K, which is comparable to the spin coated samples.

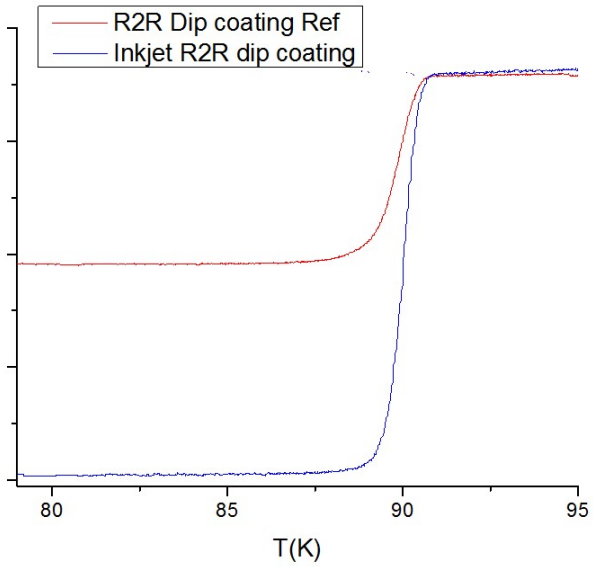

Fig. 5.31. T_c measurement of inkjet-printed and dip-coated MOD YBCO tape, with the reference that went through the same dip-coating process.

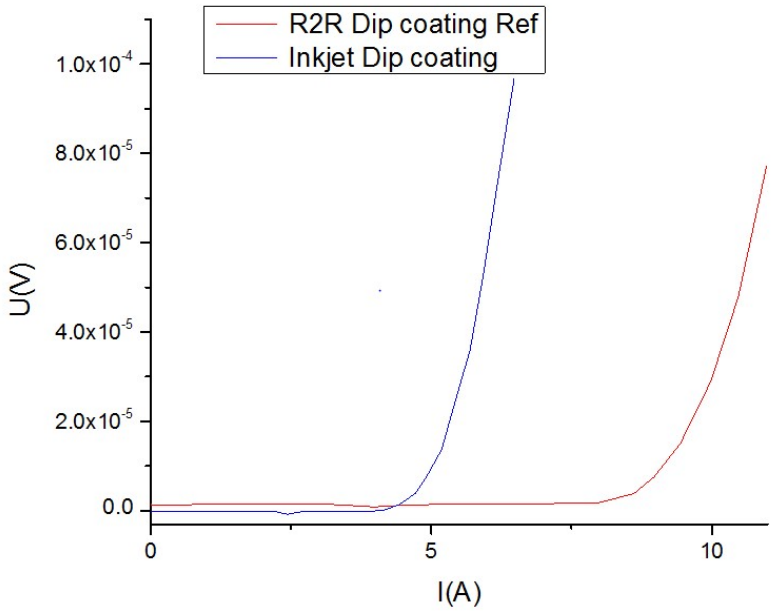

Fig. 5.32. I_c measurement of an inkjet-printed and dip-coated MOD YBCO tape, with the reference that went through the same dip-coating process.

The I_c measurement result in Fig. 5.32 shows I_c values of 5 A in the inkjet-printed sample and 9 A in the reference which corresponds to a 44% reduction. Other than the 17.5% conductive area loss by the printed lines, the reduction of I_c is primarily caused by the non-uniformity of the MOD YBCO. The decrease of I_c may be due to thinner film, pores or second phases.

Scanning Hall probe microscopy (SHPM) is employed to study the J_c distribution in the REBCO filaments. In SHPM, the inkjet-printed MOD sample is magnetized by a permanent magnet at 77K, and the remnant field is mapped by the Hall probe that scans above the sample surface (Fig. 5.33). According to the field map, 11 out of 12 superconducting filaments show the presence of a remnant field. The remnant field is absent in the 12th filament with large delaminated areas (Fig. 5.27). The number 1, 2, 8 and 9 filaments show a strong remnant field signal, which indicates that these YBCO filaments have higher J_c and better uniformity. The other filaments show a lower trapped field and thus lower J_c. The lower J_c may be caused by

multiple reasons, like non-uniformity in coating thickness and porosities. In the #6 and #7 filaments, significant defect spots are found (circled in Fig. 5.33); the defect spot has shown almost no remnant field and hence the remnant field along the defective filaments is not continuous. This indicates that the defect spot blocks the longitudinal current flow at the specific point, and the inductive screening current has to flow in two separate loops. It can be expected that the transport superconducting current cannot pass through the defect. These large defect spots are very likely caused by satellite drops during inkjet-printing (section 4.2.1.1). Three bad filaments (number 6, 7 and 12) have likely resulted in an extra 20.7% of I_c reduction, which is the major reason for the overall I_c reduction in the inkjet-printed tapes

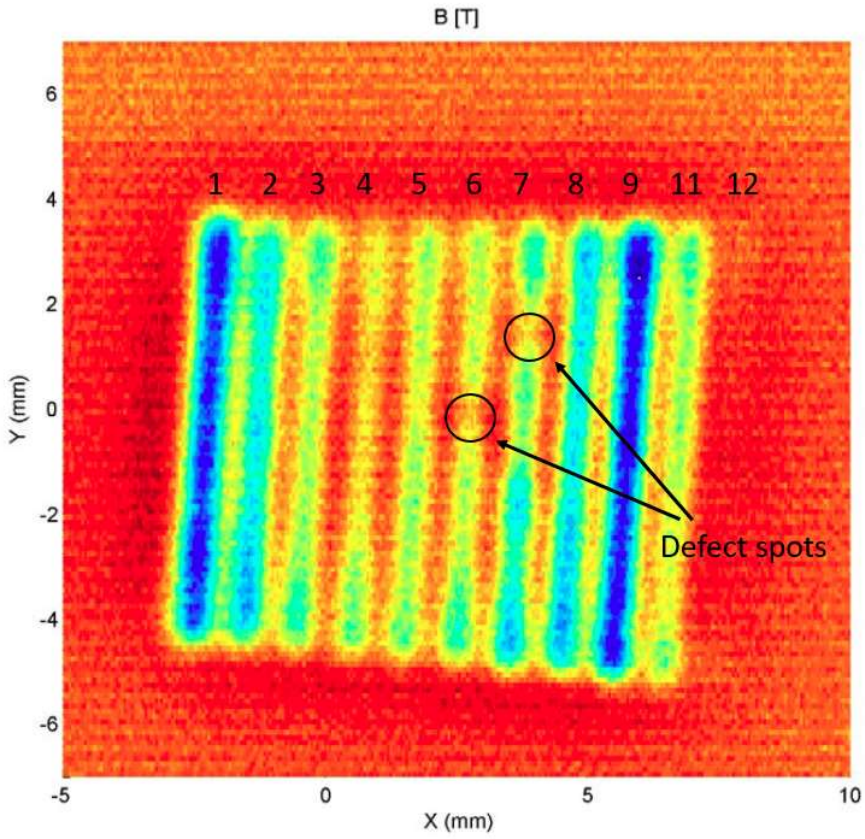

Fig. 5.33. Scanning Hall-probe microscopy of the remnant field in the inkjet-printed MOD sample.

With better MOD YBCO quality and uniformity, a significant improvement in performance might be expected. AC loss reduction of the inkjet-MOD sample could be measured due to the low I_c of the sample.

So far, the results of this work are limited by MOD YBCO quality. With further development in the technique of MOD YBCO, the all-solution fabrication approach can be a viable for multifilament 2G-HTS tape.

Chapter 6. Reel-to-reel Selective Electrodeposition

In this chapter, selective depositions are employed for building Ag overlayer and Cu stabilizer. Utilizing DC electrodeposition method, Ag and Cu are selectively deposited on the superconducting filaments.

6.1 Electrodeposition of Ag overlayer

The electrodeposition of Ag overlayer is conducted in a methanol-based non-aqueous electrolyte. In this section, the general electrodeposition process and the morphology of electrodeposited Ag are studied. The non-aqueous electrodeposition of Ag was developed by our former graduate, Y. Zhang [112]. In this section, the deposition condition is optimized and adapted to the inkjet-printed multifilamentary tapes.

6.1.1 Deposition parameters

As the protection overlayer on REBCO, a dense and uniform Ag film with a smooth surface is required.

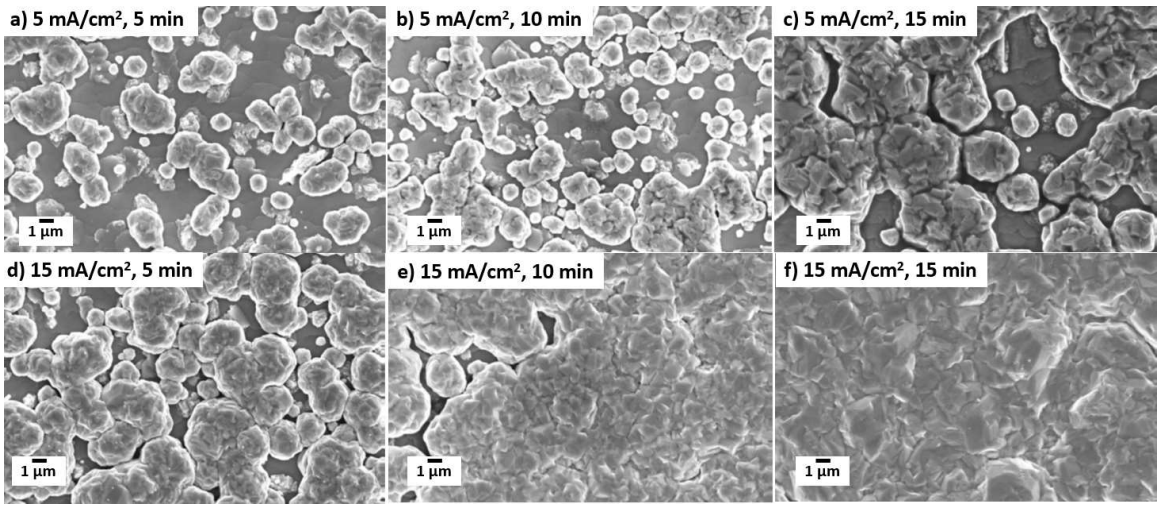

Fig. 6.1. SEM images of electrodeposited Ag on bare REBCO samples with different deposition current density and time.

Fig. 6.1 shows the SEM microscopy of electrodeposited Ag on bare REBCO samples with different deposition current densities and time. The growth of electrodeposited Ag film follows Volmer-Webber growth [192, 193]. Deposition of Ag occurred in islands and the deposited islands merged as the deposition process develops. This is because of the low concentration of electrolyte and the relatively lower conductive surface (comparing with Ag) of REBCO; the adatom cohesive force is stronger than surface adhesive force. From Fig. 6.1a to f, the deposition current density and time gradually are increased and as the result more Ag is deposited upon REBCO surface. The isolated islands grow larger and merge together. Ag deposited at 15 mA/cm^2 for 15min showed a continuous silver coating on the entire sample surface. However, the deposition current density is limited by the diffusion rate of Ag^+ ions, as shown in Fig. 6.2 and dendritic structures are found in Ag deposited at 25 mA/cm^2. At higher deposition current density, electrolytes close to the cathode surface are quickly depleted, and so, the deposition speed is controlled by the ion transfer rate. Meanwhile the electrolytes around the protrusion areas are yet not depleted and since the deposition is controlled by the electric charges, it is much faster on the protrusion area. As the result, dendrites structures are formed [194-196]. Dendritic deposition is not preferred in this work, because it cannot protect the REBCO layer below.

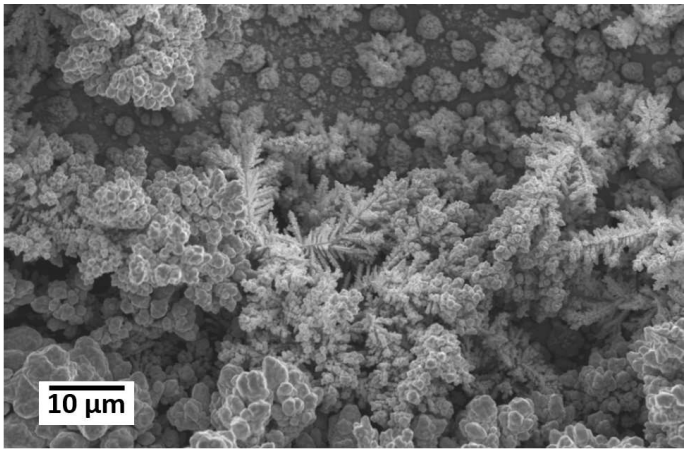

Fig. 6.2. Dendritic deposition in Ag deposited at 25 mA/cm^2

6.1.2 Oxygen annealing

Annealing is conducted after Ag electrodeposition to further improve the Ag morphology and its interfacial contact with REBCO [197]. During the heat treatment, the grain size of the electrodeposited Ag increases, Ag layer is softened and the contact with REBCO is improved [198, 199]. To prevent REBCO losing oxygen at high temperature that would result in poor superconducting performance, the annealing is done in pure oxygen. Since Ag has a good permeability to oxygen at high temperatures, the Ag deposited REBCO is annealed in 500˚C for 30min. Ag oxide degrade at the temperature of 310 ˚C, so no Ag oxide formation during the post deposition annealing [198].

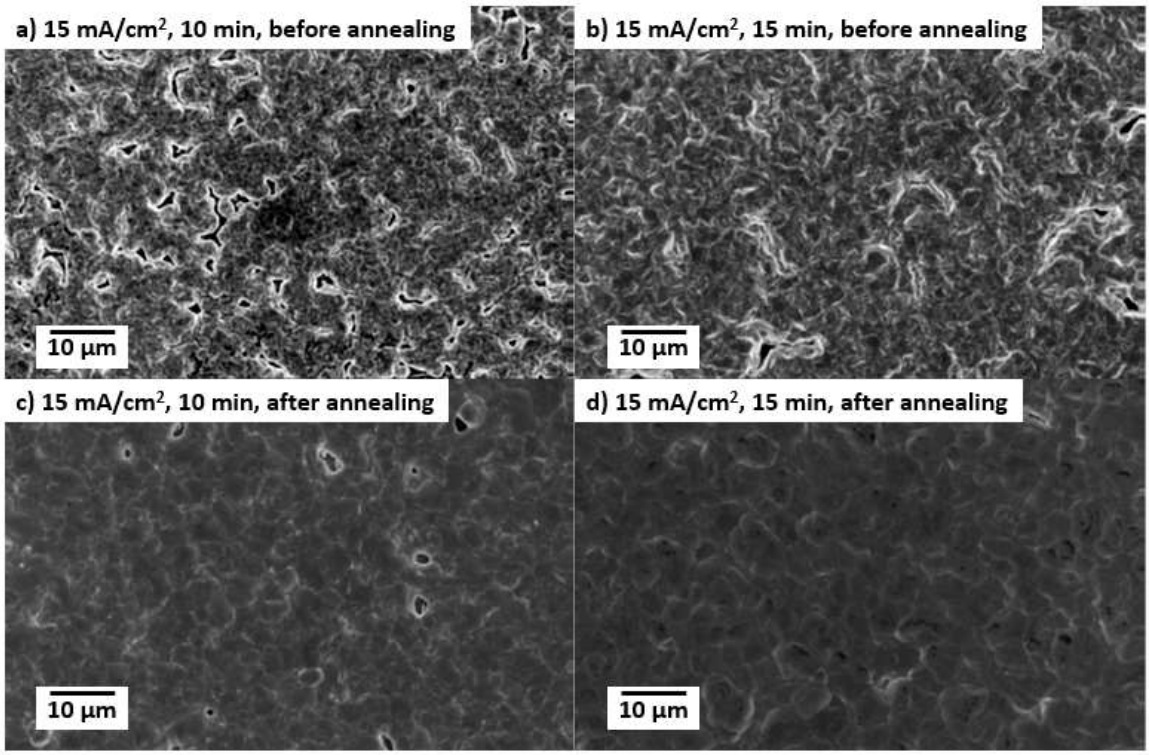

Fig. 6.3. SEM images of electrodeposited Ag before and after oxygen annealing.

Fig. 6.3 shows the SEM images of the deposited Ag before and after annealing. It can be seen that the oxygen annealing process has significantly improved the Ag surface. The edges and corners of the grains are smoothened, and the protrusions are flattened. In the sample

deposited at 15 mA/cm^2 for 10 min (Fig. 6.3a, c), it is noticed that annealing is capable of closing up the pores and gaps between Ag islands that haven't completely merged together after deposition.

The performance of Superpower MOCVD 2G-HTS REBCO tape is measured by TAPESTAR (Fig. 6.4). The average I_c of the bare 2G-HTS tape is found to be 566 A, and the I_c decreases by 2.65% to 551 A after the Ag deposition. However, the annealing process after Ag deposition significantly improved the performance of the tape, increasing the I_c over 600 A. The mechanism behind this improvement is unknown. We believe that the reduction reaction on the cathode surface may also result in reducing YBCO and so the deficiency of oxygen is probably the reason for lower I_c after deposition. By re-annealing the electrodeposited sample, the deficient oxygen is replenished.

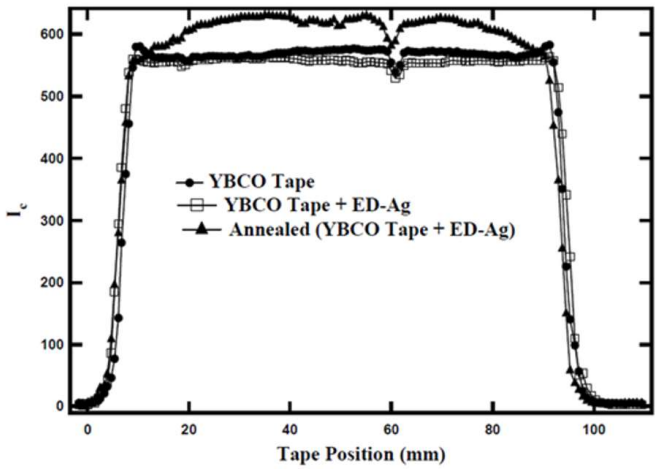

Fig. 6.4. TAPESTAR I_c measurement of 2G-HTS before and after Ag deposition and oxygen annealing.

6.1.3 Reel-to-reel fabrication

A reel-to-reel electrodeposition system has been built for scaling up the process to long tapes. A 100 m-long and 12 mm-wide 2G-HTS was previously electrodeposited with Ag at 30 cm/min

tape speed in reel-to-reel system. Fig. 6.5 shows a photograph of the 100m tape electrodeposited Ag wound on a mandrel.

TAPESTAR I_c measurements were conducted before and after Ag electrodeposition & oxygenation annealing, the results are summarized in Fig. 6.6. Similar to the short samples (Fig. 6.4), the Ag electrodeposited shows a higher average I_c (312 A) compared with the bare YBCO sample (285 A). The electrodeposition process is a potent substitution for the expensive sputtering process for making the Ag overlayer.

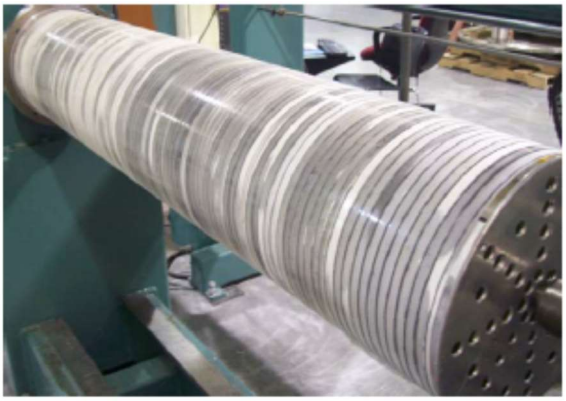

Fig. 6.5. A photograph of Ag electrodeposited on the tape with 100 m length of 2G-HTS.

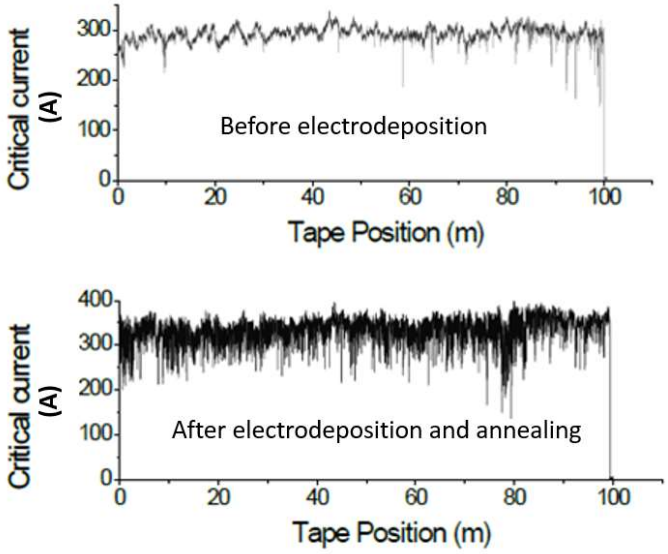

Fig. 6.6. TAPESTAR I_c measurements on the 100 m 2G-HTS tape before and after Ag electrodeposition and oxygen annealing.

However, the Ag electrodeposited tape showed a larger fluctuation in the I_c data and more I_c dropouts. The I_c dropouts determine the overall current capacity of the long tape. The I_c dropouts might be the result of multiple reasons during the immature reel-to-reel electrodeposition process, like inconsistent tape movement and fluctuations in current, incomplete rinsing and drying, etc..

6.2 Electroplating of Cu stabilizer

In this section, the electroplating process of Cu stabilizer is discussed. The work in this section starts from Ag-sputtered non-striated tapes and Cu deposition done by the reel-to-reel electroplating system.

6.2.1 Cathode current efficiency and thickness control

The cathode current efficiency is an important factor to be addressed. The process can be considered as a simple galvanic cell governed by the reaction Cu^{2+} (solution) $+2e^{-}\rightarrow$Cu(s). The current efficiency can be expressed as

$$\eta = \frac{m}{m_{theo}} \times 100\%, \tag{6-1}$$

where η is the cathode current efficiency, m is the mass of the electrodeposited material, and m_{theo} is the mass of the theoretically deposited material, which depends on the deposition current and deposition time. The theoretical thickness of the deposited Cu can be shown as

$$a_{theo} = \frac{M_{Cu} J_d t}{n \rho F}, \tag{6-2}$$

where n is the stoichiometric number, which is 2 in this case, F is Faraday constant, M_{cu} is the molar mass of Cu, ρ is the density of Cu, J_d is deposition current density, and t is the deposition time.

Samples were electroplated Cu with different deposition times (Fig. 6.7a) and current densities (Fig. 6.7b). The deposition time is controlled by the tape speed. The thickness of the deposited layers was measured and compared with the theoretical thickness. The measured thickness agrees well with the theoretical value, and the cathode current efficiency is over 99%. The high cathode current efficiency indicates that the Cu deposition reaction is the only electrochemical reaction inside the plating cell. Because the thickness of Cu layer has linear relationships with both deposition time and current density, the process shows an excellent control. Cu stabilizer of different thickness from 5 to 35 μm can be directly plated.

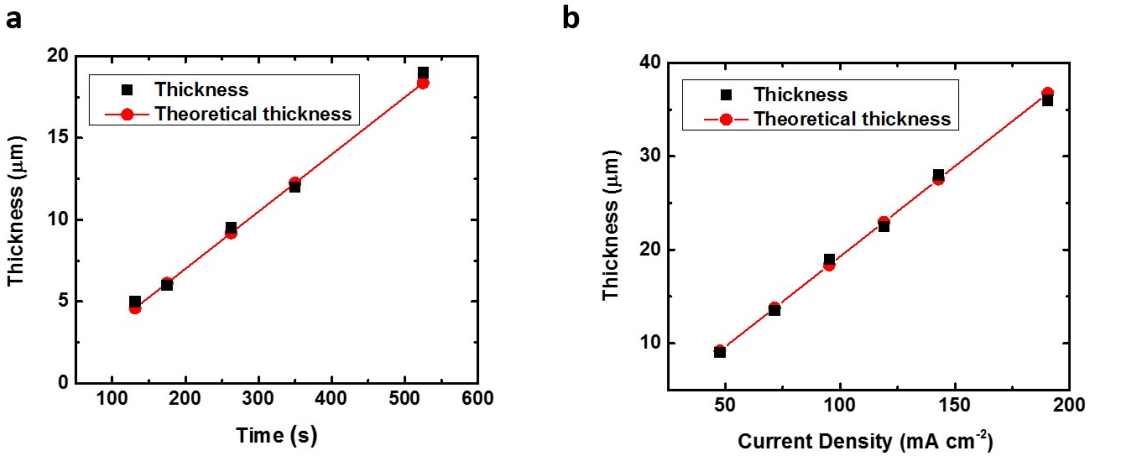

(a) Different electroplating time under 95mAcm^{-2} (deposition current 8A)

(b) Different electroplating current density for 525s (tape speed 4 cm/min)

Fig. 6.7. Relationship of Cu thickness with electroplating current density and time.

6.2.2 Thickness uniformity

Thickness uniformity is also important for the Cu stabilizer. Bumps and ridges result in reduced packing factor when the tape is wound into a coil, which results in lowered coil current density. High uniformity is required both along the length and across the width. Fig. 6.8 shows the longitudinal thickness profile of a 5 m long tape after electroplating at 95 mA/cm^2 (plating current 8 A) for 525 s (tape speed 4 cm/min). The thickness is measured every 20 cm using a micrometer. The total thickness of the Cu plated tape is 89±1 μm. The thickness of pre-

deposited tape is 50 μm and Cu is deposited on both sides of tape. The thickness of plated Cu layer is therefore 19.5±0.5 μm. Good consistency in the deposition conditions as the tape moves through the electroplating system results in a constant thickness over the length.

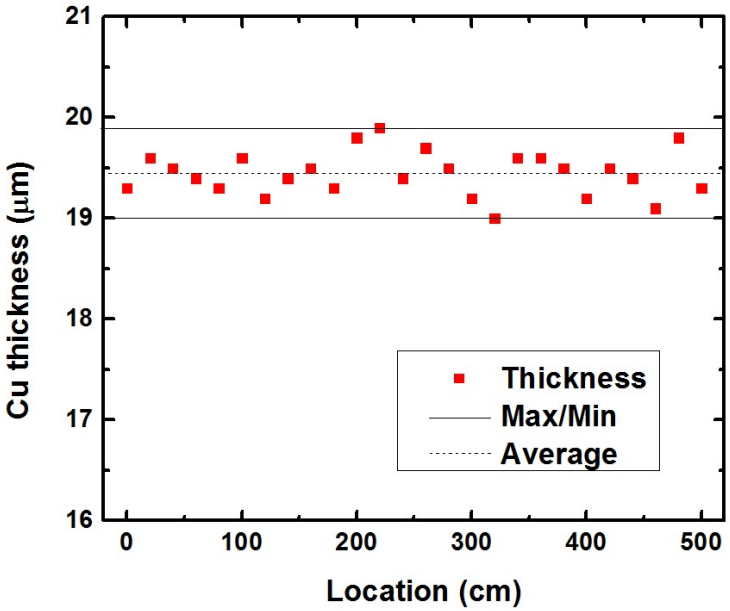

Fig. 6.8. Thickness of electroplated Cu on a 5 m long tape made in reel-to-reel electroplated system.

However, the deposition thickness across the width is a problem. Fig. 6.9 shows the Cu thickness profile across the width of the tape. The Cu deposition on the edges are significantly thicker than in the middle. The thickness difference is larger with thicker Cu deposition, especially at a higher current density. In the sample plated with 4cm/min tape speed and 95 mA/cm^2 current density, 36 μm-thick Cu is measured at the edges, which is nearly twice as thick as the Cu plated on the middle of the tape (19 μm). Dendritic structures are found on the edges of high current density (≥95 mA/cm^2) samples (Fig. 6.10a).

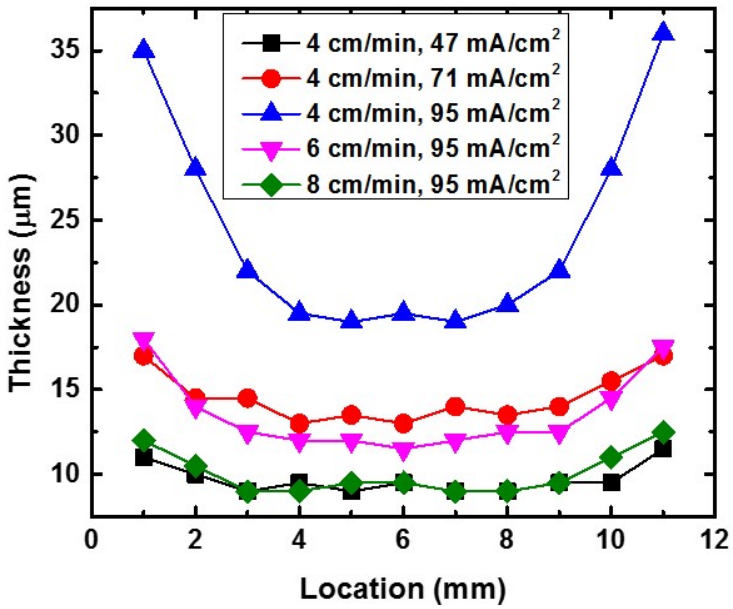

Fig. 6.9. Thickness profile of plated Cu at different current densities and tape speeds.

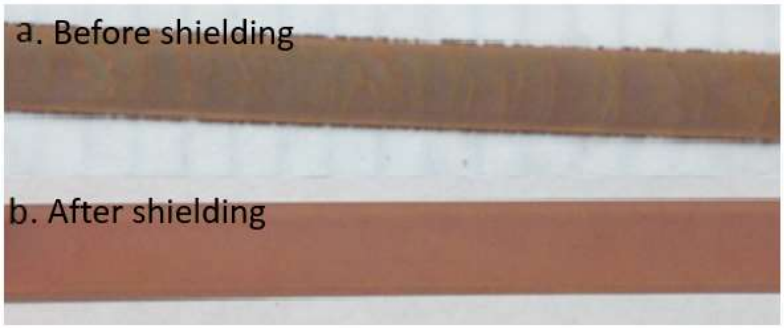

Fig. 6.10. Photos of 2G-HTS tape plated at 16 A current (380 mA/cm^2) and 8 cm/min tape speed (deposition time 263 s) before and after shielding.

A 2D-simulation of the electrolyte potential and ion influx was made based on the cross section of the plating cell. The numerical model is built based on the Nernst-Planck equation and the kinetic study on Cu/$CuSO_4$ system by Mattson et al. [120], and computed by the electrodeposition modules of COMSOL Multiphysics 5.0. Details of the model are shown in section 2.4.1.

In this model, a cathode with the dimension of 0.05×12 mm is located in the middle of the 300×200 mm plating cell. Anodes are located on both sides of the plating cell. The electrolyte has a pH of 4, a Cu concentration of 5×10^{-4} M, and the ion diffusivity is 2×10^{-9} m^2/s. The

electroplating potential is 1V. The plating temperature is 40 ˚C and the reaction is assumed to have a perfect cathode current efficiency. Fig. 6.11 shows the results of the model in the 40×28 mm area around the sample. The electrolyte potential is shown by the colored surface and the deposition material flux is shown by the streamline. A larger potential gradient and more concentrated ion-flux are found at edges of the tape, both indicating that the deposition current density is higher on the edges. The high deposition current density results in a thicker deposition and possible dendrite structure.

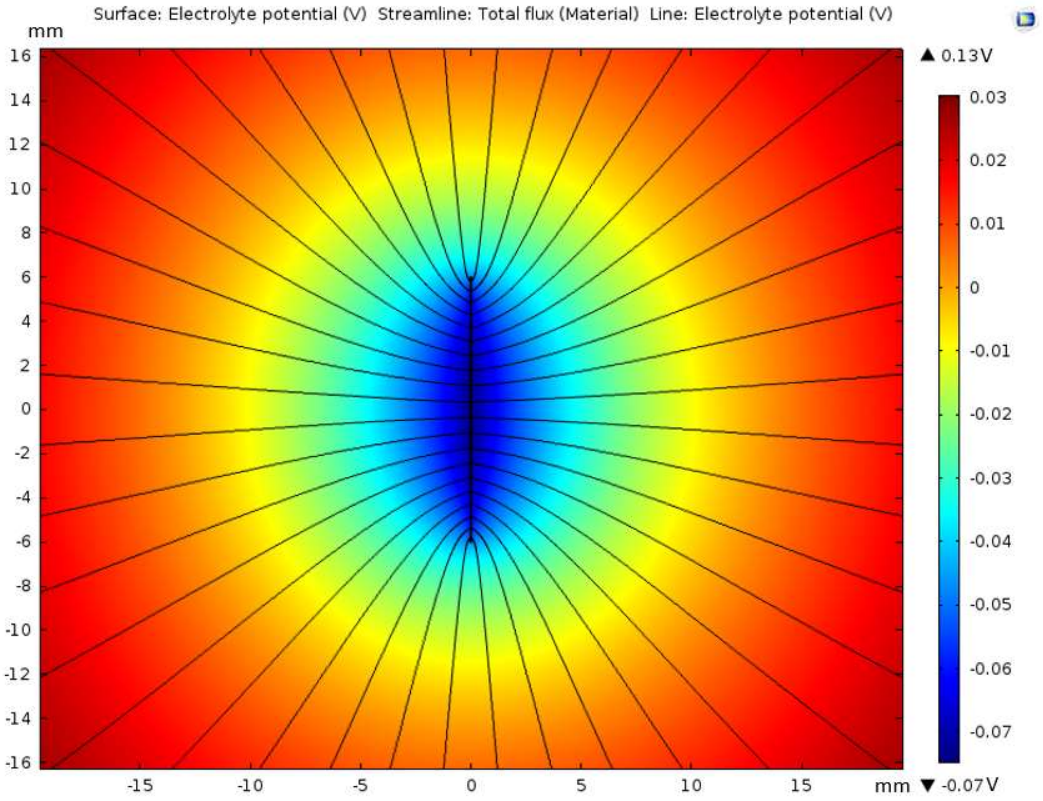

Fig. 6.11. Modeling of the electrolyte potential and ion-flux around the cathode based on Nernst-Planck equation.

To fix the distribution of both electrolyte concentration and potential gradient, changing the electrolyte geometry around the edges of the cathode is the obvious approach. Fig. 6.12 shows a similar model with two pieces of 10 mm-wide insulator blocks shielding the top and bottom edges of the cathode. With the shield applied, both the electrolyte potential and ion-flux are re-

arranged, creating a more uniform distribution environment for potential and flux field across the width of tape.

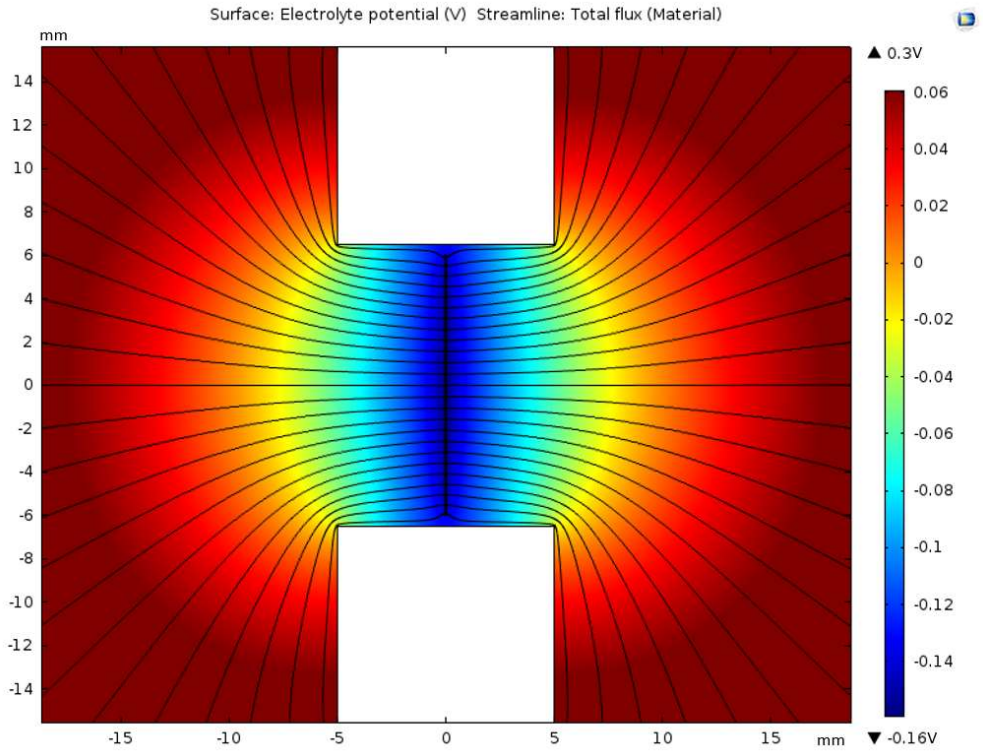

Fig. 6.12. Modeling of the electrolyte potential and ion-flux around the cathode after shielding.

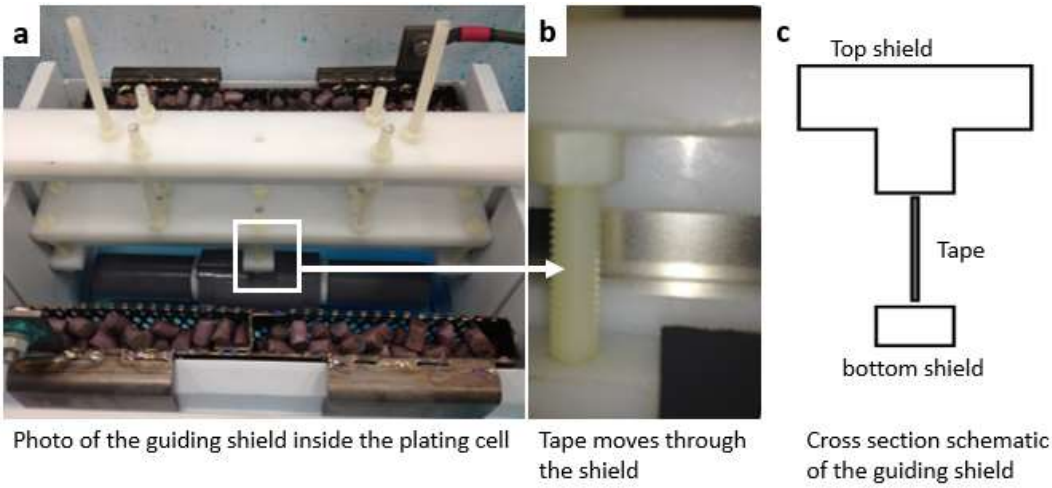

Fig. 6.13. Photos and schematic of the guiding shield applied in the plating cell.

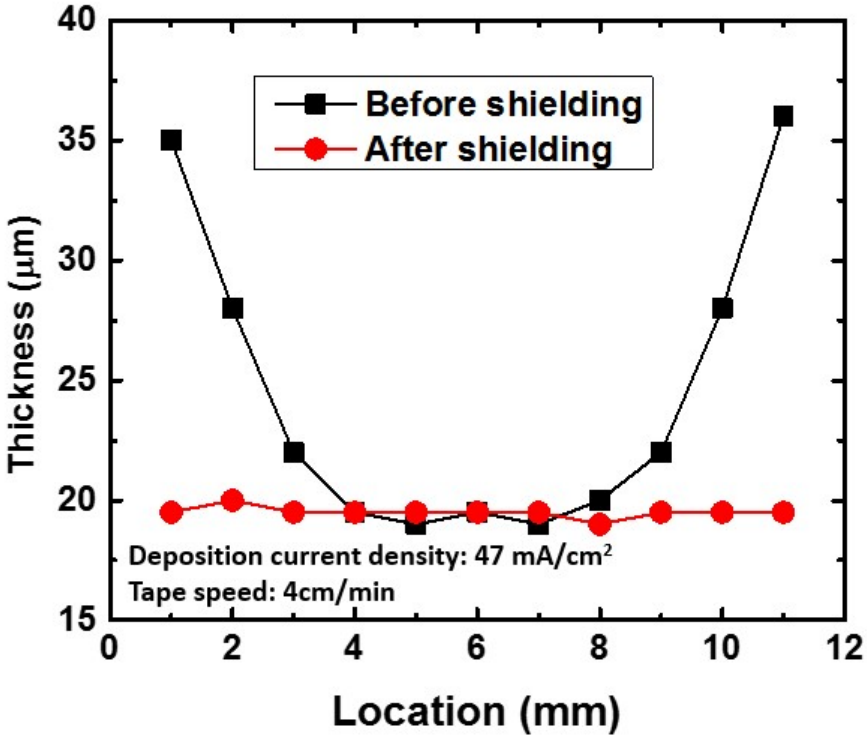

Fig. 6.14. Thickness profile of Cu layer plated before and after shielding.

To adjust the distribution of both electrolyte concentration and potential gradient, a Teflon guiding shield is deployed in the deposition cell to partially shield the electrolyte from the edge of the tape (Fig. 6.13). The insulating guiding shields are close to the top and bottom edge of the tape, creating a 13×10 mm channel through which the tape can freely pass. The experimental results agree well with the modeling. After the shield is deployed, no dendritic deposition is observed (Fig. 6.10b). The thickness on the edge has significantly decreased, and the thickness difference between the center region and the edges is less than 0.5 μm (Fig. 6.14).

6.2.3 Surface smoothness

A smooth surface is needed for the electrodeposited samples. Trenches and pores on the tape surface can trap some solution inside and enable galvanic corrosion in the tape after deposition. The deposition current density and electrolyte temperature are two major factors controlling the surface micro morphology.

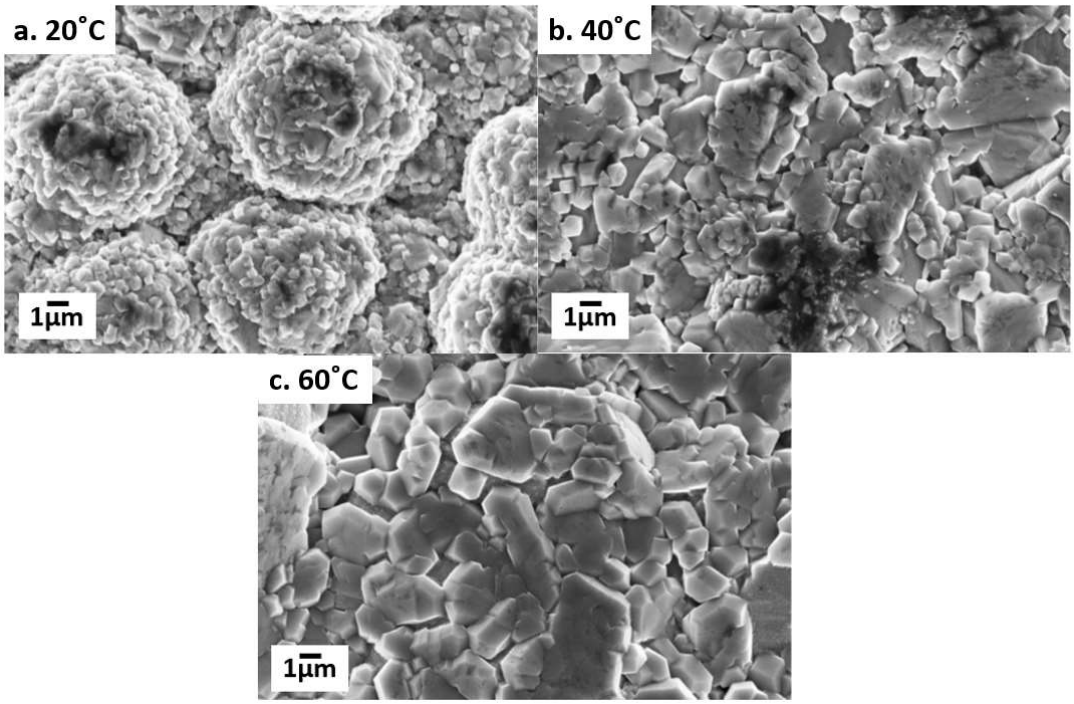

Fig. 6.15. SEM images of the Cu surface electroplated at different temperatures.

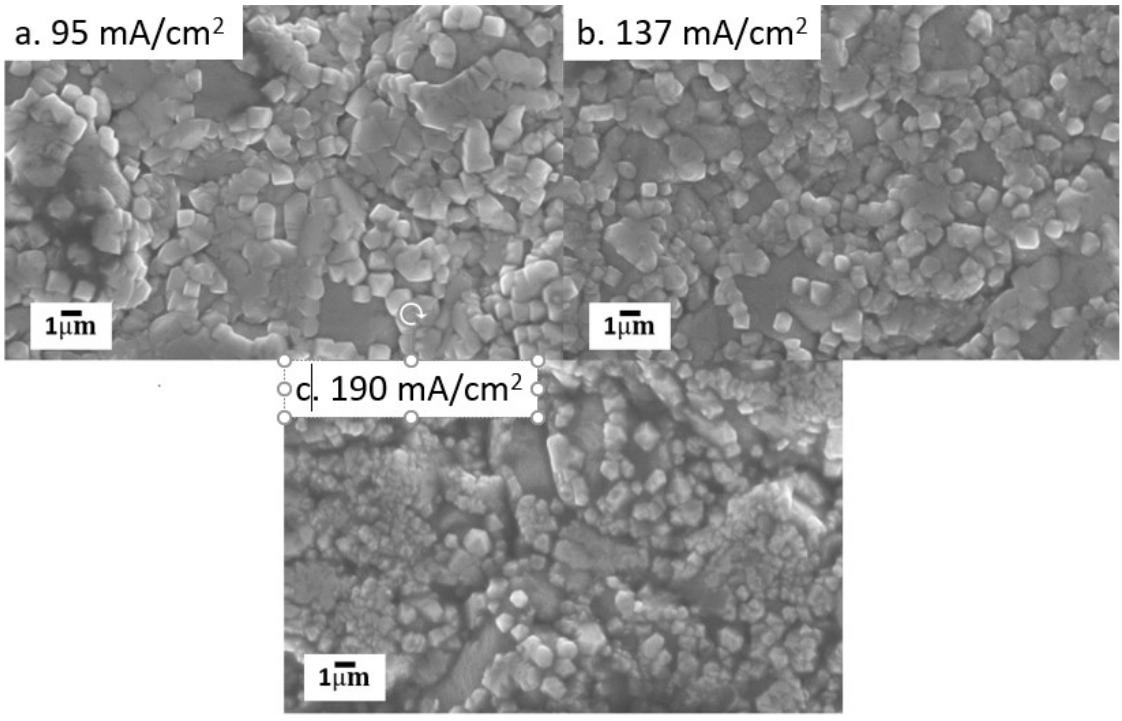

Fig. 6.16. SEM images of the Cu surface electroplated under different current densities.

Electrolyte temperature is an important factor for this process. Fig. 6.15 shows the surface morphology of three samples plated at different temperatures (20, 40, 60 ˚C). All three samples

are completely covered by Cu. In the 20 ˚C sample, the plated Cu showed a rough surface (R_a=11.3 μm) filled with spherical clusters. The surface is smoother with increasing electrolyte temperature because the higher temperature results in lower electrolyte viscosity and higher ion diffusivity. The 60 ˚C sample has the best surface ($R_a \leq 2.0$ μm), but the fast evaporation of solvent in the high-temperature bath might affect the electrolyte consistency in a long run. Therefore, 40 ˚C is chosen as the standard condition for the deposition runs, which provides a relatively smooth surface (R_a=3.5 μm) and the electrolyte is stable for long run.

Fig. 6.16 shows the surface of the samples plated with 20μm of Cu at three different current densities (95, 137, 190 mA/cm^2). The tape speed is adjusted accordingly to obtain the same plating thickness. All of the three samples show some granular smooth surface (R_a=2.8, 3.4 and 4.2 μm). It is also noticed that a higher current density results in more Cu clusters which stand out on the smooth Cu surface. This is the result of Cu^{2+} ion diffusion rate not being able keep up with deposition and consequently, the electrolyte close to the tape surface is depleted. Further increasing current density might result in a dendritic structure[200]. All three samples show no degradation in performance and no sign of galvanic corrosion is observed on the Cu surface. So, all three conditions are acceptable considering the required plating quality. Judging from processing speed and productivity, a higher current density is preferred. However, current over 16 A (190 mA/cm^2) might result in intensive Joule heat on the tape and electric sparks on the brush contacts, which might damage the tape during the plating process.

6.2.4 Interfacial bonding enhancement

It is noticed that the bonding between the selectively electroplated Cu stabilizer and the underlying Ag overlayer might be the weak link in the multifilament layer-by-layer architecture. Delamination of Cu layer has been observed during tape cutting, soldering and coil winding. It is anticipated that a weak bonding might lead to delamination by Lorenz force in high-field

applications of magnets, motors and generators. Two effective approaches are demonstrated to enhance the interfacial bonding to improve the delamination strength of 2G-HTS.

6.2.4.1 Effect of pH value of electrolyte.

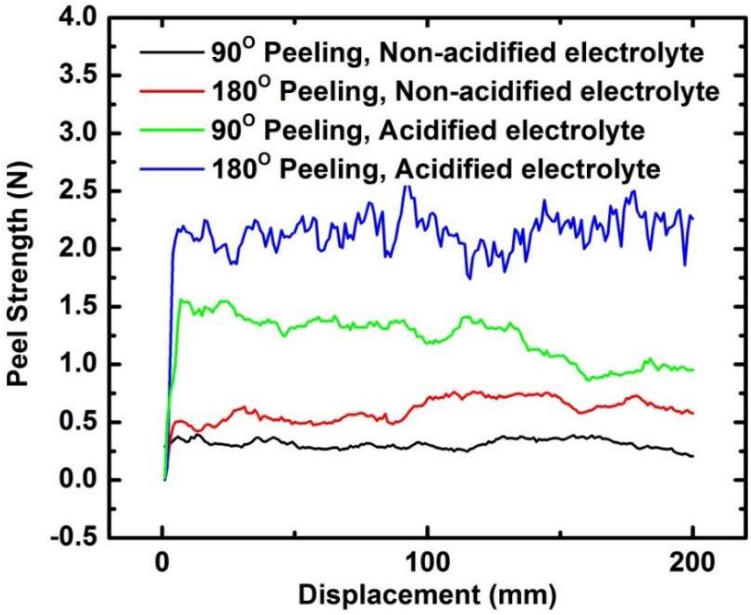

Fig. 6.17. Peel test in 90° and 180° peeling modes to investigate the bonding between Cu stabilizer and Ag overlayer of 2G-HTS tapes plated with Cu in different pH baths.

The pH value of the electrolyte is a crucial factor in the electrodeposition processes. This section shows the effects of electrolyte pH on the bonding strength between Cu stabilizer and Ag overlayer on the multifilament 2G-HTS tape. The basic approach is to acidify $CuSO_4$ electrolyte with 5×10^{-4} M of H_2SO_4, reducing the pH value from 3.5 to 2.8. The qualities of the selectively-electroplated Cu layers in both non-acidified and acidified electrolytes are examined by peel test.

Fig. 6.17 shows the peel test results of the Cu electroplated 2G-HTS tapes made in both acidified and non-acidified baths. The bonding between the Cu stabilizer and Ag overlayer is

significantly improved by lowering the electrolyte pH. The peeling forces increase from an average of 0.3 N to 1.2 N in 90° peeling and 0.6 to 2.2 N in 180° peeling.

To understand the pH effects on the electrodeposition process, the electrochemical impedance spectroscopy(EIS) technique is employed to characterize the impedances of the Cu electroplating process. Fig. 6.18 shows the EIS spectra of the Cu electroplating processes carried out in non-acidified and acidified electrolytes. The left intercept of the depressed semicircle on the real impedance axis represents the electrolyte resistance. It is easy to see that the electrolyte area resistance is reduced from 26.3 to 15.8 Ω cm^2 by acidifying the electrolyte. In the case of constant current density, a higher electrolyte conductivity brings about a lower overpotential from ohmic resistances for Cu electroplating. Moreover, the span of the depressed semicircle of the EIS spectra, representing the polarization impedance of the charge transfer process, is also reduced from 6.6 to 3.7 $\Omega \cdot cm^2$ by the addition of H_2SO_4 into the electrolyte. This verifies that the Cu electroplating becomes more feasible by adding H_2SO_4 into the electrolyte.

Both smaller polarizations from ohmic and kinetic impedances result in finer microstructure of the Cu electrodeposition layer and better bonding of the Cu layer and the Ag overlayer on the 2G-HTS tape [116]. Both EIS spectra also indicate a spur at low frequencies, where diffusion impedance is dominant. A spur with a lower degree means that the electrodes are not smooth at the surface, not precisely parallel and not large enough in size [201]. Because both Cu electroplating experiments are conducted with an identical setup, the different degrees of the spurs are caused by the different surface morphology of the electrodes. The EIS spectra of the Cu electroplating in the non-acidified and the acidified electrolytes has spurs at 0˚ and 30˚, respectively. This suggests that the Cu coating formed in the acidified electrolyte is smoother, and benefits from smaller ohmic and kinetic impedances, as discussed above.

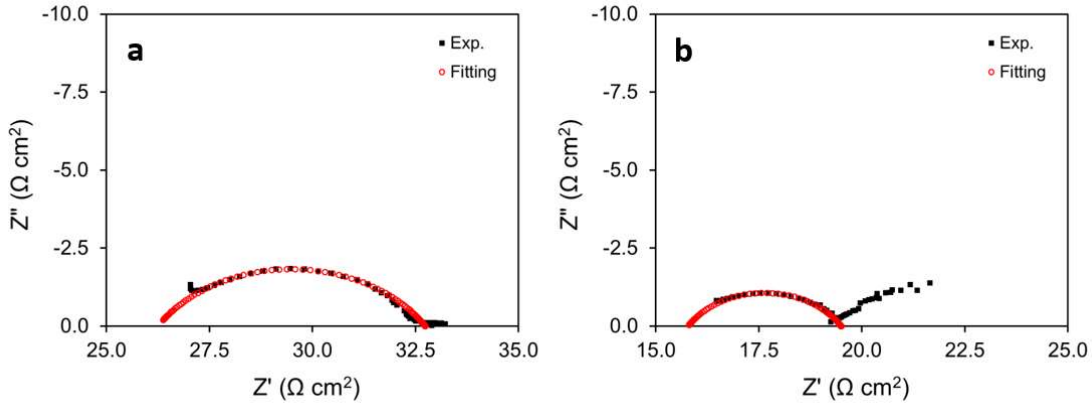

Fig. 6.18. Electrochemical Impedance Spectra of the Cu electroplaed on 2G-HTS tapes in non-acidified (a) and acidified electrolytes (b).

SEM is employed to characterize the morphology of the Cu electrodeposition layer and the peeled surface to verify the EIS results explained above. Fig. 6.19a and b show the SEM images of the plated Cu surfaces. Ag over layer is completely covered by Cu. The Cu layer electroplated in the non-acidified electrolyte (Fig. 6.19a) has a rougher surface than that made in the acidified electrolyte (Fig. 6.19b), which is supported by the difference in the degree of spurs in the previous EIS results. It is also obvious that the electrodeposited Cu particles made in the acidified electrolyte are significantly smaller, which is the result of the lowered overpotential of the Cu electroplating process due to the lower electrolyte and kinetic polarization resistances.

Fig. 6.19c and d show the peeled (90˚) surfaces of the tapes electroplated Cu in non-acidified and acidified electrolytes respectively. The peeled surface is on the Cu-Ag interface with Cu granular structure that is produced in the initial deposition. The strength of such interface determines bonding strength between the Cu and Ag layers. The Ag and Cu layers can be identified by the morphology because the sputtered Ag overlayer is relatively smooth with large, flat grains compared with the granular Cu. On the surface of the sample electroplated in the non-acidified electrolyte (Fig. 6.19c), Cu particles of about 0.7 μm size are found all over the surface. These particles are significantly larger than those (0.2 μm) on the surface of the sample that is

electroplated in the acidified electrolyte (Fig. 6.19d). Smaller particles have larger surfaces for bonding, leading to a higher bonding strength among the particles and the underlying layer. This might explain the higher peeling force of the sample made in the acidified electrolyte than that of the sample made in the non-acidified electrolyte, as shown in Fig. 6.17.

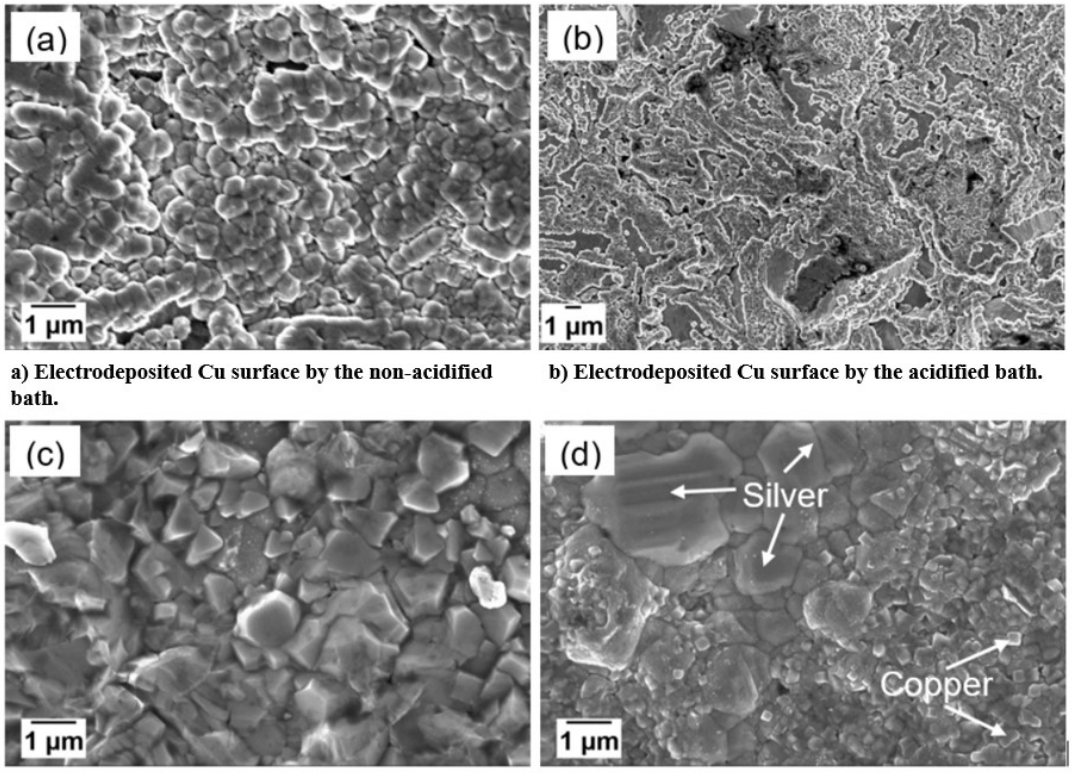

a) Electrodeposited Cu surface by the non-acidified bath.

b) Electrodeposited Cu surface by the acidified bath.

c) Sample surface after peeling the Cu obtained from non-acidified bath.

d) Sample surface after peeling the Cu obtained from acidified bath.

Fig. 6.19. SEM images of the surfaces of Cu layers electroplated in different electrolytes and the peeled surfaces after 90° peeling off the Cu stabilizer.

Although the results prove that acidifying the electrolyte enhances the bonding strength, further acidifying the electrolyte (pH<2.8) is not preferable because a lower pH is hazardous to the superconductor. It is known that REBCO is very vulnerable and the experiences of reaction below when it is exposed to acidic environment [122], as

$$YBa_2Cu_3O_7 + 14H^+ + \frac{1}{2}H_2O \rightarrow Y^{3+} + 2Ba^{2+} + 3Cu^{2+} + H^+ + 7H_2O + \frac{1}{4}O_2. \qquad 6\text{-}3$$

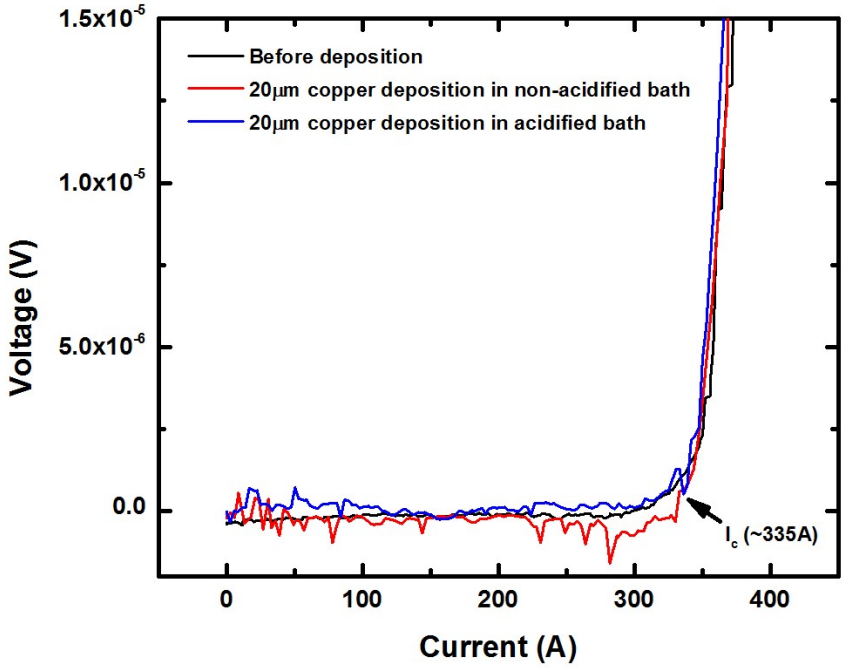

Fig. 6.20. I_c measurement at 77 K of the 12-filament 2G-HTS tapes before and after Cu electroplating in non-acidified and acidified electrolytes.

The multifilament tapes of 2G-HTS have the grooves where REBCO layers are exposed to the acidic electrolyte during the electrodeposition process. This exposure makes REBCO at a high risk of degradation due to the reaction with protons. To verify that no negative effects are brought to the 2G-HTS tapes during selective electroplating in acidified electrolyte, the I_c of the samples before and after electroplating in both acidified and non-acidified electrolytes are measured at 77 K (Fig. 6.20). All of the three samples exhibit almost identical I-V curves in four probe measurements with a I_c of 330 A. The results suggest that this Cu electroplating process is safe to the multifilament tapes of 2G-HTS in the aqueous electrolytes with pH>2.5. This is because the electroplated Cu quickly seals up the exposed REBCO surfaces and stop the damage. The counter interaction between the etching of REBCO and deposition of Cu has left us a certain window where we can perform good Cu deposition with minimal damage of the REBCO. Further acidifying of the electrolyte is hazardous to the tapes, as we found that the samples electroplated in an electrolyte with pH=2.1 show no superconductivity.

6.2.4.2 Plating cell modification

It is noticed that the initial seeding (morphology of the Cu particles) of the Cu deposition on the Ag layer is vital to the bonding strength between the Cu and Ag layers. With the design of the system used in this study, the electrolyte gushes out from the electroplating cell at the tape entrance (Fig. 6.21a). Thus, the initiation of electroplating actually takes place in this unstable region with heavy turbulent flow. It is reported that coarse granular structure is formed by heavy turbulence [202], and the deposition might be interrupted by high flow rate [203]. In correcting this particular problem, a pair of solution fences is added to the tape entrance to block the outflow of the electrolyte, while the tape can pass through freely (Fig. 6.21b and c).

To verify the impacts of the turbulent and jetting flows on the Cu deposition quality, especially in the initial stage of the electrodeposition, a long piece of 2G-HTS tape is electroplated for 5 s in the original electroplating cell without movement. The microstructures of the deposited Cu at the middle of the cell and that at the entrance region are inspected by SEM (Fig. 6.22). It can be seen that the Cu layer made in the middle of the cell is smooth and consists of fine-grained Cu particles. Even though the deposition time is only 5 s, the Ag overlayer is completely covered by Cu. However, in the tape entrance region, the electrodeposition shows larger Cu particles that formed on the Ag layer instead of covering the entire surface (Fig. 6.22b). These results are consistent with the reports in the literature [202, 203]. Therefore, in the regular electroplating process, large Cu particles are formed on the Ag surface before the tape moves into the electroplating cell. The coarsened seeds can result in smaller bonding strength between the Cu deposition layer and the Ag overlayer. The modification, as shown in Fig. 6.21b and c, can effectively stop the electrolyte from gushing out of the tape entrance.

a) original electroplating cell with outflow gushing out through the tape entrance

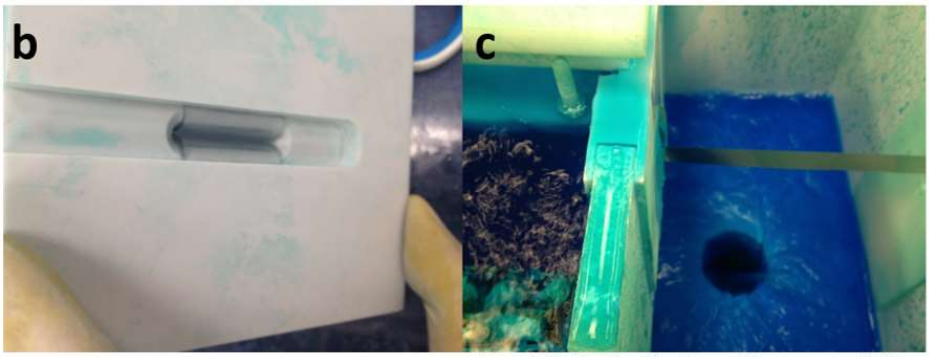

b) a solution fence built in the tape entrance

c) modified cell with the outflow successfully blocked

Fig. 6.21. Photographs of electrolyte flow at the tape entrance of the plating cell and modifications applied to it.

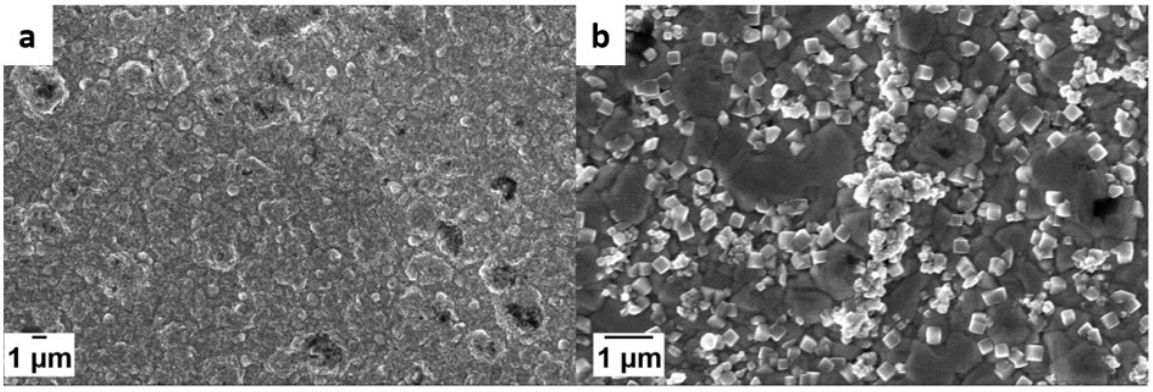

(a) Cu deposited in the middle of the cell

(b) Cu deposited at the entrance region.

Fig. 6.22. SEM images of the microstructure of the Cu layers after electrodeposition for 5 seconds.

Fig. 6.23 presents the test results in 90˚ and 180˚ peeling of the 2G-HTS tapes electroplated in original and modified cells with the same electroplating conditions. The electrolytes are acidified with pH=2.8. The peel strengths of the tapes electroplated in the modified cell are 2.7 N

in 90˚ peeling and more than 3.0 N in 180˚ peeling, which are significantly larger than that (1.2 N in 90˚ peeling and 2.2 N in 180˚ peeling) of the tapes electroplated in the original cell. During the peel tests, we noticed that the majority of delamination initiates and develops in the REBCO layer of the samples electroplated in the modified cell. This result indicates that the bonding strength between the Cu layer and Ag overlayer exceeds the force needed to break the REBCO layer from the underlying buffer layer. The Cu-Ag bonding is no longer the weak link in the multilayer architecture of the 2G-HTS tapes, and thus delamination is unlikely at the Cu-Ag interface during the applications.

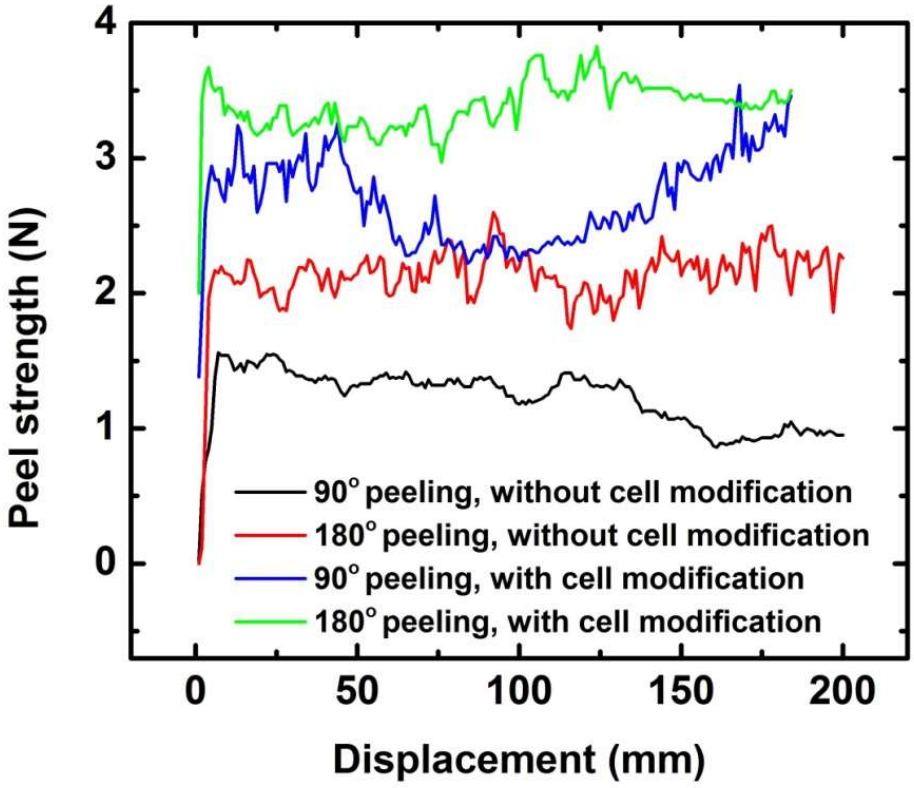

Fig. 6.23. 90° and 180° peel test results of the 2G-HTS tapes electroplated in original and modified cells with the same electroplating conditions.

6.3 Selective electrodeposition

6.3.1 Selective electrodeposition Ag overlayer on inkjet-printed tapes

Selective Ag deposition is achieved on inkjet-printed multifilament tapes of 2G-HTS which was shown and discussed in Chapter 4. The electrodeposition conditions are discussed in this section.

6.3.1.1 Growth of Ag islands and electric coupling between filaments.

Even though the large resistivity difference between the insulator lines and the REBCO filaments has successfully biased the electrolyte potential distribution and ion flux, there are still certain amounts of the deposition on the printed lines. The deposited Ag on the lines are in the form of small isolating Ag islands.

Fig. 6.24 shows the micrographs of tapes with different Ag electrodeposition times after printed BTO lines and MOCVD REBCO filaments. As discussed in section 6.1.1, the amount of Ag deposition increases with the deposition time. The Ag deposition on the inkjet-printed lines follows the similar pattern. With the deposition current density of 15 mA/cm^2, only a small amount of Ag islands is found after 10 min of deposition (Fig. 6.24a), but as the deposition time increases, the amount of Ag deposited on the line increases drastically. After 15min of deposition (Fig. 6.24b), a large number of Ag islands are found. The Ag islands merge with each other, potentially creating a conductive current pass between the filaments and result in electric coupling loss. On further increase of the deposition time, the Ag islands merge into a continuous film after 30 min of deposition (Fig. 6.24c). As the result, a balance point in electrodeposition parameters, by which the Ag deposition is capable to cover REBCO filaments without electric coupling across the BTO lines.

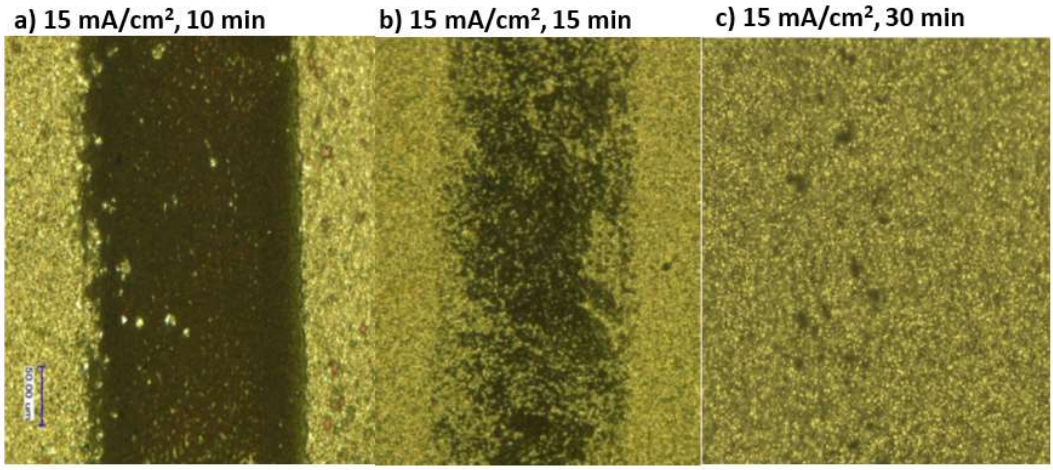

Fig. 6.24. Micrographs of tapes with different Ag electrodeposition times after printed BTO lines and MOCVD REBCO filaments.

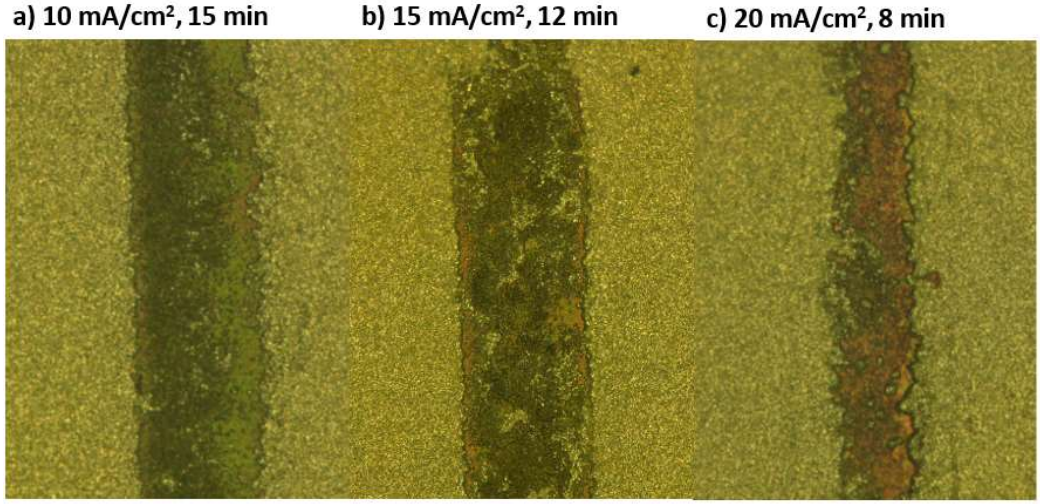

Fig. 6.25. Micrographs of tape with different deposition current densities after printed BTO lines and MOCVD REBCO filaments.

Fig. 6.25 shows two samples deposited at different deposition current densities; the deposition time is adjusted accordingly to make sure the REBCO filaments are completely covered with Ag. Ag islands are small in the 10 mA/cm^2 sample. As the deposition current density increases, the island size increases. It is also noticed that in the 20 mA/cm^2 sample, Ag deposition on the REBCO filaments start to grow toward the middle of the filaments. As a result, lower deposition current is more preferable.

6.3.1.2 Selective electrodeposition on the multifilament sample

In order to obtain good uniformity of Ag coating on each filament, the deposition current needs to be evenly distributed. Fig. 6.26a shows a 12-filament 2G-HTS tape after printed BTO lines and Ag electrodeposition. A significant Ag density difference is noticed between the filaments in the middle and both sides. Fig. 6.26b is microscopic image on the fourth line, showing that a dense Ag layer is deposited on the fifth filament while the fourth filament has only a few Ag islands on top. The uneven deposition is caused by the uneven potential distribution along the sample. The cathode contact is made on the top of the sample in the beaker-size electrodeposition cell. Even though the 2G-HTS tape is conductive to serve as the cathode by itself, the intrinsic high resistance of Hastelloy results in a strong voltage drop in the sample, in both transverse and longitudinal directions. In the filamentized sample with the highly insulating BTO lines, the voltage drop has become more significant, which leads to an uneven coating between the filaments.

A sample holder was made to solve this issue (Fig. 6.27). A piece of underlying Ag tape is applied between the glass shield and the sample. The Ag tape is in contact with the back of the 2G-HTS which significantly improves the conductivity of the cathode, so the electrolyte potential can be evenly distributed between the filaments. A glass shield is applied on the holder, covering the back of the silver tape from being deposited on and partially blocking the electrolyte contact on the tape edges (similar to the Teflon shielding in section 6.2.2). Uniform and dense Ag layer is deposited on each filament (Fig. 6.26c). The thickness of the Ag layer on each filament is shown in Fig. 6.28.

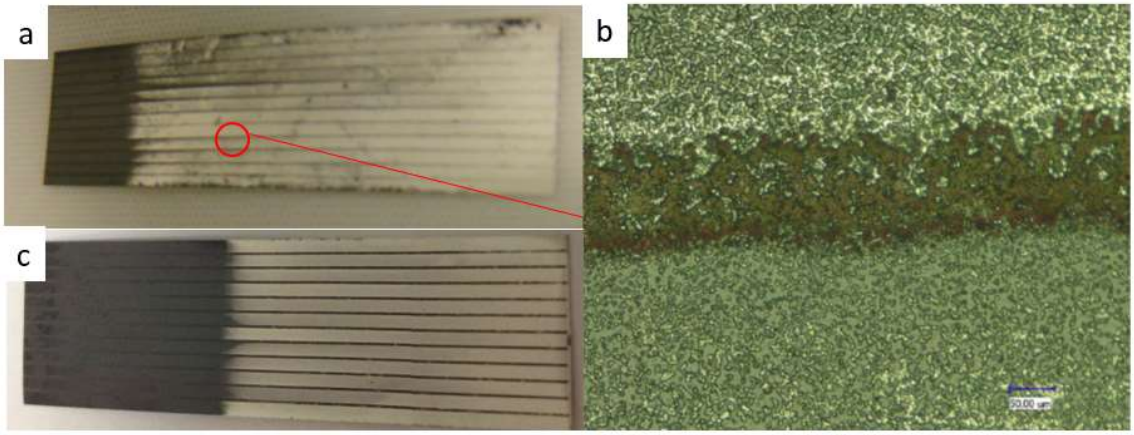

a) Electrodeposited Ag on inkjet-printed tapes without the sample holder
b) Optical microscopic image revealing the uneven deposition
c) Uniform Ag deposition on inkjet-printed tapes with the sample holder

Fig. 6.26. Optical photos of Ag deposition on the multifilament tape with and without the cathode sample holder after printed BTO lines and MOCVD REBCO filaments.

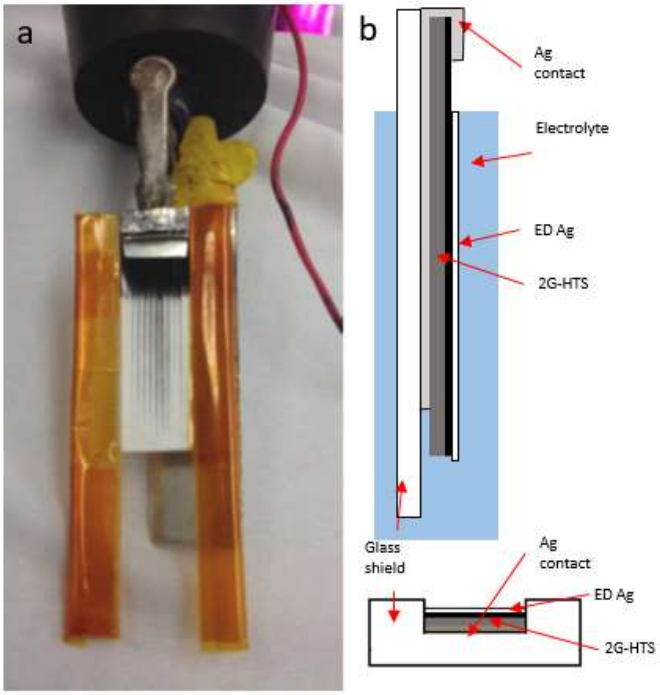

a) Cathodic sample holder for Ag electrodeposition on inkjet-printed 2G-HTS
b) Lateral view and plan view schematic of the sample holder.

Fig. 6.27. Cathode sample holder for Ag deposition on the multifilament tape.

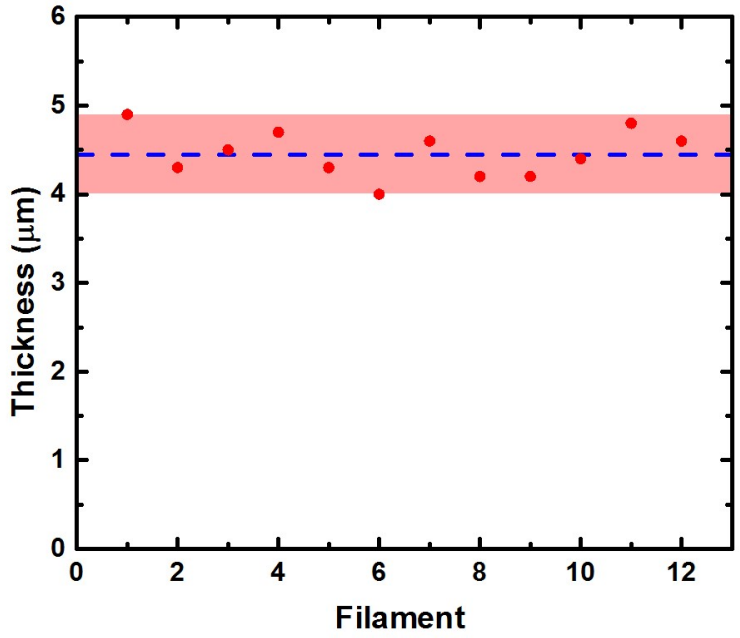

Fig. 6.28. Thickness of electrodeposited Ag on BTO inkjet-printed multifilamentary 2G-HTS.

For reel-to-reel process, however, the cathode connection is applied from both sides of the tape by rollers, and the tape keeps moving through a Teflon shield. Uniform coating is achieved both transversely and longitudinally on the 12-filament sample.

6.3.2 Selective electroplating Cu on the laser-striated samples

Selective electroplating Cu on the laser-striated tape can be achieved if the resistance on the grooves in much higher that of the superconducting filaments, just as the highly insulating inkjet-printed BTO barrier in section 4.1.3 enables the selective deposition of Ag. The groove surface of laser-striated Hastelloy tape is oxidized to become insulating. The oxide layer on the grooves will insulate the deposition current, and so the groove surface will remain Cu free. The selective Cu plating would keep the neighboring filaments insulated from each other and prevent the coupling loss [204, 205].

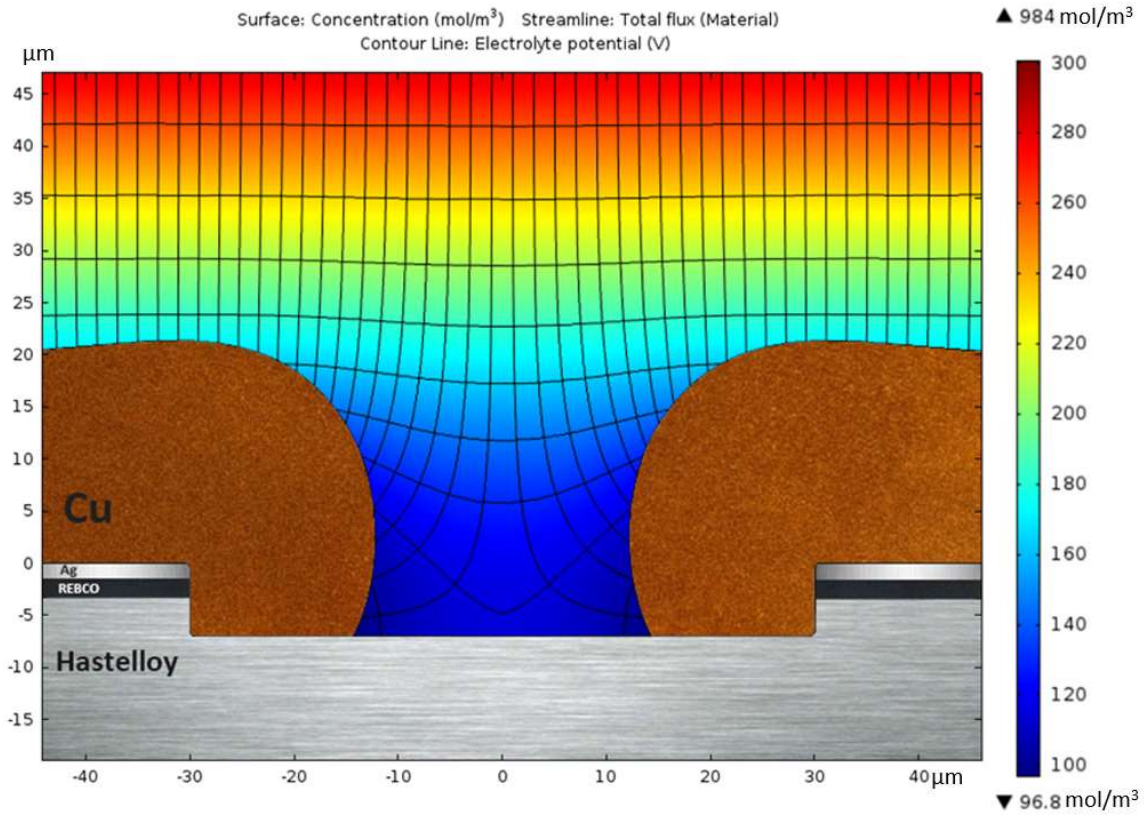

Fig. 6.29. Modeling of the selective electroplating on groove based on Nernst-Planck equation.

A numerical model based on Nernst-Planck equation is employed to study the selective deposition on the grooves. In this model, the superconducting filaments are separated by a groove with 60 µm width and 7 µm depth. It is assumed that the Hastelloy surface is covered by an insulating oxide. The electrolyte has a pH of 4, a Cu concentration of 5×10^{-4} M, and an ion diffusivity of 2×10^{-9} m^2/s. The plating temperature is 40 ˚C. It is assumed that the reaction has perfect cathode current efficiency.

Fig. 6.29 shows the electrolyte concentration, electrolyte potential and ion flux around a groove. The Cu^{2+} ion concentration is shown by the color surface, the electrolyte potential is shown by the contour lines, and the ion flux is represented by the streamline. Cu deposition layer is also shown on the image. The insulating oxide on the groove surface results in no flow of deposition current. Both the electrolyte potential and ion flux are biased toward the Ag-

coated surface of superconducting filaments. The model shows that the deposited Cu tends to grow from both sides of the groove and closes up the gap, which also depletes the Cu^{2+} ions in the electrolyte inside the groove. No Cu is directly deposited on the groove surface.

6.3.2.1 Oxidation of the exposed Hastelloy on the grooves

The oxidation of the exposed Hastelloy is developed by former graduate student from our group, I. Kesgin [12, 13, 154, 206]. The key of selectively depositing Cu is to oxidize the exposed Hastelloy of the laser-striated grooves. The oxidation is accomplished by annealing the sample at 550 ˚C for 2 h in oxygen (Fig. 6.30) [12].

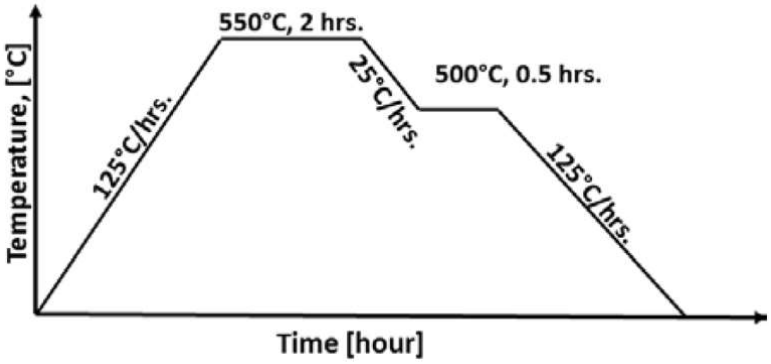

Fig. 6.30. Oxidation process on the laser-striated grooves of Hastelloy for insulation.

After the oxidation, FIB/SEM is employed to investigate the cross section of the oxide layer on the groove (Fig. 6.31) [12]. A layer of Pt is deposited before the FIB cross-section milling to protect the oxide layer. Comparing the groove cross section before (Fig. 6.31a) and after (Fig. 6.31b) oxidation, the oxide layer on the groove can be identified. Fig. 6.31c is the higher magnification image of the cross section. It shows the oxide layer between the Hastelloy and deposited Pt.

With the oxide formed on the Hastelloy surface, selective electrodeposition is successfully conducted on the laser-striated samples.

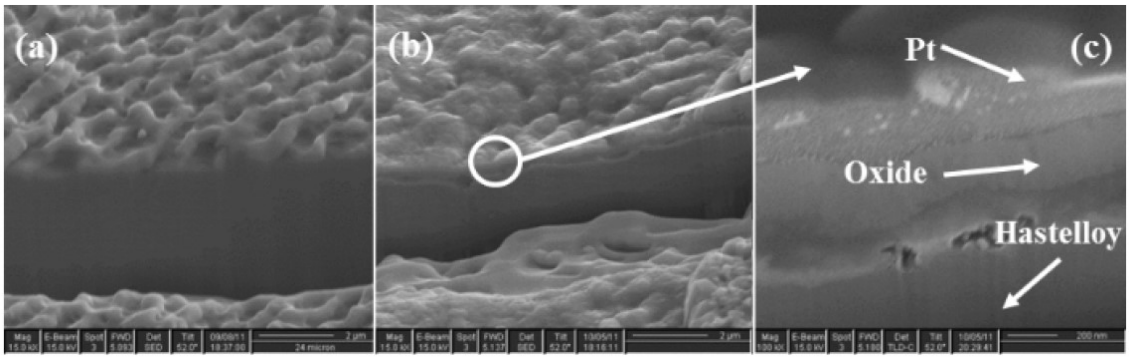

Fig. 6.31. FIB/SEM images of the laser ablation groove before and after oxidation.

6.3.2.2 Selective electroplating of Cu stabilizers

With the groove surface oxidized, selective electroplating can be conducted on the laser-striated samples.

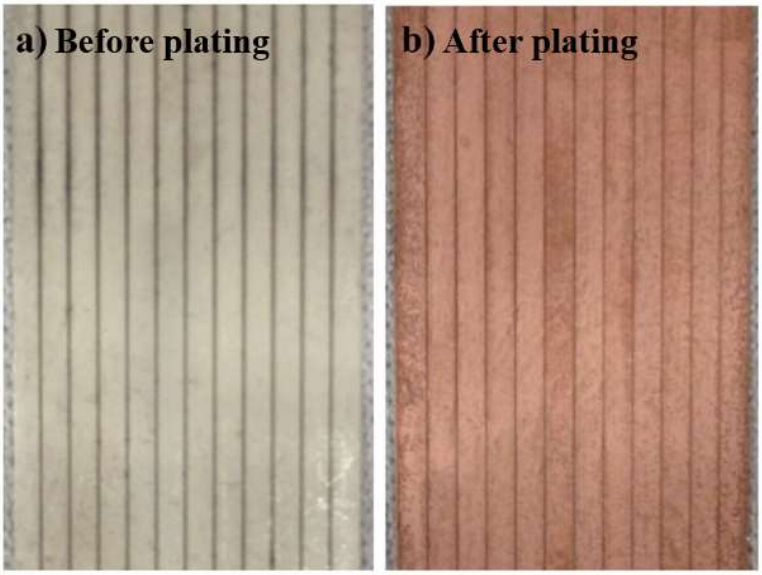

Fig. 6.32. Photos of 12-filament 2G-HTS sample before and after Cu electroplating.

Fig. 6.32 shows photographs of a 12-filament 2G-HTS before and after reel-to-reel selective electroplating. The 2G-HTS tape with 12 mm width is striated into 12 filaments with 0.93 mm

width. After electroplating, all filaments have been uniformly coated with 15 μm of Cu, and the laser-striated tracks are clearly visible. The continuous reel-to-reel deposition has enabled us to selectively plate Cu on a 12-filament 2G-HTS tape over 30 m in length (Fig. 6.33). A consistent coating is achieved along the length of the tape.

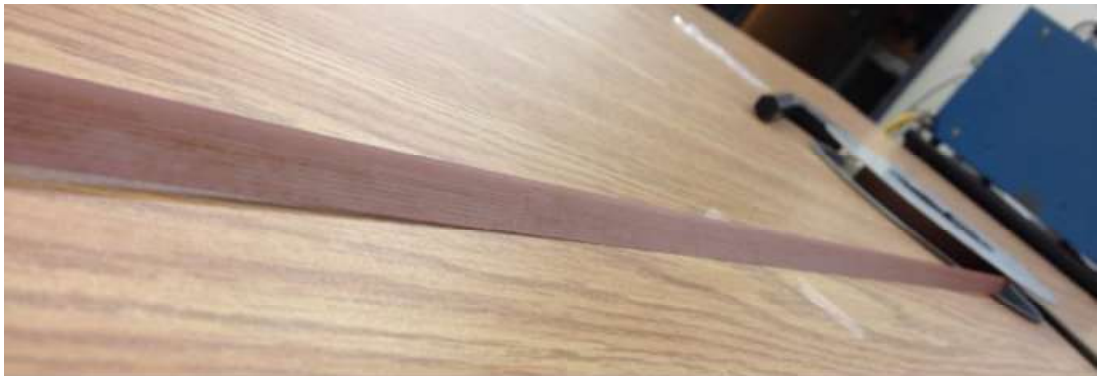

Fig. 6.33. Photo of 12-filament 2G-HTS tape with 30m length after reel-to-reel Cu electroplating.

It is critical to electrically decouple the filaments from each other. The electrical coupling between them can result in AC loss even higher than that of non-striated tape. Optical microscopy is employed to inspect the grooves after electroplating (Fig. 6.34). A cliff-like boundary is formed between the electroplated filament surface and non-plated grooves. Comparing the groove surface before and after Cu plating, it is noticed that the Cu starts to grow from both sides of the groove toward the center. For 15 μm of Cu plated on top, the width of insulating gap is reduced to 46 μm from the initial 72 μm (Fig. 6.34b). When the thickness of the plated Cu is greater than 30 μm, the Cu coatings on adjacent filaments merge with each other and completely couple the filaments (Fig. 6.34d). Sometimes, small Cu islands can be observed in the middle of the groove (Fig. 6.34c), which might increase the risk of bridging the neighboring filaments.

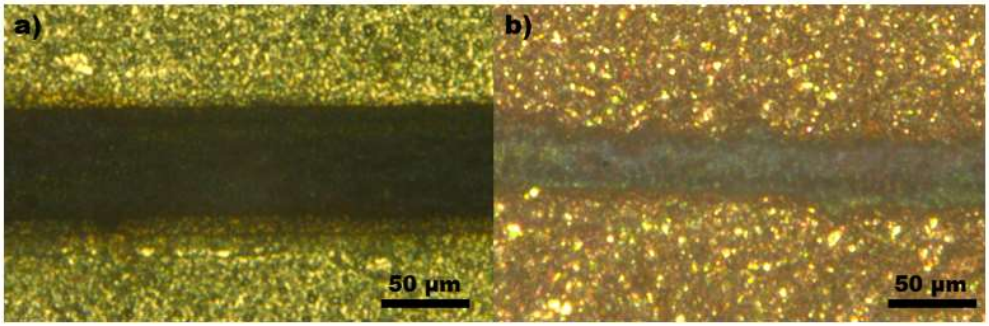

a) Laser-ablated groove before electroplating.

b) 15µm of Cu selective deposited over the sample.

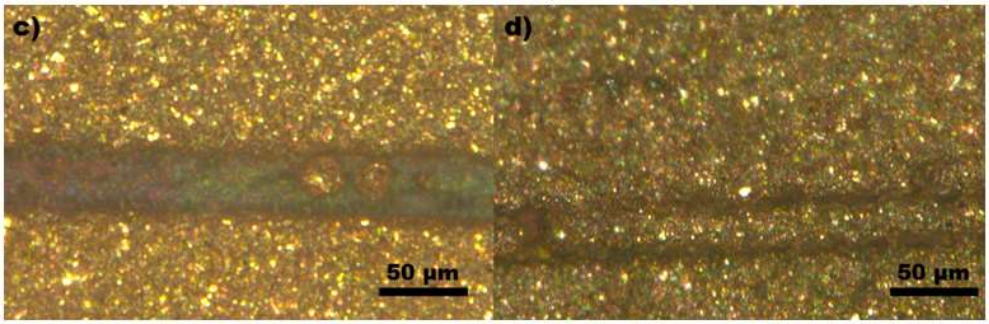

c) Small Cu islands deposited on the middle of the grooves.

d) Over 30µm of Cu deposition will completely close up the groove.

Fig. 6.34. Optical microscopy of the laser-striated samples with different thicknesses of plated Cu layer.

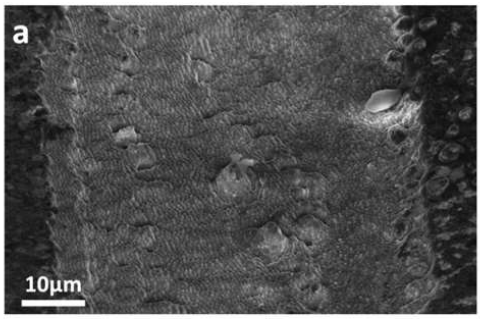

a) Laser-striated lines before electroplating Cu.

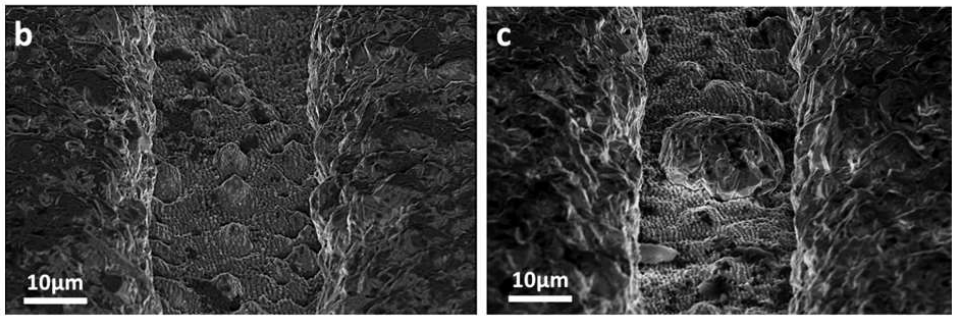

b) Laser-striated lines after electroplating Cu.

c) Small copper islands are found in the middle of the grooves

Fig. 6.35. SEM images of laser striated tapes after selectively-electroplated Cu on top.

SEM microstructures of the grooves are shown in Fig. 6.35. A dense and insulating oxide surface on the groove is seen to effectively prevent the deposition of Cu (Fig. 6.35a, b). Some Cu islands are observed in the middle of the grooves (Fig. 6.35c). The Cu islands nucleates from the molten pits created by the laser ablation. EDX is employed to investigate the groove surface and the seeding site after the Cu island is removed (Table 6.1).

Table 6.1. EDX ananlysis on groove and seeding site after Cu island removed.

Element	Ni	Cr	Mo
Hastelloy	55.6%	15.8%	15.6%
Regular groove surface	57.0%	17.4%	10.8%
Eutectic molten pit	49.9%	20.6%	22.7%

According to the Ni-Cr-Mo liquidus projection of Hastelloy (Fig. 6.36) [207], the eutectic phase of Hastelloy consists of a higher concentration of molybdenum. The eutectic phase is very likely formed inside the molten pits after the Hastelloy surface is partially melted during the ablation process. It is known that molybdenum oxide shows metallic conductivity due to its distorted octahedral structure [208]. A low resistivity on the molybdenum-rich site results in Cu deposition on top.

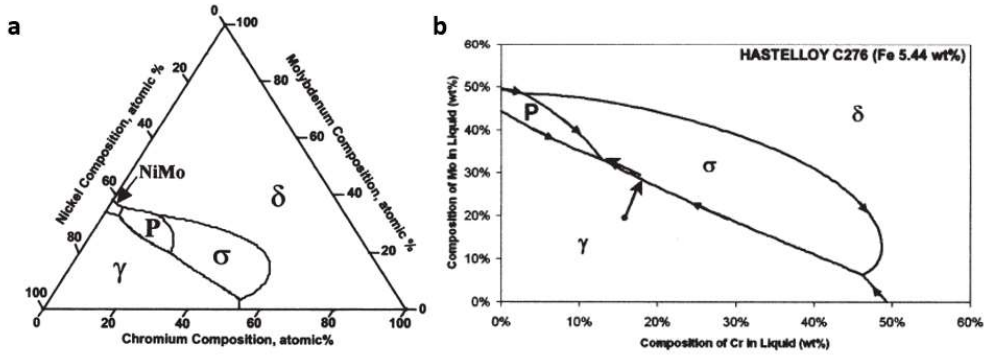

(a) Ternary liquidus projection of Ni-Cr-Mo system

(b) Calculated Ni-Cr-Mo pseudo-ternary liquidus surfaces of Hastelloy C276

Fig. 6.36. Ternary liquidus projection of Ni-Cr-Mo system and Hastelloy C-276.

6.3.2.3 Infield transport critical current

The initial 2G-HTS tape before laser-ablation and electroplating has a critical current (I_c) of 420 A at 77 K. The tape that is striated into 12-filaments and plated with 25 μm of Cu exhibited an I_c= 378 A, which corresponds to a reduction in critical current of 10.0%. The average groove width is 72 μm, so 6.6% of the volume of REBCO is removed by laser scribing the 11 grooves, which explains the measured reduction in I_c.

Angular dependent I_c in a 1 T magnetic field is measured at 77 K (Fig. 6.37) and it was found that the striated and electroplated sample showed less than 6% reduction at all angles. The maximum reduction is observed when applied field H is perpendicular to the sample, where the I_c is reduced from the original 139 to 131 A (5.8% reduction) after striation and plating.

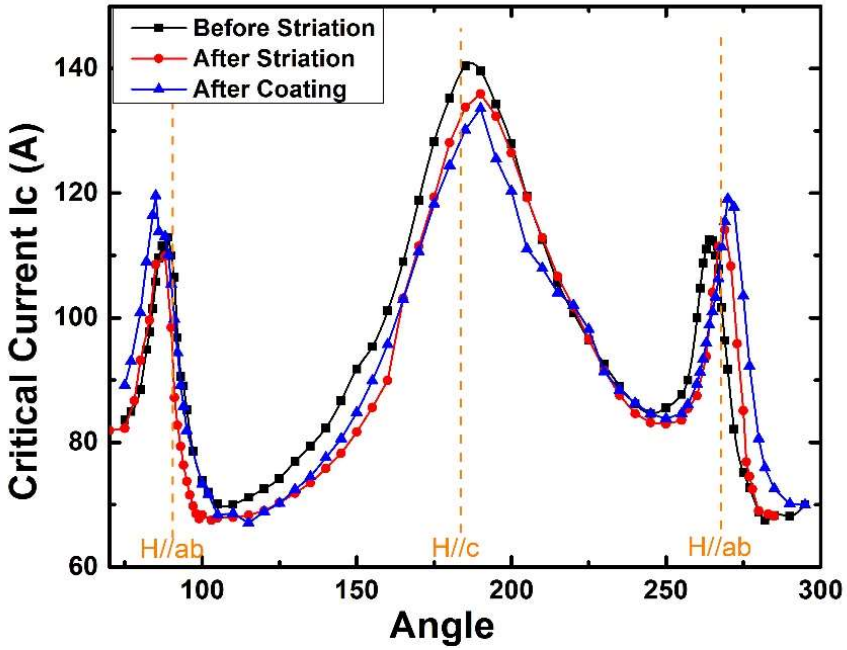

Fig. 6.37. Angular dependence vs. critical current measurement at 77 K and 1 T.

The critical current results show that the oxygenation and electroplating process has minimal impact on the tape's critical current. The extra reduction of I_c might be caused by the diffusion of elements from the Hastelloy into the REBCO film during the oxidation process,

possible degradation during the electroplating process, or simply the non-uniformity of the original REBCO layer.

6.3.2.4 AC loss

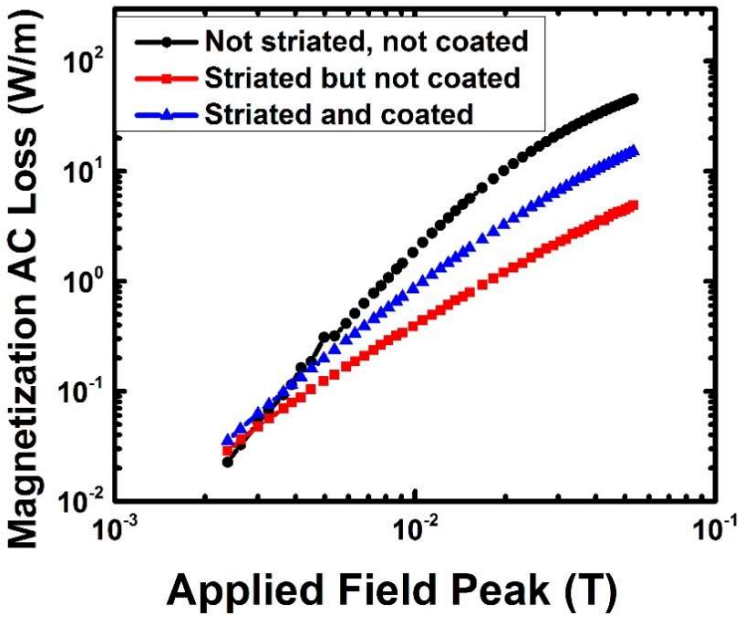

Fig. 6.38. Magnetization AC loss measurement at 100 Hz on the 12-filament tape with 25 μm thick Cu stabilizer.

Fig. 6.38 exhibits the results from magnetization AC loss measurement at 100 Hz on the 12-filament tape with 25 μm thickness Cu stabilizer, a normal tape without laser-striated and plating Cu, and a laser-striated tape without plating Cu. All three samples show AC losses increase with increasing the applied field; there is less difference at the lower field but a larger difference at the higher field.

The AC losses of the three samples follow the tendency of W (not striated, not coated)>W (striated, coated)>W (striated, not coated). The measured loss in the striated tape converges toward that of the non-striated tape in the low-field region, but the loss reduction keeps increasing with the applied field and becomes more significant in the high-field region. For

H_0=0.02 T, the magnetization AC losses are 13.4 W/m for the non-striated tape, 1.45 W/m for the striated tape, but 3.9 W/m for the coated Cu tape.

A 12-filament sample with 0.93 mm wide filaments is expected to show a13.9 times reduction of AC loss compared to the tape with 12 mm width and same J_c, based on Brandt-Indenbom model. The laser-striated sample without plated Cu shows more than 9.24 times reduction of AC loss in the higher field region (H_0>0.02 T). The extra loss might be caused by electric coupling between the filaments. The re-deposition of the evaporated or molten conductive material (Ag or Hastelloy) during laser ablation might create some low resistive pass for coupling current [33]. The laser-striated sample with plated Cu shows higher losses, more than 3.44 times reduction of AC loss in the higher field region (H_0>0.02 T), which indicates the strong electric coupling between the filament after plated Cu. The electroplated Cu has partially coupled the superconducting filaments. It is noticed that the two filaments on the edges of the tape are coupled through the Cu deposition on the back of tape.

Fig. 6.38 also reveals that in the low-field region, the measured loss in the striated tape converges toward that of the non-striated tape. Such a behavior is believed to be the result of non-uniform J_c distribution across the tape [209] and magnetic coupling in the striated tapes [210].

Chapter 7. Conclusions

In this dissertation, three different approaches are developed toward an etch-free, all solution fabrication and full stabilized multifilament 2G-HTS tape, including of inkjet printing BTO insulator lines, MOD YBCO for superconductor filaments, and selective electrodeposition of Ag overlayer/Cu stabilizer.

7.1 Inkjet printing BTO insulator lines

- An etch-free fabrication of multifilament of 2G-HTS is done with inkjet printing replacing the laser-striation process. Material selection and ink preparation, control of drop stream and line formation, multi-lines inkjet-printing insulator are studied. A 1 m-long 12-filament tape has been demonstrated to show the feasibility of reel-to-reel inkjet printing of insulator lines.
- Six ceramics are selected as sol-gel inks. Among the six ceramics, SnO_2 exhibits a high resistance at 77K, but room temperature resistance is not large enough to selectively electrodeposited Ag. Fe_2O_3 reacts with Cu to form a high resistance interface, but the influence area is too large to degrade REBCO properties. MgO's resistivity is not high enough for selective electrodeposition Ag without electric coupling. BZO exhibits good selective deposition of Ag, but resistance across the line is only 1.34 μΩ at 77 K. BTO resistance (89.2 mΩ) at 77 K is large enough to avoid the electric coupling and selective electrodeposition can be achieved, REBCO grows in a random-orientation on BTO and in an epitaxial orientation on buffer. Cu doping into BTO is tried to improve dielectric property, but there are some REBCO clusters on BCTO lines which can actually the benefit the growth of Ag islands. Therefore, BTO is only suitable for ink material for this work.

- The preferred viscosity window for inkjet printing is found to be 3-10 cSt. Viscosity of sol-gel inks can be modified with the solute concentration. MgO ink with a concentration of 0-2.0 M can cover the viscosity range of 0.5-8.3 cSt. Methanol or methanol/acetic acid mixture is used for diluting the inks.
- DEA is used as a surfactant and complex agent. The viscosities of MgO inks with added 0 to 2 ml DEA raised from 2.8 to 3.0 cSt. Addition of DEA brings significant improvement on the line morphology, fewer cracks, smooth surface and narrower line. Due to the supercooled nature of DEA, inks with too much DEA will be solidified after long time standing, and so only 2 ml DEA is used for MgO ink. For BTO and BZO inks, which have 5 ml DEA, are prepared before printing.
- Two buffers of CeO_2 and LMO used selected as the printing substrate. BTO ink has a better wettability on CeO_2 buffer, which benefits the liquid expansion on the tape surface, and results in wider printed lines in the same condition. However, the better wettability also prevents bubble formation and so BTO can printed on CeO_2 tape at a higher temperature. Wettability can be modified by pre-printing heat treatments,
- Two nozzles with 30 μm and 60 μm orifice are used in this work. The lines printed with 60 μm orifice are 210 μm wide and 400nm tall, and with 30 μm orifice, the lines are 170 μm wide and less than 100 nm tall. Due to the difficulties of adjusting parameters and nozzle cleaning with the 30 μm nozzle, 60 μm nozzles were chosen in this work.
- Control parameters of drop stream and line-formation are studied. For BTO inks, the drop streams are stably jetted with 0.2 psi feeding pressure and 28 V signal strength with 60μm nozzle; the straight lines are continuously printed on LMO buffer with

600 Hz jetting frequency, 0.5 m/min tape speed and 110 ˚C susceptor temperature. Bubbles form above 110 ˚C which result in round-shape cracks.

- 12-filament tapes are obtained by printing 11 parallel BTO insulator lines in longitudinal direction with 1mm equal interval on the 12 mm-wide buffer tape. Each line is about 0.17 mm wide and over 0.9 μm thick. Twelve 0.84 mm-wide superconducting REBCO/YBCO filaments were created after MOCVD/MOD.
- T_c of BTO printed 12-filament tape (92.4 K) is comparable to the reference (92.0 K), indicating that the REBCO deposited is unaffected by the printed lines. I_c of 12-filament tape is 72 A, which is 25% lower than that of the non-striated sample (96 A). The 17.5% conducting area occupied by the 11 BTO lines is major reason of I_c reduction. The extra loss comes from defects induced by the inkjet printing process and non-uniformity of the REBCO.
- The AC loss per cycle increases with increasing applied field. The calculations for non-striated or striated tape with Brandt-Indenbom model show AC loss decrease for more than one order of magnitude. The measured data from the 12-filament tape agrees well with the calculations for striated tape from Brandt-Indenbom model which shows 17.6 times lower loss than a 12 mm non-striated tape. The AC loss per cycle is independent of the frequency of the applied field, indicating the coupling loss between the filaments is negligible.

7.2 MOD YBCO superconductor filaments

- An all solution fabrication multifilament 2G-HTS tape has been demonstrated with TFA-MOD bottom-up process as the substitution of MOCVD top-down process. YBCO filaments have been successfully deposited by TFA-MOD on the buffer tapes.

Precursor preparation, spin and dip coating, calcination and crystallization have been studied, subsequent selective depositing Ag overlayer was achieved.

- The precursor concentrations were optimized. Barium-rich phases are found at Y:Ba:Cu=1:2:3, XRD peak intensity is significantly lowered by reducing Ba to Y:Ba:Cu=1:1.8:3, which leads to a better T_c of 87.9 K. A loss of 4-9% of Cu was found during the deposition which needs to be compensated in the precursor. The T_c increases by 0.9 K as Cu content increases from 1:1.8:3 to 1:1.8:3.3.
- Precursor concentration can be adjusted by dissolution. The higher the concentration, the higher the viscosity and thicker the deposition. By spin coating, a 246 nm thick of well-textured YBCO is obtained from a precursor of 1.0 M metallic ion concentration. The film thickness increased to 478 nm using 1.5 M solution. Up to 1138 nm thick films can be achieved with 3.0 M precursor but YBCO formation failed in such thick films. Small cracks were found on one corner of the 1.5 M sample and larger cracks on all of the 3 M sample, where cracks formed before the solution film solidified. Similar to spin coating, 671 nm-thick film is obtained with 1.5 M precursor and 278 nm film with 1.0 M precursor with dip coating. The precursor concentrations used in this work are 1.5 M for spin coating and 1.0 M for dip coating.
- LMO and CeO_2 buffers were used as substrates for MOD growth. With LMO buffer, YBCO growth is faster but T_c is only 84.7 K and long platelet-shape YBCO-211 second phases are found after heat treatment, which might be responsible to T_c degradation. For CeO_2 buffer, YBCO growth is slower but a higher T_c of 88 K was achieved.
- Water vapor was introduced to prevent Cu loss from sublimation in calcination and as a reactant in crystallization. TFA-MOD YBCO tapes were heat-treated under different

humidity conditions; no YBCO was found without water vapor and well-textured YBCO was achieved in above 2.3% humidity conditions. The diffraction peak intensity of YBCO increases with increasing humidity, but higher humidity leads to rough surfaces and large porosity. T_c of the samples prepared at 4.2% humidity shows the best result (T_c = 89.2 K).

- Calcination is conducted in moist oxygen, the gel film is dried and Metal TFA is decomposed into nanocrystalline CuO, amorphous Y-Ba-O-F and some organic residues. A smooth coating is obtained at very slow ramping (0.1 ˚C/min) from 200 ˚C to 260 ˚C in calcination, because the ramping rate (0.2 ˚C/min) results in severely cracking on all over the tape surface.
- As the crystallization temperature increases, the film porosity is progressively reduced and the grains are coarsened. A-axis grains are identified easily due to their needle-like shape. YBCO tends to form more a-axis grains at lower temperatures. The sample treated at 750 ˚C shows the best T_c of 89.8 K, followed 89.5 K T_c at 760 ˚C.
- As the crystallization time increases, the porosity is reduced. CuO and Ba-O-F second phase are weakened with longer crystallization time. The misoriented grains appear after 150 min, needle-shaped out-of-plane grains start to appear at 270 min and become large in numbers at 520 min. T_c of the sample treated at 750 ˚C for 150 min is 89.3 K.
- TFA-MOD was adopted on the inkjet-printed sample with dip coating. Dip coated solution films show automatic separation of filaments by the printed BTO lines due to the hydrophobic BTO surface. Selective deposition of YBCO is therefore achieved. Selectively-eletrodeposited Ag was obtained and clear borderline is oberved between the Ag-coated filaments and Ag-free lines. The T_c value of the inkjet-printed and dip coated tape is 89 K as same as that of spin-coated sample. The I_c value is 5 A in the

printed tape and 9 A in the reference tape. Other than a 17.5% conductive area loss from the inkjet-printed lines, the extra reduction of the I_c is caused by non-uniformity and defects in YBCO layer, which leads to reduction in transport current capacity of certain filaments.

7.3 Selective electrodeposition Ag overlayer and Cu stabilizer

- Selective DC electrodeposition for Ag overlayer and Cu stabilizer of 2G-HTS are demonstrated. Ag electrodeposition parameters, oxidation annealing and Ag island growth, as well Cu electroplating qualities, oxidation on groove and modeling of selective electroplating are studied.
- Both process has been scaled up by reel-to-reel fabrication, Ag electrodeposition has been demonstrated on a 100 m-long tape, and selective Cu electroplating is achieved on 30 m-long laser-striated 12-filament tape with sputter Ag surface.

7.3.1 Selective electrodeposition of Ag overlayer

- Selective electrodeposition of Ag is possible from the resistivity difference between BTO line and REBCO filament. As the current density and time are gradually increased, more and more Ag islands grow upon filaments and merge together to form a dense and uniform Ag overlayer. A dense Ag layer is obtained at the condition of 15 mA/cm^2 current density for 15min. The dendritic structures are found in Ag deposited by 25 mA/cm^2 current density, which are not preferable because of their incapability in covering entirely filaments.
- Annealing Ag coating at 500 ˚C for 30min in oxygen is very effective in improving the density, smoothness and interfacial bonding force, and to prevent REBCO from oxygen deficiency in high temperature. Average I_c of the bare 2G-HTS before Ag deposition is 566 A. After Ag deposition the I_c is reduced to 551 A, that is 2.65%

reduction. The loss can be recover by the annealing process, and the REBCO performance is remarkably enhanced to over 600 A.

- For more uniform distribution of deposition flux, a piece of underlying Ag contact is providing the conductive support to the resistive 2G-HTS tape to prevent the potential drop along the cathode. A shielding is applied to prevent the charging effect on the edges. Ag coating with 4.5±0.5 μm is achieved on each filament. Similar to the short samples, a higher average I_c (312 A) was obtained compared with the bare YBCO sample (285 A). But there are larger fluctuations in the measurement data and more I_c dropouts which usually determine the current capacity of the long tape.
- For inkjet-printed tape, a dense Ag coating is need on the REBCO filaments but minimal Ag deposition on the BTO lines. The conditions of 10 mA/cm^2 for 15 min is selected for smaller size and lower density of Ag islands on the BTO lines while REBCO filaments are completely covered. For multifilamentary tapes, deposition current needs to be evenly distributed between the filaments; a piece of Ag tape is loaded on the sample holder to improve the conductivity of 2G-HTS.

7.3.2 Selective electroplating of Cu stabilizer

- The cathode current efficiency is more than 99% for Cu plated in reel-to-reel system. Cu layer thickness is increased with increasing current density and deposited time, which is controlled from 5 to 30 μm. Good consistent deposition conditions in reel to reel electroplating system result in good longitudinal thickness uniformity of 19.5±0.5 μm in a 5 m long tape . However, the thickness differences are larger across the width. Guiding shields are mounted in plating cell to obstruct partially ion flux from the edges of tape by which the thickness differences are reduced within 1.0 μm for a 19.5 μm Cu layer.

- The coating smoothness is increased as increasing the electrolyte temperature which results in lower electrolyte viscosity and higher ion diffusivity. Three surface roughness (R_a=11.3, 3.5 and 2.0 μm) values were respectively obtained at different electrolyte temperatures of 20, 40 and 60 ˚C. The 40˚C electrolyte is chosen as a standard condition for stable long run of the electrolyte. Current density has less impact on the roughness. For a 20 μm Cu coating, current densities of 95, 137 and 190 mA/cm^2 result in roughness of 2.8, 3.4 and 4.2 μm, respectively. All samples show granular smooth surface, no degradation in performance and no sign of galvanic corrosion. Further increasing current density (over 190 mA/cm^2) might result in intensive Joule heat on tape and sparks on the electric brushes.
- A model on Nernst-Planck equation is developed to analyze the selective electroplating Cu. The process is successfully conducted after the oxide films on Hastelloy grooves are formed at 550 ˚C for 2 h in oxygen. All filaments are covered by uniform Cu layer. The Cu layer grows from the both sides of filament toward the center of groove and the gap width is reduced from initial 72 μm to 46 μm when Cu layer on top is 15 μm thick. Two adjacent filaments touch when the thickness is more than 30 μm. There are some small Cu islands in the middle of grooves, which might increase the risk of electrical coupling.
- The bonding force between Cu and Ag layers is significantly improved by acidifying electrolyte and blocking outflow at the tape entrance. Peeling forces are increased from 0.3 to 1.2 N in 90° peeling and 0.6 to 2.2 N in 180° peeling as the pH value is changed from 3.5 to 2.8. There are smaller Cu particles and smoother surface on the sample plated in acidified bath. The I_c reduction is not observed in samples plated with electrolyte pH>2.5, but no superconductivity is found in samples plated with electrolyte pH=2.1, which shows over-acidifying is hazardous. Modification on the tape entrance of the

plating cell by blocking the gushing flow results in a finer seeding and more homogeneous Cu layer, which improved the peeling force from 1.2 to 2.7 N in 90° peeling and 2.2 to 3.0 N in 180° peeling. The binding of Cu-Ag interface is no longer a weak link of the tape.

- The I_c at 77 K is 420A in the initial 2G-HTS tape before laser-striation, and 378 A in the laser-striated tape both before and after plating 25μm Cu. The I_c reduction is 10.0% in zero field and less than 6% at all angles in 1T magnetic field. The maximum reduction is 5.8% from the original 139 to 131A after striating and plating when the applied field H is perpendicular to the sample.
- AC losses increase with increasing the applied field. The measured loss in the striated tape converges toward that of the non-striated tape in the low-field, but the loss reduction keeps increasing with the applied field and becomes more significant in the high-field. For H_0=0.02 T, the magnetization AC losses are 13.4 W/m for the non-striated tape, and 1.45W/m for the striated tape, but 3.9 W/m for the striated and Cu coated tape. The theoretical reduction value of AC loss is 13.90 times based on Brandt-Indenbom model. The measured reduction values of AC loss in the higher field (H_0>0.02T) are more than 9.24 times in the laser-striated tape without plated Cu, and more than 3.44 times in the laser-striated tape with plated Cu. The lower AC loss reduction value in the striated and coated tape might be due to electric coupling between filaments.

7.4 Future works

The ultimate goal of this project is to develop an etch-free reel-to-reel solution fabrication process for multifilament 2G-HTS, fabricate a long tape and wind it into coils to study its potential in application.

The low I_c is the major drawback of the inkjet-printing multifilamentary process. Precision printing of narrower and thicker lines is crucial to achieve higher I_c in the inkjet-printed samples. Narrowing down the width of each lines not only result in reduction of area loss, but also enables us of printing more lines on the buffer, which leads to further reduction in AC loss. Meanwhile, in this thesis, the thickness of the MOCVD REBCO layer is limited by the thickness of the printed lines. With better control on the feeding pressure, increasing the ink viscosity and using smaller nozzles can potentially achieve higher printing precision.

To guarantee the uniformity of the printed line, multifilament tapes in this work are printed with a single nozzle. Simultaneously printing all the lines with multiple nozzle is essential for long tape reel-to-reel fabrication.

For the inkjet printing/MOD process, improvements on J_c of the MOD YBCO is required for actual application multi filamentary tapes. Improving the precursor purity is the key for better YBCO deposition. Uniformity of the YBCO film is another important factor, this can be addressed by using other solution coating techniques like slot-die coating, blade coating or inkjet printing.

The technique of selective electrodeposition of Ag overlayer and Cu stabilizer is relatively sophisticate. Deposition on long tape has been already demonstrated in this thesis. However, electrical coupling trough the electrodeposited layer needs to be minimized. Controlling the uniformity of the inkjet-printed lines/laser-striated grooves to suppress the Ag/Cu island formation is the key.

Other than the regular Cu stabilization demonstrated in this thesis, the requirement on stabilization varies with different application. Material and geometry of the stabilizer layer should be tailored accordingly. For example, superconducting fault current limiter (FCL) is

using the magnetic quench effect to limit the fault current. Cu-Ni alloy is more suitable for such application as resistive stabilizer layer is needed.

A laser-striated and Cu stabilized long tapes have been winded into a coil to demonstrate the viability of the multifilament structure in real applications. Fig. 7.1 shows a superconducting racetrack coil winded with Cu-stabilized 12-filament 2G-HTS tape. AC loss of the coil will be tested in the near future.

Fig. 7.1. Photo of a superconducting racetrack coil winded with 12-filament Cu-stabilized 2G-HTS tape.

In a larger scheme, solution fabrication can reduce the manufacture price of the 2G-HTS by a great margin. In this thesis, solution fabrication of the superconductor and stabilizer layer has been demonstrated. Multiple researches on fabricating the textured buffer layer by solution methods has been conducted across the world [73, 74, 76, 104, 105]. Integrating the solution fabrication processes in to a complete procedure can substantially push 2G-HTS towards real-world applications.

References

[1] *Configuration of SuperPower® 2G HTS Wire* http://www.superpower-inc.com/content/2g-hts-wire.

[2] C. C. Clickner, J. W. Ekin, N. Cheggour, C. L. H. Thieme, Y. Qiao, Y. Y. Xie, and A. Goyal, "Mechanical Properties of Pure Ni and Ni-Alloy Substrate Materials for Y-Ba-Cu-O Coated Superconductors," *Cryogenics,* vol. 46, pp. 432-438, Jun 2006.

[3] V. Selvamanickam, G. B. Galinski, G. Carota, J. DeFrank, C. Trautwein, P. Haldar, U. Balachandran, M. Chudzik, J. Y. Coulter, P. N. Arendt, J. R. Groves, R. F. DePaula, B. E. Newnam, and D. E. Peterson, "High-Current Y-Ba-Cu-O Superconducting Films by Metal Organic Chemical Vapor Deposition on Flexible Metal Substrates," *Physica C: Superconductivity and its Applications,* vol. 333, pp. 155-162, May 2000.

[4] M. N. Wilson, *Superconducting Magnets*, Oxford University Press, 1983.

[5] C. B. Cobb, P. N. Barnes, T. J. Haugan, J. Tolliver, E. Lee, M. Sumption, E. Collings, and C. E. Oberly, "Hysteretic Loss Reduction in Striated YBCO," *Physica C-Superconductivity and Its Applications,* vol. 382, pp. 52-56, Oct 2002.

[6] F. Gomory, M. Vojenciak, E. Pardo, M. Solovyov, and J. Souc, "AC losses in Coated Conductors," *Superconductor Science and Technology,* vol. 23, p. 9, Mar 2010.

[7] E. H. Brandt and M. Indenbom, "Type-II-Superconductor Strip with Current in a Perpendicular Magnetic Field," *Physical Review B,* vol. 48, pp. 12893-12906, 1993.

[8] M. P. Oomen, "AC Loss in Superconducting Taped and Cables," Doctor of philosophy in applied physics, University of Twente, 2000.

[9] K. V. Namjoshi and P. P. Biringer, "Low-Frequency Eddy-Current Loss Estimation in Long Conductors by Using the Moment of Inertia of Cross-Sections," *IEEE Transactions on Magnetics,* vol. 24, pp. 2181-2185, Sep 1988.

[10] W. J. Carr, "Loss in a Striated Coated Conductor," *Superconductor Science and Technology,* vol. 20, pp. 168-175, Mar 2007.

[11] N. Amemiya, N. Takamasa, J. Zhenan, and Y. Kenji, "Influence of Film Width and Magnetic Field Orientation on AC Loss in YBCO Thin Film," *Superconductor Science and Technology,* vol. 17, p. 485, 2004.

[12] I. Kesgin, G. Majkic, and V. Selvamanickam, "Effect of Selectively Electrodeposited Stabilizer Thickness on AC Loss Behavior of Fully-Filamentized HTS Wire," *IEEE Transactions on Applied Superconductivity,* vol. 23, p. 5, Jun 2013.

[13] I. Kesgin, G. Majkic, and V. Selvamanickam, "Fully Filamentized HTS Coated Conductor via Striation and Selective Electroplating," *Physica C: Superconductivity and its Applications,* vol. 486, pp. 43-50, 2013.

[14] S. Takacs, "Coupling Losses in Flat Cables and Coated Conductors," *Superconductor Science and Technology,* vol. 19, pp. 738-741, Aug 2006.

[15] S. Y. Shin, J. H. Lee, and H. W. Park, "Mechanical and Electrical Properties of In-Bi Solder at Bi-2212 Superconductor Interface with Annealed Ag spray layers and Ag precoating layers," *Transactions of Nonferrous Metals Society of China,* vol. 19, pp. 961-964, Aug 2009.

[16] L. J. Masur, D. Buczek, E. Harley, T. Kodenkandath, X. Li, J. Lynch, N. Nguyen, M. Rupich, U. Schoop, J. Scudiere, E. Siegal, C. Thieme, D. Verebelyi, W. Zhang, and J. Kellers, "The Status of Commercial and Developmental HTS wires," *Physica C-Superconductivity and Its Applications,* vol. 392, pp. 989-997, Oct 2003.

[17] R. M. Scanlan, A. P. Malozemoff, and D. C. Larbalestier, "Superconducting Materials for Large Scale Applications," *Proceedings of the IEEE,* vol. 92, pp. 1639-1654, Oct 2004.

[18] A. P. Malozemoff, J. Maguire, B. Gamble, and S. Kalsi, "Power Applications of High-Temperature Superconductors: Status and Perspectives," *IEEE Transactions on Applied Superconductivity,* vol. 12, pp. 778-781, Mar 2002.

[19] J. Lu, E. S. Choi, and H. D. Zhou, "Physical Properties of Hastelloy® C-276™ at Cryogenic Temperatures," *Journal of Applied Physics,* vol. 103, p. 6, Mar 2008.

[20] Y. Fu, O. Tsukamoto, and A. Furuse, "Copper Stabilization of YBCO Coated Conductor for Quench Protection," *IEEE Transactions on Applied Superconductivity,* vol. 13, pp. 1780-1783, Jun 2003.

[21] V. E. Sytnikov, V. S. Vysotsky, I. P. Radchenko, and N. V. Polyakova, "1G Versus 2G-Comparison from the Practical Standpoint for HTS Power Cales Use," *Journal of Physics: Conference Series,* vol. 97, p. 012058, 2008.

[22] F. London and H. London, "The Electromagnetic Equations of the Supraconductor," *Proceedings of the Royal Society of London A: Mathematical, Physical and Engineering Sciences,* vol. 149, pp. 71-88, Mar 1935.

[23] A. A. Abrikosov, "The Magnetic Properties of Superconducting Alloys," *Journal of Physics and Chemistry of Solids,* vol. 2, pp. 199-208, 1957.

[24] C. P. Bean, "Magnetization of High-Field Superconductors," *Reviews of Modern Physics,* vol. 36, pp. 31-39, 1964.

[25] C. P. Bean, "Magnetization of Hard Superconductors," *Physical Review Letters,* vol. 8, pp. 250-253, 1962.

[26] C. W. Chen, *Magnetism and Metallurgy of Soft Magnetic Materials*, Dover Publications, 2013.

[27] M. N. Wilson, "NbTi Superconductors with Low AC Loss: A review," *Cryogenics,* vol. 48, pp. 381-395, July 2008.

[28] N. Amemiya and Y. Ohta, "Mode of Magnetic Flux Penetration into High T_c Superconductors with Various Cross-Sectional Shape and Their AC Loss Characteristics," *Physica C: Superconductivity and its Applications,* vol. 357–360, Part 2, pp. 1134-1143, Aug 2001.

[29] B. A. Glowacki and M. Majoros, "A Method for Decreasing Transport AC Losses in Multifilamentary and Multistrip Superconductors," *Superconductor Science and Technology,* vol. 13, p. 971, 2000.

[30] N. Amemiya, S. Kasai, K. Yoda, Z. Jiang, G. A. Levin, P. N. Barnes, and C. E. Oberly, "AC Loss Reduction of YBCO Coated Conductors by Multifilamentary Structure," *Superconductor Science and Technology,* vol. 17, pp. 1464-1471, 2004.

[31] P. N. Barnes, G. A. Levin, C. Varanasi, and M. D. Sumption, "Low AC Loss Structures in YBCO Coated Conductors with Filamentary Current Sharing," *IEEE Transactions on Applied Superconductivity,* vol. 15, pp. 2827-2830, Jun 2005.

[32] M. D. Sumption, E. W. Collings, and P. N. Barnes, "AC loss in striped (filamentary) YBCO coated conductors leading to designs for high frequencies and field-sweep amplitudes," *Superconductor Science and Technology,* vol. 18, p. 122, 2005.

[33] N. Amemiya, K. Yoda, S. Kasai, J. Zhenan, G. A. Levin, P. N. Barnes, and C. E. Oberly, "AC Loss Characteristics of Multifilamentary YBCO Coated Conductors," *IEEE Transactions on Applied Superconductivity,* vol. 15, pp. 1637-1642, 2005.

[34] K. Suzuki, M. Yoshizumi, T. Izumi, Y. Shiohara, M. Iwakuma, A. Ibi, S. Miyata, and Y. Yamada, "Development of Scribing Process of Coated Conductors for Reduction of AC Losses," *Physica C: Superconductivity and its Applications,* vol. 468, pp. 1579-1582, Sep 2008.

[35] D. W. Hazelton, Y. Y. Xie, Y. Qiao, E. Zhang, and V. Selvamanickam, "SuperPower's Second Generation HTS Conductor Design for Stability and Low AC Losses," *AIP Conference Proceedings,* vol. 824, pp. 859-868, 2006.

[36] Y. Y. Xie, M. Marchevsky, X. Zhang, K. Lenseth, Y. Chen, X. Xiong, Y. Qiao, A. Rar, B. Gogia, R. Schmidt, A. Knoll, V. Selvamanickam, G. G. Pethuraja, and P. Dutta, "Second-Generation HTS Conductor Design and Engineering for Electrical Power Applications," *IEEE Transactions on Applied Superconductivity,* vol. 19, pp. 3009-3013, 2009.

[37] Ľ. Kopera, V. Šmatko, W. Prusseit, M. Polák, R. Semerad, V. Štrbík, and J. Šouc, "In Situ Patterning of Filamentary YBCO Coated Conductors," *Physica C: Superconductivity and its Applications,* vol. 468, pp. 2351-2355, 2008.

[38] B. A. Glowacki and M. Mosiadz, "The Role of Sol Gel Processing in the Development of High-Temperature Superconductors for AC Applications," *Journal of Sol-Gel Science and Technology,* vol. 51, pp. 335-347, 2009.

[39] S. C. Hopkins, D. Joseph, T. B. Mitchell-Williams, A. Calleja, V. R. Vlad, M. Vilardell, S. Ricart, X. Granados, T. Puig, X. Obradors, A. Usoskin, M. Falter, M. Backer, and B. A. Glowacki, "Inkjet Printing of Multifilamentary YBCO for Low AC Loss Coated Conductors," in *11th European Conference on Applied Superconductivity*. vol. 507, S. Farinon, I. Pallecchi, A. Malagoli, and G. Lamura, Eds., ed, IOP Publishing Ltd, 2014.

[40] G. Majkic, I. Kesgin, Y. Zhang, Y. Qiao, R. Schmidt, and V. Selvamanickam, "AC Loss Filamentization of 2G HTS Tapes by Buffer Stack Removal," *IEEE Transactions on Applied Superconductivity,* vol. 21, pp. 3297-3300, 2011.

[41] X. Cai, I. Kesgin, R. Schmidt, Y. Chen, and V. Selvamanickam, "Completely Etch-Free Fabrication of Multifilamentary Coated Conductor Using Inkjet Printing and Electrodeposition," *IEEE Transactions on Applied Superconductivity,* vol. 23, Jun 2013.

[42] G. A. Levin, J. Murphy, T. J. Haugan, and J. Š. more, "AC Losses of Copper Stabilized Multifilament YBCO Coated Conductors," *IEEE Transactions on Applied Superconductivity,* vol. 23, 2013.

[43] M. Vojenciak, A. Kario, B. Ringsdorf, R. Nast, D. C. van der Laan, J. Scheiter, A. Jung, B. Runtsch, F. Gomory, and W. Goldacker, "Magnetization ac loss reduction in HTS CORC® cables made of striated coated conductors," *Superconductor Science and Technology,* vol. 28, p. 9, Oct 2015.

[44] N. Plakida, *High-Temperature Cuprate Superconductors: Experiment, Theory, and Applications*, Springer, 2010.

[45] D. J. Hayes, D. B. Wallace, M. T. Boldman, and M. Int Soc Hybrid, "Picoliter Solder Droplet Dispensing," in *Ishm 92 Proceedings : Proceedings of the 1992 International Symposium on Microelectronics*. vol. 1847, ed, SPIE - Int Soc Optical Engineering, 1992, pp. 316-321.

[46] H. J. Chang, M. H. Tsai, and W. S. Hwang, "The Simulation of Micro Droplet Behavior of Molten Lead-Free Solder in Inkjet Printing Process and its Experimental Validation," *Applied Mathematical Modelling,* vol. 36, pp. 3061-3073, Jul 2012.

[47] S. H. Rahul, K. Balasubramanian, and S. Venkatesh, "Inkjet Printing of Yttria Stabilized Zirconia Nano Particles on Metal Substrates," *International Journal of Precision Engineering and Manufacturing,* vol. 16, pp. 2553-2561, Nov 2015.

[48] D. Tripkovic, J. Vukmirovic, B. Bajac, N. Samardzic, E. Djurdjic, G. Stojanovic, and V. V. Srdic, "Inkjet Patterning of *In Situ* Sol-Gel Derived Barium Titanate Thin Films," *Ceramics International,* vol. 42, pp. 1840-1846, 2016.

[49] C. W. Sele, T. von Werne, R. H. Friend, and H. Sirringhaus, "Lithography-Free, Self-Aligned Inkjet Printing with Sub-Hundred-Nanometer Resolution," *Advanced Materials,* vol. 17, p. 997, Apr 2005.

[50] M. Mosiadz, R. I. Tomov, S. C. Hopkins, G. Martin, B. Holzapfel, B. A. Glowacki, and Iop, "Inkjet Printing of Multiple $Ce_{0.8}Gd_{0.2}O_2$ Buffer Layers on a Ni-5% W Substrate," in *9th European Conference on Applied Superconductivity*. vol. 234, ed, IOP Publishing Ltd, 2010.

[51] F. Zhang, C. Tuck, R. Hague, Y. F. He, E. Saleh, Y. Li, C. Sturgess, and R. Wildman, "Inkjet Printing of Polyimide Insulators for the 3D Printing of Dielectric Materials for Microelectronic Applications," *Journal of Applied Polymer Science,* vol. 133, p. 11, May 2016.

[52] R. I. Tomov, M. Krauz, J. Jewulski, S. C. Hopkins, J. R. Kluczowski, D. M. Glowacka, and B. A. Glowacki, "Direct Ceramic Inkjet Printing of Yttria-Stabilized Zirconia Electrolyte Layers for Anode-Supported Solid Oxide Fuel Cells," *Journal of Power Sources,* vol. 195, pp. 7160-7167, 2010.

[53] H. Sirringhaus, T. Kawase, R. H. Friend, T. Shimoda, M. Inbasekaran, W. Wu, and E. P. Woo, "High-Resolution Inkjet Printing of All-Polymer Transistor Circuits," *Science,* vol. 290, pp. 2123-2126, Dec 2000.

[54] V. Marin, E. Holder, M. M. Wienk, E. Tekin, D. Kozodaev, and U. S. Schubert, "Ink-Jet Printing of Electron Donor/Acceptor Blends: Towards Bulk Heterojunction Solar Cells," *Macromolecular Rapid Communications,* vol. 26, pp. 319-324, Feb 2005.

[55] T. Aernouts, T. Aleksandrov, C. Girotto, J. Genoe, and J. Poortmans, "Polymer Based Organic Solar Cells Using Ink-jet Printed Active Layers," *Applied Physics Letters,* vol. 92, p. 033306, 2008.

[56] K. Crowley, E. O'Malley, A. Morrin, M. R. Smyth, and A. J. Killard, "An Aqueous Ammonia Sensor Based on an Inkjet-Printed Polyaniline Nanoparticle-Modified Electrode," *Analyst,* vol. 133, pp. 391-399, 2008.

[57] J. Jang, J. Ha, and J. Cho, "Fabrication of Water-Dispersible Polyaniline-Poly(4-styrenesulfonate) Nanoparticles For Inkjet-Printed Chemical-Sensor Applications," *Advanced Materials,* vol. 19, pp. 1772-1775, 2007.

[58] H. Kipphan, *Handbook of Print Media - Technologies and Production Methods*, Springer, 2001.

[59] Y. Wang and J. Bolkor, "Ultra-High-Resolution Monolithic Thermal Bubble Inkjet Print Head," *Journal of Micro-Nanolithography Mems and Moems,* vol. 6, p. 10, Oct-Dec 2007.

[60] A. K. Sen and J. Darabi, "Droplet Ejection Performance of a Monolithic Thermal Inkjet Print Head," *Journal of Micromechanics and Microengineering,* vol. 17, pp. 1420-1427, Aug 2007.

[61] Q. Gao, Y. He, J. Z. Fu, J. J. Qiu, and Y. A. Jin, "Fabrication of Shape Controllable Alginate Microparticles Based on Drop-on-Demand Jetting," *Journal of Sol-Gel Science and Technology,* vol. 77, pp. 610-619, Mar 2016.

[62] K. Li, J. K. Liu, W. S. Chen, L. Ye, and L. Zhang, "A Novel Bearing Lubricating Device Based on the Piezoelectric Micro-Jet," *Applied Sciences-Basel,* vol. 6, p. 15, Feb 2016.

[63] S. Ali, J. Bae, and C. H. Lee, "Organic Diode with High Rectification Ratio Made of Electrohydrodynamic Printed Organic Layers," *Electronic Materials Letters,* vol. 12, pp. 270-275, Mar 2016.

[64] P. Richner, S. J. P. Kress, D. J. Norris, and D. Poulikakos, "Charge Effects and Nanoparticle Pattern Formation in Electrohydrodynamic NanoDrip Printing of Colloids," *Nanoscale,* vol. 8, pp. 6028-6034, 2016.

[65] D. Soltman and V. Subramanian, "Inkjet-Printed Line Morphologies and Temperature Control of the Coffee Ring Effect," *Langmuir,* vol. 24, pp. 2224-2231, Mar 2008.

[66] M. S. Onses, E. Sutanto, P. M. Ferreira, A. G. Alleyne, and J. A. Rogers, "Mechanisms, Capabilities, and Applications of High-Resolution Electrohydrodynamic Jet Printing," *Small,* vol. 11, pp. 4237-4266, Sep 2015.

[67] B. J. de Gans and U. S. Schubert, "Inkjet Printing of Well-Defined Polymer Dots and Arrays," *Langmuir,* vol. 20, pp. 7789-7793, Aug 2004.

[68] D. Soltman, B. Smith, S. J. S. Morris, and V. Subramanian, "Inkjet Printing of Precisely Defined Features Using Contact-Angle Hysteresis," *Journal of Colloid and Interface Science,* vol. 400, pp. 135-139, Jun 2013.

[69] J. Perelaer, B. J. de Gans, and U. S. Schubert, "Ink-Jet Printing and Microwave Sintering of Conductive Silver Tracks," *Advanced Materials,* vol. 18, p. 2101, Aug 2006.

[70] H. Minemawari, T. Yamada, H. Matsui, J. Tsutsumi, S. Haas, R. Chiba, R. Kumai, and T. Hasegawa, "Inkjet Printing of Single-Crystal Films," *Nature,* vol. 475, pp. 364-367, Jul 2011.

[71] K. Pataky, T. Braschler, A. Negro, P. Renaud, M. P. Lutolf, and J. Brugger, "Microdrop Printing of Hydrogel Bioinks into 3D Tissue-Like Geometries," *Advanced Materials,* vol. 24, p. 391, Jan 2012.

[72] P. C. Duineveld, "The Stability of Ink-Jet Printed Lines of Liquid with Zero Receding Contact Angle on a Homogeneous Substrate," *Journal of Fluid Mechanics,* vol. 477, pp. 175-200, Feb 2003.

[73] H. S. Chen, R. V. Kumar, and B. A. Glowacki, "Chemical Solution Deposited Lanthanum Zirconium Oxide Thin Films: Synthesis and Chemistry," *Materials Chemistry and Physics,* vol. 122, pp. 305-310, Jul 2010.

[74] H. S. Chen, R. V. Kumar, and B. A. Glowacki, "Study on Chemical-Solution-Deposited Lanthanum Zirconium Oxide Film Based on the Taguchi Method," *Journal of Sol-Gel Science and Technology,* vol. 51, pp. 102-111, Jul 2009.

[75] M. Mosiadz, R. I. Tomov, S. C. Hopkins, G. Martin, D. Hardeman, B. Holzapfel, and B. A. Glowacki, "Inkjet Printing of $Ce_{0.8}Gd_{0.2}O_2$ Thin Films on Ni-5%W Flexible Substrates," *Journal of Sol-Gel Science and Technology,* vol. 54, pp. 154-164, 2010.

[76] M. Mosiadz, K. L. Juda, K. Vandaele, S. C. Hopkins, A. Patel, B. A. Glowacki, I. Van Driessche, J. Soloducho, M. Falter, and M. Backer, "Inkjet Printing, Pyrolysis and Crystallization of $YBa_2Cu_3O_{7-\delta}$ Precursor Layers for Fully Chemical Solution Deposited Coated Conductors," in *Superconductivity Centennial Conference 2011*. vol. 36, ed, Elsevier Science 2012, pp. 1450-1455.

[77] K. Vandaele, M. Mosiadz, S. C. Hopkins, A. Patel, I. Van Driessche, and B. A. Glowacki, "The Influence of Heat Treatment Parameters on Pyrolysed TFA-Derived YBCO Films Deposited by Inkjet Printing," *Materials Research Bulletin,* vol. 47, pp. 2032-2039, Aug 2012.

[78] E. Bartolome, V. R. Vlad, A. Calleja, M. Aklalouch, R. Guzman, J. Arbiol, X. Granados, A. Palau, X. Obradors, T. Puig, and A. Usoskin, "Magnetic and Structural Characterization of Inkjet-Printed ($YBa_2Cu_3O_{7-x}$)-Y-TFA/(MOD)CZO/(ABAD)YSZ/SS Coated Conductors," *Superconductor Science and Technology,* vol. 26, Dec 2013.

[79] I. V. Driessche, J. Feys, S. C. Hopkins, P. Lommens, X. Granados, B. A. Glowacki, S. Ricart, B. Holzapfel, M. Vilardell, A. Kirchner, and M. B. cker, "Chemical Solution Deposition Using Ink-Jet Printing for YBCO Coated Conductors," *Superconductor Science and Technology,* vol. 25, p. 065017, 2012.

[80] A. Usoskin, H. C. Freyhardt, A. Issaev, J. Dzick, J. Knoke, M. P. Oomen, M. Leghissa, and H. W. Neumueller, "Large Area YBCO-Coated Stainless Steel Tapes With High Critical Currents," *IEEE Transactions on Applied Superconductivity,* vol. 13, pp. 2452-2457, Jun 2003.

[81] A. Usoskin and H. C. Freyhardt, "YBCO-Coated Conductors Manufactured by High-Rate Pulsed Laser Deposition," *MRS Bulletin,* vol. 29, pp. 583-589, Aug 2004.

[82] Y. Iijima, K. Kakimoto, M. Kimura, K. Takeda, and T. Saitoh, "Reel to Reel Continuous Formation of Y-123 Coated Conductors by IBAD and PLD Method," *IEEE Transactions on Applied Superconductivity,* vol. 11, pp. 2816-2821, Mar 2001.

[83] B. Utz, R. Semerad, M. Bauer, W. Prusseit, P. Berberich, and H. Kinder, "Deposition of YBCO and NBCO Films on Areas of 9 Inches in Diameter," *IEEE Transactions on Applied Superconductivity,* vol. 7, pp. 1272-1277, Jun 1997.

[84] V. Selvamanickam, Y. M. Chen, X. M. Xiong, Y. Y. Xie, M. Martchevski, A. Rar, Y. F. Qiao, R. M. Schmidt, A. Knoll, K. P. Lenseth, and C. S. Weber, "High Performance 2G Wires: From R&D to Pilot-Scale Manufacturing," *IEEE Transactions on Applied Superconductivity,* vol. 19, pp. 3225-3230, Jun 2009.

[85] V. Selvamanickam, Y. Chen, X. Xiong, Y. Y. Xie, J. L. Reeves, X. Zhang, Y. Qiao, K. R. Lenseth, R. M. Schmidt, A. Rar, D. W. Hazelton, and K. Tekletsadik, "Recent Progress in Second-Generation HTS Conductor Scale-up at SuperPower," *IEEE Transactions on Applied Superconductivity,* vol. 17, pp. 3231-3234, Jun 2007.

[86] Y. Yasuji, K. Taiki, D. Takafumi, and K. Shugo, "Grain Boundary Flux Pinning Mechanism of Liquid-Phase-Sintered Bulk $YBa_2Cu_3O_x$," *Japanese Journal of Applied Physics,* vol. 46, p. 574, 2007.

[87] Y. Yamada, "Liquid-Phase Epitaxy Processing of $RBa_2Cu_3O_{7-\delta}$," *Superconductor Science and Technology,* vol. 13, p. 82, 2000.

[88] T. Araki and I. Hirabayashi, "Review of a Chemical Approach to $YBa_2Cu_3O_{7-x}$-Coated, Superconductors - Metalorganic Deposition Using Trifluoroacetates," *Superconductor Science and Technology,* vol. 16, pp. R71-R94, Nov 2003.

[89] M. W. Rupich, D. T. Verebelyi, W. Zhang, T. Kodenkandath, and X. P. Li, "Metalorganic Deposition of YBCO Films for Second-Generation High-Temperature Superconductor Wires," *MRS Bulletin,* vol. 29, pp. 572-578, Aug 2004.

[90] A. Takeshi, H. Izumi, S. Junko, and I. Yuichi, "High Critical Current Density Scheme of $YBa_2Cu_3O_{7-x}$ Films by the Metalorganic Deposition Using Trifluoroacetates," *Superconductor Science and Technology,* vol. 15, p. 913, 2002.

[91] T. Araki, K. Yamagiwa, and I. Hirabayashi, "Fabrication of $YBa_2Cu_3O_{7-x}$ Film by Metalorganic Deposition Method Using Trifluoroacetates and its Process Conditions," *Cryogenics,* vol. 41, pp. 675-681, Sep 2001.

[92] T. Araki, M. Hayashi, and H. Fuke, "Growth Mechanism During Firing Process of Single-Coated Thick YBCO Films by TFA-MOD," *IEEE Transactions on Applied Superconductivity,* vol. 23, p. 5, Jun 2013.

[93] T. Araki, T. Niwa, Y. Yamada, I. Hirabayashi, J. Shibata, Y. Ikuhara, K. Kato, T. Kato, and T. Hirayama, "Growth Model and the Effect of CuO Nanocrystallites on the Properties of Chemically Derived epitaxial Thin Films of $YBa_2Cu_3O_{7-x}$," *Journal of Applied Physics,* vol. 92, p. 3318, 2002.

[94] T. Araki, "Purified Coating Solution and Growth Scheme of the $YBa_2Cu_3O_{7-x}$ Superconductors in Metal Organic Deposition Using Trifluoroacetates," *Bulletin of the Chemical Society of Japan,* vol. 77, pp. 1051-1061, 2004.

[95] T. Araki, M. Hayashi, N. Kobayashi, and H. Fuke, "Required Crack-Preventing Chemicals and Chemical Background for Single-Coated Technology to YBCO Thick Films by TFA-MOD," *IEEE Transactions on Applied Superconductivity,* vol. 25, pp. 1-4, 2015.

[96] T. Araki, T. Yuasa, H. Kurosaki, Y. Yamada, I. Hirabayashi, T. Kato, T. Hirayama, Y. Iijima, and T. Saito, "High-J_c $YBa_2Cu_3O_{7-x}$ Films on Metal Tapes by the Metalorganic

deposition method using trifluoroacetates," *Superconductor Science and Technology,* vol. 15, pp. L1-L3, Jan 2002.

[97] T. Niwa, T. Araki, T. Muroga, Y. Iijima, Y. Yamada, T. Saitoh, I. Hirabayashi, and Y. Shiohara, "Calcining Conditions for $YBa_2Cu_3O_{7-x}$ Films by Metalorganic Deposition Using Trifluoroacetates," *IEEE Transactions on Applied Superconductivity,* vol. 13, pp. 2747-2750, Jun 2003.

[98] M. Miura, B. Maiorov, S. A. Baily, N. Haberkorn, J. O. Willis, K. Marken, T. Izumi, Y. Shiohara, and L. Civale, "Mixed Pinning Landscape in Nanoparticle-Introduced $YGdBa_2Cu_3O_y$ Films Grown by Metal Organic Deposition," *Physical Review B,* vol. 83, p. 8, May 2011.

[99] A. Satoshi, N. Masafumi, W. Kazuo, M. Masashi, Y. Masateru, I. Teruo, and S. Yuh, "Flux Pinning Properties of TFA-MOD $(Y,Gd)Ba_2Cu_3O_x$ Tapes with $BaZrO_3$ Nanoparticles," *Superconductor Science and Technology,* vol. 23, p. 014006, 2010.

[100] A. Goyal, J. Li, P. M. Martin, A. Gapud, E. D. Specht, M. Paranthaman, X. Li, W. Zhang, T. Kodenkandath, and M. W. Rupich, "Enhanced Flux-Pinning in Dy-Doped, MOD YBCO Films on RABiTS," *IEEE Transactions on Applied Superconductivity,* vol. 17, pp. 3340-3342, Jun 2007.

[101] F. Z. Ding, H. W. Gu, T. Zhang, H. Y. Wang, F. Qu, X. Y. Peng, and W. W. Zhou, "Enhanced flux pinning in MOD-YBCO films with co-doping of $BaCeO_3$ and Y_2O_3 nanoparitcles," *Acta Physica Sinica,* vol. 62, p. 6, Jul 2013.

[102] J. Matsuda, K. Nakaoka, T. Izumi, Y. Yamada, and Y. Shiohara, "Microstructure Evolution of YBCO Films Deposited by Advanced TFA-MOD Process," *Physica C: Superconductivity and its Applications,* vol. 468, pp. 1017-1023, Jul 2008.

[103] M. W. Rupich, X. Li, S. Sathyamurthy, C. Thieme, and S. Fleshler, "Advanced Development of TFA-MOD Coated Conductors," *Physica C: Superconductivity and its Applications,* vol. 471, pp. 919-923, 2011.

[104] X. Obradors, T. Puig, A. Pomar, F. Sandiumenge, S. Piñol, N. Mestres, O. Castaño, M. Coll, A. Cavallaro, A. Palau, J. Gázquez, J. C. González, J. Gutiérrez, N. Romà, S. Ricart, J. M. Moretó, M. D. Rossell, and G. v. Tendeloo, "Chemical Solution Deposition: a Path Towards Low Cost Coated conductors," *Superconductor Science and Technology,* vol. 17, p. 1055, 2004.

[105] Z. Yue, T. Xiao, W. Wei, and G. Jean-Claude, "Phase Evolution of $YBa_2Cu_3O_{7-x}$ films by all-chemical solution deposition route for coated conductors," *Journal of Physics: Conference Series,* vol. 507, p. 012056, 2014.

[106] W. Schwarzacher, O. I. Kasyutich, P. R. Evans, M. G. Darbyshire, G. Yi, V. M. Fedosyuk, F. Rousseaux, E. Cambril, and D. Decanini, "Metal nanostructures prepared by template electrodeposition," *Journal of Magnetism and Magnetic Materials,* vol. 199, pp. 185-190, Jun 1999.

[107] R. N. Bhattacharya, J. Chen, P. Spagnol, J. Y. Huang, and Z. F. Ren, "Superconductor Bi-oxide films via an electrodeposition process," *Superconductor Science & Technology,* vol. 17, pp. 120-124, Jan 2004.

[108] S. Rekhi, G. L. Bhalla, and G. C. Trigunayat, "Recovery of Superconductivity in the Water Degraded YBCO Samples," *Physica C: Superconductivity and its Applications,* vol. 307, pp. 51-60, Oct 1998.

[109] N. P. Bansal and A. L. Sandkuhl, "Chemical Durability of High-Temperature Superconductor $YBa_2Cu_3O_{7-x}$ in Aqueous Environments," *Applied Physics Letters,* vol. 52, p. 323, 1988.

[110] L. A. Angurel, M. Bona, J. M. Andrés, D. Muñoz-Rojas, and N. Casañ-Pastor, "High Quality Silver Contacts on Ceramic Superconductors Obtained by Electrodeposition from Non-aqueous Solvents," *Superconductor Science and Technology,* vol. 18, p. 135, 2005.

[111] R. N. Bhattacharya, J. Mann, Y. Qiao, Y. Zhang, and V. Selvamanickam, *Electrodeposited Ag-Stabilization Layer for High Temperature Superconducting Coated Conductors: Preprint*, 2010.

[112] Y. Zhang, "Electrodeposition of Silver Stabilizer Layer for Second Generation Superconducting Tapes," Master of Science in Materials Engineering, Department of Mechanical Engineering, University of Houston, 2011.

[113] S. Zhang, F. Cao, L. Chang, J. Zheng, Z. Zhang, J. Zhang, and C. Cao, "Electrodeposition of High Corrosion Resistance Cu/Ni–P Coating on AZ91D Magnesium Alloy," *Applied Surface Science,* vol. 257, pp. 9213-9220, 2011.

[114] X. Gao, J. Tang, Y. Zuo, Y. Tang, and J. Xiong, "The Electroplated Palladium–Copper Alloy Film on 316L Stainless Steel and its Corrosion Resistance in Mixture of Acetic and Formic Acids," *Corrosion Science,* vol. 51, pp. 1822-1827, Aug 2009.

[115] S. Arai and M. Endo, "Carbon Nanofiber–Copper Composite Powder Prepared by Electrodeposition," *Electrochemistry Communications,* vol. 5, pp. 797-799, 2003.

[116] J. Reid, "Copper Electrodeposition: Principles and Recent Progress," *Japanese Journal of Applied Physics Part 1-Regular Papers Short Notes & Review Papers,* vol. 40, pp. 2650-2657, Apr 2001.

[117] F. C. Walsh and M. E. Herron, "Electrocrystallization and Electrochemical Control of Crystal Growth: Fundamental Considerations and Electrodeposition of Metals," *Journal of Physics D: Applied Physics,* vol. 24, p. 217, 1991.

[118] N. D. Nikolić, L. J. Pavlović, M. G. Pavlović, and K. I. Popov, "Morphologies of Electrochemically Formed Copper Powder Particles and their Dependence on the Quantity of Evolved Hydrogen," *Powder Technology,* vol. 185, pp. 195-201, 7/10/ 2008.

[119] D. Grujicic and B. Pesic, "Electrodeposition of Copper: the Nucleation Mechanisms," *Electrochimica Acta,* vol. 47, pp. 2901-2912, Jul 2002.

[120] E. Mattsson and J. O. Bockris, "Galvanostatic Studies of the Kinetics of Deposition and Dissolution in the Copper + Copper Sulphate System," *Transactions of the Faraday Society,* vol. 55, pp. 1586-1601, 1959.

[121] J. M. Rosamilia, B. Miller, L. F. Schneemeyer, J. V. Waszczak, and H. M. Obryan, "Aqueous Electrochemistry of Cuprate-Based High-T_c Superconductors," *Journal of the Electrochemical Society,* vol. 134, pp. 1863-1864, Jul 1987.

[122] J. M. Rosamilia and B. Miller, "Electrodeposition on Cuprate-Based Superconductors in Nonaqueous Media," *Journal of the Electrochemical Society,* vol. 136, pp. 1053-1059, Apr 1989.

[123] Y. S. Chang, S. M. Ma, F. L. Yang, and C. S. Li, "Direct Electroplating Copper Film on the High-Tc Superconductor $YBa_2Cu_3O_{7-X}$ in Aqueous-Solution and its Electric Characteristic," *Materials Chemistry and Physics,* vol. 28, pp. 121-131, May 1991.

[124] U. Floegel-Delor, T. Riedel, D. Wippich, B. Goebel, R. Rothfeld, F. N. Werfel, A. Usoskin, A. Rutt, and Iop, "Copper - HTS Hybrid Conductor Architecture," in *9th European Conference on Applied Superconductivity*. vol. 234, ed, IOP Publishing Ltd, 2010.

[125] U. Floegel-Delor, T. Riedel, D. Wippich, R. Rothfeld, P. Schirrmeister, R. Koenig, F. N. Werfel, A. Usoskin, and A. Rutt, "Operation and Experience of a 2 km Coated Conductor REEL-to-REEL Copper Pulse Plating Facility," in *11th European Conference on Applied*

Superconductivity. vol. 507, S. Farinon, I. Pallecchi, A. Malagoli, and G. Lamura, Eds., ed, IOP Publishing Ltd, 2014.

[126] U. Floegel-Delor, T. Riedel, P. Schirrmeister, D. Wippich, R. Rothfeld, R. Koenig, and F. N. Werfel, "Optimum Design of Copper Stabilizer on Coated Conductors," *IEEE Transactions on Applied Superconductivity,* vol. 25, p. 4, Jun 2015.

[127] X. Cai, I. Kesgin, and V. Selvamanickam, "Reel-to-Reel Selective Electroplating of Cu Stabilizer for Multifilamentary Coated Conductors," *IEEE Transactions on Applied Superconductivity,* vol. 25, p. 4, Jun 2015.

[128] X. W. Cai, I. Kesgin, R. Schmidt, Y. M. Chen, and V. Selvamanickam, "Completely Etch-Free Fabrication of Multifilamentary Coated Conductor Using Inkjet Printing and Electrodeposition," *IEEE Transactions on Applied Superconductivity,* vol. 23, p. 5, Jun 2013.

[129] X. Li, R. Deng, Y. Li, B. Yao, Z. Ding, J. Qin, and Q. Liang, "Effect of Mg Doping on Optical and Electrical Properties of SnO_2 Thin Films: An Experiment and First-Principles Study," *Ceramics International,* vol. 42, pp. 5299-5303, 2016.

[130] P. Pascariu, A. Airinei, M. Grigoras, N. Fifere, L. Sacarescu, N. Lupu, and L. Stoleriu, "Structural, Optical and Magnetic Properties of Ni Doped SnO_2 Nanoparticles," *Journal of Alloys and Compounds,* vol. 668, pp. 65-72, May 2016.

[131] B. Orel, M. Macek, F. Svegl, and K. Kalcher, "Electrochromism of Iron-Oxide Films Prepared via the Sol-Gel Route by the Dip-Coating Technique," *Thin Solid Films,* vol. 246, pp. 131-142, Jun 1994.

[132] N. Özer and F. Tepehan, "Optical and Electrochemical Characteristics of Sol–Gel Deposited Iron Oxide Films," *Solar Energy Materials and Solar Cells,* vol. 56, pp. 141-152, Jan 1999.

[133] H. S. Choi and S. T. Hwang, "Sol-Gel-Derived Magnesium Oxide Precursor for Thin-Film Fabrication," *Journal of Materials Research,* vol. 15, pp. 842-845, Apr 2000.

[134] M. S. Mastuli, N. Kamarulzaman, M. A. Nawawi, A. M. Mahat, R. Rusdi, and N. Kamarudin, "Growth Mechanisms of MgO Nanocrystals via a Sol-Gel Synthesis Using Different Complexing Agents," *Nanoscale Research Letters,* vol. 9, pp. 1-9, Mar 2014.

[135] A. Merazga, F. Al-Subai, A. M. Albaradi, A. Badawi, A. Y. Jaber, and A. A. B. Alghamdi, "Effect of Sol-Gel MgO Spin-Coating on the Performance of TiO_2-Based Dye-Sensitized Solar Cells," *Materials Science in Semiconductor Processing,* vol. 41, pp. 114-120, Jan 2016.

[136] E. Celik, Y. Akin, I. H. Mutlu, W. Sigmund, and Y. S. Hascicek, "$BaZrO_3$ Insulation Coatings for HTS Coils," *Physica C: Superconductivity and its Applications,* vol. 382, pp. 355-360, Nov 2002.

[137] H. Yang, C. Zhou, X. Liu, Q. Zhou, G. Chen, W. Li, and H. Wang, "Piezoelectric Properties and Temperature Stabilities of Mn- and Cu-Modified $BiFeO_3$–$BaTiO_3$ High Temperature Ceramics," *Journal of the European Ceramic Society,* vol. 33, pp. 1177-1183, Jun 2013.

[138] H. T. Langhammer, T. Müller, R. Böttcher, V. Mueller, and H. P. Abicht, "Copper-doped Hexagonal Barium Titanate Ceramics," *Journal of the European Ceramic Society,* vol. 24, pp. 1489-1492, 2004.

[139] N. Kumada, H. Ogiso, K. Shiroki, S. Wada, Y. Yonesaki, T. Takei, and N. Kinomura, "Rising T_c in Bi and Cu Co-doped $BaTiO_3$," *Materials Letters,* vol. 64, pp. 383-385, Feb 2010.

[140] S. Keysar, Y. Cohen, S. Shagal, S. Slobodiansky, and G. S. Grader, "Effect of Aging on Alumina Gels Rheology and Aerogels Surface Area," *Journal of Sol-Gel Science and Technology,* vol. 14, pp. 131-136, 1999.

[141] G. A. Pozarnsky, L. Wright, and A. V. Mccormick, "Effects of Aging Time on V_2O_5 Sol-Gel Coatings," *Journal of Sol-Gel Science and Technology,* vol. 3, pp. 57-62, 1994.

[142] Q. Chang, S. Cerneaux, X. Wang, X. Zhang, Y. Wang, and J.-e. Zhou, "Evidence of ZrO_2 Sol–Gel Transition by Gelation Time and Viscosity," *Journal of Sol-Gel Science and Technology,* vol. 73, pp. 208-214, 2014.

[143] X. D. Lv, T. Li, H. W. Gu, and F. Z. Ding, "Influence of Water Vapor Pressure on Superconducting Properties of YBCO Film by TFA-MOD," *Journal of Superconductivity and Novel Magnetism,* vol. 23, pp. 1295-1299, Oct 2010.

[144] M. Mosiadz, K. L. Juda, S. C. Hopkins, J. Soloducho, and B. A. Glowacki, "An In-Depth *In Situ* IR Study of the Thermal Decomposition of Copper Trifluoroacetate Hydrate," *Journal of Fluorine Chemistry,* vol. 135, pp. 59-67, Mar 2012.

[145] C. F. Sanchez-Valdes, T. Puig, and X. Obradors, "*In Situ* Study Through Electrical Resistance of Growth Rate of Trifluoroacetate-Based Solution-Derived $YBa_2Cu_3O_7$ films," *Superconductor Science and Technology,* vol. 28, p. 11, Feb 2015.

[146] H. Chen, F. Feng, T. Qu, and Z. Han, "The Influence of Gas Flow Rate on the Growth of YBCO Films Prepared by TFA-MOD," *IEEE Transactions on Applied Superconductivity,* vol. 19, pp. 3123-3126, 2009.

[147] S. Nomoto, R. Teranishi, T. Honjo, T. Izumi, and Y. Shiohara, "Numerical Analysis of YBCO Crystal Growth in the TFA-MOD Process," *Materials Transactions,* vol. 46, pp. 922-929, 2005.

[148] B. Wuyts, V. V. Moshchalkov, and Y. Bruynseraede, "Resistivity and Hall Effect of Metallic Oxygen-Deficient $YBa_2Cu_3O_x$ Films in the Normal State," *Physical Review B,* vol. 53, pp. 9418-9432, Apr 1996.

[149] G. Fedor, "Characterization of High-Temperature Superconductors by AC Susceptibility Measurements," *Superconductor Science and Technology,* vol. 10, p. 523, 1997.

[150] Q. Y. Chen, "Ac Inductive Measurement - Its Application to the Studies of High-T_c Superconductivity," in *Magnetic Susceptibility of Superconductors and Other Spin Systems*, R. A. Hein, T. L. Francavilla, and D. H. Liebenberg, Eds., ed New York, Plenum Press Div Plenum Publishing Corp, 1991, pp. 81-105.

[151] G. Grimaldi, M. Bauer, and H. Kinder, "Continuous Reel-to-Reel Measurement of Critical Currents of Coated Conductors," *Applied Physics Letters,* vol. 79, p. 4390, 2001.

[152] S. Furtner, R. Nemetschek, R. Semerad, G. Sigl, and W. Prusseit, "Reel-to-reel Critical Current Measurement of Coated Conductors," *Superconductor Science and Technology,* vol. 17, p. S281, 2004.

[153] X. F. Li, A. B. Yahia, G. Majkic, and V. Selvamanickam, "Scanning Hall Probe Microscopy on Laser Striated Multifilament Coated Conductor," *IEEE Transactions on Applied Superconductivity,* vol. 25, pp. 1-4, 2015.

[154] I. Kesgin, "Processing and Electromagnetic Properties of Low AC Loss Multifilamentary Rare Earth-Barium-Copper-Oxide Superconductor Tapes," Doctor of Philosophy in Mechanical Engineering, Department of Mechanical Engineering, University of Houston, 2013.

[155] M. Marchevsky, E. Zhang, Y. Y. Xie, V. Selvamanickam, and P. G. Ganesan, "AC Losses and Magnetic Coupling in Multifilamentary 2G HTS Conductors and Tape Arrays," *IEEE Transactions on Applied Superconductivity,* vol. 19, pp. 3094-3097, Jun 2009.

[156] C. E. Oberly, G. L. Rhoads, P. N. Barnes, L. Long, D. J. Scott, and W. J. Carr, "The Importance of Interfilamentary Barrier Resistance in YBCO Coated Conductor to Minimize AC Losses," in *Advances in Cryogenic Engineering*. vol. 614, B. Balachandran, D. Gubser, and K. T. Hartwig, Eds., ed, American Institute of Physics, 2002, pp. 621-630.

[157] C. A. J. Damen, H. J. H. Smilde, D. H. A. Blank, and H. Rogalla, "Selective Epitaxial Growth for YBCO Thin Films," *Superconductor Science and Technology,* vol. 11, p. 437, 1998.

[158] V. Smatko, F. Hanic, J. Souc, E. Kovácová, and V. Strbík, "Selective Deposition of Epitaxial YBCO Films on Al_2O_3/CeO_2 Substrate and Titanium Oxide Mask Applicable for Patterning of Stable Microbridges," *Superconductor Science and Technology,* vol. 11, p. 458, 1998.

[159] S. K. H. Lam and B. Sankrithyan, "HTSC Devices Fabricated by Selective Epitaxial Growth," *Superconductor Science and Technology,* vol. 12, p. 215, 1999.

[160] E. Demencik., M. Vojenciak, A. Kario, R. Nast, A. Jung, W. Goldacker, and F. Grilli, "AC Loss and Coupling Currents in YBCO Coated Conductors With Varying Number of Filaments," *IEEE Transactions on Applied Superconductivity,* vol. 24, pp. 1-8, 2014.

[161] R. Mallick, "Synthesis and Testing of Tin-Oxide Nanowires for Flux Pinning in 2nd Generation Superconductors," Master of Science in Mechanical Engineering, Department of Mechanical Engineering, University of Houston, 2015.

[162] J. Jang, H. Kang, H. C. N. Chakravarthula, and V. Subramanian, "Fully Inkjet-Printed Transparent Oxide Thin Film Transistors Using a Fugitive Wettability Switch," *Advanced Electronic Materials,* vol. 1, 2015.

[163] B. N. Joshi, H. Yoon, and S. S. Yoon, "Structural, optical and electrical properties of tin oxide thin films by electrostatic spray deposition," *Journal of Electrostatics,* vol. 71, pp. 48-52, Feb 2013.

[164] L. Spanhel and M. A. Anderson, "Semiconductor Clusters in the Sol-Gel Process - Quantized Aggregation, Gelation, and Crystal-Growth in Concentrated ZnO Colloids," *Journal of the American Chemical Society,* vol. 113, pp. 2826-2833, Apr 1991.

[165] J. Livage, J. P. Jolivet, and E. Tronc, "Proceedings of the Fifth International Workshop on Glasses and Ceramics from Gels Electronic Properties of Mixed Valence Oxide Gels," *Journal of Non-Crystalline Solids,* vol. 121, pp. 35-39, May 1990.

[166] A. A. Armenio, V. Pinto, A. Mancini, A. Augieri, V. Galluzzi, F. Rizzo, A. Rufoloni, A. Vannozzi, and G. Celentano, "Analysis of the Growth Process and Pinning Mechanism of Low-Fluorine MOD $YBa_2Cu_3O_{7-\delta}$ Films With and Without $BaZrO_3$ Artificial Pinning Centers," *IEEE Transactions on Applied Superconductivity,* vol. 25, p. 5, Jun 2015.

[167] V. Selvamanickam, M. H. Gharahcheshmeh, A. Xu, Y. Zhang, and E. Galstyan, "Requirements to Achieve High In-Field Critical Current Density at 30K in Heavily-Doped (Gd,Y)$Ba_2Cu_3O_x$ Superconductor Tapes," *Superconductor Science and Technology,* vol. 28, p. 5, Oct 2015.

[168] P. Paturi, M. Malmivirta, H. Palonen, and H. Huhtinen, "Dopant Diameter Dependence of J_c(B) in Doped YBCO Films," *IEEE Transactions on Applied Superconductivity,* vol. 26, p. 5, Apr 2016.

[169] H. L. Zhang, F. Z. Ding, H. W. Gu, Z. B. Dong, and F. Qu, "Fabrication of High-J_c $BaTiO_3$-doped $YBa_2Cu_3O_{7-\delta}$ Thin Films by the Low-Fluorine TFA-MOD Approach," *Journal of Alloys and Compounds,* vol. 664, pp. 5-10, Apr 2016.

[170] E. B. Rinker, D. W. Oelschlager, A. T. Colussi, K. R. Henry, and O. C. Sandall, "Viscosity, Density, and Surface Tension of Binary Mixtures of Water and N-Methyldiethanolamine and Water and Diethanolamine and Tertiary Mixtures of These Amines with Water over the Temperature Range 20-100˚C," *Journal of Chemical & Engineering Data,* vol. 39, pp. 392-395, Apr 1994.

[171] H. M. Dong, W. W. Carr, and J. F. Morris, "An Experimental Study of Drop-on-Demand Drop Formation," *Physics of Fluids,* vol. 18, p. 16, Jul 2006.

[172] H. C. Wu, H. J. Lin, Y. C. Kuo, and W. S. Hwang, "Simulation of Droplet Ejection for a Piezoelectric Inkjet Printing Device," *Materials Transactions,* vol. 45, pp. 893-899, Mar 2004.

[173] A. Shakeri, H. Abdizadeh, and M. R. Golobostanfard, "Synthesis and Characterization of Thick PZT Films via Sol–Gel Dip Coating Method," *Applied Surface Science,* vol. 314, pp. 711-719, Sep 2014.

[174] *MicroFab Technologies Inc. Products-Optics Subsystems* http://www.microfab.com/optics.

[175] G. A. Levin and P. N. Barnes, "Concept of Multiply Connected Superconducting Tapes," *IEEE Transactions on Applied Superconductivity,* vol. 15, pp. 2158-2161, Jun 2005.

[176] S. Jindasuwan, P. Sujaridworakun, S. Jinawath, and S. Supothina, "Effect of Heat Treatment Temperature on Surface Topography and Hydrophobicity of Polydimethylsiloxane/Titanium Oxide Hybrid Films," *Macromolecular Symposia,* vol. 264, pp. 90-94, 2008.

[177] V. R. Shinde, C. D. Lokhande, R. S. Mane, and S.-H. Han, "Hydrophobic and Textured ZnO Films Deposited by Chemical Bath Feposition: Annealing Effect," *Applied Surface Science,* vol. 245, pp. 407-413, May 2005.

[178] B. Gao, Z. H. Cai, J. Ni, F. Fan, L. L. Ying, C. Y. Bai, Y. M. Lu, Z. Y. Liu, and C. B. Cai, "Crystallization Characteristics of $YBa_2Cu_3O_{7-\delta}$ Film during TFA-MOD," *Journal of Superconductivity and Novel Magnetism,* vol. 25, pp. 17-23, Jan 2012.

[179] Y. Q. Chen, X. R. Yin, Y. Feng, W. B. Bian, M. J. Li, and J. F. Niu, "High-Efficiency Preparation of High-Quality YBCO Superconducting Films Using an Ultralow-Fluorine Sol-Gel Method," *Journal of Sol-Gel Science and Technology,* vol. 74, pp. 249-255, Apr 2015.

[180] L. E. Scriven, "Physics and Applications of DIP Coating and Spin Coating," *MRS Proceedings* vol. 121, p. 717, 1988.

[181] C. J. Brinker, A. J. Hurd, G. C. Frye, K. J. Ward, and C. S. Ashley, "Sol-gel Thin Film Formation," *Journal of Non-Crystalline Solids,* vol. 121, pp. 294-302, May 1990.

[182] K. Nakaoka, H. Ichikawa, M. Miura, Y. Sutoh, M. Yoshizumi, T. Izumi, Y. Yamada, and Y. Shiohara, "Investigation on Starting Solution of TFA-MOD Process for High-Speed Production of YBCO Coated Conductors," *Physica C-Superconductivity and Its Applications,* vol. 469, pp. 1326-1328, Aug-Oct 2009.

[183] S. Sato and I. Nakada, "Structure of Y_2BaCuO_5: a Refinement by Single-Crystal X-Ray Diffraction," *Acta Crystallographica Section C,* vol. 45, pp. 523-525, 1989.

[184] H. Jian-feng, Z. Xie-rong, C. Li-yun, and X. Xin-bo, "Preparation of Y_2BaCuO_5 nanoparticles by a co-precipitation process with the aid of ultrasonic irradiation," *Journal of Materials Processing Technology,* vol. 209, pp. 2963-2966, Mar 2009.

[185] M. Yurtcan, O. Simsek, M. Yilmaz, U. Hasar, M. Ertugrul, and O. Bayram, "Influence of Deposition Pressure (O_2) on the YBCO (Y123) Thin Films Prepared by Pulsed Laser Deposition," *Journal of Superconductivity and Novel Magnetism,* vol. 26, pp. 1873-1877, 2013.

[186] M. Fukumoto, H. Kodaka, T. Okada, H. Yoshida, and K. Yasohama, "Dependence of Inductively Measured Critical Temperature on Frequency and Amplitude of Applied Field in an *in situ* Nb3Sn superconductor," *Journal of Applied Physics,* vol. 59, p. 1395, 1986.

[187] K. No, D. Yoon, W. Suck Shin, W. Kim, and G. Shim, "Effects of Y2BaCuO5 on the Directional Growth of YBa2Cu3Ox Superconductor," *Journal of Materials Science,* vol. 29, pp. 2345-2349, 1994// 1994.

[188] A. Takeshi, K. Haruhiko, Y. Yutaka, H. Izumi, S. Junko, and H. Tsukasa, "Coating Processes for $YBa_2Cu_3O_{7-x}$ Superconductor by Metalorganic Deposition Method Using Trifluoroacetates," *Superconductor Science and Technology,* vol. 14, p. 783, 2001.

[189] T. Honjo, Y. Nakamura, R. Teranishi, Y. Tokunaga, H. Fuji, J. Shibata, S. Asada, T. Izumi, Y. Shiohara, Y. Iijima, T. Saitoh, A. Kaneko, and K. Murata, "Fabrication and Growth Mechanism of YBCO Coated Conductors by TFA-MOD Process," *Physica C: Superconductivity and its Applications,* vol. 392–396, Part 2, pp. 873-881, Oct 2003.

[190] K. Katayama, K. Nakahata, M. Yoshizumi, T. Izumi, and Y. Shiohara, "Improvement of Film Thickness Uniformity in TFA-MOD Coated Conductors," *Physics Procedia,* vol. 45, pp. 157-160, 2013.

[191] D. Grosso, "How to Exploit the Full Potential of the Dip-Coating Process to Better Control Film Formation," *Journal of Materials Chemistry,* vol. 21, pp. 17033-17038, 2011.

[192] J. A. Venables, *Introduction to Surface and Thin Film Processes*, Cambridge University Press, 2000.

[193] A. Pimpinelli and J. Villain., *Physics of Crystal Growth*, Cambridge University Press, 1998.

[194] W. A. Ainsworth, "Electrolytic Growth of Silver Dendrites," *Science,* vol. 146, pp. 1294-1295, 1964.

[195] K. Sreejith, J. Nuwad, C. Thinaharan, G. K. Dey, and C. G. S. Pillai, "Electrodeposition of silver nanodendrites," *Nanotechnology,* vol. 18, p. 125610, 2007.

[196] Z. Wang, Z. Zhao, and J. Qiu, "A General Strategy for Synthesis of Silver Dendrites by Galvanic Displacement under Hydrothermal Conditions," *Journal of Physics and Chemistry of Solids,* vol. 69, pp. 1296-1300, May 2008.

[197] T. Liu, Y. G. Zhao, T. B. Li, M. H. Zhu, L. W. Zhang, H. S. Huang, M. L. Liu, Y. L. Zhou, M. He, H. B. Lu, and B. S. Cao, "Correlation Between the Morphology of Ag and the Contact Resistivity of the Ag/$YBa_2Cu_3O_{7-\delta}$ Thin Film Contact," *Journal of Superconductivity,* vol. 14, pp. 455-459, 2001.

[198] P. G. Slade, *Electrical Contacts: Principles and Applications*, Taylor & Francis, 2013.

[199] J. M. Rosamilia and B. Miller, "Additive Enhanced Nonaqueous Electrodeposition of Silver on $Ba_2YCu_3O_7$," *Journal of Materials Research,* vol. 5, pp. 1612-1615, 1990.

[200] N. D. Nikolic, K. I. Popov, L. J. Pavlovic, and M. G. Pavlovic, "Morphologies of Copper Deposits Obtained by the Electrodeposition at High Overpotentials," *Surface and Coatings Technology,* vol. 201, pp. 560-566, Oct 2006.

[201] E. Barsoukov and J. R. Macdonald, *Impedance Spectroscopy: Theory, Experiment, and Applications*, John Wiley & Sons, 2005.

[202] V. Fleury, M. Rosso, J. N. Chazalviel, and B. Sapoval, "Experimental Aspects of Dense Morphology in Copper Electrodeposition," *Physical Review A,* vol. 44, pp. 6693-6705, Nov 1991.

[203] Harinaldi, "On the Hydrodynamics Turbulent Control of Mass Transfer in Electrodeposition Process," *International Journal of Mechanical & Mechatronics Engineering* vol. 11, pp. 1-7, 2011.

[204] G. A. Levin, P. N. Barnes, J. W. Kell, N. Amemiya, Z. Jiang, K. Yoda, and F. Kimura, "Multifilament $YBa_2Cu_3O_{6+x}$-Coated Conductors with Minimized Coupling Losses," *Applied Physics Letters,* vol. 89, p. 3, Jul 2006.

[205] N. Amemiya, S. Kasai, K. Yoda, Z. N. Jiang, G. A. Levin, P. N. Barnes, and C. E. Oberly, "AC loss reduction of YBCO coated conductors by multifilamentary structure," *Superconductor Science & Technology,* vol. 17, pp. 1464-1471, Dec 2004.

[206] I. Kesgin, G. A. Levin, T. J. Haugan, and V. Selvamanickam, "Multifilament, Copper-Stabilized Superconductor Tapes with Low Alternating Current Loss," *Applied Physics Letters,* vol. 103, p. 3, Dec 2013.

[207] M. J. Perricone, J. N. Dupont, and M. J. Cieslak, "Solidification of Hastelloy Alloys: An Alternative Interpretation," *Metallurgical and Materials Transactions A,* vol. 34A, pp. 1127-1132, May 2003.

[208] K. W. Harrison, C. D. Corolewski, M. D. McCluskey, J. Lindemuth, S. Ha, and M. G. Norton, "Electronic Transport in Molybdenum Dioxide Thin Films," *Journal of Materials Science-Materials in Electronics,* vol. 26, pp. 9717-9720, Dec 2015.

[209] O. Tsukamoto, N. Sekine, M. Ciszek, and J. Ogawa, "A Method to Reduce Magnetization Losses in Assembled Conductors Made of YBCO Coated Conductors," *IEEE Transactions on Applied Superconductivity,* vol. 15, pp. 2823-2826, Jun 2005.

[210] Y. Mawatari, "Critical State of Periodically Arranged Superconducting-Strip Lines in Perpendicular Fields," *Physical Review B,* vol. 54, pp. 13215-13221, Nov 1996.